EXAMINING SOURCES AND DYNAMICS OF SOIL NITRIC OXIDE USING STABLE ISOTOPE TECHNIQUES

by

Zhongjie Yu

B. S. in Geographical Sciences, East China Normal University, 2008

M. S. in Environmental Geochemistry, East China Normal University, 2011

M. S. in Environmental Geophysics, Rutgers University, 2013

Submitted to the Graduate Faculty of

The Kenneth P. Dietrich School of Arts and Sciences in partial fulfillment

of the requirements for the degree of

Doctor of Philosophy

University of Pittsburgh

2018

UNIVERSITY OF PITTSBURGH

KENNETH P. DIETRICH SCHOOL OF ARTS AND SCIENCES

This dissertation was presented

by

Zhongjie Yu

It was defended on

August 10, 2018

and approved by

Greg Michalski, Associate Professor, Earth, Atmospheric, and Planetary Sciences, Purdue University

Daniel Bain, Assistant Professor, Geology and Environmental Science

Brian Stewart, Associate Professor, Geology and Environmental Science

Josef Werne, Professor, Geology and Environmental Science

Dissertation Advisor: Emily Elliott, Associate Professor, Geology and Environmental Science

EXAMINING SOURCES AND DYNAMICS OF SOIL NITRIC OXIDE USING STABLE ISOTOPE TECHNIQUES

Zhongjie Yu, Ph.D.

University of Pittsburgh, 2018

Emissions of nitrogen oxides (NO_x) degrade air quality and affect global tropospheric chemistry. Nitric oxide (NO) produced during microbial nitrification and denitrification in soils is an important source of atmospheric NO_x. However, due to the diffuse nature, low concentrations, and high sensitivity to changing climatic and soil state variables, soil NO emissions are notoriously difficult to quantify. Consequently, it remains unclear how NO production is mediated by nitrogen (N) transformation processes in soil.

Stable isotope techniques are an emerging tool for characterizing the soil N cycle. This dissertation presents a comprehensive methodological framework for examining soil NO dynamics and its driving forces using stable N and oxygen (O) isotopes. A new analytical method was developed to measure N isotopes of soil-emitted NO (δ^{15}N-NO) with a precision of ±1.1‰. Application of this new method in laboratory and field soil wetting experiments yielded results with important implications for understanding the mechanisms that sustain wetting-triggered NO emission pulses. To bridge NO emission with soil N transformations, a numerical model exploiting NO_3^- ^{17}O anomaly (Δ^{17}O) as a conservative tracer was developed to quantify soil nitrification and NO_3^- consumption rates. Field application of this model revealed co-occurring nitrification and denitrification in surface soil after a snowmelt event, leading to insights into the isotopic systematics of soil NO_3^- cycling. Coupling the δ^{15}N-NO analysis with the Δ^{17}O-based model, a series of laboratory experiments was conducted to characterize NO production during nitrification and denitrification in an agricultural soil. The results show that nitrification and denitrification

have distinguishable isotopic imprints on NO production and that denitrification is a significant, yet under-characterized source of soil NO production even under conditions strongly favoring nitrification. Finally, a year-long measurement of NO_3^- in surface soil and lysimeter water was conducted at three field sites with contrasting N availability. The measured NO_3^- concentrations and dual isotopes ($\delta^{15}N$ and $\delta^{18}O$) were used in an isotopic mass balance model to examine ecosystem N saturation, hydrological NO_3^- leaching, and denitrification. Overall, the results from this work provide process-based information about soil NO dynamics and its underlying processes that may help constrain soil NO emission at various scales.

TABLE OF CONTENTS

LIST OF TABLES

LIST OF FIGURES

PREFACE

Wherever I go I will always be at home with my wife and son. I'm extremely grateful to have Ying and James whose smiles, love, and support were an integral part of my perseverance along this journey. I would also like to thank my parents and grandparents. It is their foundation upon which I build that allows for our generational rise in education and quality of life. I will forever be grateful to all of them.

I thank my adviser, Dr. Emily Elliott, for giving me the time, resources, support, generosity and encouragement to carry out my research. Her method of mentoring has taught me the value of hard work, independent thinking, and the benefits of letting curiosity shape your learning. I could not have asked for a better advisor than Emily.

My Ph.D. committee, including Drs. Daniel Bain, Greg Michalski, Brian Stewart, and Josef Werne, has been great. They have been helpful and provided much encouragement throughout my research. Special thanks to Dr. Bain for his guidance on chemical analysis and his patience and willingness to answer my questions about soils and hydrology.

I would like to acknowledge Dr. Elliott and the Andrew Mellon Predoctoral Fellowship for financially supporting me during my Ph.D. I am honored and thankful to have received the Henry Leighton Memorial Graduate Award as well.

Thank you to my fellow (past and present) students and colleagues in the Department of Geology and Environmental Science. Katherine Redling and Richard Dabundo have been providing invaluable technical support to my research. I appreciate all the hard work and help of Robert Rossi and Duo Wu (Lanzhou University) during field work. The following people were extremely helpful during the past 5 years: Dr. David Felix, Dr. Marion Divers, Dr. Lucy Rose,

Justin Coughlin, Kassia Groszewski, Becky Forgrave, Angela Chung, Mark River, Troy Ferland, Vivan Feng, Madeline Ellgass, Madeline Gray, Thomas Gasmire the University Machine Shop staff, and Lori Neu the University Glass Shop staff.

I have some advice for those wishing to pursue graduate education. To me, good researchers are just like professional athletes. There is no substitute for hard work. Time and perseverance are critical. However, suffering is a part of earning the Ph.D. It's not the number of times you get knocked down by failed experiments that matters, but that you pick yourself up, solve the problem, and move forward every time. When looking for direction, ask yourself: what do I want to learn about next? And lastly, even though you or others may put you down, or you have doubts about your knowledge or research skills, recognize and have the self confidence in your ability *to learn*.

1.0 INTRODUCTION

1.1 BACKGROUND

1.1.1 Production and emission of nitric oxide in soils

Global emissions of nitric oxide (NO) have increased dramatically over the last century primarily due to human activity (IPCC, 2013). Once emitted, NO is rapidly oxidized to nitrogen dioxide (NO_2) in the troposphere, and these compounds (collectively referred to NO_x) affect tropospheric ozone (O_3) production, secondary organic aerosol formation, and the atmospheric lifetime of carbon and methane, and can cause ecosystem acidification and eutrophication and human respiratory distress (Morin et al., 2008). Although fossil fuel combustion is the largest source of atmospheric NO_x (Jaeglé et al., 2005), NO is also produced in and emitted from natural and fertilized soils. While current bottom-up models based on extrapolation of individual field measurements place global soil NO emission at 6.6~10 Tg $N \cdot yr^{-1}$ (IPCC, 2013), accounting for about 15% of the global NO_x inventory, recent comparisons of these models and satellite-based NO_2 observations revealed significant underestimates of global soil NO emission (Bertram et al., 2005).

Numerous studies have demonstrated that microbial nitrification and denitrification are the primary sources of NO in soils (Liu et al., 2016). Heterotrophic denitrification is performed by

facultative anaerobic microorganisms through sequential reduction of nitrate (NO_3^-) or nitrite (NO_2^-) via NO and nitrous oxide (N_2O) to dinitrogen (N_2) under anoxic conditions (Figure 1.1) (Zumft, 1997). The enzymatic system of denitrification comprises a series of dedicated periplasmic and membrane-bound reductases with NO_2^- reductase (NIR) and NO reductase (NOR) being the key enzymes that mediate NO production and consumption, respectively. As a free intermediate in denitrification, NO serves as an electron acceptor for energy conservation and growth (Ye et al., 1994). On the other hand, NO reduction functions to prevent accumulation of NO to toxic levels (Schreiber et al., 2009). In pure cultures of heterotrophic denitrifiers, a change in oxygen (O_2) concentration often leads to transient production of NO (Kester et al., 1997; Bergaust et al., 2008). This transient production is attributed to selective O_2 inhibition to NOR and/or delay in synthesis of the denitrification system (Schreiber et al., 2009).

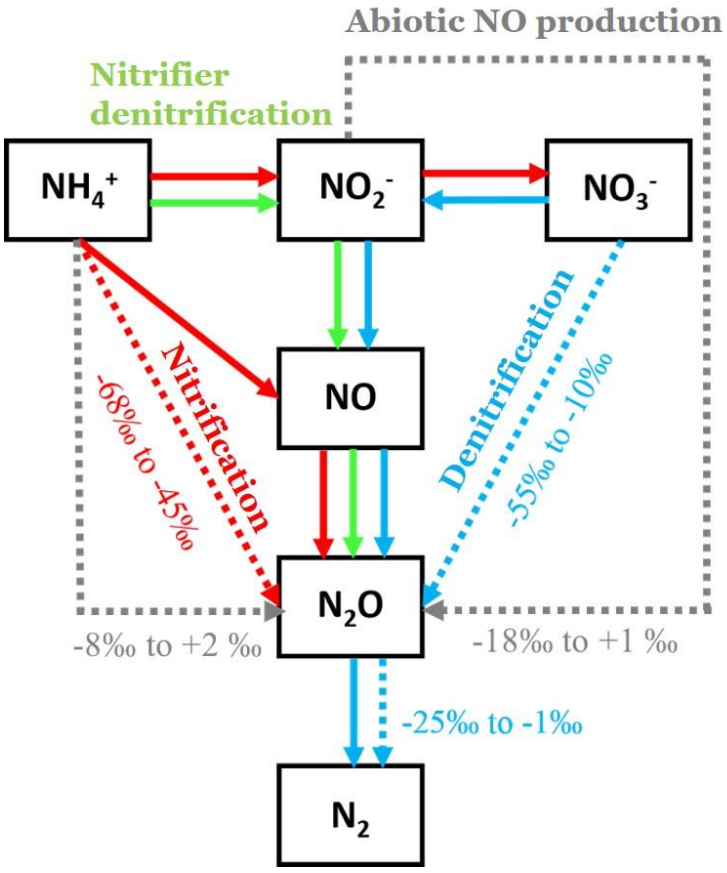

Figure 1.1 Microbial and abiotic pathways for NO turnover. Solid arrows with different colors denote soil NO-producing processes: nitrification (red), nitrifier denitrification (green), denitrification (blue), and abiotic reactions (grey). Dashed arrows denote apparent N isotope effects ($\delta_{product} - \delta_{substrate}$) associated with the respective processes.

Nitrification is the aerobic oxidation of ammonium (NH_4^+) via NO_2^- to NO_3^-. In the first step of nitrification performed by chemoautotrophic ammonia-oxidizing bacteria (AOB) or archaea, NH_4^+ is oxidized to hydroxylamine (NH_2OH), then further oxidized from NH_2OH to NO_2^- (Figure 1.1) (Shaw et al., 2006). High levels of NO can be produced by pure cultures of AOB, but the mechanism is not completely understood (Schreiber et al., 2012). Generally, two different pathways are inferred. First, the NH_2OH oxidation involves NO as an intermediate, which may

lead to NO release under certain physiological conditions (Hendrich et al., 2002). Second, the activity of nitrifier-encoded NIR and NOR reduces NO_2^- to NO and N_2O, termed "nitrifier denitrification" (Wrage et al., 2001). Results from pure culture investigations generally suggest that NH_2OH oxidation contributes to NO production mainly at high O_2 and NH_4^+ concentrations, whereas nitrifier denitrification is more active at low O_2 concentrations with the presence of NO_2^- (Yu et al., 2010; Wunderlin et al., 2012).

Soil NO emissions have also been intensively studied under complex field conditions. It has been shown that soil NO emissions vary greatly with climate and edaphic conditions but are most strongly correlated with soil nitrogen (N) availability, soil water content, and temperature. Hence soil NO emissions are dependent on regional temperature and precipitation patterns and fertilizer management practices (Bouwman et al., 2002). First proposed by Firestone and Davidson (1989), the "hole-in-the-pipe" (HIP) model has long been used as a conceptual model that bridges the ecological and microbiological factors controlling soil NO and N_2O emissions (Figure 1.2). Using a metaphor of a fluid flowing through a leaky pipe, rates of nitrification and denitrification are analogous to the flow of N through the pipe, whereas the sizes of the holes in the pipe determine the relative fractions of NO and N_2O that leak out. In this conceptual model, the substrates of nitrification and denitrification (i.e., NH_4^+ and NO_3^-) correlate with the sum of NO and N_2O emissions, while soil water content controls the ratio of NO and N_2O emissions. In particular, NO is assumed to be the dominant gas in dry, well-aerated soils where nitrification is often prevalent (Figure 1.2).

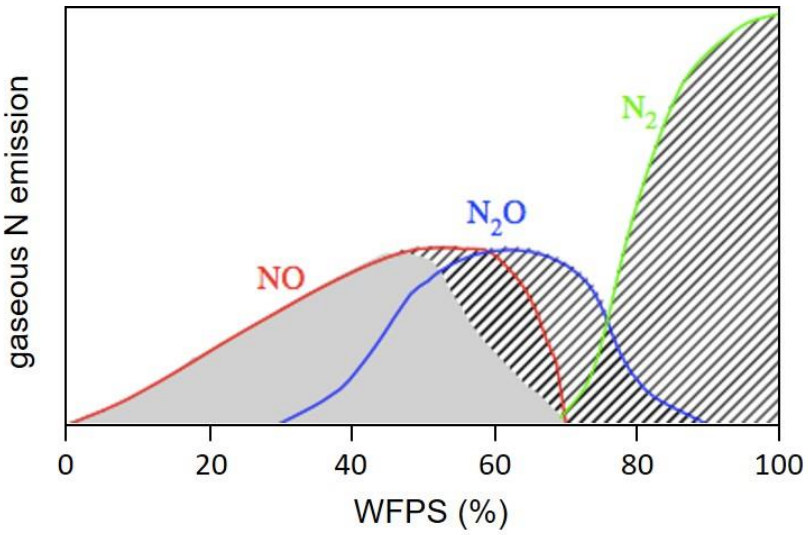

Figure 1.2 Relative contributions of nitrification (solid grey shading) and denitrification (hatched shading) to gaseous N emissions as a function of water-filled pore space in the HIP model. Modified from Firestone and Davidson, (1989).

However, recent observations that span large spatial and temporal scales challenge the simplicity of the HIP model for predicting soil NO emission. For example, in forested systems, the optimal soil water content for NO emission can vary from 15% water filled pore space (WFPS) to 65% WFPS and is partially determined by soil physical structure (e.g., particle size distribution and bulk density) (Schindlbacher et al., 2004). In agricultural soils, NO emission can be stimulated by high soil water content (e.g., 70-90% soil water holding capacity (WHC)) possibly due to activation of nitrifier denitrification under hypoxic conditions (Zhu et al., 2013). Further, in a study of incubated soil cores from a UK grassland, Loick et al. (2016) argued that denitrification in soil microsites is largely overlooked as a source of NO emission under moist to dry soil conditions. More importantly, pulse-like emissions of NO following rewetting of dry soil have often been observed in field conditions and may contribute up to 25% of annual emissions on a regional scale (Davidson et al., 1992; Bertram et al., 2005). However, the dynamic controls that

drive soil NO pulses under various field conditions remain mysterious (Homyak et al., 2016). This highlights a pressing need for new methods to disentangle the complexity of soil NO dynamics and its coupling to soil N transformations.

1.1.2 Source partitioning of soil nitrogen gas emissions using stable nitrogen isotopes

Natural abundance stable N isotopes (notated as $\delta^{15}N$ in ‰) in various soil N-containing compounds have long been used as an integrative tracer of soil N cycling. In order to extract the greatest information from the distribution of $\delta^{15}N$ values among various soil N compounds, the isotope effects for the relevant microbial reactions are needed. Recently, $\delta^{15}N$ values of soil-emitted N_2O ($\delta^{15}N\text{-}N_2O$) have been used to differentiate microbial N_2O formation pathways with varying degrees of success. In culture studies, N_2O produced during nitrification is associated with a large isotope effect ($\delta^{15}N\text{-}N_2O$ - $\delta^{15}N\text{-}NH_4^+$ = -68‰ to -45‰; Yoshida et al., 1984; Sutka et al., 2006) such that the produced N_2O is more depleted in ^{15}N than those produced during heterotrophic denitrification where $\delta^{15}N\text{-}N_2O$ is collectively controlled by N_2O production ($\delta^{15}N\text{-}N_2O$ - $\delta^{15}N\text{-}NO_3^-$ = -55‰ to -10‰) (Barford et al., 1999; Toyoda et al., 2005; Snider et al., 2009; Lewicka-Szcaebak et al., 2014) and N_2O reduction to N_2 ($\delta^{15}N\text{-}N_2$ - $\delta^{15}N\text{-}N_2O$ = -25‰ to -1‰) (Menyailo and Hungate, 2006; Ostrom et al., 2007; Well and Flessa, 2009) (Figure 1.1). Based on these results, $\delta^{15}N\text{-}N_2O$-based isotope models have been constructed to estimate the relative importance of nitrification and denitrification to soil N_2O emissions (Pérez et al., 2006; Decock and Six, 2013). However, given the fact that multiple reaction steps are involved in microbial N_2O production, and thus can complicate the use of $\delta^{15}N\text{-}N_2O$, modeled source contributions to soil N_2O emissions often have large uncertainties (e.g., ±40%) (Decock and Six, 2013).

Because NO is the direct precursor of N_2O in most microbial N transformation pathways, incorporation of the $\delta^{15}N$ values of soil NO ($\delta^{15}N$-NO) into soil N isotope systematics is expected to substantially improve source partitioning for both NO and N_2O emissions (Russow et al., 2009). However, soil $\delta^{15}N$-NO is notoriously hard to measure due to the its intermittent and diffuse nature, low concentration, and the high chemical reactivity of soil-emitted NO. So far, only a few studies have reported $\delta^{15}N$ values of NO from fertilized soils by collecting NO using denuders or impregnated filters (Ammann et al., 1999; Li and Wang et al., 2008; Felix and Elliott, 2014). While all of these studies report low $\delta^{15}N$-NO values (e.g. -49‰ to -20‰) characteristic of biogenic sources, limited information can be drawn from these studies to actually examine the biogeochemical controls on soil NO dynamics, due to low measurement precision and accuracy. In addition, there is also a growing interest in using $\delta^{15}N$ values of atmospheric N oxides (e.g., NO_2 and HNO_3) as a tracer to partition NO_x emission sources over large spatial and temporal scales (Hastings et al., 2013; Elliott et al., 2007; Elliott et al., 2009; Hastings et al., 2009), given that soil-emitted NO has significantly lower $\delta^{15}N$ values than NO_x from other major sources (Li and Wang, 2008; Felix and Elliott, 2013). Despite the promising potential, quantitative use of $\delta^{15}N$-NO is largely constrained by the absence of a robust method for collection of soil-emitted NO for N isotopic analysis.

1.1.3 Triple nitrate isotopes as a tracer of soil nitrification and denitrification

Natural abundance stable isotope ratios of N and oxygen (O) in NO_3^- (notated as $\delta^{15}N$-NO_3^- and $\delta^{18}O$-NO_3^-, respectively) are increasingly used to trace soil nitrification and denitrification at various spatiotemporal scales (Granger and Wankel, 2016; Denk et al., 2017). The tracing power of dual NO_3^- isotopes stems from the distinct isotopic fractionations associated with nitrification

and denitrification processes. Specifically, microbial nitrification strongly discriminates against ^{15}N, so that nitrification-produced NO_3^- has $\delta^{15}N$ values significantly lower than that of substrate NH_4^+ (Mariotti et al., 1981; Casciotti et al., 2003). Nitrification also imprints a biogenic $\delta^{18}O$ signature to NO_3^- (Casciotti et al., 2010; Buchwald and Casciotti, 2010) that is significantly lower than atmospheric NO_3^-, the other major NO_3^- source to natural ecosystems (Kendall et al., 2007). On the other hand, denitrification imparts large and coupled enrichment of both $\delta^{15}N$-NO_3^- and $\delta^{18}O$-NO_3^- values in pure culture studies (Granger et al., 2008; Granger et al., 2010) and can be used as a diagnostic signal of denitrification (Granger and Wankel, 2016). However, while plotting NO_3^- in dual isotope space can provide qualitative information regarding the occurrence of nitrification and denitrification processes (Figure 1.3a), quantitative process rate estimates cannot be readily obtained using dual NO_3^- isotopes, especially under dynamic soil redox conditions where nitrification and denitrification can co-occur (Hall et al., 2016).

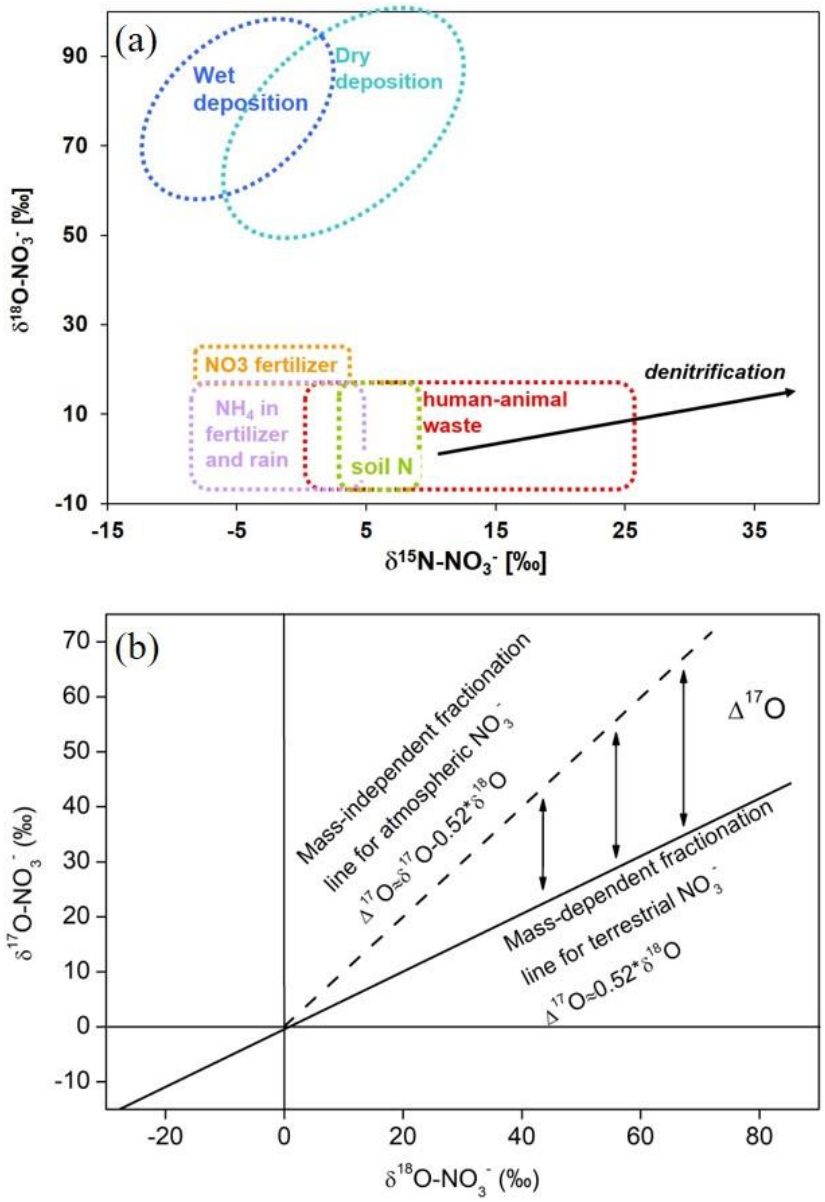

Figure 1.3 (a) Commonly reported values of $\delta^{15}N$ and $\delta^{18}O$ of nitrate for various sources (modified from Kendall et al. (2007)). Isotopic enrichment of the residual nitrate pool is depicted by the denitrification arrow. (b) Triple isotope plot of $\delta^{18}O$, $\delta^{17}O$, and $\Delta^{17}O$ (modified from Michalski et al. (2004)) The mass-dependent and mass-independent relationships between $\delta^{18}O$ and $\delta^{17}O$ are shown for different nitrate sources.

The NO_3^- ^{17}O anomaly has provided a new means by which soil nitrification and denitrification processes can be quantitatively characterized (Michalski et al., 2004; Fang et al., 2015). Atmospheric NO_3^- contains an anomalous ^{17}O excess over that which is expected based on ^{18}O abundances (Figure 1.3b) (Michalski et al., 2003). This deviation from the mass-dependent fractionation is attributed to O atom transfer from ozone during the formation of atmospheric NO_3^- (Thiemens, 2006) and quantified by a $\Delta^{17}O$ notation (Miller, 2002; Young et al., 2002). Because biological NO_3^- transformations in soil, such as nitrification and denitrification, obey the mass-dependent fractionation law (Figure 1.3b), $\Delta^{17}O$ of NO_3^- has great potential to resolve NO_3^- dynamics in a manner analogous to $^{15}NO_3^-$ tracer studies (Michalski et al., 2004). While $\Delta^{17}O$ has been increasingly used to examine atmospheric NO_3^- deposition and its subsequent retention in terrestrial and aquatic ecosystems (Riha et al., 2014; Rose et al., 2015a), few studies have explored the quantitative use of $\Delta^{17}O$ for probing microbial NO_3^- transformation and NO production in soils.

1.2 OBJECTIVES

While soil NO emissions have been increasingly measured using various methods ranging from laboratory incubations to satellite-based continental surveys, the biogeochemical mechanisms driving soil NO emission are still poorly understood and these impede development of process-based models of soil NO emission. Although the promise of stable isotope techniques for tracing soil N cycling has been demonstrated through various applications, no studies have characterized soil NO dynamics systematically using stable isotopes.

This dissertation presents a comprehensive methodological framework for examining soil NO dynamics using stable N and O isotopes. To achieve this, four stepwise research objectives were proposed:

(1) Develop a quantitative method for collection of soil-emitted NO for N isotopic analysis (δ^{15}N-NO) (Chapter 2; published in *Environmental Science & Technology*, 2017, 51, 6268-6278).

(2) Develop a numerical model to quantify soil NO_3^- cycling rates using Δ^{17}O of soil NO_3^- (Δ^{17}O-NO_3^-) (Chapter 3; in review, *Soil Biology & Biochemistry*).

(3) Characterize dynamics and microbial sources of soil NO under controlled conditions through combined use of δ^{15}N-NO and Δ^{17}O-NO_3^- (Chapter 4).

(4) Assess soil N cycling and its implications for ecosystem N retention at three field sites differing in N availability using dual NO_3^- isotopes (Chapter 5).

The outcomes from this research provide new information on the microbial and environmental controls of soil NO emissions and NO-producing processes. This knowledge will be useful for understanding how soil NO emissions contribute to watershed N retention and ultimately the land-atmosphere interactions of reactive N.

2.0 NOVEL METHOD FOR NITROGEN ISOTOPIC ANALYSIS OF SOIL-EMITTED NITRIC OXIDE

2.1 INTRODUCTION

Emissions of nitrogen oxides ($NO_x = NO + NO_2$) degrade air quality and affect global tropospheric chemistry (IPCC, 2013; Richter et al., 2005), posing a significant danger to ecosystem and human health (Jacob et al., 1996; Jang et al., 2002; Likens et al., 1996; Akimoto et al., 2003). Although fossil fuel combustion is currently the largest source of atmospheric NO_x (Jaeglé et al., 2005; Zhang et al., 2003), NO is also produced in and emitted from natural and fertilized soils (Galbally and Roy, 1978; Skiba et al., 1993; Yienger and Levy, 1995). Due to the spatial segregation of different NO_x sources and the short boundary layer lifetime of NO_x, there are substantial areas of the world (e.g., tropical and agricultural regions) where the local NO_x budget is controlled exclusively by soil NO emissions (Jacob et al., 1996; Jaeglé et al., 2005; Bertram et al., 2005; Hudman et al., 2010; Steinkamp and Lawrence, 2011; Vinken et al., 2014). In these regions, soil NO emissions govern the formation and lifetime of tropospheric ozone (O_3) and hydroxyl radical, driving reaction chains that produce environmentally important trace gases (e.g., nitric acid and peroxyacetyl nitrate) and biogenic secondary aerosols (Jang et al., 2002; Hudman et al., 2010; Steinkamp et al., 2009).

Various processes, both microbial (Skiba et al., 1993; Zumft, 1997; Kester et al., 1997; Firestone and Davidson, 1989) and abiotic (Venterea and Rolston, 2000; McCalley and Sparks, 2009; Homyak et al., 2017), are capable of producing NO in soils. Although the strong dependence of soil NO emission on edaphic and climatic factors has long been demonstrated by laboratory and

field studies (Yang and Meixner, 1997; Van Dijk et al., 2002; Hall and Matson, 1999; Davidson et al., 2000a; Davidson et al., 2000b), a process-based understanding of soil NO dynamics is lacking (Steinkamp and Lawrence, 2011; Hudman et al., 2012). More importantly, soil NO emission often exhibits an episodic nature (e.g., time scale of minutes), with pulse-like emission events being often triggered by rewetting of dry soils (Bertram et al., 2005; Hudman et al., 2010; Jaeglé et al., 2004; Oikawa et al., 2015; Davidson, 1992a; Davidson, 1992b; Homyak et al., 2016). In dry agricultural soils, massive NO pulses triggered by coupled fertilization and precipitation during warm seasons can result in daily O_3 enhancement up to 16 ppbv (Hudman et al., 2010). Unfortunately, the sources of and processes controlling the pulsed soil NO emission are still mysterious (Hudman et al., 2010; Steinkamp and Lawrence, 2011), making it difficult to model and up-scale field-observed NO fluxes. While empirical bottom-up models estimate that soil NO emission accounts for about 15% of the global NO_x inventory (IPCC, 2013), inversion of satellite-based NO_2 observations have indicated significant underestimates in soil NO emission (e.g., up to a factor of 3) at various spatiotemporal scales (Wang et al., 2007). Indeed, with the substantial reductions in NO_x emissions from combustion sources in many countries (Hudman et al., 2007), soils as a source of atmospheric NO_x may be more important than we thought, and there is a pressing need to elucidate mechanisms underlying soil NO dynamics Hudman et al., 2010; Steinkamp and Lawrence, 2011).

Stable nitrogen (N) isotope compositions at natural abundances (notated as $\delta^{15}N$) in various soil N-containing compounds are a robust tracer of soil N cycling (Mariotti et al., 1981; Sutka et al., 2006; Park et al., 2011; Denk et al., 2017). Incorporation of $\delta^{15}N$-NO measurements into the soil N isotope systematics is expected to provide a new process-level information of key mechanisms regulating NO production and consumption in soil. Moreover, there is a growing

interest in using $\delta^{15}N$ of atmospheric N oxides (e.g., NO_2 and nitrate (NO_3^-)) as a tracer to partition NO_x emission sources over large spatial and temporal scales (Hastings et al., 2013; Elliott et al., 2007; Elliott et al., 2009; Hastings et al., 2009). This interest stems from the observations that NO_x emitted from different sources has distinct $\delta^{15}N$ values (Felix et al., 2012; Redling et al., 2013; Walters et al., 2015a; Walters et al., 2015b; Fibiger et al., 2016) and that soil-emitted NO is presumably lower in $\delta^{15}N$ than NO_x from other natural and anthropogenic sources (Li and Wang, 2008; Felix and Elliott, 2013).

Despite its promising potential, soil $\delta^{15}N$-NO is rarely measured due to the intermittent nature and low magnitudes of soil NO emission. A summary of published NO_x collection methods is provided in Table A-1 in Appendix A), highlighting that none of existing methods have been rigorously verified for their suitability for soil-emitted NO. In pioneering work, Li and Wang (2008) fertilized a soil monolith in the laboratory and collected NO by first converting NO to NO_2 using a chromium trioxide (CrO_3)-impregnated solid oxidizer and then trapping the converted NO_2 in an annular denuder as nitrite (NO_2^-) for $\delta^{15}N$ analysis. However, it is well documented that NO oxidation efficiency of the CrO_3 oxidizer varies dramatically with sample relative humidity (RH) (e.g., <50% at RH>60%) (Hutchinson et al., 1998; Robinson et al., 1999). Due to this overlooked humidity interference, it is unclear whether N isotopic fractionation can occur during the NO oxidation under varying soil conditions. Recently, Fibiger et al. (2014) presented a NO_x collection method that utilizes a $KMnO_4$+NaOH solution to actively collect NO_x as NO_3^- for $\delta^{15}N$-NO_x determination. Sample $\delta^{15}N$-NO_x must be calculated using an isotope mass balance due to a high reagent blank in the solution (5-7 µM NO_3^-, $\delta^{15}N$=~2‰) (Fibiger et al., 2014). While the precision of this approach is ±1.5‰, this method is incompatible for $\delta^{15}N$-NO measurement of low and diffuse soil NO emissions, because larger error is propagated from the isotope mass balance

calculation if concentration and $\delta^{15}N$ value of collected soil NO are significantly lower than the blank.

Here, we present a new method for soil $\delta^{15}N$-NO determination (hereafter, "DFC-TEA method"). This method collects NO through NO conversion to NO_2 in excess O_3 and subsequent NO_2 collection in a triethanolamine (TEA) solution as NO_2^- and NO_3^- for $\delta^{15}N$ analysis. The NO collection approach is coupled to a soil dynamic flux chamber (DFC) system for simultaneous NO flux and $\delta^{15}N$-NO measurements. Both laboratory and field method verifications have been conducted to demonstrate suitability of the DFC-TEA method for accurate and precise soil $\delta^{15}N$-NO determination

2.2 EXPERIMENTAL SECTION

2.2.1 DFC system setup

The DFC is a technique that has been developed to continuously measure soil-atmosphere fluxes of various compounds including NO (Kester et al., 1997; Firestone and Davidson, 1989). A schematic of the developed DFC system is shown in Figure 1.1. The system consists of five components: air purification unit, gas dilution unit, flux chamber, NO-NO_x-NH_3 analyzer, and NO collection train. Zero air free of NO_x and O_3 is produced in the air purification unit for purging the flux chamber and providing air to a O_3 generator (Model 146i, Thermo Fisher Scientific) in the NO collection train. NO, NO_2, and ammonia (NH_3) concentrations in the chamber headspace are measured alternately by a chemiluminescent analyzer (Model 17i, Thermo Fisher Scientific) at 10 s intervals for flux calculations. For method development, reference NO, NO_2, and NH_3 from three

analytical tanks were diluted into the purging flow to simulate soil gas emissions inside the chamber. Two versions of the DFC system were developed for laboratory and field experiments. In the laboratory DFC system, a 1 L Teflon flow-through jar is used as the flux chamber. For the field DFC system, we fabricated a cylindrical flow-through chamber (39 cm I.D. and 30 L inner volume; Figure 2.1b), following considerations for minimizing pressure differentials in chamber headspace (Pape et al., 2009; Yu et al., 2014). Control tests indicate that NO transmission from the chamber is greater than 98.3%. Details about the flux measurement, the chamber tests and the specifications for each DFC component are provided in Appendix A.

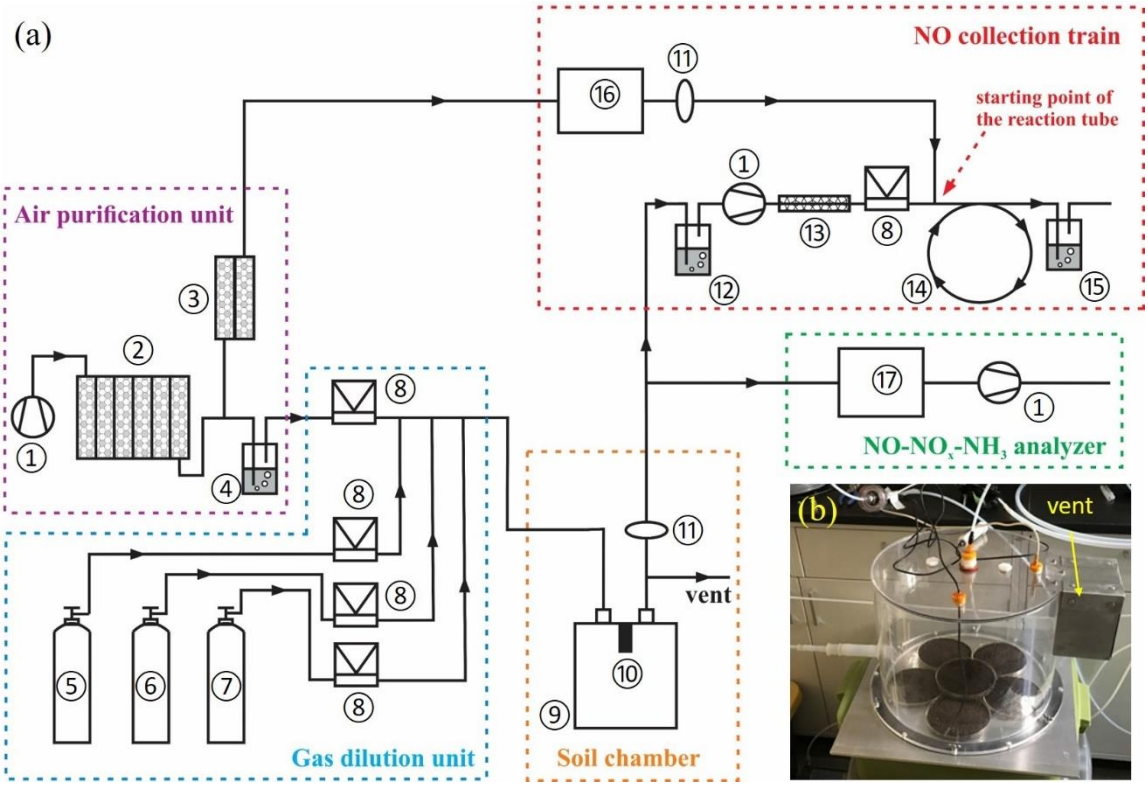

Figure 2.1 Schematic of the DFC system (not to scale). The system consists of the following: (1) diaphragm pump, (2) air purification columns, (3) drying columns, (4) humidifier, (5)-(7) NO, NO_2, and NH_3 reference tanks, (8) mass flow controller, (9) flux

chamber, (10) temperature and relative humidity sensor, (11) in-line PTFE particulate filter assembly, (12) HONO scrubber, (13) moisture exchanger, (14) reaction tube, (15) gas washing bottle containing TEA solution, (16) O_3 generator, (17) NO-NO_x-NH_3 analyzer; (b) picture showing the field chamber. Specifications of each component of the DFC system are given in the Table A-2 in Appendix A.

2.2.2 NO collection train

To collect NO for δ^{15}N-NO analysis, a Teflon-coated diaphragm pump is used to sample chamber air passing through the NO collection train (Figure 2.1). The sample flow rate (1.6 standard liter per minute (slpm)) is controlled by a mass flow controller. For the NO conversion in excess O_3, a length of Teflon tubing (9.5 mm I.D., ca. 240 cm length) serves as the reaction tube. A O_3 flow of 0.4 slpm, produced from photolysis of O_2 in zero air at 185 nm by the O_3 generator, is mixed with the sample flow at the starting point of the reaction tube (Figure 2.1). To prevent generation of HO_x radicals during the photolysis, water vapor is removed from the zero air using two drying columns and a Teflon filter is attached before the O_3 addition point to decompose remaining HO_x radicals (Miyazaki et al., 2008). Long-term (5 months) average O_3 concentration after the mixing of the sample and O_3 flows was 2911±32 ppbv as measured by an O_3 monitor (Model 202, 2B Technologies). The flow leaving the reaction tube is forced to pass through a 500 mL gas washing bottle with a fritted cylinder containing a solution of TEA (Fisher Scientific, Certified Grade) in water (20% (v/v), 70 mL). The stopper of the gas washing bottle was lengthened so that 70 mL of the solution just covered the frit.

2.2.3 Determination of reaction time

Reaction of NO with excess O_3 forms NO_2 (R1 in Table A-3 in Appendix A). In a dark environment, the efficiency of NO to NO_2 conversion is limited by the formation of higher nitrogen oxide species (i.e. nitrate radical (NO_3) and dinitrogen pentoxide (N_2O_5); R2-R5 in Table A-3 in Appendix A) (Miyazaki et al., 2008; Fuchs et al., 2009; Wild et al., 2014). In order to model the NO conversion in the reaction tube, the reaction time is needed. Following Fuchs et al. (2009) the reaction time in the reaction tube was experimentally determined by sampling zero air that contained a constant NO concentration (27 ppbv) using the NO collection train and varying the excess O_3 concentrations (266-2890 ppbv). The ending point of the reaction tube was attached to the sampling inlet of the chemiluminescent analyzer for NO concentration determination. The NO concentration decay was then fitted to a single exponential function assuming pseudo-first order loss of NO in excess O_3 (details are described in Appendix A). Due to the inner tubing of the chemiluminescent analyzer, the estimated reaction time essentially includes the reaction tube plus the analyzer inner tubing. To correct this overestimate, the reaction time of the inner tubing was estimated by repeating the experiment with the mixing point of the sample and O_3 flow directly attached to the analyzer inlet for NO concentration determination.

2.2.4 Preparation of TEA solution

Triethanolamine is a tertiary amine and has long been used to scrub acidic gases in fuel gas treating processes and to coat passive filters for ambient NO_2 monitoring (Glasius et al., 1999; Cape, 2009). We used a 20% TEA solution for NO_2 collection. Its reagent N blank was determined to be 0.12±0.04 μM (details are given in Appendix A).

It is reported that aging of the TEA solution can cause significant efficiency decrease in collecting NO_2 (Fibiger et al., 2014). This aging problem may occur to a greater degree with more diluted TEA solutions (Fibiger et al., 2014). Therefore, to minimize alteration of TEA from its original state, we sub-sampled new TEA (i.e., freshly opened bottle) into 15 mL glass vials in a glovebox with a 95% N_2 + 5% H_2 atmosphere to avoid contact with ambient air. Vials were then capped, tightly wrapped with Parafilm, sealed in Ziploc bags, and stored under dark at 4 °C until further use. One glass vial was opened to make a fresh 20% TEA solution immediately prior to each sample collection. The storage time of TEA used in this study was up to approximately 4 months since sub-sampling.

2.2.5 Measurement of NO_2^- and NO_3^- in TEA solution

Both NO_2^- and NO_3^- can be produced from the reaction between NO_2 and TEA (Glasius et al., 1999; Cape, 2009). NO_2^-+NO_3^- concentration in the TEA collection samples was measured using a modified spongy cadmium method (Jones, 1984). Detailed measurement protocol is given in Appendix A. Control tests using 10 μM NO_2^- or NO_3^- in 20% TEA solution indicate that the precision (1 σ, n=8) of the method is ±0.09 μM and ±0.36 μM for NO_2^- and NO_3^- measurements, respectively. Due to the multiple reduction and neutralization steps during the measurements and the N blank inherent to the 20% TEA solution (~0.12 μM), standards were always prepared in 20% TEA solution for concentration calibration.

2.2.6 Isotopic analysis

The isotopic composition of collected NO_2^- and NO_3^- in the TEA solution was measured using the bacterial denitrifier method (Sigman et al., 2001; Casciotti et al., 2002). In brief, denitrifying bacteria lacking the N_2O reductase enzyme (*Pseudomonas aureofaciens*) are used to convert 5-20 nmol of NO_2^- and NO_3^- into gaseous N_2O. Using He as a carrier gas, the N_2O is then purified in a series of chemical traps, cryo-focused, and finally analyzed on a GV Instruments Isoprime Continuous Flow Isotope Ratio Mass Spectrometer at *m/z* 44, 45, and 46 at the University of Pittsburgh *Regional Stable Isotope Lab for Earth and Environmental Science Research*.

Special considerations were taken during the isotopic analysis to ensure precise and accurate measurement of the $\delta^{15}N$ of the TEA collection samples. First, the TEA collection samples were neutralized using 12 N HCl to pH ~8 before sample injection to avoid overwhelming the buffering capacity of the bacterial medium (Casciotti et al., 2007). Second, in light of the expected low $\delta^{15}N$ of soil-emitted NO and the presence of NO_2^- as the dominant collection product (see below), a NO_2^- isotopic standard with low $\delta^{15}N$ value (KNO_2, RSIL20, USGS Reston; $\delta^{15}N$ = -79.6‰, $\delta^{18}O$ = 4.5‰; Casciotti et al., 2007) is used together with other international NO_3^- reference standards (IAEA-N3, USGS34, and USGS35) to calibrate $\delta^{15}N$ and $\delta^{18}O$ measurements. Third, following the IT principle (i.e., identical treatment of sample and reference material), a blank-matching strategy is used to make the isotopic standards in the same matrix (i.e., 20% TEA) as collection samples and to match both the molar N amount and injection volume (±5%) between the collection samples and the standards (Figure 2.2). This ensures that the isotopic interference of any blank N associated with the bacterial medium (Sigman et al., 2001; McIlvin et al., 2011) and the TEA solution is minimized. The percentage difference (P_{diff}) in the major N_2O (*m/z* 44) peak

area between each collection sample and RSIL20 measured within the same batch is calculated to quantify how precisely the blank-matching strategy is implemented (Figure 2.2). Finally, the $\Delta^{17}O$ ($\Delta^{17}O=\delta^{17}O - 0.52\times\delta^{18}O$) of the analyte N_2O is independently measured for collected samples with sufficient concentration for 50 nmol injection using the N_2O thermal decomposition method (Kaiser et al., 2007). The resolved $\Delta^{17}O$ is then used to correct the isobaric interference on the $\delta^{15}N$ analysis resulting from the NO oxidation by O_3 according to Kaiser et al. (2007).

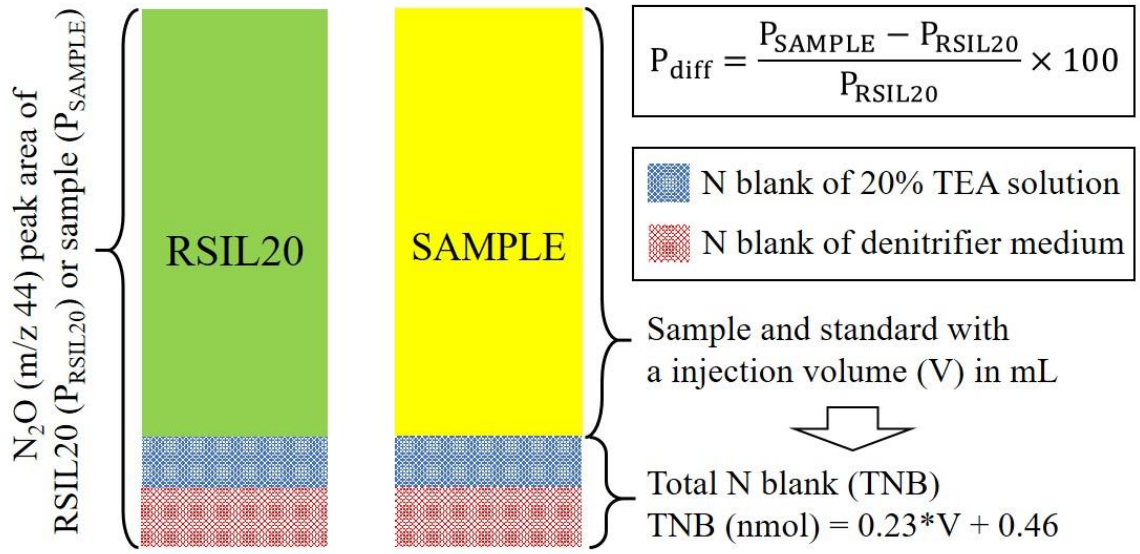

Figure 2.2 Illustration of the blank-matching strategy for correcting N blanks associated with the TEA solution and denitrifier method.

2.2.7 Quantification of method precision and accuracy

The precision of the DFC-TEA method was quantified through repeated NO collection using the reference NO tank (50.4 ppmv). The collection was conducted under a variety of conditions, including differing NO concentrations (12-749 ppbv), chamber temperatures (11.5-30.8 °C), RH

(27.1-92.0%), purging flow rates in the field chamber (5-20 slpm), and coexistence of NH_3 in high concentrations (500 ppbv). In light of the high temporal variability of soil NO emission, we limited the collection time for each sample to be less than 2 h. Given that soils can produce and emit nitrous acid (HONO) (Su et al., 2011; Oswald et al., 2013) and that HONO positively interferes NO_2 collection in TEA solution (Cape, 2009), interference of the δ^{15}N-NO analysis by soil HONO emission was minimized by forcing the sample flow to pass through a HONO scrubber (250 mL fritted gas washing bottle containing 50 mL of 1 mM phosphate buffer solution at pH 7.0) (Zhou et al., 1999) before entering the NO collection train.

While there is no certified isotopic standard for gaseous NO, the accuracy of the DFC-TEA method was evaluated through inter-calibration with a modified EPA NO_x collection method. A detailed description of the modified EPA method has been provided by Felix et al. (2012) and Walters et al. (2015a). In brief, gas samples from the NO and NO_2 tanks were collected directly into evacuated 1 L borosilicate gas sampling bulb containing 10 mL of a NO_2 absorbing solution (H_2SO_4+H_2O_2) on a vacuum line. The absorbing solution oxidizes NO_2 into NO_3^-. For the NO collection, the collection was terminated with a small vacuum remaining in the bottle. The bottle was then quickly vented to the laboratory atmosphere to allow introduction of O_2 into the bottle for the conversion of NO to NO_2. After the collection, the bottles were allowed to stand for 1 week with occasional shaking to facilitate the conversion of NO_x to NO_3^-. The residual NO_x headspace concentration was measured after a 1 week period and indicates that the collection was 100%. The absorbing solution was then collected and neutralized for δ^{15}N analysis using the denitrifier method. The results show that the NO and NO_2 tanks had δ^{15}N values of -71.4±0.5‰ (n=4) and -39.8±0.2‰ (n=3), respectively.

2.2.8 Laboratory soil δ^{15}N-NO measurements

To test the DFC-TEA method using real soil samples, approximately 4 kg of soil was collected from the upper 10 cm of an urban forest soil in Pittsburgh, PA. Before use, soil samples were sieved by passing through a 2-mm sieve and air-dried for 14 days. To trigger NO pulses, 35 g of air-dried soil samples was added to the Teflon jar, mixed thoroughly, and wetted by deionized water to achieve 100% water holding capacity. With the continuous purging of the jar headspace, the soil samples were subject to drying-out over the next 48 h, and NO was collected periodically for the δ^{15}N-NO analysis.

2.2.9 Field soil δ^{15}N-NO measurements

To verify the DFC-TEA method under varying field conditions, the field DFC system was deployed using the University of Pittsburgh *Mobile Air Quality Laboratory* to measure δ^{15}N-NO in a field soil rewetting experiment (see Figure A-10 in Appendix A for the field setup). A waterproof tarp (300 cm×240 cm) was erected over a fallow, urban plot in Pittsburgh, PA for 2 weeks (8/15/2016 - 8/29/2016) to exclude precipitation inputs. After the drying period, four soil plots were respectively wetted on four consecutive days using 500 mL of MilliQ water, 20 mM KNO_3 (δ^{15}N=46.5±0.3‰), 10 mM $NaNO_2$ (δ^{15}N=1.0±0.4‰), and 20 mM NH_4Cl (δ^{15}N=1.7±0.1‰) solutions. These N amendment solutions were chosen because they are common precursors of NO in major NO-producing processes (Denk et al., 2017). Previous studies have reported that common δ^{15}N values of N fertilizers are not very different from 0‰ (e.g., -4.4‰ to 0.3‰) (Michalski et al., 2015), while δ^{15}N values of atmospherically deposited NO_2, NO_3^- and NH_4^+ could vary over a wider range (e.g., -10‰ to 15‰), depending on source contributions

(Altieri et al., 2014). Hence, the $\delta^{15}N$ values of the amended NO_2^- and NH_4^+ are within the environmentally relevant range, whereas the $\delta^{15}N$ of the added NO_3^- is significant higher. The NO, NO_2, and NH_3 fluxes were continuously measured before and after the soil rewetting, and NO was collected periodically for the $\delta^{15}N$-NO analysis.

2.3 RESULTS AND DISCUSSION

We evaluate each step in the NO collection and report isotopic results that document the overall precision and accuracy of the $\delta^{15}N$-NO analysis. We then present $\delta^{15}N$-NO measurements from laboratory and field soil rewetting experiments that demonstrate utility of the DFC-TEA method for resolving soil NO dynamics.

2.3.1 NO conversion in excess O_3

The reaction time of the inner tubing of the chemiluminescent analyzer and the reaction tube plus the inner tubing were estimated to be 1.4 s and 6.4 s, respectively, resulting in a reaction time of the reaction tube of 5 s at the measured flow temperature (22 °C) (Figure A-7 in Appendix A). This estimated reaction time is consistent with the residence time calculated from the assumption of plug flow in the reaction tube. Based on this reaction time and the average O_3 concentration of 2911 ppbv, numerical model calculations including reactions R1-R5 and NO_3 loss on the interior tubing wall (R6 in Table A-2 in Appendix A) (Dubé et al., 2006) indicate that NO is quantitatively converted in the reaction tube and that the specific conversion of NO to NO_2 is between 98.7% and 99.0% over a wide range of NO concentrations (0-1000 ppbv) at 22 °C (Figure A-8a in

Appendix A). Notably, the remaining NO from the conversion exists primarily as N_2O_5 (Figure A-8b in Appendix A).

Deviations from controlled laboratory condition in the field may result in variations in the modeled NO conversion efficiency (Fuchs et al., 2009). We therefore modeled the effects of temperature variation and soil emission of biogenic volatile organic carbon (BVOC) (Atkinson and Arey, 2003) on the NO conversion (reactions R7 and R8 in Table A-2 in Appendix) (Atkinson et al., 2006). The results indicate that the conversion of NO to NO_2 is not likely to fall below 98% over a temperature range of 0-40°C in conjunction with high BVOC emissions (e.g., 100 ppbv isoprene in the chamber) (details on the extended modeling are given in Appendix A). In addition, slight variations in the reaction time may result from changes in temperature and pressure of the sample flow (e.g., pressure increase induced by the attachment of the gas washing bottle). While the effect of these variations on the NO conversion is difficult to empirically quantify, any uncertainty in converting NO under the tested conditions is reflected in the over method precision and accuracy for the δ^{15}N-NO measurement.

2.3.2 NO_2 collection in TEA solution

The 20% TEA solution was 100% efficient at collecting NO_2. This was confirmed by collecting a flow of reference NO_2 at 1 ppmv using the laboratory DFC system (Table 2.1). Importantly, because the 20% TEA solution foams rigorously upon sparging, the applied total flow rate (1.6 slpm of the sample flow plus 0.4 slpm of the O_3 flow) was chosen to avoid solution spill. We have also tested TEA solution from another brand (BioUltra) that foams much less rigorously (coarse bubbles). However, consistent low collection efficiency (<90%) was found using this TEA

solution. Thus, it is important to test TEA solution using a NO_2 tank to assure 100% NO_2 collection efficiency.

The measured NO recovery of the NO tank collection samples ranged between 95.0% and 103.9% across the individual sets of collection conditions, with an average value of 98.5±3.5% (Table 2.1). A nonparametric Kruskal-Wallis test indicates that none of the controlled factors (e.g., NO concentration, temperature, purging flow rate, and choice of the laboratory or field DFC systems) had a significant effect on the NO recovery (P>0.05). The deviations from 100% NO recovery likely reflect inefficiencies in the NO conversion (see above), the high uncertainty in the NO_3^- concentration determination (e.g., for the 12 ppbv and 25 ppbv NO collection samples), and/or NO loss within the system (e.g., NO loss in the HONO scrubbing solution and on the interior wall of the field chamber). Importantly, the high and consistent NO recovery is a direct evidence that the sub-sampling was effective to minimize the TEA aging problem, if any, for a storage time of at least 4 months.

For all the tank collection samples (n=52), about 90% of the collected NO or NO_2 was in the form of NO_2^-, and the remainder as NO_3^- (Table 2.1). A 90% NO_2^-+10% NO_3^- stoichiometry has been previously reported for active NO_2 sampling using TEA-coated cartridges (Cape, 2009). While a satisfactory explanation for the NO_3^- production cannot be given at this time (Cape, 2009), the observed stoichiometry is best approximated by the redox reaction between NO_2 and TEA in the presence of water that gives a theoretical 1:1 conversion of NO_2 to NO_2^- (Glasius et al., 1999; Dahal et al., 2016). Although it is well known that N_2O_5 hydrolyzes in water as HNO_3 (Riemer et al., 2009), which is preserved as NO_3^- in an alkaline TEA solution, whether N_2O_5 produced in the NO conversion can be collected in the TEA solution as NO_3^- is not possible to quantify in this case

due to the high uncertainty in the NO_3^- concentration determination (i.e., ±0.36 μM) but will be the subject of future research.

It is worth noting that collection efficiency of the 20% TEA solution may be subject to decrease over longer collection periods due to presence of O_2, O_3, and CO_2 in the sample flow that can compete with NO_2 for TEA oxidation and decrease solution pH. Given that the DFC-TEA method described here is developed to characterize transient variations of soil NO emissions, use of 20% TEA solution for prolonged collection (i.e., >2 h) should be further investigated to ensure high and consistent collection efficiency.

Table 2.1 Summary of the reference NO and NO_2 tank collection using the DFC-TEA method under varying environmental conditions. The complete dataset is given in Table A-4 in Appendix A.[a]

Sample	Time (min)	T (°C)	RH (%)	$NO_2^-+NO_3^-$ (μM)	Recovery[b] (%)	NO_2^- percent (%)	P_{diff} (%)	$\delta^{15}N$[c] (‰)	$\Delta^{17}O$ (‰)
NO_2 collection – laboratory DFC system									
1002 ppbv NO_2 (n=4)	135	23.7	25.3	132.5	101.4	87.4	3.3	-40.1	
Standard error (1 σ)				4.7	3.6	0.3	5.1	0.8	
NO collection – laboratory DFC system									
12 ppbv NO (n=3)	120	23.0	44.6	1.4	95.0	97.0	-0.7	-73.0 (-71.7)	
34 ppbv NO (n=4)	120	24.8	27.1	4.1	100.7	93.1	-1.2	-70.3 (-69.2)	
101 ppbv NO (n=4)	120	23.1	34.2	11.9	98.2	94.0	0.7	-71.0 (-69.9)	18.8
749 ppbv NO (n=4)	120	22.8	47.5	14.2	99.3	90.7	3.5	-70.6 (-69.4)	20.6
NO collection – laboratory DFC system – temperature effect									
34 ppbv NO (n=4)	120	11.5	92.0	4.0	99.8	89.3	2.4	-71.1 (-70.0)	
101 ppbv NO (n=4)	120	30.8	28.8	11.8	98.7	89.5	3.6	-70.8 (-69.7)	20.0
NO collection – laboratory DFC system – interference									
34 ppbv NO + 500 ppbv NH_3 (n=3)	120	23.0	33.1	4.0	99.5	88.2	-3.8	-70.1 (-69.0)	
101 ppbv NO + 500 ppbv NH_3 (n=4)	120	23.1	46.5	11.7	97.5	91.5	2.6	-71.2 (-70.2)	19.5
101 ppbv NO	120	22.3	89.7[d]	11.6	96.7	89.8	2.8	-71.0 (-69.9)	19.6

+ HONO (n=4)									
NO collection – field DFC system[e]									
25 ppbv NO (n=4)	120	21.4	40.8	3.1	103.9	94.3	4.3	-72.9 (-71.7)	
34 ppbv NO (n=4)	120	21.9	50.4	3.9	97.6	92.8	-1.8	-70.7 (-69.6)	
56 ppbv NO (n=3)	120	21.2	44.8	6.2	96.0	92.9	-2.0	-71.5 (-70.4)	
101 ppbv NO (n=4)	120	21.7	36.6	11.7	97.1	89.5	1.0	-71.0 (-69.9)	19.5
Mean					**98.5**	**91.7**	**1.1**	**-71.1 (-70.0)**	**19.7**
Standard error (1 σ)					**3.5**	**3.4**	**5.1**	**1.1 (1.1)**	**0.8**

a: Out of 56 NO and NO_2 tank collection samples, 52 samples yielded consistent results wherein 4 samples were detected as outliers on the basis of erroneous concentrations. These outliers were not included in this table.

b: NO (NO_2) recovery was calculated by dividing measured $NO_2^-+NO_3^-$ concentration by the theoretical concentration calculated using the collection time, sample flow rate (1.6 slpm), NO (NO_2) concentration, and the TEA solution volume. The TEA solution volume was corrected for evaporative loss by weighing the gas washing bottle containing the solution before and after each sample collection.

c: Relative to N_2 in the air. $\delta^{15}N$ values before the isobaric correction are shown in the brackets.

d: RH was measured after the HONO scrubber instead of in the Teflon chamber.

e: The chamber purging flow rates were 20 slpm, 15 slpm, 9 slpm, and 5 slpm for the 25 ppbv NO, 34 ppbv NO, 56 ppbv NO, and 101 ppbv NO collection, respectively.

2.3.3 Analytical uncertainty of the denitrifier method and the total N blank

The pooled standard deviation for each of the isotopic standards made in 20% TEA solution and measured along with individual sample sets was: 0.3‰, 0.3‰, and 0.8‰ for $\delta^{15}N$ of IAEA-N3, USGS34, and RSIL20, respectively; 0.7‰ and 0.7‰ for $\delta^{18}O$ of IAEA-N3 and USGS34, respectively; and 1.2‰ for $\Delta^{17}O$ of USGS35. The lower precision of the $\delta^{15}N$ analysis of RSIL20 (0.8‰ relative to 0.3‰ for other standards) is due to the larger uncertainty in measuring diluted RSIL20 solutions that require large injection volumes (Figure 2.3a). To further understand this

volume dependence, we estimated the total N blank associated with the $\delta^{15}N$ analysis of the TEA samples (i.e., TEA N blank + blank N associated with the denitrifier medium (Sigman et al., 2001; McIlvin et al., 2011)) by quantifying shrinkage of the N isotope-ratio scale between USGS34 and RSIL20 measured in each run of the TEA collection samples (Coplen et al., 2004) (more details are described in Appendix A). The results show that the fractional blank size (f_B) ranged between 0.04 and 0.18 across different runs and was significantly, positively correlated with the sample volume and the measured $\delta^{15}N$ of RSIL20 ($\delta^{15}N_{RSIL20\text{-}m}$) (Figure 2.3a). Fitting a linear equation to the molar amount of the total N blank and the sample volume indicates that the N blank likely consisted of a constant component of 0.46±0.12 nmol and a sample volume-dependent component of 0.23±0.06 nmol·mL^{-1} (Figure A-5 in Appendix A; Figure 2.2); this is consistent with the blank size estimated by injecting blank 20% TEA solution (details are provided in Appendix A). From the linear relationship between f_B and $\delta^{15}N_{RSIL20\text{-}m}$, the $\delta^{15}N$ of the blank N appears to be ~10‰ across different runs (Figure 2.3a). These consistent and predictable behaviors of the total N blank indicate with a high degree of confidence that its isotope effect is implicitly corrected during the $\delta^{15}N$ analysis using the blank-matching strategy.

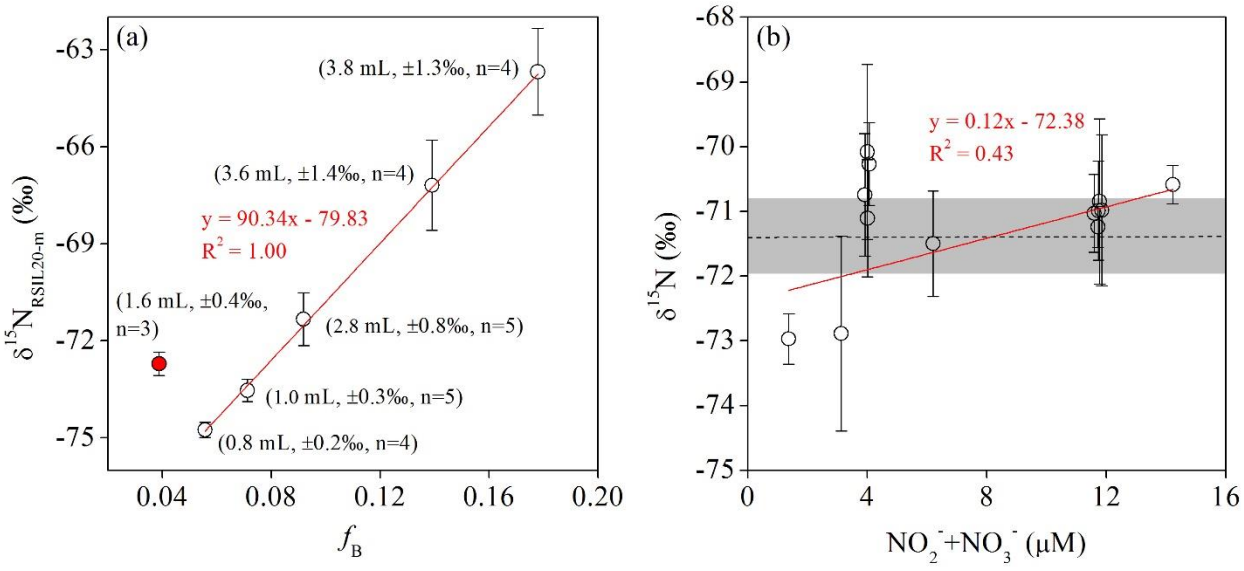

Figure 2.3 Analytical uncertainty of the denitrifier method and the total N blank. (a) The measured $\delta^{15}N$ of RSIL20 ($\delta^{15}N_{RSIL20\text{-}m}$) as a function of the fraction of analyte N_2O-N derived from the total N blank (f_B). Sample injection volume, standard deviation of $\delta^{15}N_{RSIL20\text{-}m}$, and number of replicates for the individual runs are given in the brackets. The dot in red (56 ppbv collection sample) was not included in the linear regression. (b) The measured $\delta^{15}N$ of the NO collection sample as a function of the sample $NO_2^-+NO_3^-$ concentration. The dash line and the shaded area represent the mean ± (1 σ) of the $\delta^{15}N$ of the NO tank measured using the modified EPA NO_x collection method.

2.3.4 Isobaric interference

The $\delta^{18}O$ of RSIL20 calibrated against IAEA-N3 and USGS34 ranged from -25.8±0.9‰ to -22.7±1.5‰ across different runs, with an average of -23.7±1.1‰. This results in an isotopic offset of about 28‰ between the measured apparent $\delta^{18}O$ and the "true" $\delta^{18}O$ (4.5‰) of RSIL20, in line with the branching fractionation between NO_3^- and NO_2^- during denitrification (25-30‰)

(Casciotti et al., 2007). This implies that the oxygen isotopic exchange between NO_2^- and water is limited in the alkaline TEA solution. Not surprisingly, positive $\Delta^{17}O$ values were observed in the N_2O generated from collected samples. To understand the transfer of the $\Delta^{17}O$ anomaly from O_3 during the NO conversion, a theoretical $\Delta^{17}O$ of the NO_2 produced from the $NO+O_3$ reaction (R1 in Table A-2 in Appendix A) was calculated to be 22.5±1.8‰ (details are provided in Appendix A). This theoretical $\Delta^{17}O$ value is not very different from the measured $\Delta^{17}O$ values, which had an average of 19.7±0.8‰ across different runs (Table 2.1), indicating that the $NO+O_3$ reaction essentially dominated during the NO conversion. The measured $\Delta^{17}O$ values led to a 1.0-1.2‰ correction of the measured $\delta^{15}N$ values. For samples without sufficient concentrations for $\Delta^{17}O$ measurement, the average $\Delta^{17}O$ value (19.7‰) was used for the correction. This is not a complete correction, in that the expression of the isobaric interference depends on f_B relative to each sample. Nevertheless, the resultant overcorrection on the $\delta^{15}N$ of the low concentration samples is <0.2‰ in this case, and is not explicitly addressed.

2.3.5 Overall accuracy and precision of the DFC-TEA method

The $\delta^{15}N$ of the NO tank collection samples after the isobaric correction ranged from -73.0‰ to -70.1‰ across the individual sets of the collection conditions (Table 2.1), with an average value of -71.1±1.1‰. P_{diff} ranged between -9.8% and 15.9%, 1.1±5.1% on average (Table 2.1). P_{diff} was not sensitive to the sample concentration used for blank-matching, indicating that the sample concentrations were precisely measured and diluted for the $\delta^{15}N$ analysis (Figure A-6a in Appendix A). A nonparametric Kruskal-Wallis test indicates that none of the controlled factors or P_{diff} had significant effect on the $\delta^{15}N$ values (P>0.05; Figure A-6b in Appendix A). The DFC-TEA method and the EPA NO_x collection method generally agree within 0.3‰, although

discrepancies within individual sets of collected samples ranged from -1.3‰ to 1.6‰. The largest discrepancies between the two methods occurred with the lowest sample concentrations (i.e., 12 ppbv NO collection samples) (Figure 2.3b). For these low concentration samples, isotopic analyses were conducted on 5 nmol of NO_2^-+NO_3^- (achieved with a 3.8 mL injection of the collection samples) and of a f_B of 0.18. Therefore, although P_{diff} did not correlate with the sample concentration (Figure A-6a in Appendix A), the collection samples with lower concentrations were more prone to random error in matching blank between the standards and samples due to their higher f_B. Consequently, for accurate δ^{15}N-NO analyses, soil NO should be collected to achieve >3 µM NO_2^-+NO_3^- in the solution within 2 h (equivalent to collecting a flow of >26 ppbv NO over a 2 hour period). Blank 20% TEA solution should then be used to dilute both soil NO collection samples and isotopic standards within a batch to a common concentration for injection of 10 nmol of N using the denitrifier method. Control tests using a soil NO sample collected from the laboratory rewetting experiment (δ^{15}N = -37.1‰, [NO_2^-]+[NO_3^-] = 9.2 µM) indicate that dilution-induced uncertainty in the δ^{15}N was <0.5‰ for a dilution up to three-fold but still giving >3 µM NO_2^-+NO_3^- in the solution (data not shown). This uncertainty is within the analytical uncertainty (i.e., ±0.8‰ for RSIL20). Therefore, we always group samples with similar concentrations such that the dilution factor does not exceed 3.

Overall, our inter-calibration effort demonstrates that although the NO recovery was slightly less than 100%, fractionation during chamber mixing and NO conversion and collection is effectively minimized under the tested conditions. The derived standard deviation of ±1.1‰ based on all the collection samples with an average P_{diff} of ±7% (i.e., sample peak area is within 100±7% of that of RSIL20) represents the overall accuracy and precision across the entire method, accounting for propagated errors from the total N blank and its mismatch between the standards

and samples. While the method precision is lower than that of the modified EPA method (Table A-1 in Appendix A), our integrated method featuring simultaneous NO flux measurement and collection is the first to show its suitability for unbiased soil δ^{15}N-NO determination under realistic, varying soil conditions. Furthermore, the method is more convenient than previous methods and does not require time-consuming pretreatments for δ^{15}N analysis (Table A-1 in Appendix A). Given the good result from the inter-calibration, the tank NO can be utilized as a secondary standard for correcting the isobaric interference. For instance, the tank NO can be collected before and after soil NO collection; Δ^{17}O of the tank collection samples can then be estimated using an empirical relationship scaling a 1‰ increase from accepted δ^{15}N value (-71.4‰ in this case) to every 18.8‰ increase in Δ^{17}O to correct the soil collection samples (Coplen et al., 2004).

2.3.6 Application to pulsed soil NO emissions

Pulsed NO emission was triggered by soil rewetting under both the laboratory and field conditions (Figure 2.4). In the laboratory, the pulsed NO emission had evident temporal variations with a rapid initial NO pulse being triggered upon the rewetting (Figure 2.4a). While the initial NO pulse was absent under the field conditions, possibly due to the relatively high pre-wetting soil water content (0.17 $cm^3 \cdot cm^{-3}$), the rewetting and N amendments caused significantly increased NO emission as compared to the pre-wetting emission (47±16 $nmol \cdot m^{-2} \cdot min^{-1}$). Particularly, a dramatic increase in NO emission was triggered by the NO_2^- addition (Figure 2.4b).

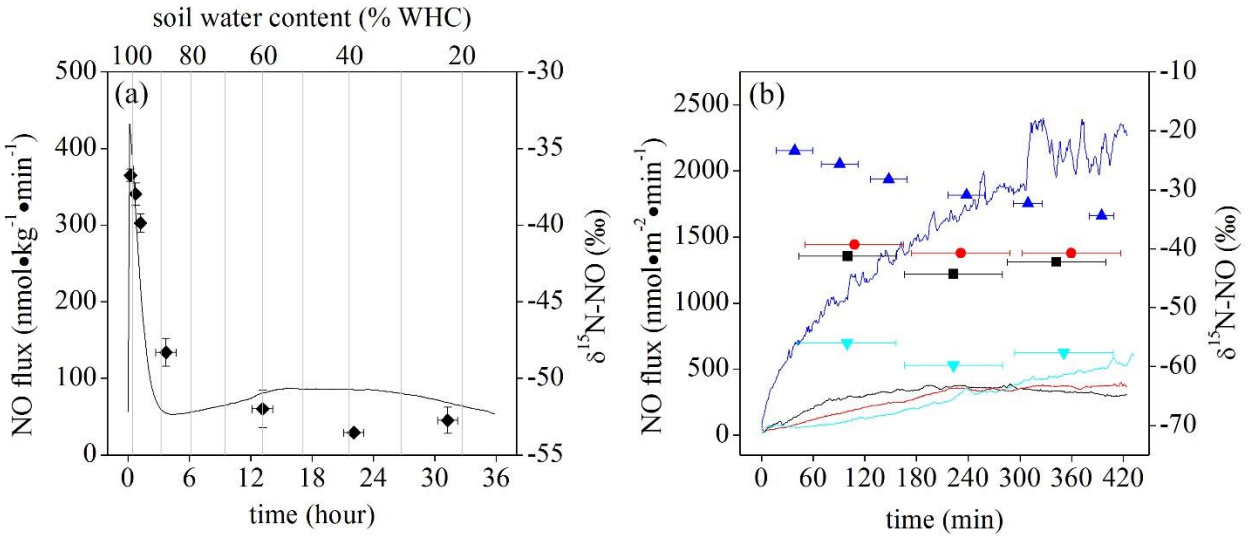

Figure 2.4 NO emission (lines) and δ^{15}N-NO (dots) results from the laboratory (a) and field (b) rewetting experiments. The error bar on the x-axis denotes the time span of each collection sample. In the field rewetting experiment, four soil plots were respectively wetted on four consecutive days using 500 mL of MilliQ water (black), 20 mM KNO_3 (red; $\delta^{15}N$=46.5±0.3‰), 10 mM $NaNO_2$ (dark blue; $\delta^{15}N$=1.0±0.4‰), and 20 mM NH_4Cl (light blue; $\delta^{15}N$=1.7±0.1‰) solutions.

Twenty and 15 samples were collected for the δ^{15}N-NO analysis from the laboratory and field experiments, respectively (Tables A-5 and A-6 in Appendix A). The average NO recovery was 102.2±5.6% and 108.6±11.0% for the laboratory and field collection samples, respectively. The >100% recovery was detected mostly in samples collected under the NO_2^- addition (NO recovery = 117.5±11.6%; Table A-6 in Appendix A). We suspect that the >100% NO recovery might result from our underestimation of the soil NO emission due to the slow response time of the chemiluminescent analyzer (>30 s), especially given that transient fluctuations in the NO flux were likely triggered by the NO_2^- addition (Figure 4.4b). Alternatively, the >100% recovery could result from soil emission of NO_y ($NO_y = NO_2 + HONO + HNO_3$ + other non-NO reactive N oxides)

(Soper et al., 2016), that can potentially be collected in the TEA solution as NO_2^- and/or NO_3^- (Cape, 2009). If soil NO_y emission was significant during measurement, it would be detected as NO_2 by our chemiluminescent analyzer with a molybdenum convertor (Dunlea et al., 2007). Because the NO_2 flux never exceed 2% of the simultaneous NO flux (Figure A-11 and Figure A-12 in Appendix A), contributions of NO_y emission to the NO recovery and the measured δ^{15}N-NO are considered negligible. Future application of the DFC-TEA method can be coupled to a faster NO measurement system and existing denuder and wet chemistry methods (Zhou et al., 1999; De Santis et al., 1996) that quantitatively scrub NO_y without significant loss of NO.

The measured soil δ^{15}N-NO exhibited intriguing patterns that are indicative of mechanisms underlying the soil NO emissions (Figure 4.4). In the laboratory rewetting of the air-dried soil samples, the initial NO pulse had higher δ^{15}N values (-36.7~-39.9‰) than NO emission after 12 h post-wetting (-52.0~-53.6‰; Figure 4.4a). Recent work by Homyak et al. (2016) provided evidence that in arid soils, abiotic reactions govern the rapid initial NO pulse, whereas microbial processes control later emissions as microbes recover from drought stress. Therefore, the higher δ^{15}N-NO values associated with the initial NO pulse may suggest that abiotic reactions likely bear a smaller isotopic fractionation on NO production than microbial processes. However, the temporal variation of δ^{15}N-NO could also result from changing rates of microbial NO production (Mariotti et al., 1982) or sequential resuscitation of different microbial groups during the rewetting (Placella et al., 2012). Further constraints on the relevant isotope effects are needed to tease apart the relative importance of abiotic and microbial pathways sustaining pulsed NO emissions in soils. In the field rewetting experiment where an initial NO pulse was lacking, the measured soil δ^{15}N-NO responded differently to the added N precursors (Figure 4.4b). First, the δ^{15}N-NO values that evolved from the NH_4^+ (-59.8‰ to -56.0‰) and NO_2^- (-34.4‰ to -23.4‰) amendments were

significantly lower and higher relative to the control (MilliQ water addition; -44.3‰ to -41.3‰), respectively, in spite of the almost equal $\delta^{15}N$ of the added NH_4^+ and NO_2^-. Secondly, despite the high $\delta^{15}N$ of the added NO_3^- (i.e., 46.5‰), the $\delta^{15}N$-NO values measured from the NO_3^- amendment (-40.7‰ to -39.4‰) were not significantly different from those in the control. The measured soil $\delta^{15}N$-NO and its differential responses to the amended N sources indicate that various soil NO-producing processes (e.g., nitrification, denitrification, and chemodenitrification), stimulated by different N amendments, likely bear distinguishable isotopic imprints on NO production, similar to what has been observed in soil nitrous oxide (N_2O) studies (Mariotti et al., 1981; Sutka et al., 2006; Park et al., 2011). For example, N_2O production in soil was found to be associated with a larger isotope effect for nitrification of NH_4^+ (e.g., -45‰ to -67‰) than denitrification of NO_2^- (e.g., -35‰ to -22‰) (Mariotti et al., 1981; Sutka et al., 2006; Park et al., 2011). Thus, soil $\delta^{15}N$-NO measurement could potentially provide important implications for understanding couplings between soil NO and N_2O emissions, in that NO is the precursor of N_2O in most abiotic and microbial processes (Zumft, 1997; Firestone and Davidson, 1989). Finally, the measured soil $\delta^{15}N$-NO values are significantly lower than other measured NO_x emissions sources, confirming use of soil $\delta^{15}N$-NO as a robust tracer of regional N deposition (Elliott et al., 2007; Elliott et al., 2009). Quantification of isotope effects associated with NO dynamics in soils therefore represents an important avenue for future research on the soil-atmosphere cycling of reactive N.

3.0 PROBING SOIL NITRIFICATION AND NITRATE CONSUMPTION USING $\Delta^{17}O$ OF SOIL NITRATE

3.1 INTRODUCTION

Production and consumption of soil nitrate (NO_3^-) affects a myriad of ecosystem processes, including net primary production and carbon (C) sequestration (Lebauer and Treseder, 2008), ecosystem biodiversity (Tilman et al., 1996), soil acidification (Högberg et al., 2006), surface- and groundwater quality (MacDonald et al., 2002), and production of climatically important trace gases via denitrification (Singh et al., 2010). Determination of soil nitrification and NO_3^- consumption rates is therefore critical for gauging nitrogen (N) retention and loss in ecosystems and its response to the intensified N release from anthropogenic activities (Galloway et al., 2008).

Since the landmark work by Kirkham and Bartholomew (1954), the ^{15}N isotopic pool dilution has been the most accessible means for determining gross nitrification and NO_3^- consumption rates in soil. The principal of this technique is based on isotopic labeling of the soil NO_3^- pool with $^{15}NO_3^-$. Gross production and consumption rates can then be estimated from concurrent $^{15}NO_3^-$ dilution by NO_3^- production at natural abundance isotopic composition and disappearance of the $^{15}NO_3^-$ tracer by NO_3^--consumption processes, such as microbial NO_3^- assimilation and denitrification (Hart et al., 1994; Stark and Hart, 1997; Booth et al., 2005). Further method development has expanded on the ^{15}N dilution concept by combining ^{15}N labeling of multiple soil N pools (e.g., NO_3^-, ammonium (NH_4^+) and organic N) with process-based model analysis to trace N fluxes between various product pools, allowing a more complete inquiry into soil NO_3^- dynamics and its role in the soil N cycle (Myrold and Tiedje, 1986; Mary et al., 1998;

Müller et al., 2004). However, while ^{15}N tracer-based methods operated in the short term are a powerful tool for measuring gross N transformation rates, one of the drawbacks of these methods is that they provide only a "snapshot" view of soil N dynamics, and therefore may not account for longer-term variations in N cycling in a heterogeneous soil environment (Groffman et al., 1993). Moreover, with the ^{15}N tracer-based techniques, it remains challenging and laborious to quantify denitrification, which can possibly represent a significant portion of gross NO_3^- consumption rates (Groffman et al., 2006; Morse et al., 2015).

The natural abundance stable isotope ratios of nitrogen ($^{15}N/^{14}N$) and oxygen ($^{18}O/^{16}O$) in NO_3^- (notated as $\delta^{15}N\text{-}NO_3^-$ and $\delta^{18}O\text{-}NO_3^-$, respectively) are increasingly used to differentiate sources and track biogeochemical transformations acting on NO_3^- at various spatiotemporal scales (Granger and Wankel, 2016; Denk et al., 2017). The unique power of the dual NO_3^- isotopes stems from the distinct isotopic fractionations associated with NO_3^- production and consumption processes, which arise owing to relative differences in mass of the involved isotopically substituted N and O species (Casciotti et al., 2013). Laboratory studies using pure cultures of bacteria have revealed strong isotopic discrimination against ^{15}N for autotrophic nitrification (Mariotti et al., 1981; Casciotti et al., 2003), suggesting that nitrification draws down $\delta^{15}N\text{-}NO_3^-$ to be significantly lower than $\delta^{15}N$ of NH_4^+ and organic N in NH_4^+-rich soil (Hall et al., 2016). Nitrification also imprints a characteristic $\delta^{18}O$ to NO_3^- that reflects kinetic and equilibrium isotope effects during incorporation of the three O atoms from soil H_2O and O_2 into nitrified NO_3^- (Casciotti et al., 2010; Buchwald and Casciotti, 2010). On the other hand, both assimilatory and dissimilatory NO_3^- reduction impart coupled enrichment of $\delta^{15}N\text{-}NO_3^-$ and $\delta^{18}O\text{-}NO_3^-$ in pure culture studies (Granger et al., 2008; Granger et al., 2010), which can be used as a diagnostic signal of NO_3^- consumption (Granger and Wankel, 2016). Importantly, the isotope effects for denitrification uncovered in

culture observations are significantly larger than those for NO_3^- assimilation (Granger et al., 2008; Granger et al., 2010), leading to elevated $\delta^{15}N\text{-}NO_3^-$ and $\delta^{18}O\text{-}NO_3^-$ of residual NO_3^-. The large kinetic fractionation by denitrification has been exploited in isotope models to assess patterns and controls on denitrification at the watershed scale (Houlton et al., 2006; Fang et al., 2015). However, given that the dual isotope-based model estimates are often highly sensitive to uncertainties in the relevant isotope effects (Fang et al., 2015), the dual NO_3^- isotopes are best suited for constraining relative rather than absolute rates of NO_3^- production and consumption (Casciotti et al., 2013).

Recent developments in the field of NO_3^- ^{17}O anomaly has provided a new means by which ambiguities in NO_3^- dynamics inferred from the dual NO_3^- isotope measurements may be clarified (Michalski et al., 2002; Kaiser et al., 2007). Given the three stable isotopes of O (i.e., ^{16}O, ^{17}O, and ^{18}O), fractionation of $^{17}O/^{16}O$ relative to $^{18}O/^{16}O$ in a normal O isotope fractionation process is proportional to the mass difference between the respective O isotopologues, and this is referred as mass-dependent isotopic fractionation (see Section 3.2.1 for more details) (Thiemens, 2006). Atmospheric NO_3^- is known to contain an anomalous ^{17}O excess over that expected based on ^{18}O abundances (Michalski et al., 2003). This deviation from the mass-dependent fractionation is attributed to O atom transfer from ozone during the formation of atmospheric NO_3^- (Thiemens, 2006) and quantified by a $\Delta^{17}O$ notation (see Section 3.2.1 for more details) (Miller, 2002; Young et al., 2002). Because the production of nonzero $\Delta^{17}O\text{-}NO_3^-$ values is strictly a photochemical effect, post-depositional NO_3^- consumption processes in soil, such as denitrification and NO_3^- assimilation, obey the mass-dependent fractionation law, leaving the $\Delta^{17}O\text{-}NO_3^-$ nearly unaltered (Michalski et al., 2004). On the other hand, deposition-derived $\Delta^{17}O\text{-}NO_3^-$ signals in soil can be diluted by nitrification-produced NO_3^-, which has $\Delta^{17}O \approx 0$ (Michalski et al., 2004). Therefore, $\Delta^{17}O\text{-}NO_3^-$ has great potential to resolve NO_3^- dynamics in a manner analogous to $^{15}NO_3^-$ tracer

studies (Michalski et al., 2004). Nevertheless, while $\Delta^{17}O\text{-}NO_3^-$ has been increasingly used as an indicator of atmospheric NO_3^- deposition at the watershed scale (Riha et al., 2014; Rose et al., 2015; Fang et al., 2015), its quantitative use in measuring gross nitrification and NO_3^- consumption rates has not been explored in soil systems, nor have its mechanistic couplings with $\delta^{15}N\text{-}NO_3^-$ and $\delta^{18}O\text{-}NO_3^-$.

In this proof-of-concept study, we investigated the effectiveness of $\Delta^{17}O\text{-}NO_3^-$ for probing soil nitrification and NO_3^- consumption using $\Delta^{17}O$-based analytical and numerical models. Laboratory soil incubations were conducted where soil samples spanning a wide range of properties were amended with a sodium NO_3^- fertilizer mined in the Atacama Desert, Chile (Allganic Nitrogen Plus 15-0-2, SQM North America Corp., USA). Since this NO_3^- fertilizer was derived from atmospheric NO_3^- deposited over thousands of years, it has a high $\Delta^{17}O\text{-}NO_3^-$ (18.6±0.1‰, n=4). After the NO_3^-amendment, soil $\Delta^{17}O\text{-}NO_3^-$ was measured periodically and interpreted to quantitatively characterize gross soil nitrification and NO_3^- consumption using the $\Delta^{17}O$-based models. *In situ* field soil sampling was also conducted in a temperate upland meadow following snowmelt input of $\Delta^{17}O$-enriched NO_3^- to the surface soil to assess the usefulness of $\Delta^{17}O\text{-}NO_3^-$ as a natural tracer of soil NO_3^- dynamics. Together, this work demonstrates that $\Delta^{17}O\text{-}NO_3^-$ measurement offers a new lens through which to view the soil NO_3^- biogeochemistry, one that reconciles diverse perspectives of soil NO_3^- cycling rates and isotopic fractionations.

3.2 MATERIALS AND METHOD

3.2.1 Mass-dependent fractionation and definition of $\Delta^{17}O$

The detailed theoretical basis of mass-dependent fractionation and derivation of the $\Delta^{17}O$ notation have been reviewed by Miller (2002), Young et al. (2002), and Kaiser et al. (2004). A brief summary is provided here to ease the model description and interpretation of the soil $\Delta^{17}O$-NO_3^- data.

The mass differences between the three O isotopes affect their partitioning rates between chemical species and phases, resulting in subtle, albeit measurable, changes in the minor/major isotope ratios ($^{17}R=^{17}O/^{16}O$ and $^{18}R=^{18}O/^{16}O$), known as isotopic fractionation. The degree of isotopic fractionation in kinetic processes can be quantified by a kinetic fractionation factor (α_k), which is defined by the instantaneous change in the isotope ratio of the reaction product (R_P) at a given substrate isotope ratio (R_S): $\alpha_k = R_S/R_P$. In equilibrium reactions, isotope ratios of two species, A and B, at equilibrium can be related by an equilibrium fractionation factor, $\alpha_{eq} = R_A/R_B$. By convention, isotopic fractionation can also be expressed in units of ‰ as an isotope effect (ε): $\varepsilon=(\alpha-1)\times1000$. For both kinetic and equilibrium fractionations of the three O isotopes, the isotopic fractionation factors for ^{17}R ($^{17}\alpha$) and ^{18}R ($^{18}\alpha$) are related by the mass-dependent fractionation law:

$$^{17}\alpha = \left(^{18}\alpha\right)^{\beta} \qquad \text{Equation (1)}$$

where β is the three-isotope exponent determined exclusively by the masses of the respective O isotopologues involved in the reaction. Importantly, β is not equal to a single value but varies generally between 0.51 and 0.53 for different O fractionation processes (Miller, 2002; Young et al., 2002). A value of 0.52, however, is chosen as a starting point for all the relevant processes

considered in this study (e.g., O incorporation during nitrification, O exchange between H_2O and nitrite (NO_2^-), and NO_3^- consumption; see Section 3.2.3 for more details), consistent with previous studies on $\Delta^{17}O$-NO_3^- in terrestrial and aquatic ecosystems (Michalski et al., 2004; Riha et al., 2014; Rose et al., 2015).

With a β of 0.52, mass-dependent fractionations of the three O isotopes can be represented by a single curve on the O three-isotope plot in which isotope ratios (^{17}R and ^{18}R) are expressed as fractional differences from a reference material ($^{17}R_{ref}$ and $^{18}R_{ref}$) lying on the same curve (i.e., Vienna Standard Mean Ocean Water (VSMOW) in this study) (Miller, 2002):

$$\frac{^{17}R}{^{17}R_{ref}} = \left(\frac{^{18}R}{^{18}R_{ref}}\right)^{0.52} \quad \text{Equation (2)}$$

By using delta notation ($\delta=[(R/R_{ref})-1]\times 1000$, in unit of ‰) and natural log transformation, Equation (2) becomes:

$$\ln\left(\frac{\delta^{17}O}{1000}+1\right) = 0.52\ln\left(\frac{\delta^{18}O}{1000}+1\right) \quad \text{Equation (3)}$$

Thus, a plot of $\ln(\delta^{17}O/1000+1)$ against $\ln(\delta^{18}O/1000+1)$ produce a straight line of slope 0.52 in the O three-isotope space, representing the mass-dependent fractionation law. On this basis, anomalous ^{17}O excess or deficiency ($\Delta^{17}O$), characterized by the departure from the mass-dependent fractionation line as a result of mass-independent isotope effects (e.g., photochemical ozone formation), is defined in delta notation as:

$$\Delta^{17}O = \left[\ln\left(\frac{\delta^{17}O}{1000}+1\right) - 0.52\ln\left(\frac{\delta^{18}O}{1000}+1\right)\right]\times 1000 \quad \text{Equation (4)}$$

Following Equation (4), two considerations must be kept in mind when interpreting $\Delta^{17}O$-NO_3^- data. First, because $\Delta^{17}O$ defined in Equation (4) is not linear in $\delta^{18}O$ or $\delta^{17}O$, simple mass balance and mixing calculations with $\Delta^{17}O$ should be regarded as approximations (Kaiser et al., 2004). Second, given that β (i.e., the slope of the mass-dependent fractionation line) may not be

equal to a single value for a complex fractionation process involving multiple steps or O species (e.g., nitrification), $\Delta^{17}O$ values very close to zero should not be construed as indication of mass-independent processes (Young et al., 2002).

3.2.2 $\Delta^{17}O$ dilution model

Because $\Delta^{17}O$-NO_3^- behaves similarly to the $^{15}NO_3^-$ tracer during soil NO_3^- production and consumption (Michalski et al., 2004), classical isotope dilution equations (Kirkham and Bartholomew, 1954; Smith et al., 1994) were applied to calculate gross soil nitrification and NO_3^- consumption rates:

$$R_N = -\frac{[NO_3^-]_2 - [NO_3^-]_1}{t_2 - t_1} \times \frac{\ln\left(\frac{E_2}{E_1}\right)}{\ln\left(\frac{[NO_3^-]_2}{[NO_3^-]_1}\right)} \quad \text{Equation (5)}$$

$$R_{NC} = -\frac{[NO_3^-]_2 - [NO_3^-]_1}{t_2 - t_1} \times \left(1 + \frac{\ln\left(\frac{E_2}{E_1}\right)}{\ln\left(\frac{[NO_3^-]_2}{[NO_3^-]_1}\right)}\right) \quad \text{Equation (6)}$$

where R_N and R_{NC} are gross nitrification and NO_3^- consumption rates ($\mu g\ N \cdot g^{-1} \cdot d^{-1}$), respectively; $[NO_3^-]$ is the soil NO_3^- concentration ($\mu g\ N \cdot g^{-1}$); the subscripts 1 and 2 denote two soil sampling times t_1 and t_2, respectively. Throughout this paper, soil N concentrations and transformation rates are expressed on the basis of soil oven-dry weight unless stated otherwise. In the case of $^{15}NO_3^-$ tracer studies, *E* denotes excess ^{15}N over natural abundance. Analogously, in our case, *E* is $\Delta^{17}O$-NO_3^-, an index of excess ^{17}O over that expected from ^{18}O and the mass-dependent fractionation law. A derivation of Equations (5) and (6) with $\Delta^{17}O$-NO_3^- as the input is given in Appendix B.

3.2.3 $\Delta^{17}O$-based numerical model

Given that the tracing power of $\Delta^{17}O$-NO_3^- relies on mass-dependent fractionation law and that nitrification is a multi-step, multi-phase fractionation process, it is important to carefully and explicitly evaluate the effects of isotopic fractionations on $\Delta^{17}O$-NO_3^- as a conservative tracer of soil nitrification and NO_3^- consumption. Equally important is to couple $\Delta^{17}O$-NO_3^- with the dual NO_3^- isotopes to assess what new insights the triple NO_3^- isotopes can contribute to the NO_3^- biogeochemistry in soil. To meet these needs, a numerical model was devised based on current understanding of the biochemistry and isotopic systematics of nitrification and NO_3^- consumption (Figure 3.1).

Three soil N pools are considered in the numerical model: organic N, NH_4^+, and NO_3^- (Mary et al., 1998; Müller et al., 2004) (Figure 3.1). Mineralization of organic N produces NH_4^+, which can be returned to the organic N pool as microbial biomass N via microbial NH_4^+ assimilation or nitrified to NO_3^-, while NO_3^- can be consumed via microbial assimilation and denitrification. Each of these N transformation processes is associated with a kinetic N isotope effect (see Denk et al. (2017) for a review) (Figure 3.1). During the two-step process of nitrification, the oxidation of NH_4^+ to NO_2^- incorporates one O atom from O_2 and one from H_2O; the subsequent oxidation of NO_2^- to NO_3^- incorporates an O atom derived from H_2O (Figure 3.1). Recent work has revealed kinetic isotope effects associated with enzymatic incorporation of each of the three O atoms into the nitrified NO_3^-, as well as the isotopic equilibrium of O atoms between NO_2^- and H_2O during the first oxidation step (see Granger and Wankel (2016) for a review) (Figure 3.1). Moreover, NO_3^- consumption processes fractionate the O isotopes of NO_3^- to a similar degree as the N isotopes (Figure 3.1).

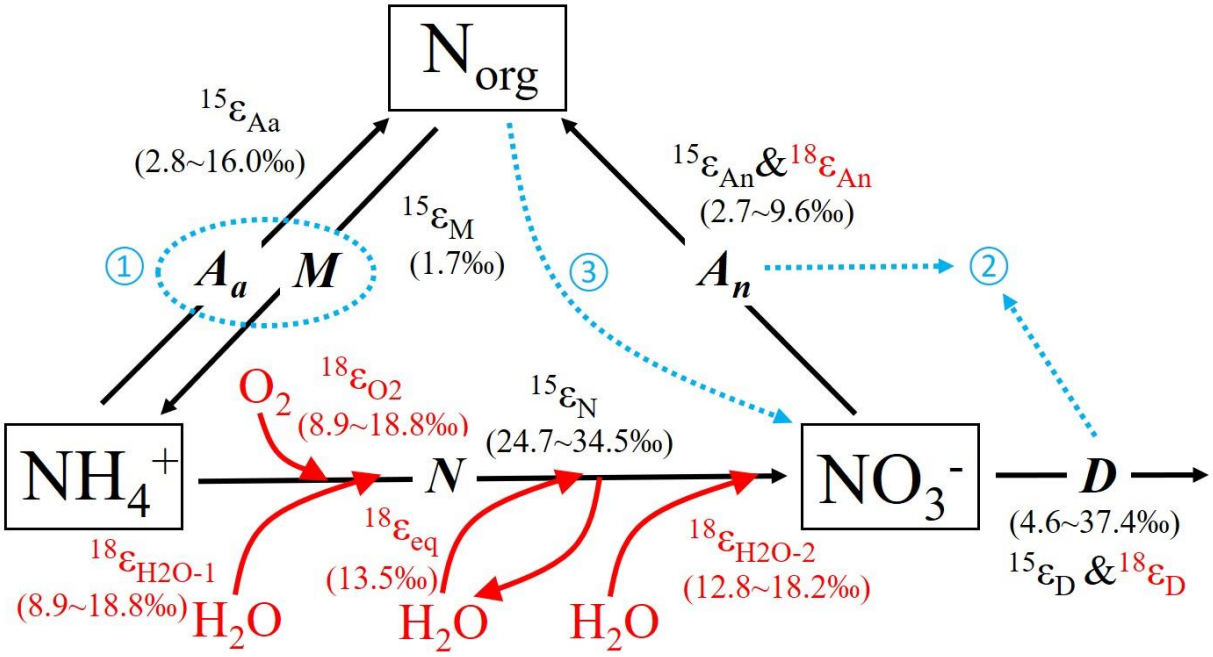

Figure 3.1 Conceptual schematic for relevant N transformation processes between the NO_3^-, NH_4^+ and organic N pools. The black arrow lines denote N mass flows. M=gross mineralization; N=gross nitrification with NH_4^+ as the substrate; A_a and A_n=gross microbial assimilation of NH_4^+ and NO_3^-, respectively; D=gross denitrification. Each of these N transformation processes is associated with a kinetic isotope effect ($^{15}\varepsilon$). Characteristic estimates for $^{15}\varepsilon$ are adopted from Denk et al. (2017) and given in parentheses. The red arrow lines denote O incorporation during nitrification through kinetic O extraction from O_2 and H_2O and equilibrium O exchange with H_2O. The estimates for O isotope effects ($^{18}\varepsilon$) associated with the O incorporation are adopted from Granger and Wankel (2016) and given in parentheses. It is assumed that N and O isotope effects for microbial NO_3^- assimilation and denitrification are coupled (i.e., $^{15}\varepsilon$=$^{18}\varepsilon$). The blue dashed arrow lines and cycle illustrate the accommodation of the conceptual model for parameterizing the $\Delta^{17}O$-based numerical model: ① mineralization and NH_4^+ assimilation are combined to be a net flux between the

NH_4^+ and organic N pools (i.e., net mineralization); ② microbial NO_3^- assimilation and denitrification are combined to be gross NO_3^- consumption; ③ in cases where the NH_4^+ pool is depleted, NO_3^- production is directly modeled from the organic N pool (i.e., coupled mineralization and nitrification).

The numerical model was parameterized with following considerations (Figure 3.1). First, NO_2^- is not explicitly included in the model because it was not in significant concentrations in either the incubation experiments or the field sampling. Therefore, N and O isotope effects for NO_2^- oxidation to NO_3^- are considered not expressed. Second, mineralization and NH_4^+ assimilation fluxes are combined to be a net mineralization flux between the organic N and NH_4^+ pools to lower the number of unknowns in the model such that the model system is determined (i.e., number of unknowns not exceed number of measured variables (Mary et al., 1998)). Third, in cases where the soil NH_4^+ pool is depleted due to tightly coupled mineralization and nitrification, NO_3^- production and its N isotope effect are modeled from the organic N pool. Fourth, NO_3^- assimilation and denitrification are not partitioned in the model. Instead, a N isotope effect is estimated for overall gross NO_3^- consumption, which reflects the relative importance of denitrification. Finally, and most importantly, the fractionations of $^{17}O/^{16}O$ and $^{18}O/^{16}O$ for all the kinetic and equilibrium O fractionation processes in the model are related using the mass dependent fractionation law (i.e., Equation (2)).

Using the model structure described above, a set of differential equations was constructed to simulate the N and O isotopologue pools of soil NO_3^- (i.e., ^{14}N, ^{15}N, ^{16}O, ^{17}O, and ^{18}O) and NH_4^+ (i.e., ^{14}N and ^{15}N). While the kinetics of the net mineralization is fixed to be zero-order, nitrification and NO_3^- consumption can either follow zero- or first-order kinetics. Under default

settings the model simulates nitrification using the O isotope effects summarized by Granger and Wankel (2016) (i.e., midrange values shown in Figure 3.1), 23.5‰ and -10‰ for $\delta^{18}O$ of soil O_2 and H_2O, respectively, and 0.2 for the fractional O exchange between NO_2^- and H_2O catalyzed by nitrifiers (Casciotti et al., 2010). The mathematical formulation of the model adopting zero-order kinetics for all the N transformation processes is provided in Appendix B.

We applied the model to test the robustness of $\Delta^{17}O\text{-}NO_3^-$ in tracing nitrification and NO_3^- consumption in two specific cases. First, zero-order rates of gross nitrification and NO_3^- consumption were fitted using the measured time series of soil NO_3^- concentration and $\Delta^{17}O\text{-}NO_3^-$ and compared to those estimated by the $\Delta^{17}O$ dilution model. To investigate the leverage of β, the $\delta^{18}O$ of the O sources, and the O isotope effects on the rate estimates, these factors were varied simultaneously over a respective range of values (Table B-1) within the model using a Monte Carlo routine (1000 times). In the second case, process rates (or rate constants) and N isotope effects of the net mineralization, nitrification, and NO_3^- consumption were optimized using the measured concentrations and $\delta^{15}N$ values of soil NH_4^+ and NO_3^- in tandem with $\Delta^{17}O\text{-}NO_3^-$. To uniquely solve this model system, concentration and $\delta^{15}N$ of soil organic N are required. However, because soil organic N was not measured in this study, we assumed it can be approximated by the total soil N in terms of pool size and $\delta^{15}N$ value similar to previous natural abundance studies of soil N isotopes (e.g., Decock and Six, 2013; Snider et al., 2015; Hall et al., 2016). In both cases, the isotopologue-specific differential system of equations was solved numerically using a Runge-Kutta method with a variable time step (Solver ode45, Matlab, Mathworks, USA) and the measured initial values of the isotopologue pools. The resultant isotopologue abundances were converted to concentrations and isotopic compositions (in delta notation) for interpretation. A non-linear optimization applying Trust-Region-Reflective least squares algorithm (Matlab,

Mathworks, USA) was then used to find the unknown N process rates (or rate constants) and N isotope effects that minimize the quadratic weighted error between modeled and measured results (Mary et al., 1998). To avoid local minima, the optimization procedure was repeated three times with different initial values for fitted parameters and only considered successful when the same set of parameters was obtained in the three replicate runs. Approximate 95% confidence intervals were calculated for parameter estimates using an error covariance matrix.

3.2.4 Laboratory soil incubations

We sampled soils from four sites in and around Pittsburgh, Pennsylvania, USA: a conventional corn field receiving mineral fertilizers (hereafter, agricultural site), a mowed, poorly drained, grassy, upland meadow in a forest clearing (meadow site), an urban mixed hardwood forest experiencing partial cutting (forest site), and a restored urban riparian floodplain with herbaceous vegetation (riparian site). Soil samples were collected using a stainless-steel corer (5 cm inner diameter) to a depth of 7 cm at each site. Prior to sampling at the forest site, the upper layer (Oi horizon, approximately 5 mm thick) of the forest floor was removed from the sampling area. In the laboratory, fresh soils were sieved by passing through 2 mm sieves and left to air-dry at room temperature (22 °C) for later analyses. Basic characteristics of each soil can be found in Table 3.1. For the four soils, pH ranged from 5.0 to 5.7. The forest soil was highly humified and had the highest total and organic C content, followed by the riparian, meadow, and agricultural soils. Total N was highest in the forest soil (0.9%) and lowest in the agricultural soil (0.2%), whereas $\delta^{15}N$ of total N was highest in the agricultural soil (5.3‰) and lowest in the meadow soil (2.2‰). Inhibitor-based nitrification (Belser and Mays, 1980) and denitrification (Groffman et al., 1999) potentials were measured within two days before the incubation experiments. Nitrification potential was

significantly higher in the forest, riparian, and agricultural soils with high antecedent NO_3^- concentrations than in the meadow soil, where NH_4^+ dominated the inorganic N pool (Table 3.1). Denitrification potential was 3.6, 8.5, and 9.7 μg $N \cdot g^{-1} \cdot d^{-1}$ for the meadow, forest, and riparian soils, respectively (Table 3.1).

Table 3.1 Soil characteristics, N transformation rates, and isotope effects estimated using the numerical model in the laboratory incubation experiments.

Soil	Agricultural	Meadow	Forest	Riparian
		Soil characteristics*		
Taxonomic classification	Alfisol	Ultisol	Ultisol	Entisol
Texture (% sand, % silt, % clay)	silt loam (21, 58, 21)	silty clay loam (31, 67, 2)	silt loam (19, 62, 19)	silt loam (20, 62, 18)
Bulk density ($g \cdot cm^{-3}$)	1.22	1.13	0.87	0.92
pH (1:1 water)	5.7	5.0	5.4	5.6
Gravimetric soil water content (g $H_2O \cdot g^{-1}$)※	0.22	0.72	0.65	0.57
Total carbon (%)	1.8	6.6	13.2	8.4
Organic carbon (%)	1.8	6.4	9.9	7.5
Total nitrogen (%)	0.2	0.5	0.9	0.5
$\delta^{15}N$ of total nitrogen (‰)	5.3	2.2	3.7	3.9
C:N ratio (mol:mol)	11.4	14.6	17.3	19.6
Antecedent NH_4^+ (μg $N \cdot g^{-1}$)	0.7	19.1	0.7	0.5
Antecedent NO_3^- (μg $N \cdot g^{-1}$)	29.8	2.1	18.7	15.7
Nitrification potential (μg $N \cdot g^{-1} \cdot d^{-1}$)	14.6	2.6	21.5	14.7
Denitrification potential (μg $N \cdot g^{-1} \cdot d^{-1}$)	NA	3.6	8.5	9.7
	***Estimated N transformation rates and N isotope effects**†			
Net mineralization (μg $N \cdot g^{-1} \cdot d^{-1}$)‡	0.90±0.37	2.13±0.11	NA	NA
Gross nitrification (μg $N \cdot g^{-1} \cdot d^{-1}$)	9.75±0.15	1.71±0.02	10.32±0.67	5.85±0.22
Gross NO_3^- consumption (μg $N \cdot g^{-1} \cdot d^{-1}$)	0.81±0.15	0.75±0.02	5.45±0.67	2.87±0.22
N isotope effect for net mineralization (‰)	0.0±5.0	4.4±3.2	NA	NA
N isotope effect for nitrification (‰)	32.8±1.4	28.4±2.1	1.7±3.1§	1.8±2.2§
N isotope effect for NO_3^- consumption (‰)	0.0±15.0	8.1±4.9	0.0±5.1	0.2±4.6

***** Each datum is an average based on three replicate measurements.

※ Gravimetric soil water content corresponding to 100% field capacity for the meadow, forest, and riparian soils and 80% for the agricultural soil.

† The estimated N transformation rates and isotope effects are presented as mean plus and minus margin of error of the 95% confidence interval.

‡ Net mineralization is defined as the net flux of mineralization and NH_4^+ assimilation between the NH_4^+ and organic N pools.

§ N isotope effect for NO_3^- production from the organic N pool via the coupled mineralization and nitrification.

To initiate the incubation experiments for the meadow, forest, and riparian soils, 35 g (dry weight equivalent) of the sieved soils were weighed into six sets of 250 mL Nalgene bottles with eight bottles per set. The soils were then fertilized with the Chilean NO_3^- ($\delta^{15}N\text{-}NO_3^-$=0.3±0.1‰, $\delta^{18}O\text{-}NO_3^-$=55.8±0.1‰) and ammonium sulfate ($(NH_4)_2SO_4$; $\delta^{15}N\text{-}NH_4^+$=1.9±0.3‰) dissolved in deionized Milli-Q water at the same N concentration to achieve field capacity water content (Table 3.1) and a $\Delta^{17}O\text{-}NO_3^-$ of 5‰. The field capacity water content and NH_4^+ addition were adopted here to simulate $\Delta^{17}O\text{-}NO_3^-$ input via wet deposition where the initial $\Delta^{17}O\text{-}NO_3^-$ in the incubated soils is consistent with the highest $\Delta^{17}O\text{-}NO_3^-$ (4.7‰) observed at the meadow site during the field snowmelt sampling (see below). The N addition to these soils increased the soil NO_3^- concentrations by about 27%, while the soil NH_4^+ concentrations were increased by <3% to >100%, depending on the antecedent concentrations (Table 3.1). Long-term $\delta^{18}O$ of the Milli-Q water produced in our lab is -10.1±0.2‰ (n=12). After the amendment, the bottles were sealed with Parafilm with seven pin holes for gas exchange and incubated in the dark at room temperature. Soil extractions were carried out 0.5, 12, 24, 48, 72 and 96 h after the fertilizer application. At each extraction, the eight replicate samples were divided into two groups and four of them were extracted for NH_4^+ determination using 175 mL of 2 M KCl. We followed Costa et al. (2011) to extract soil NO_3^- for determination of concentration and the triple NO_3^- isotopes. Each of the four remaining bottles was combined with 70 mL deionized Milli-Q water and vortexed for 10 minutes at 3200 rpm. The slurry was then centrifuged for 10 minutes at 2000 rpm, and the resultant

supernatant was filtered through a sterile 0.2 μm filter. The agricultural soil was incubated using a similar protocol in which higher amount of soil (100 g dry weight equivalent), lower soil water content (80% of field capacity; Table 1), less frequent sampling (four times over four days), larger additions of NO_3^- (15 μg $N \cdot g^{-1}$) and NH_4^+ (90 μg $N \cdot g^{-1}$), and higher initial $\Delta^{17}O\text{-}NO_3^-$ (6‰) were adopted for the incubation to accommodate measurements of N trace gas emission in a separate study.

3.2.5 Field snowmelt sampling

In situ soil sampling was conducted at the meadow site following a snowmelt event. This site was located at a toe-slope position and subject to continuous monitoring of surface soil temperature and water content (5 cm depth) since 2016 (Figure B-1a). Snow precipitation occurred on February 9, 2017, resulting in a maximum snow depth of about 25 cm, equivalent to about 3 cm of snow water, as recorded by the nearest (3 miles) snow monitoring station (PA-SM-3, National Operational Hydrologic Remote Sensing Center, NOAA). Three snowpack samples were collected on February 10 before the onset of the snowmelt. After the completion of the snowmelt, eight soil cores (5 cm inner diameter, 7 cm depth) were collected daily from February 11 through February 15 within a 5 by 5 m square. During this time period, soil experienced temperature fluctuated between 2.5 °C and 6.0 °C and remained nearly saturated (Figure B-1b). The sampled intact soil cores were stored at 4 °C and immediately transported back to the laboratory where they were gently broken up by hand, slightly air-dried, sieved through a 4 mm mesh, and extracted for determination of NO_3^- concentration and the triple NO_3^- isotopes on the same day as previously described.

3.2.6 Chemical and isotopic analyses

Analyses for NO_3^- and NO_2^- in the soil extracts were carried out on a Dionex Ion Chromatograph ICS-2000 with a precision (1σ) of ±5.0 μg $N \cdot L^{-1}$ and ±2.5 μg $N \cdot L^{-1}$, respectively. NH_4^+-N analyses were carried out on a fluorometer (Trilogy, Turner Designs, USA) using a modified fluorometric OPA method for soil KCl extracts (Kang et al., 2003; Taylor et al., 2007) with a precision of ±7.0 μg $N \cdot L^{-1}$.

The $\delta^{15}N$ and $\delta^{18}O$ of the extracted soil NO_3^- were measured using the denitrifier method (Sigman et al., 2001; Casciotti et al., 2002). In brief, denitrifying bacteria lacking the nitrous oxide (N_2O) reductase enzyme (*Pseudomonas aureofaciens*) are used to convert 20 nmol of NO_3^- into gaseous N_2O. Using He as a carrier gas, the N_2O is then purified in a series of chemical traps, cryofocused, and finally analyzed on a GV Instruments Isoprime continuous flow isotope ratio mass spectrometer (CF-IRMS). International NO_3^- reference standards IAEA-N3, USGS34, and USGS35 were used to calibrate the $\delta^{15}N$ and $\delta^{18}O$ measurements. The long-term precision for the $\delta^{15}N$ and $\delta^{18}O$ analyses are ±0.3‰ and ±0.5‰, respectively. The $\Delta^{17}O$ of soil NO_3^- was measured using the coupled bacterial reduction and thermal decomposition method described by Kaiser et al. (2007). After converting 200 nmol of soil NO_3^- sample to N_2O, the N_2O was thermally converted to O_2 and N_2 by reduction over a gold surface at 800 °C. The O_2 and N_2 were separated using a 5Å molecular sieve gas chromatograph and the O_2 was analyzed for $\delta^{17}O$ and $\delta^{18}O$ by the CF-IRMS. The $\Delta^{17}O$ was calculated using Equation (4) and calibrated by USGS34, USGS35, and a 1:1 mixture of USGS34 and USGS35. The precision for $\Delta^{17}O$ analysis of USGS35 and the USGS35:USGS34 mixture is ±0.3‰. According to Kaiser et al. (2007), the measured $\Delta^{17}O$ was used in reduction of molecular isotope ratios of N_2O to correct the isobaric interference (i.e., *m/z* 45) on the $\delta^{15}N$ analysis using the denitrifier method.

The $\delta^{15}N$ of the extracted soil NH_4^+ was measured by coupling the ammonia (NH_3) diffusion method (Zhang et al., 2015) and the hypobromite (BrO^-) oxidation method (Zhang et al., 2007) with the denitrifier method (Felix et al., 2013). Briefly, an aliquot of soil KCl extract having 20 to 60 nmol NH_4^+ was pipetted into a 20 mL serum vial containing an acidified glass fiber disk. The solution was made alkaline by adding Magnesium oxide (MgO) to volatilize NH_3 which is subsequently captured on the acidic disk. After removal of the disk, NH_4^+ was eluted using deionized Milli-Q water, diluted to 10 µM, oxidized by BrO^- to NO_2^-, and finally measured for $\delta^{15}N$ as NO_2^- at 20 nmol using the denitrifier method as described above. International NH_4^+ reference standards IAEA-N1, USGS25, and USGS26 undergone the same preparation procedure as the soil samples were used along with the NO_3^- reference standards to correct for blanks and instrument drift. The precision for the $\delta^{15}N$-NH_4^+ analysis is ±0.5‰.

3.3 RESULTS

3.3.1 Laboratory soil incubations

For all the four soils studied in the laboratory, the NO_3^- concentrations increased significantly over the incubation period (Figure 3.2c). Nitrite was detectable in the agricultural, forest, and riparian soils but its concentrations did not exceed 1% of the NO_3^- concentrations throughout the incubations. The large increase in the NO_3^- concentration during the incubation period in the agricultural soil was accompanied by significant declines in the NH_4^+ concentration (Figure 3.2a) and the $\delta^{15}N$-NO_3^- (Figure 3.2d), whereas the $\delta^{15}N$-NH_4^+ increased during the incubation (Figure 3.2b). Declining $\delta^{15}N$-NO_3^- and increasing $\delta^{15}N$-NH_4^+ were also observed for the meadow soil

(Figure 3.2b and 3.2d), although the NH_4^+ concentration remained relatively stable throughout the experimental period (Figure 3.2a). The added NH_4^+ was rapidly consumed within 12 h after the amendment in the forest and riparian soils (Figure 3.2a), leading to a steep increase in the NO_3^- concentrations and $\delta^{15}N\text{-}NO_3^-$ values (Figure 3.2c and 3.2d). Thereafter, the NH_4^+ concentrations were <1 μg $N \cdot g^{-1}$ and the $\delta^{15}N$ values of NO_3^- and NH_4^+ remained relatively constant, despite the steady increases in the NO_3^- concentrations (Figure 3.2).

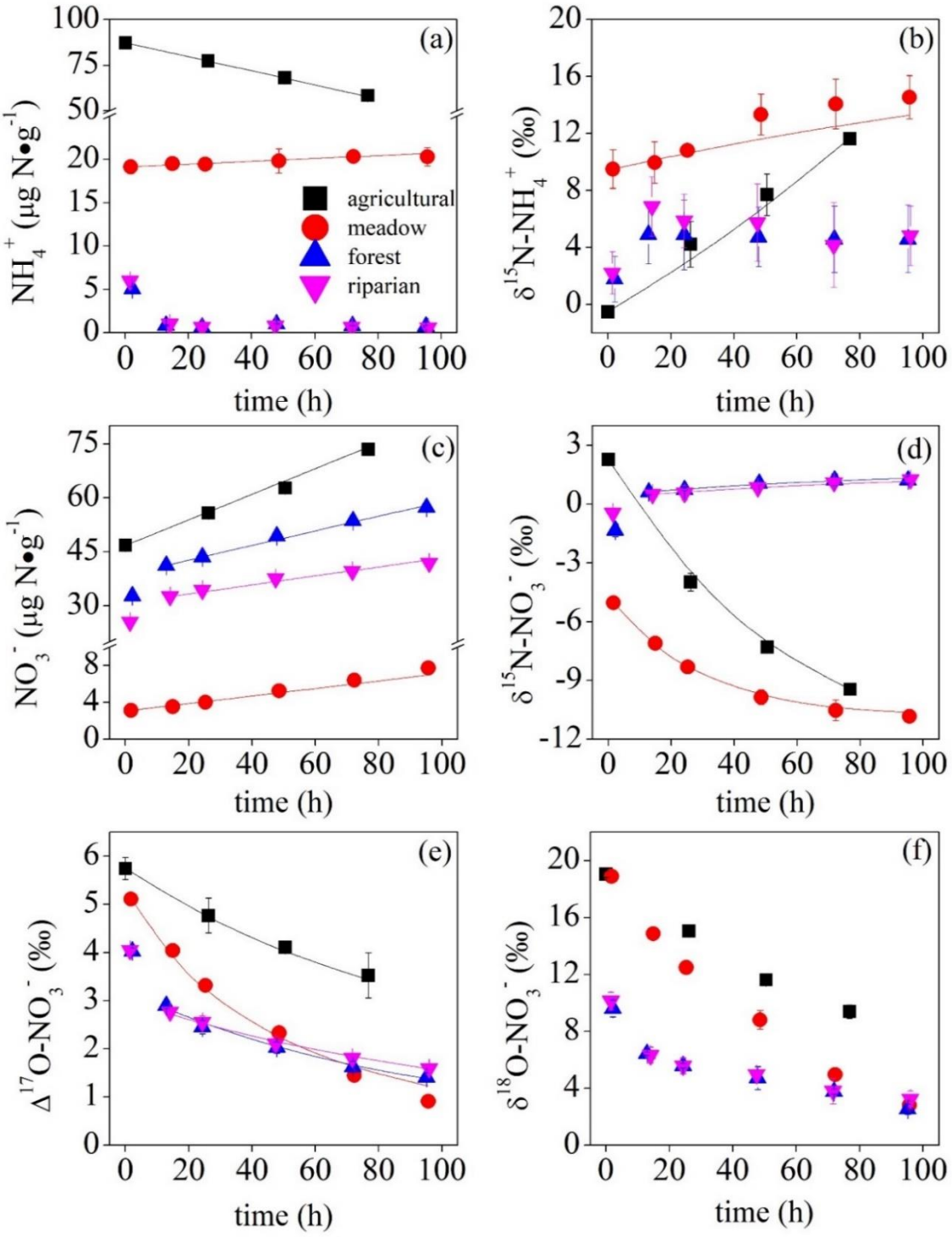

Figure 3.2 Measured (symbols) and modeled (lines) concentrations and isotopic compositions of NH_4^+ and NO_3^- after application of the Chilean NO_3^- fertilizer to the four soils in the laboratory incubation experiments. The error bar denotes standard deviation of

the replicate measurements. If no bars are evident, the errors were less than the size of the symbol.

The applied $\Delta^{17}O\text{-}NO_3^-$ tracer was nearly fully recovered 0.5 h after the amendment in the agricultural and meadow soils, whereas the recovery was only about 80% for the forest and riparian soils (Figure 3.2e). For the four soils, $\Delta^{17}O\text{-}NO_3^-$ values declined progressively by 2.5‰ to 4.2‰ during the incubation period (Figure 3.2e), and the pooled standard deviation of the replicate $\Delta^{17}O\text{-}NO_3^-$ measurements was ±0.13‰. A concurrent decrease in $\delta^{18}O\text{-}NO_3^-$ values was observed for all four soils (Figure 3.2f), resulting in positive linear relationships between $\Delta^{17}O\text{-}NO_3^-$ and $\delta^{18}O\text{-}NO_3^-$ (Figure 3.3b). $\Delta^{17}O\text{-}NO_3^-$ values also varied linearly with $\delta^{15}N\text{-}NO_3^-$ values, yet the linear relationships are different among the soils: positive for the agricultural and meadow soils and negative for the forest and riparian soils (Figure 3.3a).

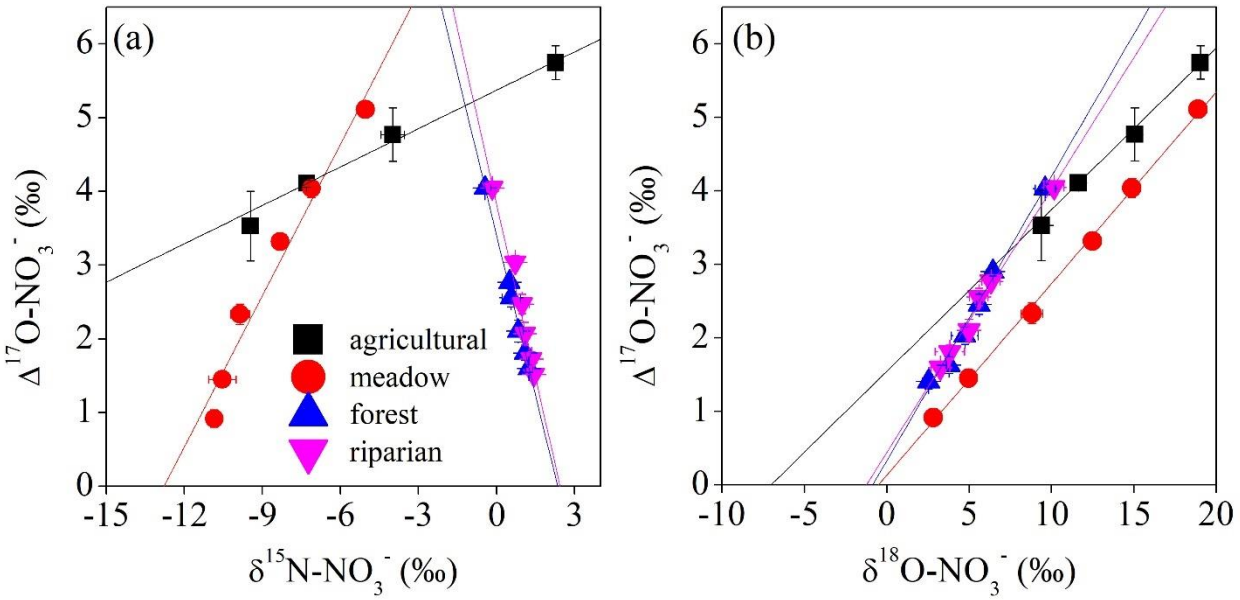

Figure 3.3 Relationships between $\Delta^{17}O\text{-}NO_3^-$ and $\delta^{15}N\text{-}NO_3^-$ (a) and between $\Delta^{17}O\text{-}NO_3^-$ and $\delta^{18}O\text{-}NO_3^-$ (b) in the laboratory incubation experiments. The error bar denotes

standard deviation of the replicate measurements. The lines represent linear regression fits for the respective relationships for the four soils.

When applied to every two consecutive soil extractions, a wide range of gross nitrification (1.2 to 26 μg $N \cdot g^{-1} \cdot d^{-1}$) and NO_3^- consumption (0.1 to 9 μg $N \cdot g^{-1} \cdot d^{-1}$) rates were estimated using either the $\Delta^{17}O$ dilution model or the numerical models for the four soils (Figure 3.4). Relative to the numerical model, the $\Delta^{17}O$ dilution model tended to underestimate gross nitrification and NO_3^- consumption rates by 7.0±3.6% and 17.1±10.8%, respectively, for the four soils (Figure 3.4). Sensitivity analysis indicated that the numerically solved rate estimates are stable over the relevant range of β, the $\delta^{18}O$ values of O sources (i.e., O_2 and H_2O), and the kinetic and equilibrium O isotope effects during nitrification and NO_3^- consumption (Table B-1), with typical standard deviation derived from 1000 Monte Carlo iterations being less than 6% of the simulated mean values for gross nitrification and NO_3^- consumption rates (Figure B-2).

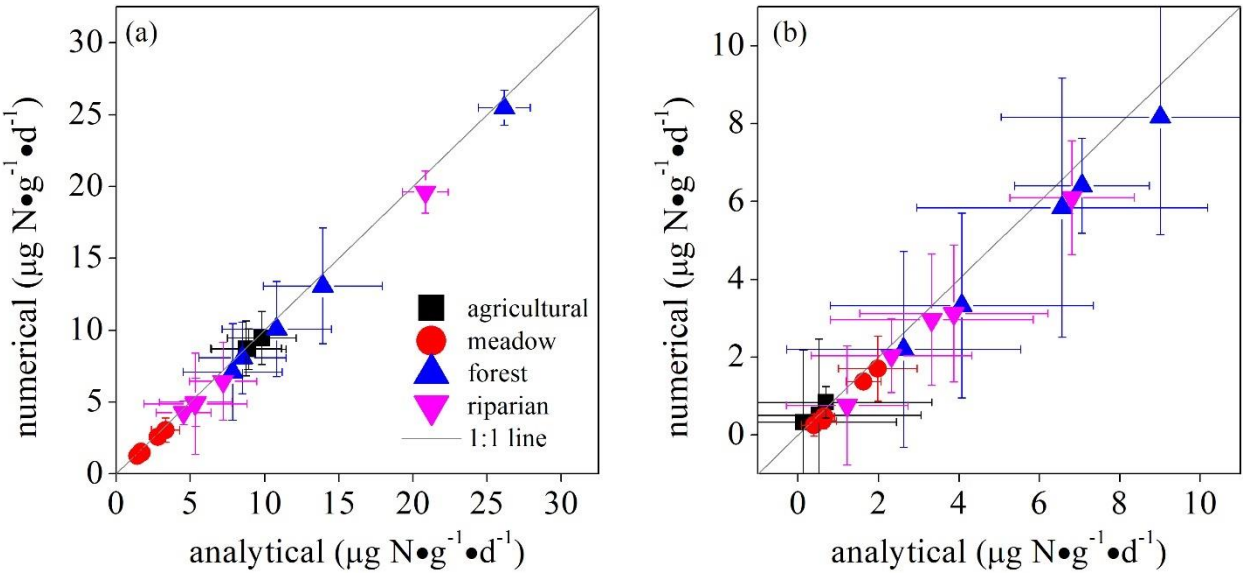

Figure 3.4 Gross nitrification (a) and NO_3^- consumption (b) rates estimated using the analytical $\Delta^{17}O$ dilution model and the numerical model for every two consecutive soil samplings in the laboratory incubation experiments. The error bars denote the 95% confidence intervals of the estimated rates.

Both nitrification and NO_3^- consumption were best described by zero-order kinetics for the agricultural and meadow soils when the gross rates were optimized using the numerical model for the entire duration of the incubations. Because the NH_4^+ pool was quickly depleted after the amendment in the forest and riparian soils (Figure 3.2a), preventing accurate estimation of nitrification through the NH_4^+ pool, zero-order rates of the coupled mineralization and nitrification were estimated for these two soils using data measured 12 h after the amendment. Excellent agreement was obtained between the observed and simulated concentrations and isotopic compositions (Figure 3.2). The good quality of fit was confirmed by the high fraction of the total variation explained by the model, as indicated by a R^2 >0.95 for all four soils. The only noticeable difference relative to the standard deviation of the replicate measurements was a slight underestimation of the $\delta^{15}N\text{-}NH_4^+$ in the meadow soil during the last three sampling intervals. The estimated gross nitrification rate was higher in the forest (10.32±0.67 μg $N \cdot g^{-1} \cdot d^{-1}$) and agricultural (9.75±0.15 μg $N \cdot g^{-1} \cdot d^{-1}$) soils than in the riparian (5.85±0.22 μg $N \cdot g^{-1} \cdot d^{-1}$) and meadow (1.71±0.02 μg $N \cdot g^{-1} \cdot d^{-1}$) soils (Table 3.1). Nitrification was associated with a large N isotope effect in the agricultural (32.8±1.4‰) and meadow (28.4±2.1‰) soils, whereas the isotope effect for the coupled mineralization and nitrification was small in the forest and riparian soils (Table 3.1). Significant NO_3^- consumption (0.75±0.02 to 5.45±0.67 μg $N \cdot g^{-1} \cdot d^{-1}$) relative to the gross nitrification were indicated in the meadow, forest, and riparian soils (Table 3.1). Only NO_3^-

consumption in the meadow soil, however, was associated with an appreciable N isotope effect (8.1±4.9‰) (Table 3.1).

3.3.2 Field snowmelt sampling

The snow water samples had a NO_3^- concentration of 0.26±0.04 mg $N \cdot L^{-1}$ and a $\Delta^{17}O$ of 25.1±0.1‰. The snowmelt event captured in this study introduced snow NO_3^- into the surface soil, leading to nonzero $\Delta^{17}O\text{-}NO_3^-$ values for the first (2.1±1.5‰) and second (1.9±1.3‰) days of soil sampling (Figure 3.5c), although large deviations were observed in the replicate measurements (n=8) probably due to soil heterogeneity. A significant decline in the $\Delta^{17}O\text{-}NO_3^-$ occurred between day 2 and day 3 such that the $\Delta^{17}O\text{-}NO_3^-$ values measured for the last three days of sampling (-0.4±0.4 to 0.3±0.6‰) were not significantly different from zero (Figure 3.5c). Post-snowmelt variations in the soil NO_3^- concentration and the dual NO_3^- isotopes were more complex. The NO_3^- concentration appeared to be significantly increased on day 5 (Figure 3.5a), while both $\delta^{15}N\text{-}NO_3^-$ and $\delta^{18}O\text{-}NO_3^-$ increased significantly from day 1 through day 3 and then decreased toward day 5 (Figure 3.5b and 3.5d). The $\Delta^{17}O\text{-}NO_3^-$ was significantly and negatively correlated with the $\delta^{15}N\text{-}NO_3^-$ if only data measured in the first three sampling days was used in the linear regression (Figure 3.6a). A negative, albeit not statistically significant (P=0.051), association was also found between the $\Delta^{17}O\text{-}NO_3^-$ and the $\delta^{18}O\text{-}NO_3^-$ for the first three sampling days (Figure 3.6a). Significant and negative correlations were also detected between the $\delta^{15}N\text{-}NO_3^-$ and the natural logarithm of the NO_3^- concentration (Figure 3.6b). When plotting the $\delta^{15}N\text{-}NO_3^-$ and the $\delta^{18}O\text{-}NO_3^-$ together, a significant linear relationship with a slope of 0.63 emerged for the entire sampling period (Figure 3.6c). The linear regression fit was improved and the slope of the regression line was increased to 0.89 if only data measured in the first three sampling days was included (Figure 3.6c). The

numerical model was used to fit the NO_3^- concentration and $\Delta^{17}O\text{-}NO_3^-$ for the first three sampling days when nonzero $\Delta^{17}O\text{-}NO_3^-$ was generally measurable (Figure 3.5c) and found that gross nitrification and NO_3^- consumption rates were 1.3±2.1 μg $N \cdot g^{-1} \cdot d^{-1}$ and 1.7±2.1 μg $N \cdot g^{-1} \cdot d^{-1}$, respectively.

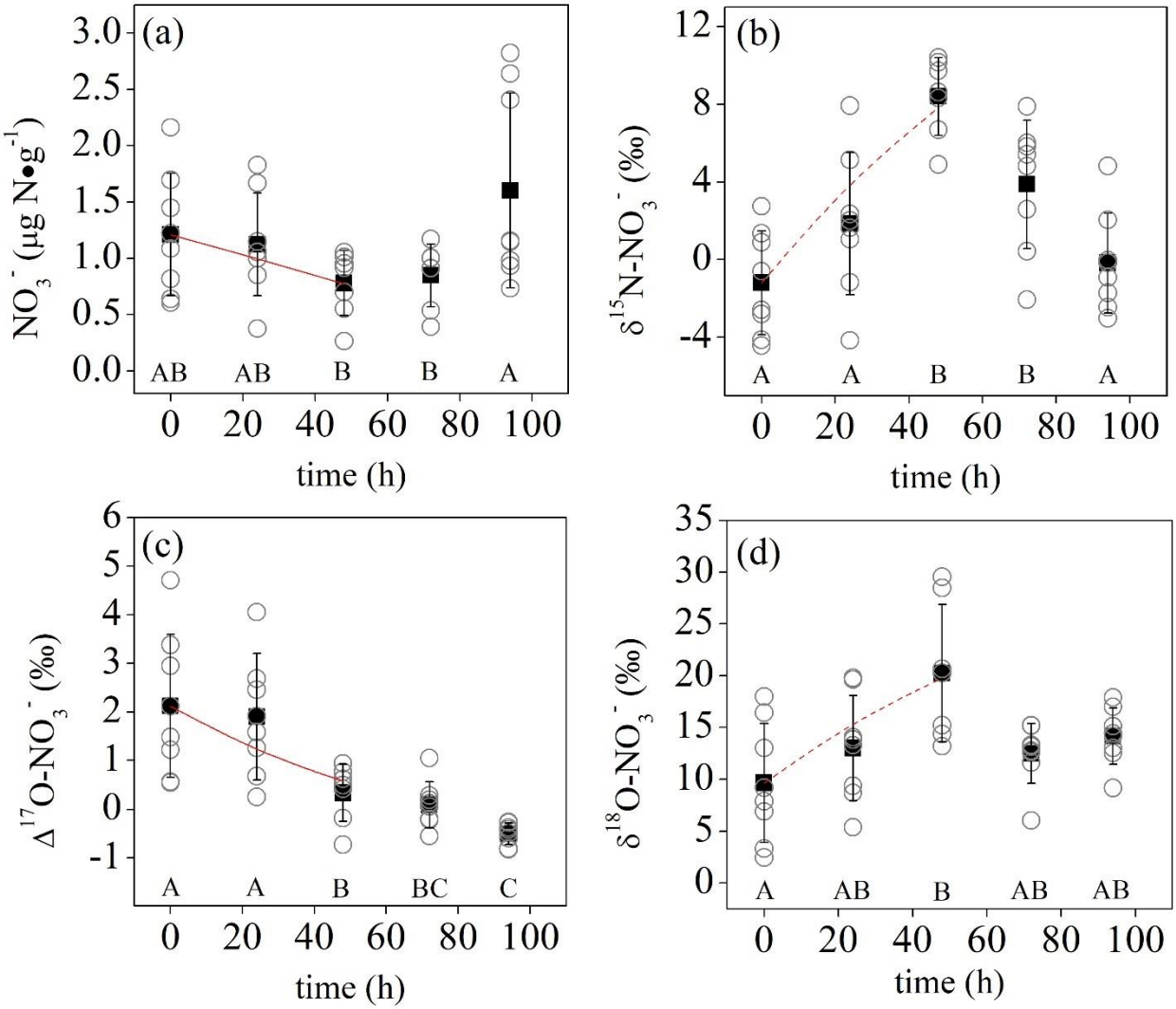

Figure 3.5 Measured (symbols) and modeled (solid and dashed lines) concentrations and isotopic composition of NO_3^- from the field sampling following the snowmelt. Mean and standard deviation (solid black squares and error bars) are calculated based on eight

replicate measurements (open gray cycles). The letters below the symbols denote significant differences determined by one-way ANOVA with a pairwise Bonferroni test (P<0.05).

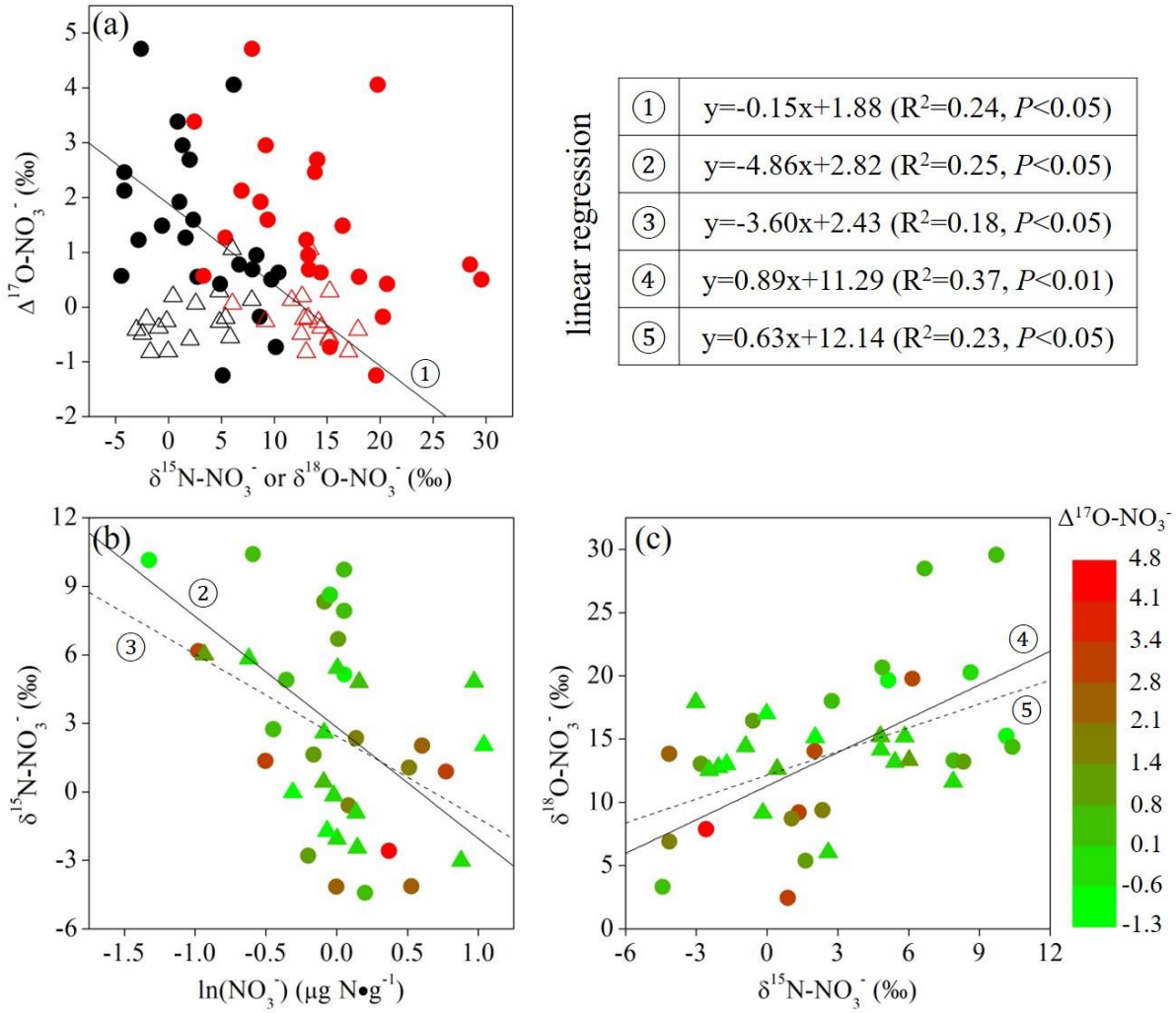

Figure 3.6 Relationships among soil NO_3^- concentration and the triple NO_3^- isotopes in the field soil sampling following the snowmelt. (a) Relationships between $\Delta^{17}O\text{-}NO_3^-$ and $\delta^{15}N\text{-}NO_3^-$ (black symbols) and between $\Delta^{17}O\text{-}NO_3^-$ and $\delta^{18}O\text{-}NO_3^-$ (red symbols). (b) Relationship between $\delta^{15}N\text{-}NO_3^-$ and the natural logarithm of soil NO_3^- concentration in association with $\Delta^{17}O\text{-}NO_3^-$ (color scale). (c) Relationship between $\delta^{15}N\text{-}NO_3^-$ and $\delta^{18}O\text{-}NO_3^-$ in association with $\Delta^{17}O\text{-}NO_3^-$ (color scale). In all the panels, data measured for day 1 through

day 3 and for day 4 through day 5 are shown as cycles and triangles, respectively. The solid and dashed lines represent linear regression fits for the first three sampling days and the entire sampling duration, respectively. The linear regression fits are labeled and corresponding to the regression equations shown in the inserted table.

3.4 DISCUSSION

3.4.1 $\Delta^{17}O\text{-}NO_3^-$ as a conservative tracer of gross soil nitrification and nitrate consumption

Applying $\Delta^{17}O\text{-}NO_3^-$ with the isotopic dilution model implicitly assumes that: (1) the added $\Delta^{17}O$ label is well mixed in the soil, (2) both nitrification and NO_3^- consumption can be described by zero-order kinetics during measurement intervals, (3) $\Delta^{17}O\text{-}NO_3^-$ is linear in terms of mixing, (4) nitrification-produced NO_3^- has $\Delta^{17}O=0$, and (5) NO_3^- consumption does not in itself alter $\Delta^{17}O\text{-}NO_3^-$. While the first two assumptions are probably met in short-term laboratory incubation experiments (Smith et al, 1994; Davidson et al., 1991), the last three assumptions are difficult to test in complex soil environments with co-occurring nitrification and NO_3^- consumption.

The numerical model that explicitly simulates the O isotopologue pools of NO_3^- at the process-level provides a benchmark for examining the conservative nature of $\Delta^{17}O\text{-}NO_3^-$. Based on the numerical model, a wide range of gross nitrification and NO_3^- consumption rates was estimated for the four soils (Figure 3.4). The sensitivity of the estimated gross nitrification and NO_3^- consumption rates to β and magnitude of the O isotopic fractionations (1 σ) was on average 2.6±1.5% and 6.0±2.0% (Figure B-2 in Appendix B), respectively, for the four soils, which were

much lower than the average margin of error (95% confidence level) of the estimated gross nitrification (20.2±12.0%) and NO_3^- consumption (38.4±16.7%) rates propagated from the analytical and experimental errors (Figure 3.4). Therefore, the results from the sensitivity test suggest that although $\delta^{18}O$ and $\delta^{17}O$ of NO_3^- are controlled by the O isotopic fractionations and their respective β values during nitrification and NO_3^- consumption, no precise knowledge of these controlling factors need be known to apply $\Delta^{17}O$-NO_3^- for estimating gross nitrification and NO_3^- consumption rates using the numerical model, even though the $\Delta^{17}O$ calculations are made relative to $\delta^{18}O$ and $\delta^{17}O$ values.

Compared to the numerical model, the $\Delta^{17}O$ dilution model tended to underestimate gross nitrification and NO_3^- consumption rates (Figure 3.4). This underestimation is probably due to slight violations of the presumptions inherent to the isotopic dilution concept as a consequence of the variability of β in characterizing the mass-dependent fractionations during multi-step fractionation processes (Miller, 2002; Young et al., 2002) and the nonlinear mixing behavior of $\Delta^{17}O$ defined using Equation 4 (Kaiser et al., 2004; Luz and Barkan, 2005). However, the difference between the rates estimated using the two models is generally within the margin of error of the respective estimates (Figure 3.4), indicating that application of the $\Delta^{17}O$ dilution model will lead to acceptable levels of uncertainty under analytical and experimental conditions similar to those documented in this study.

It should be note that when either model was applied to every two consecutive soil samplings, the large uncertainties in the estimated rates, especially the gross NO_3^- consumption rates (Figure 3.4), are largely ascribed to artifacts in the tracer-based rate estimation. It is well recognized in ^{15}N tracer-based studies that gross rate estimates are most reliable when N transformations are relatively fast so that the tracer pool is significantly diluted within

measurement intervals (Davidson et al., 1991; Hart et al., 1994; Smith et al., 1994). In our case, decline of the $\Delta^{17}O\text{-}NO_3^-$ ranged from 0.21‰ to 1.28‰ between every two consecutive samplings for the four soils (Figure 3.2e) and was generally modest relative to the precision of the replicate $\Delta^{17}O\text{-}NO_3^-$ measurements (i.e., ±0.13‰). If the gross nitrification and NO_3^- consumption rates are estimated for intervals spanning every other soil sampling, errors in the gross nitrification and NO_3^- consumption rates are reduced to 13.9±8.2% and 26.4±12.8%, respectively, on average for the four soils (results not shown). This indicates that error propagation in estimating the gross nitrification and NO_3^- consumption rates is a signal-to-noise problem in nature (Davidson et al., 1991). It is therefore not surprising to see that the gross NO_3^- consumption rates, which were significantly lower than the gross nitrification rates in this study, had larger relative errors. From this perspective, the numerical model that estimates gross N transformation rates based on multiple observations is generally more appropriate for the studied soils.

3.4.2 $\Delta^{17}O\text{-}NO_3^-$ as a bridge between soil NO_3^- cycling rates and isotopic fractionations

When applying the numerical model to the entire period of sampling, the good agreement between the observed and modeled results indicates that gross nitrification and NO_3^- consumption followed zero-order kinetics throughout the short-term incubation experiments in the four soils (Figure 3.2). While zero-order kinetics might be favored by the high N availability in the agricultural soil (Shi and Norton, 2000), the constant rates of nitrification and NO_3^- consumption in the three unfertilized soils suggest that the NO_3^- dynamics might be coupled with C transformations, which operated through much larger pool sizes (Myrold and Tiedje, 1986; Mary et al., 1998). The estimated gross nitrification and NO_3^- consumption rates for the four soils are well within the range of values reported in a meta-analysis of ^{15}N tracer-based gross nitrification and NO_3^- consumption rates for

woodland, grassland, and agricultural soils (Booth et al., 2005) (Table 3.1). The estimated gross nitrification rates also followed the same trend as the nitrification potential, an index of autotrophic nitrifier abundance, and the total N content across the four soils (Table 3.1), suggesting the high consistency of our $\Delta^{17}O$-based modeling approach. Furthermore, while the estimated gross NO_3^- consumption was significantly lower than the gross nitrification rate in the agricultural soil (Table 3.1), the ratio of gross NO_3^- consumption to gross nitrification ranged between 0.44 and 0.53 for the three unfertilized soils (Table 3.1). This range is consistent with the average ratio (0.59) found for a wide variety of natural soils in ^{15}N tracer-based studies (Booth et al., 2005) and the established paradigm that NO_3^- consumption is positively correlated with nitrification in unmanaged soils (Booth et al., 2005).

In addition to revealing NO_3^- cycling rates, tracing soil nitrification and NO_3^- consumption using $\Delta^{17}O$-NO_3^- provides a unique opportunity to couple NO_3^- transformation with dynamics of the dual NO_3^- isotopes, which cannot be achieved using the ^{15}N tracer-based techniques. During the incubations, $\Delta^{17}O$-NO_3^- values varied linearly with $\delta^{15}N$-NO_3^- values in the four soils (Figure 3.3a). Since $\Delta^{17}O$-NO_3^- behaves closely as a conservative tracer during nitrification and NO_3^- consumption as discussed above, we interpret the observed linear covariation between $\Delta^{17}O$-NO_3^- and $\delta^{15}N$-NO_3^- to have arisen from a two-component mixing between the standing pool of NO_3^- with a nonzero $\Delta^{17}O$-NO_3^- originating from the Chilean NO_3^- fertilizer and a microbial source of NO_3^- that has $\Delta^{17}O=0$ and appeared to be variable in $\delta^{15}N$ among the four soils. The $\delta^{15}N$ of this microbially-mediated NO_3^- ($\delta^{15}N_M$) can be estimated by extrapolating the linear regression of $\Delta^{17}O$-NO_3^- and $\delta^{15}N$-NO_3^- to the x axis (i.e., the x-intercept) where $\Delta^{17}O=0$ (Figure 3.3a). The values of $\delta^{15}N_M$ obtained in this way were -29.2±2.4‰, -12.8±1.1‰, 2.3±0.2‰, and 2.4±0.1‰

for the agricultural, meadow, forest, and riparian soils, respectively (errors are given as one standard deviation of the x-intercept) (Figure 3.3a).

To investigate how $\delta^{15}N_M$ is controlled by nitrification and NO_3^- consumption, a forward modeling of the numerical model was conducted by varying the key parameters in the model (i.e., N transformation rates and N isotope effects) and simultaneously tracking their covariations with $\delta^{15}N_M$. The results confirmed the linear relationship between $\Delta^{17}O\text{-}NO_3^-$ and $\delta^{15}N\text{-}NO_3^-$ under various simulated conditions of nitrification and NO_3^- consumption (Figure 3.7) and revealed that the variations in $\delta^{15}N_M$ can be explained by a steady state isotope model:

$$\delta^{15}N_M = \delta^{15}N_N + \frac{R_{NC}}{R_N} * {}^{15}\varepsilon_{NC} \qquad \text{Equation (7)}$$

where $\delta^{15}N_N$ is the $\delta^{15}N$ end-member of nitrification-produced NO_3^- and ${}^{15}\varepsilon_{NC}$ is the N isotope effect for NO_3^- consumption. Since $\delta^{15}N_N$ can be estimated from the $\delta^{15}N$ of nitrification substrate ($\delta^{15}N_S$) and the N isotope effect associated with nitrification (${}^{15}\varepsilon_N$), equation 7 can be rewritten as:

$$\delta^{15}N_M = \left(\delta^{15}N_S - {}^{15}\varepsilon_N\right) + \frac{R_{NC}}{R_N} * {}^{15}\varepsilon_{NC} \qquad \text{Equation (8)}$$

An illustration of the pattern underlying Equation 8 is shown in Figure 3.7 by varying either ${}^{15}\varepsilon_N$ or ${}^{15}\varepsilon_{NC}$ while holding the other parameters constant in the numerical model. According to Equation 8 and Figure 3.7, the sign and magnitude of the linear regression of $\Delta^{17}O\text{-}NO_3^-$ and $\delta^{15}N\text{-}NO_3^-$ depends on the difference between $\delta^{15}N_M$ and the initial $\delta^{15}N$ of the standing NO_3^- pool and is ultimately controlled by the difference between ${}^{15}\varepsilon_N$ and ${}^{15}\varepsilon_{NC}$ given constant $\delta^{15}N_S$, R_N, and R_{NC} (Figure 3.7).

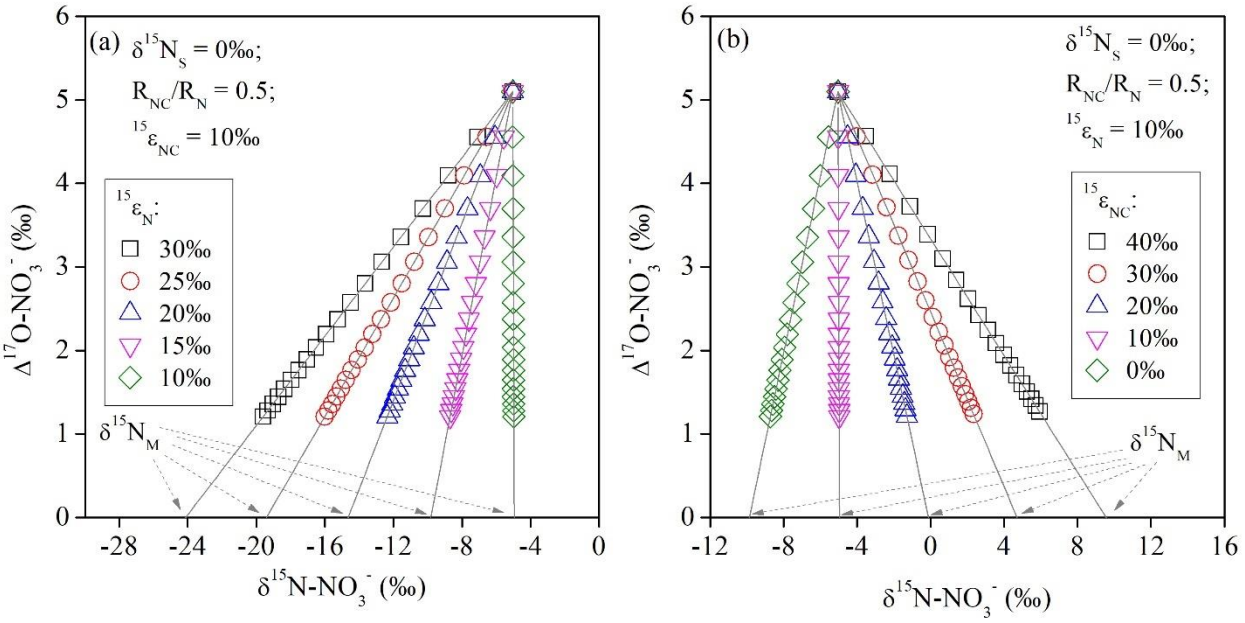

Figure 3.7 Forward analysis of the numerical model showing evolution of $\Delta^{17}O\text{-}NO_3^-$ and $\delta^{15}N\text{-}NO_3^-$ values during simulated nitrification and NO_3^- consumption. In the forward modeling, either $^{15}\varepsilon_N$ (a) or $^{15}\varepsilon_{NC}$ (b) was varied within range shown in the legends while holding $\delta^{15}N_S$, R_N, and R_{NC} constant in the model. Parameter values used in the forward modeling are: R_{NC}/R_N=0.5, $\delta^{15}N_S$=0‰, and initial $\Delta^{17}O\text{-}NO_3^-$=5‰. The gray lines are linear regression fits of $\Delta^{17}O\text{-}NO_3^-$ and $\delta^{15}N\text{-}NO_3^-$ with the x intercept denoting $\delta^{15}N_M$.

The distinct $\delta^{15}N_M$ values revealed for the four soils are in accordance with the estimated $^{15}\varepsilon_N$ and $^{15}\varepsilon_{NC}$ using the numerical model and are reflective of the relationships between the gross NO_3^- cycling rates and soil properties. Large $^{15}\varepsilon_N$ (32.8±1.4‰) was estimated for the agricultural soil where gross nitrification was directly stimulated by the NH_4^+ fertilization (Figure 3.2; Table 3.1). The large $^{15}\varepsilon_N$ resulted in the low $\delta^{15}N_N$ and $\delta^{15}N_M$, driving the positive relationship between the $\Delta^{17}O\text{-}NO_3^-$ and the $\delta^{15}N\text{-}NO_3^-$ (Figure 3.3a). The estimated $^{15}\varepsilon_N$ was highly consistent with results from culture studies using ammonia-oxidizing bacteria and archaea under optimum

substrate conditions (e.g., 25‰ to 35‰) (Mariotti et al., 1981; Casciotti et al., 2003), highlighting the fully expressed isotope effect of nitrification in NH_4^+-rich soils (Mariotti et al., 1981). It is important to note that since $^{15}\varepsilon_N$ is estimated using both $\delta^{15}N\text{-}NO_3^-$ and $\delta^{15}N\text{-}NH_4^+$ values and is constrained by the $\Delta^{17}O$-derived rate estimates in the numerical model, any deviation from complete mass balance between NH_4^+ and NO_3^- due to concurrent net mineralization and/or NO_3^- consumption is accounted for in the estimate of $^{15}\varepsilon_N$ (Casciotti et al., 2003). Gross NO_3^- consumption in the agricultural soil was very low and associated with a $^{15}\varepsilon_{NC}$ not significantly different from zero (Table 3.1), reflecting the low microbial NO_3^- demand imposed by the C limitation (Shi and Norton, 2000; Cheng et al., 2017).

In contrast to the agricultural soils, small and positive $\delta^{15}N_M$ values were estimated for the forest and riparian soils (Figure 3.3a), consistent with the expectation that the isotope effect for nitrification is under-expressed under NH_4^+-limiting conditions (Mariotti et al., 1981). The positive $\delta^{15}N_M$ values in conjunction with the high gross nitrification rates in these two soils are evidence that nitrifiers were likely living in close-enough association with mineralizers to immediately deplete available NH_4^+ (Inselsbacher et al., 2013). Although we were not able to derive estimates for microbial NH_4^+ assimilation using the $\Delta^{17}O$-based numerical model, there is evidences that autotrophic nitrifiers are able to compete with heterotrophs for NH_4^+ in soils with high overall N availability, shifting the cycling of inorganic N to be NO_3^--dominated (Corre et al., 2002; Schimel and Bennett, 2004). A large and active autotrophic nitrifier community was also confirmed by the measured high nitrification potential in these two soils (Table 3.1). Moreover, the NO_3^- production and accumulation in the forest and riparian soils might also be partially contributed by heterotrophic nitrification, where organic N and NH_4^+ is converted to NO_2^- or NO_3^- by a diverse group of organisms (Müller et al., 2004). Since heterotrophic nitrifiers can utilize both organic N

and NH_4^+, they were found to account for an increased proportion of nitrification rates at low pH, especially in soils containing low C:N organic matter (Booth et al., 2005; Müller et al., 2004; Inselsbacher et al., 2013). Essentially, the estimated small $^{15}\varepsilon_N$ for the forest and riparian soils are in line with the minor isotopic fractionation during mineralization (i.e., <2‰) documented in previous studies (Denk et al., 2017), and highlight the direct connection between the organic N and NO_3^- pools. On the other hand, gross NO_3^- consumption was associated with a negligible $^{15}\varepsilon_{NC}$ in these two soils (Table 3.1), suggesting that the NO_3^- was dominantly consumed via microbial assimilation (Figure 3.1) (Denk et al., 2017). Substantial NO_3^- assimilation has long been reported in grassland and forest soils (Schimel et al., 1989; Davidson et al., 1992; Stark and Hart, 1997). Microbial NO_3^- assimilation as the dominant NO_3^- sink in the forest and riparian soils is congruent with the greater availability of organic C and the depleted NH_4^+ pool that might have promoted microbial demand for NO_3^- and rapid NO_3^- recycling in these two soils (Davidson et al., 1992; Inselsbacher et al., 2013; Cheng et al., 2017).

Both gross nitrification and NO_3^- consumption were associated with a significant isotope effect in the meadow soil (i.e., 28.4±2.1‰ and 8.1±4.9‰, respectively) (Table 3.1), resulting in a negative $\delta^{15}N_M$ and a positive relationship between $\Delta^{17}O\text{-}NO_3^-$ and $\delta^{15}N\text{-}NO_3^-$ (Figure 3.3a). The large $^{15}\varepsilon_N$ is consistent with the theoretical consideration that full expression of the kinetic isotope effect of nitrification is favored under conditions of high NH_4^+ availability but low nitrification rates (Mariotti et al., 1981; Maggi et al., 2008). Compared to the forest and riparian soil, the low nitrification potential of the meadow soil indicates a small population of autotrophic nitrifiers (Table 3.1) (Davidson et al., 1991). It is possible that nitrifiers were out-competed by heterotrophs for available NH_4^+ in the meadow soil, as previously observed for NH_4^+-rich soils with overall modest N availability (Schimel and Bennett, 2004). The tight cycling of N between the organic N

and NH_4^+ pools seems to be supported by significant net mineralization (Table 3.1) and the generally elevated $\delta^{15}N\text{-}NH_4^+$ values (Figure 3.2b), although firm conclusions cannot be drawn without further constraints on gross mineralization and NH_4^+ assimilation. Unlike the other three soils, the significant $^{15}\varepsilon_{NC}$ in the meadow soil implies the occurrence of denitrification as an important NO_3^- sink in the meadow soil. The hypothesis that denitrification was active is supported by the higher clay content that might favor formation of anaerobic microsites even in sieved, well-mixed soils (Keiluweit et al., 2018) and the presence of denitrifying bacteria as revealed in the denitrification potential assay (Table 3.1). Moreover, high NH_4^+ concentrations in the meadow soil could inhibit microbial assimilation of NO_3^- (Rice and Tiedje, 1989; Mary et al., 1998) and therefore increase the relative importance of NO_3^- consumption via denitrification. Unfortunately, there are currently large uncertainties in the isotope effects for microbial NO_3^- assimilation and denitrification measured in culture- and soil-based studies (Figure 3.1) (Denk et al., 2017), preventing quantitative partitioning of the respective pathways using the estimated $^{15}\varepsilon_{NC}$. However, knowing $^{15}\varepsilon_{NC}$ itself is important and sets the stage for further investigation into the NO_3^- consumption pathways.

From the above discussion, we conclude that the coupled measurement and modeling of $\Delta^{17}O\text{-}NO_3^-$ and $\delta^{15}N\text{-}NO_3^-$ can bridge soil NO_3^- cycling rates with isotopic fractionations and help explain mechanisms causing variations in gross nitrification and NO_3^- consumption. The clear differences among the studied four soils in terms of gross N rates and N isotope effects highlight the proximate control of the soil microbial community structure on soil NO_3^- cycling. Soil microbial activity is in turn strongly affected by a wide range of physical and chemical factors, such as soil texture, soil organic C, and availability of N sources for microbial use. While kinetic isotope effects are a fundamental parameter to probe microbial activity underlying soil N

transformations (Mariotti et al., 1981), it is often the case that an effect demonstrated clearly in culture studies is more equivocal in a complex soil environment (Maggi et al., 2008). Our $\Delta^{17}O$-based modeling approach capable of deriving gross N rates and N isotope effects simultaneously is therefore an effective way to reduce ambiguities in the N isotope systematics of soil NO_3^- cycling and to help constrain the $\delta^{15}N$ end-member of nitrification-produced NO_3^-, which is notoriously hard to predict in dual isotope-based ecosystem models (Hall et al., 2016). On the other hand, as the first attempt to use $\Delta^{17}O$-NO_3^- as a tracer of soil NO_3^- cycling, we focused on nitrification and NO_3- consumption and followed the established notion in soil ^{15}N tracer studies to make the numerical model as simple as possible (Mary et al., 1998; Müller et al., 2004). Future work could extend the numerical model to include further realistic N transformation pathways (e.g., gross mineralization and NH_4^+ assimilation) and associated isotope effects (Denk et al., 2017). Moreover, because N assimilation is an input rate for only a part of the organic N pool which is itself a small proportion of the total soil N (Myrold and Tiedje, 1986; Smith et al., 1994), a robust estimate of the active organic N pool size and its $\delta^{15}N$ should be of primary importance for future application of the numerical model.

Finally, as revealed by a series of forward modeling analyses focusing on the linear correlations between $\Delta^{17}O$-NO_3^- and $\delta^{18}O$-NO_3^- (Figure 3.3b), Equation 7 is equally applicable to deriving the $\delta^{18}O$ end-member of nitrification-produced NO_3^- ($\delta^{18}O_N$) (results not shown). In this case, $\delta^{18}O_N$ is collectively controlled by the $\delta^{18}O$ of the substrates (O_2 and H_2O), the O isotope effects associated with the O atom incorporation, and the extent to which the O is exchanged between NO_2^- and H_2O (Casciotti et al., 2010; Buchwald and Casciotti, 2010). However, as the NO_3^- consumption processes did not fractionate the NO_3^- isotopes significantly in the agricultural, forest, and riparian soils, the $\delta^{18}O_N$ can be approximated by the x intercept of the linear regression

of $\Delta^{17}O\text{-}NO_3^-$ and $\delta^{18}O\text{-}NO_3^-$ (i.e., $\delta^{18}O_M$) for these three soils. The estimated $\delta^{18}O_N$ ranged from -7.0±0.6‰ to -0.9±0.3‰ (Figure 3.3b). Although we did not have constraints on the factors controlling the $\delta^{18}O_N$ except the $\delta^{18}O$ value of the added Milli-Q water (-10.1‰), the estimated $\delta^{18}O_N$ values intersect the range of $\delta^{18}O_N$ reported for temperate forest soils (e.g., -4‰ to 15‰; Fang et al. (2012)). Nevertheless, in previous studies $\delta^{18}O_N$ was routinely estimated from an isotopic mass balance based on the net accumulation of NO_3^- during aerobic soil incubations. Using the $\Delta^{17}O$-based modeling approach, we show that substantial NO_3^- consumption can occur under aerobic soil conditions. It is not clear how the reported $\delta^{18}O_N$ in the literature was affected by failure to account for potential NO_3^- consumption in the mass balance calculation. We argue that the coupled measurement and modeling of $\Delta^{17}O\text{-}NO_3^-$ and $\delta^{18}O\text{-}NO_3^-$ is a superior approach to derive unbiased estimates of $\delta^{18}O_N$, which are critical for its quantitative use in tracing sources and fate of NO_3^- in terrestrial and aquatic ecosystems.

3.4.3 Post-snowmelt soil NO_3^- dynamics and implications for modeling denitrification using the dual NO_3^- isotopes.

The $\Delta^{17}O\text{-}NO_3^-$ values from the field soil cores are consistent with the results from synoptic or precipitation event-based surface soil sampling in temperate and semiarid ecosystems (e.g., 0‰ to 4‰) (Figure 3.5c) (Michalski et al., 2004; Costa et al., 2011; Fang et al., 2015). Based on the $\Delta^{17}O\text{-}NO_3^-$ of snow water (25.1±0.1‰), a simple mixing calculation indicates that snow NO_3^- accounted for 8.2% and 7.4% of the surface soil NO_3^- pool on the first two sampling days, respectively, in line with the finding by Costa et al. (2011) that rainwater NO_3^- contributed 7% of surface soil NO_3^- immediately after a rain event in a temperate forest in Michigan, USA. A significant decline in the $\Delta^{17}O\text{-}NO_3^-$ was observed between day 2 and day 3 with no concomitant

change in the NO_3^- concentration during the first three days of sampling (Figure 3.5a and 3.5c), indicating cycling of NO_3^- via nitrification and NO_3^- consumption following the snowmelt. The co-occurring nitrification and NO_3^- consumption during the first three sampling days were also supported by rate estimates from the numerical model (1.3±2.1 and 1.7±2.1 μg $N \cdot g^{-1} \cdot d^{-1}$, respectively) (Figure 3.5a and 3.5b). However, these rate estimates have large uncertainties propagated from the large deviations in the replicate NO_3^- concentration and $\Delta^{17}O\text{-}NO_3^-$ measurements (Figure 3.5a and 3.5c). This reinforces the notion that for any isotope-based N tracing models, the accuracy of the model estimates strongly depends on the data quality (Inselsbacher et al., 2013). Further, it highlights the difficulty in using precipitation $\Delta^{17}O\text{-}NO_3^-$ as a natural tracer of nitrification and NO_3^- consumption in undisturbed soils where factors like root density and presence of soil microsites can lead to significant spatial heterogeneity. From this perspective, application of the label injection protocol that is commonly used in the ^{15}N tracer studies (Davidson et al., 1991) is a logical next step for testing the usefulness of $\Delta^{17}O\text{-}NO_3^-$ under field conditions.

Despite the large uncertainties in the rate estimates, pooling the measurements over the first three sampling days provides multiple lines of evidence suggesting that denitrification was an important NO_3^- consumptive pathway following the snowmelt. The $\delta^{15}N\text{-}NO_3^-$ in the surface soil displayed a significant relationship of ^{15}N enrichment with the logarithm of the NO_3^- concentration (Figure 3.6b). The slope of this relationship identifies an apparent isotope effect of 4.9‰ for the NO_3^- consumption, approximating denitrification of a quasi-closed NO_3^- pool (Yu et al., 2016). Moreover, the increase in the $\delta^{15}N\text{-}NO_3^-$ was linked to the $\delta^{18}O\text{-}NO_3^-$ (Figure 3.5b and 3.5d) as manifested in the linear relationship with a slope of 0.89 (Figure 3.6c), characteristic of denitrification activity (Groffman et al., 2006). Finally, the negative correlation between the $\Delta^{17}O$-

NO_3^- and the $\delta^{15}N\text{-}NO_3^-$ suggests a positive $\delta^{15}N_M$ which is indicative of denitrification that has a significant isotope effect (Figure 3.6a and Figure 3.7b). Indeed, the importance of denitrification in cold soils during snowmelt has been reported in temperate ecosystems where snowmelt often represents a period of soil saturation (Figure B-1 in Appendix B) and potential NO_3^- loss (Hall et al., 2016). Using direct N_2 flux measurement in a northern upland forest, Morse et al. (2015) revealed a burst of denitrification activity in apparently oxic surface soils during snowmelt, which was triggered by increased soil water content and N supply from mineralization and nitrification.

Thus, using the triple NO_3^- isotopes, we provide direct evidence for the co-occurrence of nitrification and denitrification in surface soils, which has important implications for modeling denitrification using dual NO_3^- isotopes. Because the dilution of $\Delta^{17}O\text{-}NO_3^-$ over space and time is exclusively driven by nitrification, the co-occurrence of nitrification and denitrification is best illustrated by a triple isotope plot of NO_3^- (Figure 3.6). As shown in Fig. 6, isotope enrichment diagnostic of denitrification was paralleled by nitrification. Because nitrification has opposite effects on $\delta^{15}N\text{-}NO_3^-$ and $\delta^{18}O\text{-}NO_3^-$ as revealed in the laboratory incubation of the meadow soil, co-occurring nitrification may obscure isotopic signatures from denitrification, complicating the interpretation of the dual NO_3^- isotope beyond the unidirectional NO_3^- consumption. To investigate how the identification of denitrification can be affected by the co-occurring nitrification, we ran the numerical model to fit the observed $\delta^{15}N\text{-}NO_3^-$ and $\delta^{18}O\text{-}NO_3^-$ based on the estimated gross nitrification and NO_3^- consumption rates. Although soil NH_4^+ concentration and $\delta^{15}N\text{-}NH_4^+$ were not measured for the field samples, excess NH_4^+ relative to NO_3^- was observed on an annual basis at this site (Yu and Elliott, unpublished data), suggesting that the isotope effect associated with nitrification was likely expressed following the snowmelt. Therefore, the $\delta^{15}N$ and $\delta^{18}O$ of nitrification-produced NO_3^- were assumed to be -12.8‰ and -0.5‰, respectively, in the model,

consistent with the $\delta^{15}N_M$ and $\delta^{18}O_M$ measured for the meadow soil in the incubation experiment. The results show that the observed variations in $\delta^{15}N\text{-}NO_3^-$ and $\delta^{18}O\text{-}NO_3^-$ during the first three sampling days can be possibly explained by an isotope effect of 18‰ for both enrichments of $\delta^{15}N\text{-}NO_3^-$ and $\delta^{18}O\text{-}NO_3^-$ (Figure 3.5b and 3.5d). This potentially large isotope effect for both N and O isotopic fractionations would have been obscured, if we had assessed relationships among concentration and the dual isotopes of NO_3^- without the context of the co-occurring nitrification. The isotopic imprints of denitrification would have been even more eclipsed, if the dual NO_3^- isotopes measured in the last two sampling days had been misrepresented in the analysis of denitrification, leading to lower apparent isotope effect (3.6‰) (Figure 3.6b) and a slope of the $\delta^{15}N\text{-}NO_3^-$ versus $\delta^{18}O\text{-}NO_3^-$ trajectory significantly lower than 1 (Figure 3.6c).

These modeling exercises highlight the competing fractionation from nitrification and denitrification in redox-heterogeneous environment (e.g., surface soil horizon) that may explain the long-lasting discrepancies between field- and culture-derived isotope systematics of denitrification (Granger and Wankel, 2016). In previous studies, the apparent isotope effects for denitrification derived from field observations in wet soils and freshwater systems are consistently lower than 10‰ (Mariotti et al., 1988; Osaka et al., 2010; Yu et al., 2016) and also lower than those reported in laboratory experiments with denitrifying bacteria and anaerobically incubated soil samples (Figure 3.1) (Mariotti et al., 1981; Granger et al., 2008; Denk et al., 2017). Moreover, the $\delta^{15}N\text{-}NO_3^-$ versus $\delta^{18}O\text{-}NO_3^-$ trajectory inferred from field-observed denitrification events are variable, with the slope ranging widely from 0.5 to 2 (Groffman et al., 2006), while a slope of ~1 was clearly demonstrated for denitrifying bacteria (Granger et al., 2008). Based on the above discussion, we conclude that the coupled measurement and modeling of triple NO_3^- isotopes is a

powerful tool to decipher the isotopic overprinting from nitrification and denitrification in soils, and thus allows for a more robust interpretation of denitrification in dual NO_3^- isotope space.

3.5 FINAL REMARKS

While $\Delta^{17}O$ has been increasingly used to examine atmospheric NO_3^- deposition and its subsequent retention in terrestrial and aquatic ecosystems, few studies have explored the quantitative use of $\Delta^{17}O$ in probing gross nitrification and NO_3^- consumption in soils. In this proof-of-concept study, we investigated the robustness of $\Delta^{17}O$-NO_3^- as a tracer of nitrification and NO_3^- consumption through developing and validating $\Delta^{17}O$-based analytical and numerical models. The results confirmed the conservative nature of $\Delta^{17}O$-NO_3^- and highlighted the mechanistic coupling between $\Delta^{17}O$-NO_3^- and the dual NO_3^- isotopes in characterizing isotope effects associated with nitrification and NO_3^- consumption. While care should be taken to apply $\Delta^{17}O$-NO_3^- under field conditions where its tracing power may be compromised by soil heterogeneity, coupled measurement and modeling of the triple NO_3^- isotopes has great potential to discern and quantify isotopic overprinting from nitrification and denitrification in redox-dynamic soil horizons. Given that the initial isotopic composition of nitrification-produced NO_3^- and its subsequent enrichments over space and time are at the core of quantitative isotope models aiming to quantify denitrification at the watershed scale, the combined use of the triple NO_3^- isotopes in laboratory and field settings is expected to improve the performance of these models and thus our broader understanding of denitrification. Finally, because denitrification obeys the mass-dependent fractionation law, N_2O, a potent greenhouse gas, produced from denitrification should inherit $\Delta^{17}O$ signal from $\Delta^{17}O$-labeled substrate NO_3^- and NO_2^-, while nitrification-produced N_2O should have $\Delta^{17}O \approx 0$. Hence,

the potential for using $\Delta^{17}O$ to partition soil N_2O emission from nitrification and denitrification clearly merits exploration.

4.0 AN ISOTOPIC INVESTIGATION OF NITRIC OXIDE DYNAMICS AND ITS UNDERLYING PROCESSES IN AN AGRICULTURAL SOIL

4.1 INTRODUCTION

Agricultural production of food and energy has required a tremendous increase in the application of synthetic fertilizer since 1950 (Robertson and Vitousek, 2009). To ensure crop yields, nitrogen (N) is often applied at rates in excess of a crop's yield response, resulting in gaseous N loss via soil microbial processes (Sebilo et al., 2013). According to a recent meta-analysis based on 520 field measurements worldwide, direct emissions of nitric oxide (NO) and nitrous oxide (N_2O) from agricultural soils account for 1.2% and 1.4%, respectively, of applied fertilizer N (Liu et al., 2016). Losses of N in the form of NO are of particular concern because of its adverse environmental impacts. Once emitted to the atmosphere, NO is rapidly oxidized to nitrogen dioxide (NO_2), and these compounds (collectively referred to NO_x) affect tropospheric ozone (O_3) production, secondary organic aerosol formation, atmospheric lifetime of carbon dioxide and methane, and can contribute to ecosystem acidification and eutrophication (Morin et al., 2008). Given the detrimental effects of NO emission, identification of underlying processes contributing to NO dynamics in agricultural soils is important for mitigating its emissions (Haslun et al., 2018). This, however, requires knowledge of sources and pathways of NO production spatially and temporally across different agricultural landscapes.

Microbial nitrification and denitrification are considered the dominant sources of NO in agricultural soils (Liu et al., 2016). Denitrification is performed by facultative anaerobic microorganisms through sequential reduction of nitrate (NO_3^-) or nitrite (NO_2^-) via NO and N_2O

to dinitrogen (N_2) under anoxic conditions (Figure 1.1) (Zumft, 1997). The enzymatic system of denitrification comprises a series of dedicated periplasmic and membrane-bound reductases with NO_2^- reductase (NIR) and NO reductase (NOR) being the key enzymes that mediate NO production and consumption, respectively. Nitrification is a two-step process where aerobic oxidation of ammonium (NH_4^+) via hydroxylamine (NH_2OH) to NO_2^- is mediated by ammonia-oxidizing bacteria and/or archaea, while the subsequent oxidation of NO_2^- to $NO_3^-$is catalyzed by another group of bacteria (i.e., nitrite oxidizers) (Ward, 2011). During nitrification, NO can be produced from NH_2OH as a byproduct under aerobic conditions or from NO_2^- by nitrifier-encoded NIR when O_2 availability becomes limited in soil (Figure 1.1) (Wrage et al., 2001; Shaw et al., 2006).

NO can also be produced abiotically in acidic soil environments (pH < 5) from decomposition of nitrous acid (HNO_2), the protonated form of NO_2^- (*p*Ka=3.3) (Venterea and Rolston, 2000; Medinets et al., 2015). It has been proposed that the existence of highly acidic clay surfaces and microsites (pH < 3) can promote significant rates of NO production from HNO_2 decomposition even in non-acidic soils (Venterea et al., 2005). NO can also be produced during chemical reactions between NO_2^-, reduced transition metals, and soil organic matter (Schreiber et al., 2012; Medinets et al., 2015). However, these abiotic reaction pathways were rarely acknowledged in previous studies, and their relative importance in driving soil NO emissions remains largely unknown (Medinets et al., 2015; Zhu-Barker et al., 2015).

Natural abundance stable N isotopes in various soil N-containing compounds have long been used as an integrative tracer of soil N cycling (Denk et al., 2017). Recently, stable N isotopes have been used to differentiate nitrification- and denitrification-derived N_2O (e.g., Tilsner et al., 2003; Wrage et al., 2005; Pérez et al., 2006; Park et al., 2011). These non-intrusive methods exploit

measurable changes in the stable N and oxygen (O) compositions (notated as $\delta^{15}N$ and $\delta^{18}O$) of N_2O that occur at various points along the abiotic and microbial N_2O pathways as a result of isotopic fractionation (Sutka et al., 2006). Unfortunately, commonly applied analytical techniques do not allow precise $\delta^{15}N$-NO measurement, despite its promising potential for elucidating soil NO dynamics (Yu et al., 2017). Consequently, $\delta^{15}N$-NO has been largely ignored in studies of soil N isotope systematics and thus the isotope effects associated with soil NO production and consumption remain unknown.

In this study, controlled laboratory experiments were conducted to characterize $\delta^{15}N$ of NO emitted from an agricultural soil using the newly developed DFC-TEA method described in Chapter 2. A Chilean NO_3^- fertilizer enriched in $\Delta^{17}O$ was used to fertilize the soil to assess how NO production and its $\delta^{15}N$ signature are mediated during nitrification and denitrification under aerobic and anaerobic conditions. Based on the dynamics of $\Delta^{17}O$, the gross rates and isotope effects of nitrification and denitrification were estimated using a $\Delta^{17}O$-based numerical model (Chapter 3). We show that coupled $\delta^{15}N$-NO and $\Delta^{17}O$-NO_3^- measurements shed new light on soil NO dynamics, its underlying driving forces with important implications for modeling soil NO emissions under complex environmental conditions.

4.2 METHODS AND MATERIALS

4.2.1 Soil characteristics and preparation

Soil samples were collected from a typical corn-soybean rotation field in central Pennsylvania managed by the USDA (Agricultural Research Service, University Park, PA, USA). The soil is a

well-drained Hagerstown silt loam (fine, mixed, semiactive, mesic Typic Hapludalfs) with sand, silt, and clay content being 21%, 58%, and 21%, respectively. The sampled surface layer (0 - 10 cm) had a bulk density of 1.2 $g \cdot cm^{-3}$ and a pH (1:1 water) of 5.7; soil C:N ratio was 11.4, and organic carbon content was 1.8%. In the laboratory, all soils were homogenized and sieved to 2 mm (soils were not subject to air-drying). Soils were then stored in a refrigerator at 4˚C in resealable plastic bags. The gravimetric water content of the sieved and homogenized soils was 0.14 g $H_2O \cdot g^{-1}$. Indigenous NH_4^+ and NO_3^- concentrations were 0.7 μg $N \cdot g^{-1}$ and 19.8 μg $N \cdot g^{-1}$, respectively. Throughout this paper, soil N concentrations, NO flux, and soil N transformation rates are expressed on the basis of soil oven-dry (105˚C) weight.

4.2.2 Dynamic flux chamber system

A dynamic flux chamber (DFC) system was used for continuous flux measurement and collection of soil-emitted NO. Development of the DFC system and NO flux calculation method is presented in detail in Chapter 2. The laboratory version of the DFC system was used in this study for all the incubation experiments. Importantly, instead of using a Teflon jar for NO measurement and collection as described in the original system development (Chapter 2), custom-made glass incubators modified from 1 L Pyrex medium bottles (13951L, Corning, USA) were used for all the incubation experiments to accommodate redox-sensitive (i.e. anaerobic) incubation conditions (Figure 4.1). Each glass incubator is equipped with two vacuum valves for purging and closure of the incubator headspace and was stoppered with two 42 mm Teflon septa secured by an open-topped screw cap (Figure 4.1). Tests of the apparatus demonstrated that it was gas-tight when the vacuum valves were closed and that none of the contacting materials were reactive with or a source of NO.

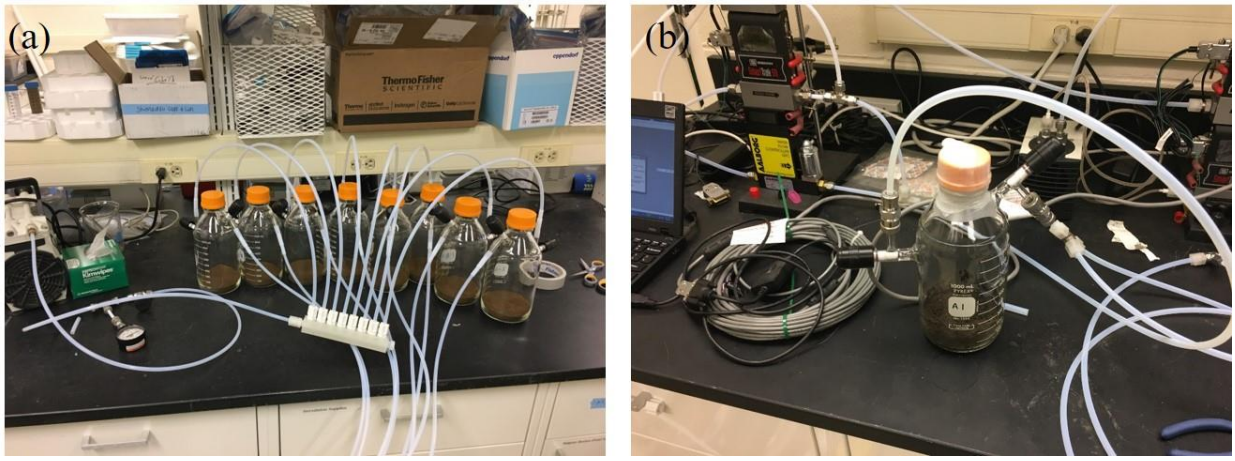

Figure 4.1 Photos showing the glass incubator being incubated on the purging manifold (a) and incorporated into the DFC system for NO flux measurement and collection.

4.2.3 Collection of NO for δ^{15}N-NO analysis

Detailed technical information about the NO collection method can be found in Chapter 2. In brief, outflow of the glass incubator was subsampled to pass through the NO collection train where NO is converted to NO_2 in excess O_3 and subsequently collected in a 20% (v/v, 70 mL) triethanolamine (TEA) solution as NO_2^- and NO_3^- for δ^{15}N analysis. Results from a comprehensive method test showed that >99% NO conversion and 98.5±3.5% NO collection are achieved over a wide range of NO concentration (12 to 749 ppb) and varying environmental conditions (e.g., temperature from 11 to 31˚C and relative humidity from 27 to 92%) (Table 2.1; Chapter 2). High concentrations of NH_3 (e.g., 500 ppb) in the sample flow do not interfere with the NO collection method. Additionally, the collection train can be coupled with an existing scrubber (1 mM phosphate buffer solution, pH = 7.0 (Zhou et al., 1999)) to remove volatile nitrous acid (HONO) from the sample

flow without compromising accuracy and precision of the δ^{15}N-NO determination (Table 2.1; Chapter 2).

4.2.4 Anaerobic incubation experiment

To measure representative δ^{15}N values for NO production under anaerobic conditions, we aimed to minimize NO consumption by reducing diffusive limitation of NO in the soil-incubator system (McKenney et al., 1982; Russow et al., 2009). This was achieved using a low soil water content (e.g., <50% water filled pore space (WFPS)) and continuous headspace flushing that lessened entrapment and build-up of NO in soil pore space. At the onset of incubation, a known amount of soil was spread out on a covered tray for pre-conditioning under room temperature for 24 h. After the pre-conditioning, the soils were amended with the Chilean NO_3^- fertilizer (δ^{15}N=0.3±0.1‰, δ^{18}O=55.8±0.1‰, Δ^{17}O=18.6±0.1‰) and an off-the-shelf ammonium sulfate reagent ($(NH_4)_2SO_4$, δ^{15}N=1.9±0.3‰). The N substrates were dissolved in deionized Milli-Q water and gravimetrically applied to the soils using a syringe equipped with a 25-gauge needle to achieve a fertilization rate of 35 µg NO_3^--N·g^{-1} and 35 µg NH_4^+-N·g^{-1} and a target soil water content of 0.21 g H_2O·g^{-1} (equivalent to 46% WFPS). The fertilized soils were homogenized using a glass rod in the tray and then transferred to a resealable plastic bag for thorough mixing to ensure homogeneous distribution of amended water and N substrates. 100 g (dry weight equivalent) soil was then weighted into each of eight glass incubators, resulting in a soil depth of about 1.5 cm. The eight glass incubators were connected in parallel to a Teflon manifold, vacuumed and filled with ultra-purity N_2 for three cycles, and then incubated with a continuous flow of N_2 at 0.015 slpm to each incubator. The sample fertilization and preparation procedures were repeated three times to establish three replicate sample batches (24 incubators in total).

The first NO measurement was conducted 24 h after the initiation of the anaerobic incubation, and daily measurements were conducted thereafter. On each day, one incubator from each replicate batch was closed using the vacuum valves, removed from the purging manifold, and then integrated into the DFC system. The DFC system was then evacuated and flushed with N_2 at least five times before the vacuum valves were opened for NO measurement and collection. This procedure prevents O_2 invasion into the incubator headspace from residual air in the DFC system. After the valves were opened, the incubator was purged for 2 minutes using a humidified flow of N_2 (4 slpm) to flush out accumulated NO during the closure. The flow rate was then reduced to 1 slpm for NO flux measurement and collection and resulted in a mean air residence time of 1 minute in the incubator headspace. Initial tests showed that further increasing the purging flow rate did not lead to significant increases in net NO production and thus indicated that removal of NO from the soil-incubator system was fast enough to suppress NO consumption at the applied flow rate (McKenney et al., 1982; Remde and Conrad, 1991). NO was continuously measured for flux and collected for δ^{15}N-NO analysis for 2 h. Replicate flux measurement and NO collection were conducted successively.

After NO collection, each incubator was opened and combined with 500 mL deionized Milli-Q water and then agitated vigorously on a stir plate for 10 minutes to extract soil NO_3^- and NO_2^- (McKenney et al., 1982). Results from initial experiments indicated that NO_2^- concentrations built up considerably during the anaerobic incubation (e.g., up to 7 μg $N \cdot g^{-1}$). Therefore, we used water rather than a KCl solution for soil extraction, as a recent study suggested that NO_2^- can be substantially lost during KCl extraction (Homyak et al., 2016). The slurry was then centrifuged for 10 minutes at 2000 rpm, and the resultant supernatant was filtered through a sterile 0.2 μm filter (Costa et al., 2011; Homyak et al., 2016). Given the potentially high NO_2^- concentrations, the

filtrate was equally divided into two 60 mL Nalgene bottles with one of them receiving sulfamic acid to remove NO_2^- immediately for NO_3^- isotope analysis (Granger et al., 2009) and the other one without the treatment for determining NO_2^- and NO_3^- concentrations and combined $\delta^{15}N$ analysis of NO_2^-+NO_3^-.

To test efficacy of the soil NO_2^- and NO_3^- extraction method, eight soil samples were anaerobically incubated for 6 days, and then half of them were opened and spiked with a NO_2^- +NO_3^- solution (3 μg NO_2^--N·g^{-1} and 15 μg NO_3^--N·g^{-1}) using a pipette. Subsequent sample extraction and measurements showed that the spiked NO_2^- and NO_3^- were 100% recovered and that the triple isotopes ($\delta^{15}N$, $\delta^{18}O$, $\Delta^{17}O$) of the indigenous and added NO_3^- were accurately determined after NO_2^- removal. In a separate test, eight soil samples were anaerobically incubated for 3 days with four of them being incubated with 10 Pascal of the nitrification inhibitor acetylene (C_2H_2) (balanced by N_2). Subsequent concentration and isotope measurements revealed no statistical difference (Welch's *t*-test, $P<0.05$) between samples with and without C_2H_2 treatment, suggesting that aerobic NO_3^- production by autotrophic ammonia oxidizers was negligible during the soil incubation and extraction (Herrmann et al., 2007). These results indicate that our soil incubation and extraction methods are robust.

4.2.5 Aerobic incubation experiment

Aerobic soil incubation experiments were conducted using three isotopically different NH_4^+ fertilizers to assess the relative contribution of nitrification to soil NO production: (1) $\delta^{15}N$-NH_4^+=1.9‰ (low level), (2) $\delta^{15}N$-NH_4^+=22.5‰ (intermediate level), and (3) $\delta^{15}N$-NH_4^+=45.0‰ (high level). The lab $(NH_4)_2SO_4$ reagent was used in the low $\delta^{15}N$ treatment. NH_4^+ fertilizers with

intermediate and high levels of $\delta^{15}N$ enrichment were prepared by gravimetrically mixing NH_4^+ reference materials IAEA-N2 ($\delta^{15}N\text{-}NH_4^+$=20.3‰) and USGS26 ($\delta^{15}N\text{-}NH_4^+$=53.7‰). For each $\delta^{15}N\text{-}NH_4^+$ treatment, three replicate sample batches, each consisting of eight soil samples (100 g dry weight equivalent), were prepared using the same pre-conditioning and fertilization protocol described for the anaerobic incubation experiments. The soils were fertilized with the desired NH_4^+ fertilizer (90 μg $N \cdot g^{-1}$) along with the Chilean NO_3^- fertilizer (15 μg $N \cdot g^{-1}$) and incubated with a target soil water content of 0.21 g $H_2O \cdot g^{-1}$ (46% WFPS). Immediately after the fertilization, two soil samples from each replicate batch were extracted using 500 mL of deionized water for soil NO_2^- and NO_3^- as described above and 500 mL of 2 M KCl solution for determination of soil NH_4^+. The remaining samples were incubated under a controlled flow of synthetic air (20% O_2 + 80% N_2) on the purging manifold.

Two replicate NO flux measurements and collections were conducted at 24 h and 48 h after fertilization, respectively. Because NO emissions were low under the aerobic condition (see below), all the remaining soil samples in each replicate batch were connected in parallel on the purging manifold for incorporation into the DFC system to achieve a high enough NO concentration (i.e., >30 ppb) for reliable NO collection. A flow of synthetic air was supplied at a rate of 0.25 slpm to each soil incubator for flux measurement and NO collection. Control tests using an analytical NO tank indicated that NO oxidation by O_2 in the DFC system was negligible at the applied flow rate. During the NO flux measurements, 5% to 8% of the total NO+NO_y in the sample flow was consistently in the form of NO_y (NO_y = NO_2 + HONO + HNO_3 + other non-NO reactive N oxides). This NO_y signal could be removed by bubbling the sample flow through the HONO scrubber and suggests that the NO_y likely originated from biogenic HONO production in NH_4^+-fertilized soils (Scharko et al., 2015). Therefore, the HONO scrubber was incorporated into

the NO collection train to prevent interference with the δ^{15}N-NO measurement (Yu et al., 2017). After the flux measurement and NO collection, two soil samples were extracted for determination of soil NO_3^- and NH_4^+. Results from a spiking experiment indicated that the water extraction method is also robust for extracting the aerobically incubated soils (Table C-1 in Appendix C). The remaining soil samples were incubated on the purging manifold until next measurement. Because soil NO emission was too low for NO collection at 72 h after the fertilization, NO was only measured for flux using the remaining two soil samples in each replicate batch.

4.2.6 Abiotic NO production

To estimate the potential for abiotic NO production during aerobic and anaerobic soil incubations, soil samples (100 g dry-weight equivalent) were weighted into glass incubators and sterilized by autoclaving at 121˚C and 1.3 atm for 30 minutes. Next, sterilized soil samples were pre-incubated in the closed incubators under aerobic and anaerobic conditions for 24 h and then fertilized with the Chilean NO_3^- fertilizer (35 μg NO_3^--N·g^{-1}) or the lab $(NH_4)_2SO_4$ reagent (90 μg NH_4^+-N·g^{-1}). The fertilizer solution was added to the soil surface through the Teflon septa using a sterile syringe equipped with a 25-gauge needle. Because NO_2^- was found to accumulate in the anaerobically incubated soils and significant abiotic NO production was triggered by NO_2^- addition in initial experiments, four sterilized soil samples were fertilized with a $NaNO_2$ solution (δ^{15}N-NO_2^- =1.4±0.2‰) (8 μg N·g^{-1}) for immediate flux measurement and NO collection. These samples were then incubated statically under anaerobic condition and measured periodically for NO flux until NO production was not detectable.

4.2.7 Chemical and isotopic analysis

Analysis of NO_3^- in the soil extracts was carried out on a Dionex Ion Chromatograph ICS-2000 with a precision of (1σ) of ±5.0 μg $N \cdot L^{-1}$. NO_2^- concentrations were analyzed using the Greiss-Islovay colorimetric reaction with a precision of ±1.2 μg $N \cdot L^{-1}$. NH_4^+ analyses were carried out on a fluorometer (Trilogy, Turner Designs, USA) using a modified fluorometric OPA method for soil KCl extracts (Kang et al., 2003; Taylor et al., 2007) with a precision of ±7.0 μg $N \cdot L^{-1}$.

NO_3^- and NO_2^- in the soil extracts and the TEA collection samples were measured using the denitrifier method (Sigman et al., 2001; Casciotti et al., 2002). In brief, a denitrifying bacterium (*Pseudomonas aureofaciens*) lacking the N_2O reductase enzyme are used to convert 20 nmol of NO_3^- into gaseous N_2O. The N_2O is then purified in a series of chemical traps, cryo-focused, and finally analyzed on a GV Instruments Isoprime Continuous Flow Isotope Ratio Mass Spectrometer (CF-IRMS) at *m/z* 44, 45, and 46. International NO_3^- reference standards IAEA-N3, USGS34, and USGS35 were used to calibrate the $\delta^{15}N$ and $\delta^{18}O$ measurements. The long-term precision for the $\delta^{15}N$ and $\delta^{18}O$ analyses are ±0.3‰ and ±0.5‰, respectively. $\delta^{15}N$ of NO_2^- in the soil extracts without the sulfamic acid addition was also estimated using isotopic mass balance when NO_2^- concentration were sufficiently high.

The $\Delta^{17}O$ of soil NO_3^- was measured using the coupled bacterial reduction (*Pseudomonas aureofaciens*) and thermal decomposition method described by Kaiser et al. (2007). After converting 200 nmol of soil NO_3^- sample to N_2O, the N_2O was thermally converted to O_2 and N_2 by reduction over a gold surface at 800 ˚C. The O_2 and N_2 were separated using a 5Å molecular sieve gas chromatograph and the O_2 was analyzed for $\delta^{17}O$ and $\delta^{18}O$ by the CF-IRMS. The $\Delta^{17}O$ was calculated using Equation (1) (Miller, 2002; Young et al., 2002) and calibrated by USGS34, USGS35, and a 1:1 mixture of USGS34 and USGS35. The precision for $\Delta^{17}O$ analysis of USGS35

and the USGS35:USGS34 mixture is ±0.3‰. According to Kaiser et al. (2007), the measured $\Delta^{17}O$ was used in reduction of molecular isotope ratios of N_2O to correct the isobaric interference (i.e., *m/z* 45) on the $\delta^{15}N$ analysis.

$$\Delta^{17}O = \left[\ln\left(\frac{\delta^{17}O}{1000}+1\right) - 0.52\ln\left(\frac{\delta^{18}O}{1000}+1\right)\right] \times 1000 \qquad \text{Equation (1)}$$

The $\delta^{15}N$ of NH_4^+ in the KCl extracts was measured by coupling the NH_3 diffusion method (Zhang et al., 2015) and the hypobromite (BrO^-) oxidation method (Zhang et al., 2007) with the denitrifier method (Felix et al., 2013). Briefly, an aliquot of soil KCl extract having 60 nmol NH_4^+ was pipetted into a 20 mL serum vial containing an acidified glass fiber disk. The solution was made alkaline by adding magnesium oxide (MgO) to volatilize NH_3 which was subsequently captured on the acidic disk. After removal of the disk, NH_4^+ was eluted using deionized Milli-Q water, diluted to 10 μM, oxidized by BrO^- to NO_2^-, and finally measured for $\delta^{15}N$ as NO_2^- at 20 nmol using the denitrifier method as described above. International NH_4^+ reference standards IAEA-N1, USGS25, and USGS26 underwent the same preparation procedure as the soil samples and were used along with the NO_3^- reference standards to correct for blanks and instrument drift. The precision for the $\delta^{15}N$-NH_4^+ analysis is ±0.5‰.

The original protocol for $\delta^{15}N$ analysis of the TEA collection samples was modified to overcome isobaric interference from non-zero $\Delta^{17}O$ of the collected NO_2^- and NO_3^-. This $\Delta^{17}O$ signal (~19‰) was present in all TEA collection samples as a result of the NO+O_3 reaction during the NO collection. A different denitrifying bacterium, *Pseudomonas chloroaphis*, was used in conjunction with the denitrifier method to measure all TEA-collected samples in this study. *P. chloroaphis* catalyzes O atom exchange between denitrification intermediates and H_2O during reduction of NO_3^- to N_2O (Casciotti et al., 2002) and thus has been used previously to remove $\Delta^{17}O$ signal from atmospheric NO_3^- for accurate $\delta^{15}N$-NO_3^- analysis using the denitrifier method (Coplen

et al., 2004). In this study, cultures of *P. chloroaphis* were grown in the laboratory for 8 - 10 days before use to ensure high efficiency in catalyzing the O exchange (Casciotti et al., 2002). The TEA-collected samples were neutralized with 12 N HCl to pH ~7, and then 10 nmol of NO_2^-+NO_3^- were used for δ^{15}N-NO analysis following the blank-matching strategy outlined in Chapter 2. To quantify the degree to which O is exchanged between denitrification intermediates and H_2O, NO_3^- reference materials USGS34 (δ^{18}O=-27.9‰) and USGS35 (δ^{18}O=57.5‰) were prepared in 20% TEA solution and measured for δ^{18}O-NO_3^- using *P. chloroaphis* (Coplen et al., 2004). The results showed that the biologically catalyzed O exchange was between 55% and 71% and indicated that more than half of the Δ^{17}O signal in the TEA-collected samples would be eliminated if *P. chloroaphis* was used in conjunction with the denitrifier method. A subset of the NO tank (δ^{15}N-NO=-71.4‰) collection samples acquired during the development of the DFC-TEA method were also measured using *P. chloroaphis*. The results indicate that the same accuracy and precision, i.e., ±1.1‰, is achieved for δ^{15}N-NO analysis without measuring Δ^{17}O for isobaric correction (Table C-2 in Appendix C). All isotopic analyses were conducted at the University of Pittsburgh *Regional Stable Isotope Lab for Earth and Environmental Science Research*.

4.3 RESULTS AND DISCUSSION

Because the three incubation experiments build upon each other, here we present results from the anaerobic, abiotic, and aerobic incubation experiments successively. Data from these incubation experiments are provided in Appendix C.

4.3.1 Dynamics and $\delta^{15}N$ of NO during anaerobic soil incubation

During anaerobic incubation, soil NO_3^- concentration decreased linearly from 49.3±0.1 μg $N \cdot g^{-1}$ to 24.7±0.2 μg $N \cdot g^{-1}$ (Figure 4.2a), while NO_2^- accumulated linearly from 0.4±0.1 μg $N \cdot g^{-1}$ to 6.9±0.1 μg $N \cdot g^{-1}$ (Figure 4.2b). The net NO production rate increased slowly from the first sampling day (0.063±0.008 μg $N \cdot g^{-1} \cdot h^{-1}$) to sampling day 5 (0.082±0.003 μg $N \cdot g^{-1} \cdot h^{-1}$) and then stabilized (Figure 4.2c). The measured net NO production rate is well within the range previously reported for anaerobically incubated soils (e.g., 0.005 to 0.5 μg $N \cdot g^{-1} \cdot h^{-1}$) (McKenney et al., 1982; Remde and Conrad, 1991; Medinets et al., 2015).

$\delta^{15}N\text{-}NO_3^-$ increased from 4.7±0.3‰ to 36.7±1.5‰ over the incubation (Figure 4.2d). A closed-system Rayleigh fractionation model was used to estimate the apparent isotope effect for NO_3^- reduction using the measured time series of NO_3^- concentration and $\delta^{15}N\text{-}NO_3^-$ (Mariotti et al., 1981; Granger et al., 2008). The estimated apparent isotope effect was 46.8±0.9‰ (Figure 4.3). $\delta^{15}N\text{-}NO_2^-$ was estimated for samples collected in the last three sampling days when NO_2^- accumulated to relatively high concentration (e.g., >15% of $NO_3^-+NO_2^-$). The estimated $\delta^{15}N\text{-}NO_2^-$ values were -6.9±3.7‰, -6.0±2.5‰, -0.9±1.3‰, respectively, lower than $\delta^{15}N\text{-}NO_3^-$ measured on the same sampling day by 33.6‰ to 37.0‰ (Figure 4.2e). $\delta^{15}N\text{-}NO$ increased linearly during the anaerobic incubation from -47.7±0.3‰ to -22.8±2.2‰ (Figure 4.2f), with relatively consistent offsets of 55.1±2.6‰ from the measured $\delta^{15}N\text{-}NO_3^-$ and of 22.2±1.4‰ from the measured $\delta^{15}N\text{-}NO_2^-$.

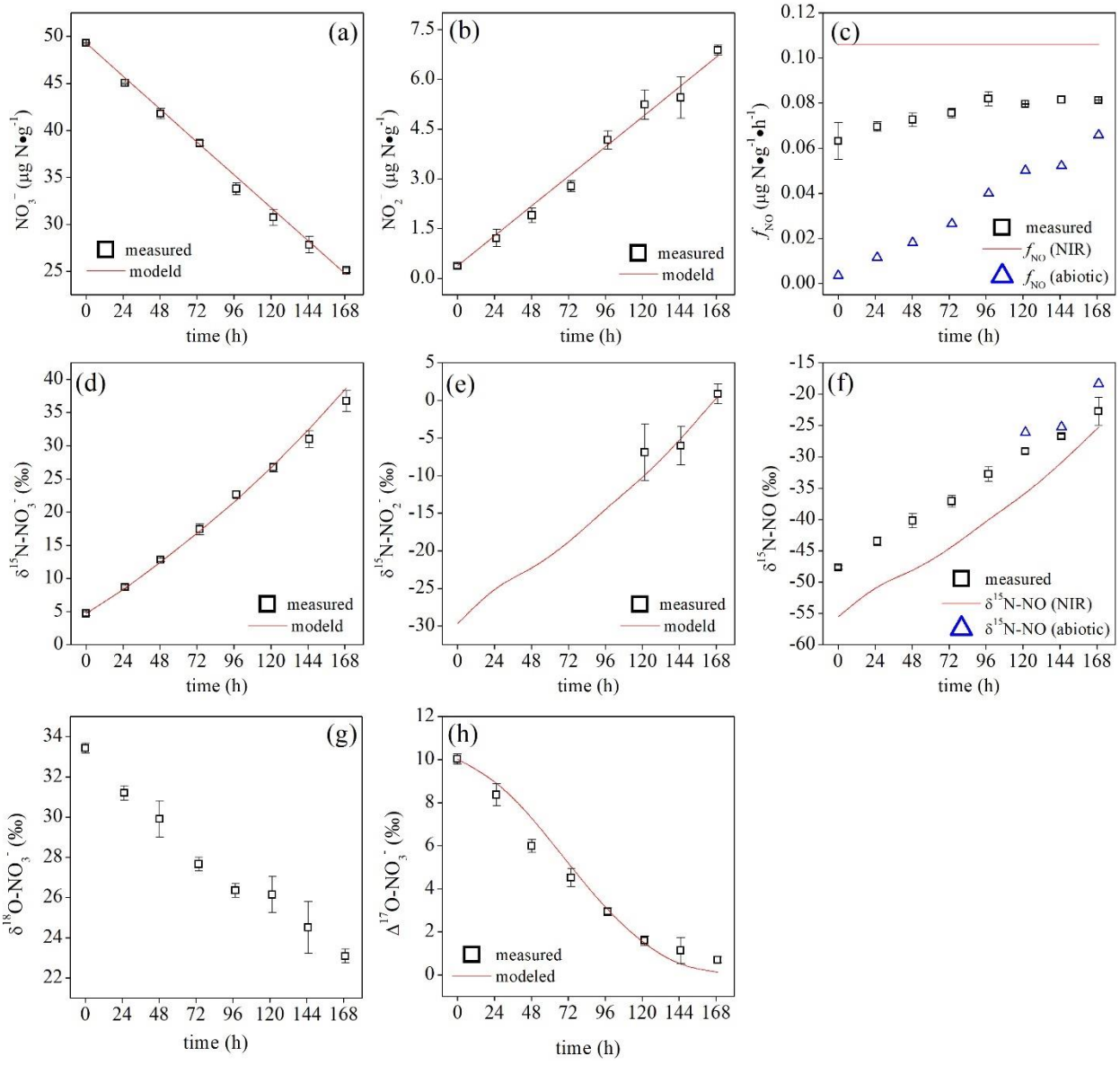

Figure 4.2 Measured (open squares) and modeled (red lines) concentrations/flux (top row: a, b, c) and $\delta^{15}N$ values (middle row: d, e, f) of NO_3^-, NO_2^-, and NO during the anaerobic incubation. $\delta^{18}O$ and $\Delta^{17}O$ of NO_3^- are shown in the bottom row ((g) and (h)). Modeled net production rate (f_{NO} (abiotic)) and $\delta^{15}N$ ($\delta^{15}N$-NO (abiotic)) of abiotically produced NO in the sterilized soils are shown in (c) and (f) for comparison.

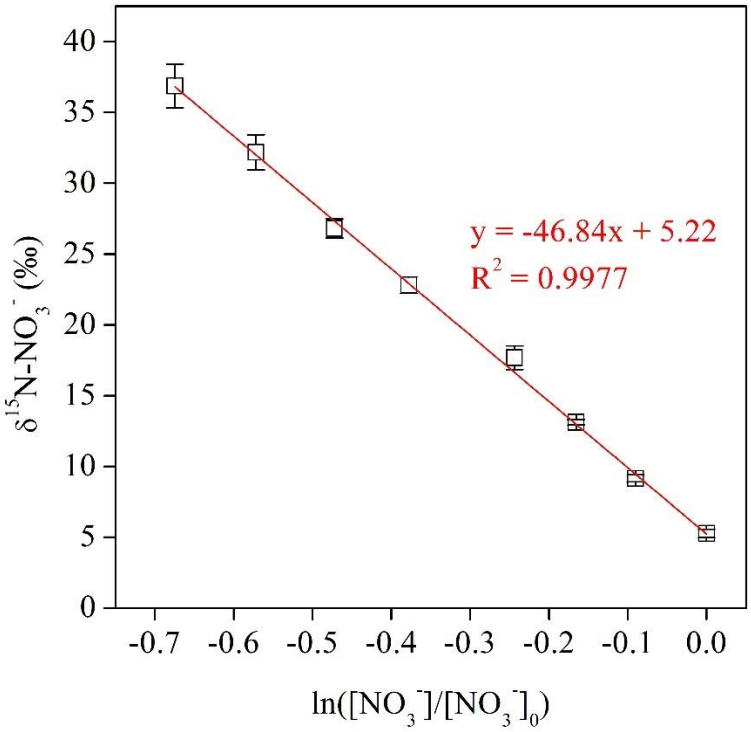

Figure 4.3 Rayleigh plot of δ^{15}N-NO_3^-. The slope of linear regression gives an estimate of the apparent isotope effect for NO_3^- reduction during the anaerobic incubation.

Surprisingly, δ^{18}O-NO_3^- was entirely decoupled from δ^{15}N-NO_3^-, decreasing progressively from 33.4±0.2‰ to 23.1±0.3‰ over the incubation (Figure 4.2g). This contrasts with the well-established paradigm that δ^{15}N-NO_3^- and δ^{18}O-NO_3^- of residual NO_3^- subject to denitrification should follow a linear trajectory with a slope of 0.5-1 (Groffman et al., 2006; Granger et al., 2008). More surprisingly, Δ^{17}O-NO_3^- decreased from 10.0±0.2‰ to 0.7±0.2‰ progressively over the course of incubation (Figure 4.2h). As Δ^{17}O-NO_3^- is not altered by mass-dependent fractionation during denitrification (Michalski et al., 2004), the decreasing Δ^{17}O-NO_3^- could indicate a biologically or chemically-driven O exchange between soil NO_3^- and H_2O and/or nitrification, even though our soil incubations were anoxic. However, it has been confirmed in controlled experiments that NO_3^- reduction catalyzed by bacterial nitrate reductase (NAR) is irreversible at

the enzyme level (Granger et al., 2008) and that abiotic O exchange between NO_3^- and H_2O is irrelevant under natural conditions (Kaneko and Poulson, 2013). Based on the complete recovery of NO_3^- concentrations and isotopes in the spiking experiment and C_2H_2 incubation, we exclude nitrification from oxygen contamination as an explanation for this observation.

Thus, the decreasing $\delta^{18}O\text{-}NO_3^-$ and $\Delta^{17}O\text{-}NO_3^-$ could imply occurrence of anaerobic NO_2^- re-oxidation catalyzed by nitrite oxidizers, as has been demonstrated by earlier pure culture studies (Friedman et al., 1986; Bock et al., 1988) and more recent observations in oxygen-deficient ocean water columns (Gaye et al., 2013; Peters et al., 2016; Kemeny et al., 2016; Babbin et al., 2017; Sun et al., 2017) and coastal sediments (Füssel et al., 2012; Wunderlich et al., 2013; Dale et al., 2014; Dähnke and Thamdrup, 2015). The enzyme catalyzing NO_2^- oxidation in nitrite-oxidizing bacteria, nitrite oxidoreductase (NXR), is structurally related to NAR and able to reduce NO_3^- to NO_2^- under anoxic conditions (Casciotti, 2009). During NO_2^- oxidation, the required oxygen atom stems from H_2O molecules, and thus NO_2^- can, in theory, be transformed into NO_3^- without the presence of dissolved oxygen by donation of electrons to redox-active intracellular components (Wunderlich et al., 2013).

$$NO_3^- + 2H^+ + 2e^- \Leftrightarrow H_2O + NO_2^-$$

As NO_2^- is also subject to abiotic oxygen exchange with water under acidic and circumneutral pH conditions (Casciotti et al., 2007; Buchwald and Casciotti, 2013), re-oxidation of NO_2^- in net denitrifying environments can effectively decrease $\delta^{18}O\text{-}NO_3^-$ and $\Delta^{17}O\text{-}NO_3^-$ by incorporating H_2O-derived oxygen atoms into NO_3^- (Dähnke and Thamdrup, 2015; Granger and Wankel, 2016). Indeed, Wunderlich et al. (2013) found that a co-culture of denitrifiers and nitrite oxidizers incorporated ^{18}O from labeled water into NO_3^- in the absence of oxygen, which was attributed to reversibility of NXR that occurred coincident with NAR-catalyzed NO_3^- reduction

(Wunderlich et al. 2013). The degree of ^{18}O incorporation into NO_3^- was also dependent on the amount of accumulated NO_2^- in the medium, such that the higher the NO_2^- accumulation, the faster the backward reaction and the more exchange with H_2O took place (Wunderlich et al. 2013).

Importantly, if the proposed NO_2^- re-oxidation is reversible at the enzyme level, $\delta^{15}N$ values of NO_3^-, NO_2^-, and NO can be significantly affected by the expression of an equilibrium N isotope effect between NO_3^- and NO_2^- during bidirectional NO_3^-/NO_2^- interconversion across NXR (Brunner et al., 2013; Kemeny et al., 2016). Previous evidence for N isotopic equilibration between NO_3^- and NO_2^- includes a study by Brunner et al. (2013) wherein a large increase in $\delta^{15}N\text{-}NO_3^-$ and a corresponding decrease in $\delta^{15}N\text{-}NO_2^-$ was measured in cultures of anaerobic ammonia oxidizing (anammox) bacteria that expressed an NXR enzyme. Based on the difference between $\delta^{15}N\text{-}NO_3^-$ and $\delta^{15}N\text{-}NO_2^-$, an inverse equilibrium isotope effect of -60.5‰ was derived that favors partitioning of ^{14}N into NO_2^-.

$$^{14}NO_2^- + {}^{15}NO_3^- \overset{^{15}\alpha_{eq}}{\Longleftrightarrow} {}^{15}NO_2^- + {}^{14}NO_3^-$$

This experimentally derived isotope effect is consistent with theoretical calculations using vibrational frequencies of NO_3^-/NO_3 and NO_2^-/NO_2 (e.g., -51.4 to -59.4‰) (Casciotti, 2009; Walters and Michalski, 2015). The NXR-catalyzed NO_2^- and NO_3^- equilibrium has been invoked as an important mechanism to explain the extremely low $\delta^{15}N\text{-}NO_2^-$ relative to $\delta^{15}N\text{-}NO_3^-$ (up to 90‰) in ocean oxygen-deficient zones where NO_2^- oxidation is inhibited by a lack of suitable electron acceptors (Kemeny et al., 2016). Given previous evidence that shows the enzymatic NO_3^- and NO_2^- interconversion is dependent on cell density and activity of nitrite oxidizers (Wunderlich et al., 2013; Dähnke and Thamdrup, 2015), it is reasonable to deduce its relevance in anaerobically incubated agricultural soils with high NO_2^- concentrations.

To test if the reaction reversibility between NO_3^- and NO_2^- can explain the observed variations in triple NO_3^- isotopes and $\delta^{15}N\text{-}NO_2^-$, we modified the $\Delta^{17}O$-based numerical model (see Chapter 3 for details) to simulate denitrification in concurrence with the NO_3^- and NO_2^- interconversion presumably catalyzed by soil nitrite oxidizers. The modeling scheme is illustrated in Figure 4.4. To first order, the reversibility was evaluated through mass and isotope balance calculations considering forward and backward reactions (Casciotti et al., 2009). In the numerical model, we assumed that the forward (NO_3^- reduction) and backward (NO_2^- oxidation) reactions are balanced in terms of mass (i.e., no net oxidation or reduction) and that both the forward and backward reactions can be described by first order kinetics:

$$^{14}k_f \cdot [^{14}NO_3^-] + {}^{15}k_f \cdot [^{15}NO_3^-] = {}^{14}k_b \cdot [^{14}NO_2^-] + {}^{15}k_b \cdot [^{15}NO_2^-] \quad \text{Equation (2)}$$

Therefore, the first order rate constants (k_f and k_b) are related by the equilibrium N isotopic fractionation ($^{15}\alpha_{eq}$) via the kinetic isotopic fractionation factors ($^{15}\alpha_k$) for the forward and backward reactions (Fry, 2006):

$$^{15}\alpha_{eq} = \frac{^{15}\alpha_{k,b}}{^{15}\alpha_{k,f}} = \frac{^{14}k_b \cdot {}^{15}k_f}{^{15}k_b \cdot {}^{14}k_f} \quad \text{Equation (3)}$$

We used an isotope effect of 25±5‰ for both NAR and NXR catalyzed NO_3^- reduction. This value is an average based on results from pure culture denitrifying bacteria (10 to 37‰, Denk et al., 2017). An inverse isotope effect of -13‰, measured for NXR-catalyzed aerobic NO_2^- oxidation (Casciotti, 2009), was used for NO_2^- oxidation under anaerobic conditions, giving rise to an equilibrium isotope effect of -37‰. Moreover, we assumed no abiotic O exchange between H_2O and the standing NO_2^- pool to ease interpretation of the model results. Details regarding the numerical optimization procedure are given in Chapter 3.

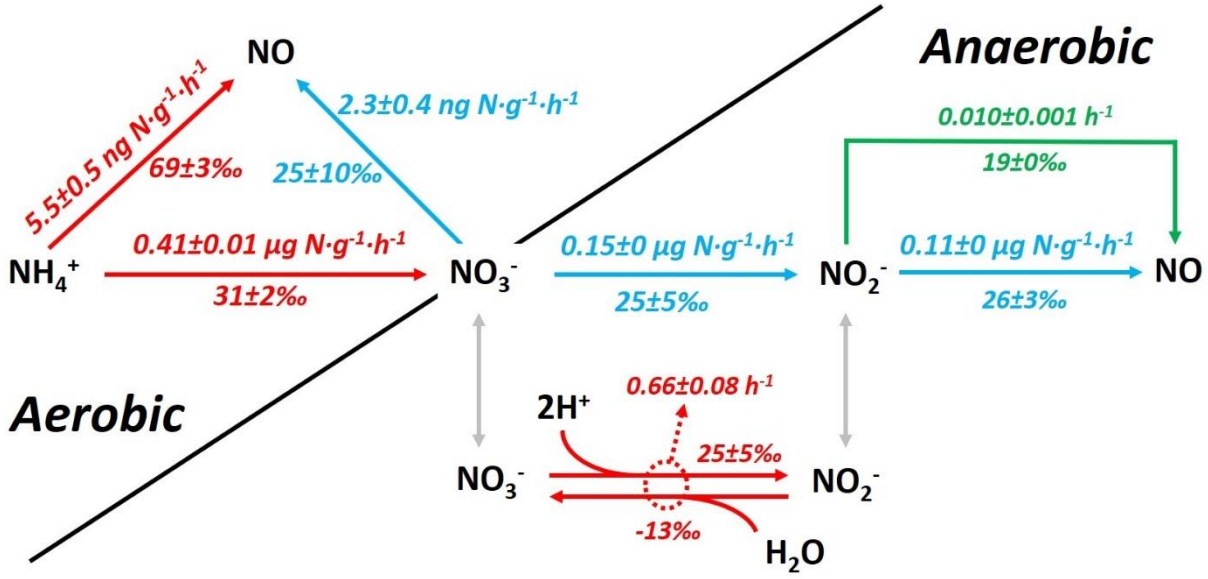

Figure 4.4 Schematic representation of NO production and its driving processes under aerobic and anaerobic conditions considered in this study. Denitrifier- and nitrifier-catalyzed N transformations are denoted by blue and red arrows, respectively. Abiotic NO production and physical NO diffusion are shown in green and grey, respectively.

Modeling results are shown in Figure 4.2 and illustrated in Figure 4.4. Because the NO_3^- and NO_2^- interconversion does not contribute to net NO_3^- or NO_2^- production, NO_3^- and NO_2^- concentrations were well-constrained assuming zero-order NO_3^- (0.15 μg $N \cdot g^{-1} \cdot h^{-1}$) and NO_2^- (0.11 μg $N \cdot g^{-1} \cdot h^{-1}$) reduction during denitrification (Figure 4.2a and 4.2b). The first-order rate constant for the anaerobic NO_2^- oxidation (i.e., k_b) was estimated to be 0.66±0.08 h^{-1}. Based on this rate constant and the assumed isotope effects, the time series of $\delta^{15}N$-NO_3^-, $\Delta^{17}O$-NO_3^-, and the large $\delta^{15}N$ offset between NO_3^- and NO_2^- were reproduced with excellent agreement (Figure 4.2d, 4.2e, and 4.2h). The only noticeable difference was slightly higher $\Delta^{17}O$-NO_3^- predicted by the model at the beginning of the incubation (Figure 4.2h). This is due to limited NO_3^- and NO_2^- interconversion as a result of low NO_2^- concentrations. It is important to note that the estimated k_b

is fairly large. With the high NO_2^- concentrations observed during the later phase of the incubation, a k_b of 0.66 h^{-1} would require an anaerobic NO_2^- oxidation rate one order of magnitude higher than the NO_2^- reduction rate. However, many factors in the modeled system can cause variations in k_b. Given the low soil pH (pH=5.7) and long NO_2^- residence time in the soil, significant abiotic oxygen exchange between NO_2^- and H_2O can be expected (Casciotti et al., 2007). By assuming 10% of the standing NO_2^- pool is in oxygen isotope equilibrium with H_2O, the estimated k_b was lowered to 0.26 h^{-1}. Similarly, further k_b could be further reduced to 0.036 h^{-1} by increasing the isotope effect for NO_3^- reduction to 37‰, the upper end of the range derived using denitrifying bacteria (Denk et al., 2017), and lowering the equilibrium N isotope effect to -55‰, as suggested by the theoretical calculations (Casciotti, 2009). This indicates that less NO_3^- and NO_2^- interconversion is required to dilute the $\Delta^{17}O$-NO_3^- signal and simultaneously increase the $\delta^{15}N$-NO_3^- values beyond enrichment caused by denitrification alone.

Compared to the modeled NO_2^- reduction rate (0.11 μg $N \cdot g^{-1} \cdot h^{-1}$), net NO production accounted for 69±6% of the modeled NO_2^- reduction throughout the anaerobic incubation (Figure 4.2c). This is consistent with previous findings that NO can be the dominant denitrification product under special experimental conditions (e.g., low soil water content and flow-through incubation) where NO diffusion is not limited (Russow et al., 2009; Loick et al., 2016). Based on the assumed isotope effects for NO_3^- reduction (25±5‰) and anaerobic NO_2^- oxidation (-13‰), the isotope effect for NO_2^- reduction to NO was predicted to be 26±5‰ (Figure 4.7), consistent with the range of isotope effects for NO_2^- reduction derived using denitrifying bacteria and anaerobically incubated soils (i.e., 4 to 33‰) (Mariotti et al., 1982; Bryan et al., 1983; Martin and Casciotti, 2016). This predicted isotope effect is also in general agreement with the measured net isotope effect for NO production from NO_2^- (i.e., 22.2±1.4‰). Applying this isotope effect to the modeled

$\delta^{15}N\text{-}NO_2^-$ resulted in a range of $\delta^{15}N\text{-}NO$ values (-56 to -25‰), which were consistently lower than the measured $\delta^{15}N\text{-}NO$ values by about 7‰ (Figure 4.2h). The difference between modeled and measured $\delta^{15}N\text{-}NO$ could be due to NO reduction to N_2O with a normal isotope effect, which, to our knowledge, has not been quantified previously in the literature. Although we are not able to provide conclusive information about the isotope effects for NO production and reduction during the anaerobic incubation at this point, the combined $\delta^{15}N\text{-}NO$ and $\Delta^{17}O\text{-}NO_3^-$ measurements provide evidence that the intrinsic isotope effect for NO_2^- reduction to NO is likely much smaller than the measured net isotope effect for NO production from NO_3^- (i.e., 55‰).

In conclusion, results from the anaerobic soil incubation demonstrate the possibility of reversible NO_3^- and NO_2^- conversion in soil environments and have important implications for characterizing denitrification and its gas products using stable N and O isotopes. Particularly, the NXR-catalyzed NO_2^- and NO_3^- interconversion is a new complication that needs to be considered when interpreting environmental $\delta^{15}N\text{-}NO_3^-$ and $\delta^{18}O\text{-}NO_3^-$ data (Wunderlich et al., 2013; Kemeny et al., 2016). As NO_2^- accumulation is often observed in anaerobically incubated agricultural soils (Chien et al., 1977; Blackmer and Bremner, 1977; McKenney et al., 1982) due to limitation of organic C and/or unbalanced expression of NAR and NIR (Betlach and Tiedje, 1981; Bakken et al., 2012), expression of the equilibrium N isotope effect can enlarge the difference between $\delta^{15}N\text{-}NO_3^-$ and $\delta^{15}N\text{-}NO_2^-$ and lead to overestimation of the isotope effect for NO_3^- reduction using the Rayleigh fractionation model (Figure 4.3). This may partially explain the significantly larger isotope effect measured in anaerobic soil incubations (10 to 53‰, mean: 31‰) relative to pure culture studies (10 to 37‰, mean: 25‰) (Denk et al., 2017). The enlarged difference between $\delta^{15}N\text{-}NO_3^-$ and $\delta^{15}N\text{-}NO_2^-$ will ultimately propagate to the net isotope effect for NO (and N_2O) production from NO_3^- and render it less useful for elucidating production mechanisms. Moreover,

enzymatic NO_2^- and NO_3^- interconversion incorporates oxygen atoms from soil H_2O into NO_3^-, causing variations in the relationship between $\delta^{15}N\text{-}NO_3^-$ and $\delta^{18}O\text{-}NO_3^-$ in net denitrifying environments (Wunderlich et al., 2013; Granger and Wankel, 2016). Indeed, net oxygen exchange between NO_3^- and H_2O has already been documented in previous soil studies. Using a Chilean NO_3^- fertilizer similar to ours (i.e., $\delta^{18}O\text{-}NO_3^- = 56‰$), Lewicka-Szczebak et al. (2014) observed a significant decrease in $\delta^{18}O\text{-}NO_3^-$ by up to 4‰ over 25 h in two anaerobically incubated arable soils, although $\Delta^{17}O\text{-}NO_3^-$ was not measured in this study. This implies that anaerobic NO_2^- re-oxidation catalyzed by reversible biochemical reactions may have wide occurrence in soils under anaerobic conditions. Based on our results, we suggest that NO_2^- accumulation may be used as an indicator for evaluating the potential of the NO_2^- reaction reversibility. In this regard, unbiased extraction and determination of soil NO_2^- is of critical importance, as it was recently uncovered that the routinely used KCl solution can lead to substantial NO_2^- lost during soil extraction (Homyak et al., 2016).

4.3.2 Abiotic NO production during anaerobic soil incubation

Addition of NO_3^- or NH_4^+ to the sterilized soil did not result in detectable NO production under either aerobic or anaerobic conditions. Addition of NO_2^- to the sterilized soil under anaerobic conditions, however, triggered immediate NO production (Figure 4.5). The net abiotic NO production rate ($f_{NO\text{-}abiotic}$) reached a steady state of 0.083±0.005 μg $N \cdot g^{-1} \cdot h^{-1}$ several minutes after the NO_2^- addition and then decreased exponentially over the next 8 days (Figure 4.5a). The decreasing NO production rate is plotted in Figure 4.5b as $\ln(f_{NO\text{-}abiotic})$ versus time. The linearity of this plot ($R^2 = 0.9943$) confirms first-order behavior of $f_{NO\text{-}abiotic}$. Therefore, abiotic NO

production from added NO_2^- can be kinetically described as $NO_2^- \rightarrow sNO$, where s is an unknown stoichiometric coefficient, and modeled using Equation (2) (McKenney et al., 1984; McKenney et al., 1990).

$$f_{NO-abiotic} = sk_{abiotic}[NO_2^-]_0 e^{-k_{abiotic}t} \quad \text{Equation (4)}$$

In Equation (2), t is time, $k_{abiotic}$ is the first-order rate constant of abiotic NO_2^- reduction, and $[NO_2^-]_0$ is the initial NO_2^- concentration. Taking the logarithm on both sides of Equation (2) yields:

$$\ln(f_{NO-abiotic}) = -k_{abiotic}t + \ln(sk_{abiotic}[NO_2^-]_0) \quad \text{Equation (5)}$$

According to Equation (3), s and $k_{abiotic}$ can be estimated using the slope and intercept of the linear regression of $\ln(f_{NO\text{-}abiotic})$ versus time (Figure 4.5b). Given $[NO_2^-]_0$=8 μg N·g^{-1}, s and $k_{abiotic}$ were estimated to be 0.52±0.05 and 0.019±0.002 h^{-1}, respectively, suggesting that 52±5% of the reacted NO_2^- was in the form of NO (Figure 4.5b). The estimated $k_{abiotic}$ is consistent with a recent study wherein $k_{abiotic}$ was estimated to range from 0.00055 to 0.73 h^{-1} for a range of soils with pH from 3.4 to 7.2 (Lim et al., 2018).

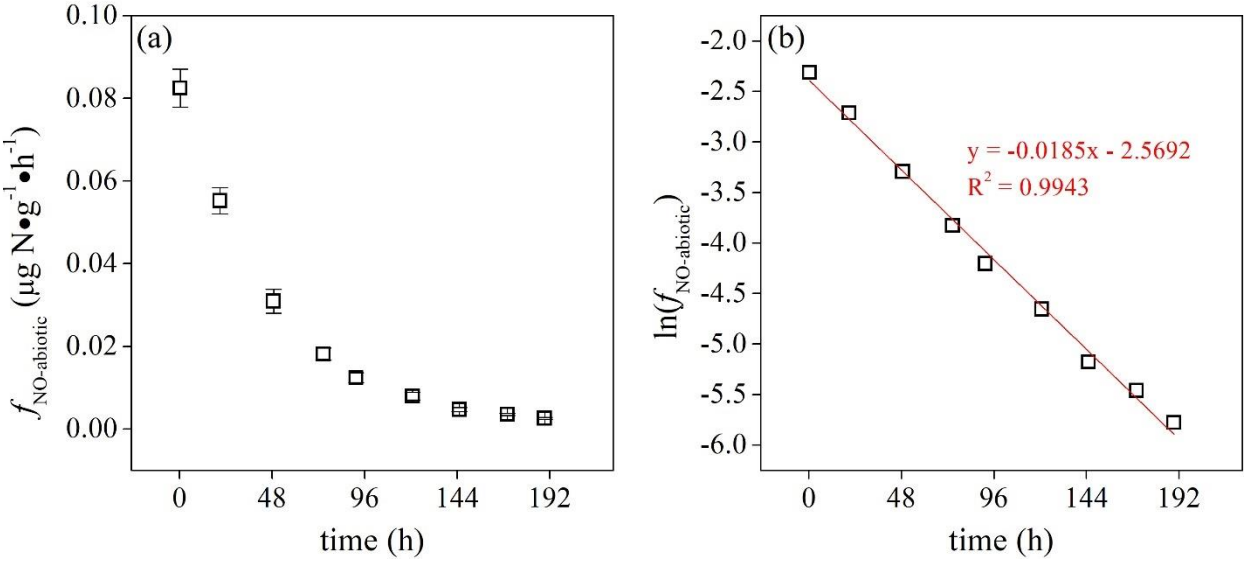

Figure 4.5 (a) Net abiotic NO production rate ($f_{NO\text{-}abiotic}$) as a function of time. (b) Plot of ln($f_{NO\text{-}abiotic}$) versus time showing first-order decay of $f_{NO\text{-}abiotic}$. The slope and intercept of the linear regression yield estimates of a first-order rate constant for abiotic NO_2^- reduction ($k_{abiotic}$) and its stoichiometric coefficient for NO production (s).

Several reaction pathways have been proposed for abiotic NO production from NO_2^- in soils. The most commonly cited pathway is the formation of NO via HNO_2 decomposition (Van Cleemput and Baert, 1984; Zumft, 1997; Venterea et al., 2005). Since HNO_2 is the direct reaction substrate, NO production from HNO_2 decomposition is highly dependent on soil pH. Although HNO_2 constituted <1% of the total NO_2^-+HNO_2 at pH 5.7, there is evidence that HNO_2 decomposition can occur on acidic clay-mineral surfaces, even though bulk soil is not acidic (Venterea et al., 2005). In addition, NO_2^- can also react with reduced transition metals (e.g., Fe(II)) and organic matter during chemo-denitrification to produce NO, N_2O, and N_2 under anoxic and circumneutral pH conditions (Schreider et al., 2012; Medinets et al., 2015). Further, NO_2^- and NO are known to the involved in abiotic nitrosation reactions with humic substances (e.g., secondary aliphates, aromates, amides), resulting in N incorporation into soil organic matter (Venterea et al., 2005; Medinets et al., 2015). Therefore, the reacted NO_2^- that could not be accounted for by NO was likely present in the forms of N_2O, N_2, and organic N in the sterilized soil (Lim et al., 2018).

Applying the estimated $k_{abiotic}$ and s to the measured NO_2^- concentrations in unsterilized soil under the anaerobic incubation revealed an increasing abiotic NO production, parallel to the NO_2^- accumulation (Figure 4.2c). The estimated abiotic NO production reached 0.066 μg $N \cdot g^{-1} \cdot h^{-1}$ at the end of the incubation, accounting for 81% of the measured net NO production. However, because net NO production was already at a high level even before significant NO_2^- accumulation

in the non-sterilized soil, the relative contribution of abiotic NO production is likely overestimated. Autoclaving is a harsh sterilization method (Trevors, 1996) and can alter soil organic matter composition by favoring hydrolysis of organic molecules. Thus, autoclaving can enhance the concentration of dissolved organic matter and increase the accessibility of reactive functional groups available to readily react with NO_2^- (Heil et al., 2015). On the other hand, because NO can be produced by extracellular enzymes in non-specific reactions (Medinets et al., 2015), other less harsh methods (e.g., gamma-irradiation) that presumably cause less severe alteration of soil properties may not completely inactivate biological NO production (Cawse and Cornfield, 1971; Venterea et al., 2005). Consequently, the relative importance of abiotic NO production in non-sterilized soils is still challenging to constrain and further research is needed to quantify abiotic reaction kinetics under conditions representative of non-sterilized soils.

The abiotically produced NO immediately after the NO_2^- addition was measured to have a $\delta^{15}N$ value of -17.8±0.4‰, which is 19.2±0.5‰ lower than the $\delta^{15}N$ of the added NO_2^-. This net isotope effect for abiotic NO production from NO_2^- is broadly consistent with the isotope effect for abiotic NO_2^- reduction (13 to 34‰) quantified in chemical reactions between NO_2^- and Fe(II) (Jones et al., 2015; Buchwald et al., 2016) and $\delta^{15}N$ offsets between N_2O and NO_2^- (8 to 29‰) in a variety of experiments using sterilized soils and batch medium (Jones et al., 2015; Buchwald et al., 2016). However, to our knowledge, none of previous studies measured $\delta^{15}N$-NO during chemical NO_2^- reduction, making it difficult to deduce reaction mechanisms by comparing our results with previous studies. It is likely that the measured isotopic offset between NO and NO_2^- reflects the number of reaction steps between the two species, individual isotopic fractionation factors for each step, and isotope effects for competing processes during abiotic NO_2^- reduction that led to production of N_2O, N_2, and organic N. Combining the measured net isotope effect with

the measured $\delta^{15}N\text{-}NO_2^-$ in the non-sterilized soil, $\delta^{15}N$ values of abiotically produced NO were predicted to be -26.1, -25.2, and -18.3‰ for the last three sampling days of the anaerobic incubation, respectively (Figure 4.2f). These values were very similar to the measured $\delta^{15}N\text{-}NO$ (-22.8 to -29.1‰), suggesting that $\delta^{15}N$ values of denitrification-produced and abiotically produced NO are likely indistinguishable.

4.3.3 Dynamics and $\delta^{15}N$ of NO during aerobic soil incubation

In all three $\delta^{15}N\text{-}NH_4^+$ treatments, soil NH_4^+ concentrations decreased linearly with increasing soil NO_3^- concentration (Figure 4.6a and 4.6b). While about 30% of the lost NH_4^+ between sampling days 1 and 2 could not be accounted for by increases in soil NO_3^- concentration, balanced NH_4^+ and NO_3^- concentration variations were observed for the last two sampling days (i.e., $NH_4^+ + NO_3^-$ concentration remained nearly constant) (Figure 4.6a and 4.6b). NO_2^- was not detectable in the soil, suggesting that the two oxidation steps of nitrification were tightly coupled. $\delta^{15}N\text{-}NH_4^+$ increased by 8.6 to 13.1‰ over the aerobic incubation in all three $\delta^{15}N\text{-}NH_4^+$ treatments (Figure 4.6e); $\delta^{15}N\text{-}NO_3^-$ varied distinctly, depending on the initial $\delta^{15}N\text{-}NH_4^+$ value (Figure 4.6d). Specifically, $\delta^{15}N\text{-}NO_3^-$ increased and decreased in the high and low $\delta^{15}N\text{-}NH_4^+$ treatments, respectively, and remained relatively constant in the intermediate $\delta^{15}N\text{-}NH_4^+$ treatment (Figure 4.6d). In all three $\delta^{15}N\text{-}NH_4^+$ treatments, $\delta^{18}O\text{-}NO_3^-$ (Figure 4.6d) and $\Delta^{17}O\text{-}NO_3^-$ (Figure 4.6h) decreased progressively over the aerobic incubation from about 19.0‰ to 9.5‰ and 5.8‰ to 3.4‰, respectively.

The $\Delta^{17}O$-based numerical model was applied to estimate gross rates and isotope effects for net mineralization, nitrification, and NO_3^- consumption using the measured NO_3^- and NH_4^+ concentrations and isotopic compositions from all three $\delta^{15}N\text{-}NH_4^+$ treatments (see Chapter 3 for

more details about the model scheme and optimization procedure). The modeling results are shown in Figure 4.6. Excellent agreement was obtained between the observed and simulated concentrations and isotopic compositions (Figure 4.6). The good quality of fit was confirmed by the high fraction of the total variation explained by the model, as indicated by a R^2>0.95 for all the individual variables. The gross nitrification rate was well described by zero order kinetics and was estimated to be 0.41±0.01 μg $N \cdot g^{-1} \cdot h^{-1}$ (Figure 4.7). Gross nitrification was associated with a large isotope effect of 31.4±2.0‰, consistent with results from pure cultures of ammonia-oxidizing bacteria and archaea (e.g., 25 to 35‰) (Mariotti et al., 1981; Casciotti et al., 2003; Santoro et al., 2011). Compared to gross nitrification, gross NO_3^- consumption and net mineralization rates were significantly lower, estimated to be 0.024±0.007 μg $N \cdot g^{-1} \cdot h^{-1}$ and -0.021±0.007 μg $N \cdot g^{-1} \cdot h^{-1}$ (negative value denotes net assimilation), respectively. The estimated gross NO_3^- consumption rate was about 6% of gross nitrification rate, confirming that nitrification dominated the soil N transformation during the aerobic incubation.

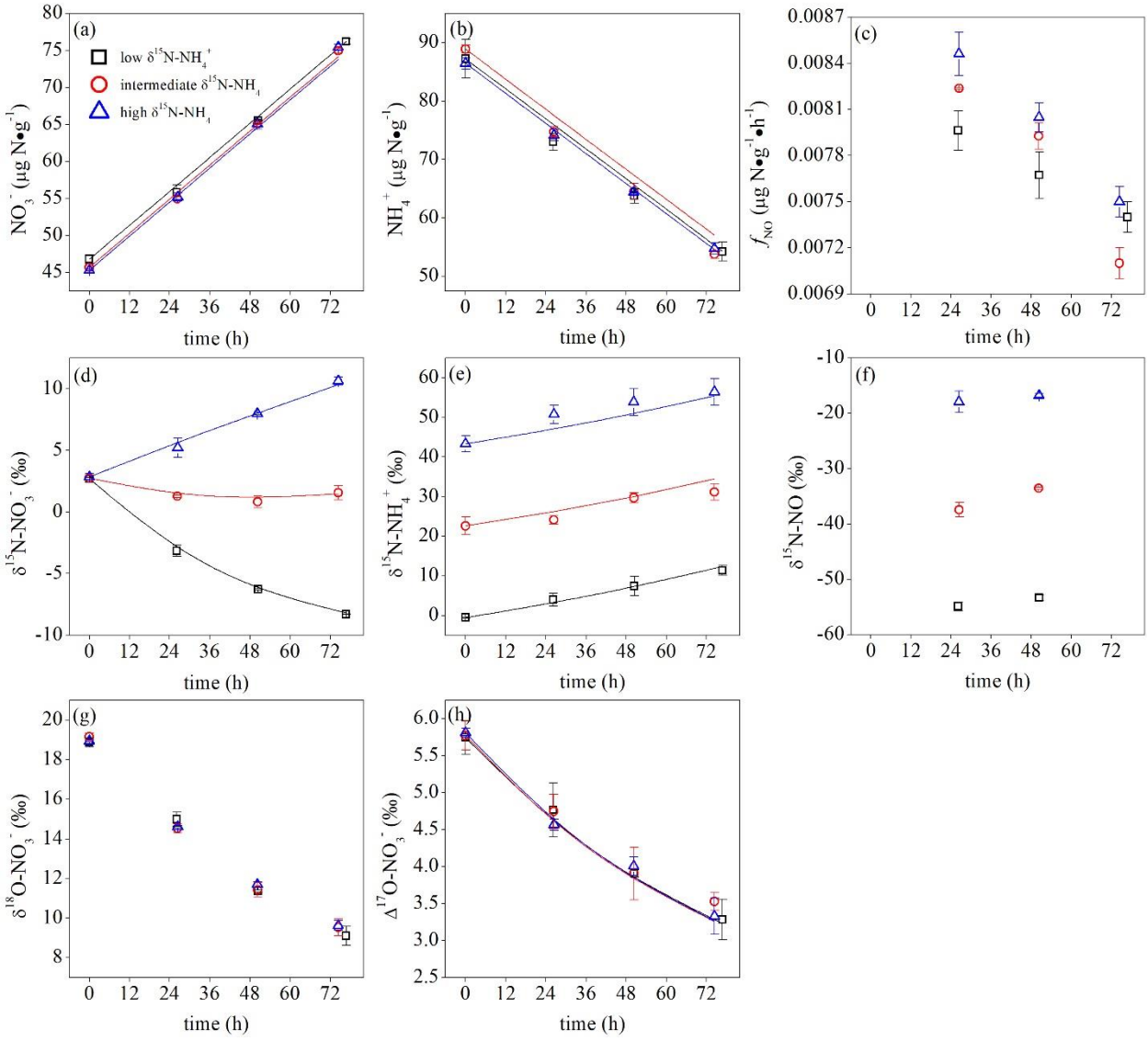

Figure 4.6 Measured (open symbols) and modeled (lines) concentrations/flux (top row: a, b, c) and $\delta^{15}N$ values (middle row: d, e, f) of NO_3^-, NH_4^+, and NO under the low, intermediate, and high $\delta^{15}N$-NH_4^+ treatments during the aerobic incubation. $\delta^{18}O$ and $\Delta^{17}O$ of NO_3^- are shown in the bottom row ((g) and (h)).

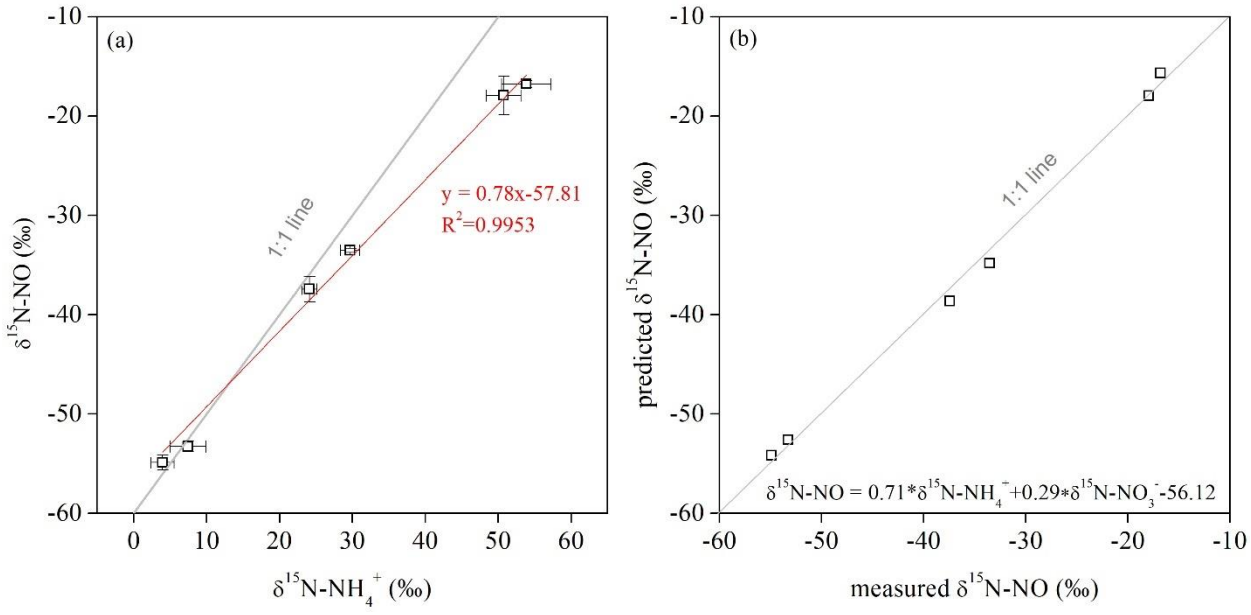

Figure 4.7 (a) The measured δ^{15}N-NO as a function of δ^{15}N-NH_4^+. (b) Comparison between the measured δ^{15}N-NO and modeled δ^{15}N-NO using the mixing equation shown in the figure.

Net NO production rates varied within a relatively narrow range, 0.0074 to 0.0085 μg $N \cdot g^{-1} \cdot h^{-1}$, during the aerobic incubation (Figure 4.6c). Compared to net NO production in the anaerobically incubated soil (0.063 to 0.082 μg $N \cdot g^{-1} \cdot h^{-1}$, Figure 4.2c), net NO production rates in the aerobic soil were about 10 times lower. The measured δ^{15}N-NO ranged from -16.8±0.3‰ to -54.9±0.8‰ (Figure 4.6f). Using the isotopically different NH_4^+ amendments in parallel incubations allows us to examine the relative contribution of NH_4^+ to the measured NO production. Specifically, if NO is exclusively produced from soil NH_4^+, we would expect to see a constant δ^{15}N offset between NO and NH_4^+ among the three treatments. However, pooling the δ^{15}N-NO measurements from the two sampling days, we found that the δ^{15}N offset varied from 58.9±1.8‰ in the low δ^{15}N-NH_4^+ treatment to 70.7±3.4‰ in the high δ^{15}N-NH_4^+ treatment. Plotting the δ^{15}N-NO with the δ^{15}N-NH_4^+ from all three treatments revealed a significant linear relationship with a

slope (0.78±0.03) significantly lower than 1 (Figure 4.6a). This deviation from 1:1 relationship suggests that sources other than NH_4^+ were contributing to the measured net NO production.

We speculate that NO_3^- was the other major source driving NO production via denitrification during the aerobic incubation, because organic N, the other potential source of NO (Rütting et al., 2007; Stange et al., 2013), is expected to have a low concentration in this agricultural soil with a low concentration of soil organic matter. Therefore, a two-source isotope mixing model was used to relate net NO production with nitrification and denitrification:

$$\delta^{15}N - NO = f_N * \left(\delta^{15}N - NH_4^+ - {}^{15}\varepsilon_N\right) + (1 - f_N) * \left(\delta^{15}N - NO_3^- - {}^{15}\varepsilon_D\right)$$

Equation (6)

where f_N is fractional net NO production from nitrification; ${}^{15}\varepsilon_N$ and ${}^{15}\varepsilon_D$ are net isotope effects for NO production from nitrification and denitrification, respectively. Rearranging Equation (5) yields Equation (6):

$$\delta^{15}N - NO = f_N * \delta^{15}N - NH_4^+ + (1 - f_N) * \delta^{15}N - NO_3^- - \left[f_N * {}^{15}\varepsilon_N + (1 - f_N) * {}^{15}\varepsilon_D\right]$$

Equation (7)

Letting the last term of Equation (6) be a constant *C*, Equation (6) can be solved for f_N and *C* using the measured δ^{15}N-NO, δ^{15}N-NH_4^+, and δ^{15}N-NO_3^-. The constant *C* represents a combined net isotope effect for NO production from soil NH_4^+ and NO_3^-. Using data from all three treatments, f_N and *C* were solved to be 0.71±0.06 and -56.2±4.5‰, respectively (Figure 4.7b), indicating that 71% and 29% of the NO were produced from nitrification and denitrification, respectively.

Therefore, our results provide evidence that denitrification can be a significant source of NO even under strong aerobic conditions. Many previous studies reported decreasing soil NO emissions with increasing soil water content (Ludwig et al., 2001; van Dijk et al., 2002; Feig et

al., 2008). Based on this pattern, nitrification is considered the dominating process for soil NO production, while the absence of NO emission during denitrification is explained by the diffusion limitation hypothesis (Firestone and Davidson, 1989; Skiba et al., 1997). This hypothesis suggests that at low oxygen concentrations, i.e., conditions that favor denitrification such as waterlogging, the NO produced is unlikely to escape from the soil to the atmosphere due to limited gas diffusion. Thus, the NO is trapped and is available as a denitrification substrate for further reduction to N_2O and/or N_2. However, there is growing evidence that extensive anoxic micro-sites can develop in otherwise well-aerated soils (Russow et al. 2009). In a series of sieved and re-packed upland soils, Keiluweit et al. (2018) observed significant micro-scale variability of soil oxygen concentrations with anoxic microsites comprising 2 to 9% of the total soil volume at moderate moisture conditions. Further, these authors demonstrated a positive correlation between the extent of anoxic microsites and bioavailable organic matter. Although organic matter concentration was low in the studied agricultural soil, it is possible that fast nitrification stimulated by high NH_4^+ concentrations can quickly draw down local oxygen levels and thus lead to the development of anoxic niches in close association with nitrification hot spots (Kremen et al., 2005). Using ^{15}N labeling and direct ^{15}NO measurement, Russow et al. (2009) demonstrated that nitrification accounted for only about 70% of NO production in a well-aerated, NH_4^+-fertilized arable soil, in strong agreement with our results based on natural abundance $\delta^{15}N$-NO measurements. Even lower contribution of nitrification to NO production, e.g., 26 to 44%, was recently reported for a series of Spanish forest soils incubated under aerobic conditions (Stange et al., 2013). Indeed, because NO is an obligatory intermediate in denitrification (Zumft, 1997; Russow et al., 2009), denitrification may have an inherently higher NO yield than nitrification, that is, a bigger “hole” for NO leaking from the denitrification “pipe” in the classic “hole-in-the-pipe” concept (Firestone and Davidson, 1989).

Combining the $\delta^{15}N$-based NO source apportionment with the estimated gross nitrification and NO_3^- consumption rates, NO yield was calculated to be 1.4% and 9.6% for gross nitrification and NO_3^- consumption, respectively (Figure 4.7). Thus, together with new evidence from recent ^{15}NO measurements, our results suggest that denitrification is an overlooked source of soil NO emissions under aerobic conditions.

Besides the NO source partitioning, the solved f_N and C also provide important information about isotope effects for NO production during nitrification and denitrification. Although $^{15}\varepsilon_N$ and $^{15}\varepsilon_D$ cannot be uniquely determined from the solved f_N and C, their relative magnitudes can be inferred. Specifically, because NO_2^- was not accumulated during the aerobic incubation, it is reasonable to assume that $\delta^{15}N$ of denitrification-produced NO may largely reflect the isotope effect for NO_3^- reduction to NO_2^-. Consequently, assuming a typical range of isotope effect for NO_3^- reduction to $^{15}\varepsilon_D$ (i.e., 15 to 35‰, Denk et al. (2017)), $^{15}\varepsilon_N$ is correspondingly estimated to range from 65 to 73‰ (69±3‰ on average) (Figure 4.7). This inferred $^{15}\varepsilon_N$ is at the upper end of the range of net isotope effect for N_2O production from ammonia-oxidizing bacteria (45 to 67‰) (Sutka et al., 2006; Frame and Casciotti et al., 2010; Yoshida et al., 1984). However, this inferred $^{15}\varepsilon_N$ is likely still conservative, as denitrification-produced NO diffusing out of anoxic niches may be enriched in $\delta^{15}N$, if a normal isotope effect is assumed for NO reduction to N_2O.

Importantly, the biochemical mechanism(s) underlying NO production in NH_4^+ oxidation is still not well understood (Schreiber et al., 2012). The current model is that NO is produced as a metabolic byproduct during the oxidation of NH_2OH to NO_2^- (Hooper et al., 1979; Schreiber et al., 2012). Therefore, as NH_4^+/NH_3 oxidation to NH_2OH is usually the rate-limiting step (Casciotti et al., 2003), the inferred large $^{15}\varepsilon_N$ can be partially explained by the large isotope effect associated with NH_2OH production (i.e., 31.4±2.0‰ estimated for this study; Figure 4.7). Moreover, NH_2OH

has a *p*Ka of 5.95, and below this pH value NH_2OH also exists in its protonated form, NH_3OH^+, which is more stable than NH_2OH (Heil et al., 2015). If NH_3OH^+ is the true substrate for NO production, an equilibrium isotope effect between NH_2OH and NH_3OH^+ may be further reflected in $^{15}\varepsilon_N$. Additionally, recent biochemical studies uncovered new pathways that involve nitroxyl hydride (HNO) as an intermediate precursor for NO production in ammonia-oxidizing archaea (Schleper and Nicol, 2010; Walker et al., 2010). Indeed, the inferred large $^{15}\varepsilon_N$ is likely governed by the combination of chemical and biochemical reactions (e.g., bond forming/breaking and acid-base equilibrium) that occur during NH_4^+ oxidation. While the net reaction results in the oxidation of NH_4^+ to NO, the reaction may proceed through multiple and likely transient intermediate nitrogenous species and/or through parallel pathways (NH_2OH/HNO), and isotope fractionation occurring at each of the reaction steps may be reflected in $^{15}\varepsilon_N$. Either way, despite the lack of detailed biochemical mechanisms for interpreting the inferred $^{15}\varepsilon_N$, our results suggest that $\delta^{15}N$ of NO produced from nitrification under aerobic conditions is likely significantly lower than that from denitrification and abiotic reactions and thus justify its use as a quantitative tracer of soil NO dynamics.

4.4 CONCLUSION

Here we have shown that complex N transformations drive soil NO production under aerobic and anaerobic conditions. Based on the $\Delta^{17}O$-NO_3^- measurements and modeling, we demonstrate for the first time that enzymatic NO_2^- and NO_3^- interconversion can occur in soils under anaerobic conditions. Due to this reversibility, oxygen atoms from H_2O can be incorporated into soil NO_3^-,

complicating the use of dual NO_3^- isotopes in tracing denitrification in redox-dynamic environment. The expression of the equilibrium N isotope effect during the NO_3^- and NO_2^- interconversion can have large effects on the distribution of N isotopes in soil NO_3^- and NO_2^- pools and lead to enlarged isotopic offsets between NO_3^- and denitrification gas products. Comparing NO production under different conditions, we found that denitrification and abiotic reactions have a higher potential for NO production than nitrification. Therefore, their role in driving NO emission under field conditions clearly deserve further investigation. Finally, results from the comprehensive δ^{15}N-NO measurements suggest that NO produced from nitrification and denitrification are distinguishable by δ^{15}N-NO due to a large isotope effect associated with NO production from nitrification under aerobic conditions. We conclude that the coupled δ^{15}N-NO and Δ^{17}O-NO_3^- measurement offers a new perspective on the sources and dynamics of NO production in soils. Future efforts should be dedicated to applying this technique at the field scale to better improve our knowledge of NO emission in agricultural soils.

5.0 FAST NITRATE CYCLING IN SOILS OF NITROGEN-ENRICHED ECOSYSTEMS REVEALED BY STABLE NITRATE ISOTOPES

5.1 INTRODUCTION

Human activity dominates the creation of reactive nitrogen (N) globally and has substantially altered the biogeochemical N cycle (Canfield et al., 2010). Alongside, total atmospheric emissions of nitrogen oxides (NO_x) and ammonia (NH_3) have significantly increased since the pre-industrial era (Galloway et al., 2008), and have resulted in a dramatic increase in atmospheric deposition of reactive N at the global scale (25-40 Tg $N \cdot yr^{-1}$) (Denman et al., 2007). Because most terrestrial and aquatic ecosystems are naturally N-limited, a wide range of ecosystem responses to the elevated N deposition has been recorded. On the one hand, N input via atmospheric deposition may be beneficial, in that it stimulates ecosystem productivity and thus enhances carbon (C) uptake (MacDonald et al., 2011). In particular, effects of N deposition on growth and C sequestration are related to three main mechanisms: accelerated photosynthesis, increased C allocation to plant woody biomass, and slower decomposition rates which leads to accumulation of surface litter and soil organic matter (Janssens et al., 2010; Fleischer et al., 2013). Although the actual size of this so-called "nitrogen's carbon bonus" is uncertain (Nadelhoffer et al., 1999; Magnani et al., 2007; Janssens & Luyssaert, 2009), atmospheric N deposition is considered a primary driver of the "missing" terrestrial C sink of ~2.4 Pg $C \cdot yr^{-1}$ (Le Quéré et al., 2012). On the other hand, chronic N deposition at elevated levels can have detrimental effects to terrestrial and aquatic ecosystems, including increased nitrification rates (Ferretti et al., 2014), decreased soil fertility (Adams et al., 2007), and increased nitrate (NO_3^-) leaching from soils leading to soil acidification and surface

water eutrophication (Fernandez et al. 2010). Because N is not the primary limiting factor under excess N availability, growth stimulation by N deposition may not be supported by other nutrients, and thus may in turn result in ecosystem decline and accelerated N leaching loss (Durka et al., 1994).

To characterize the variable consequences of elevated N deposition to terrestrial ecosystems, the hypothesis of "nitrogen saturation" was first proposed by Aber and colleagues (Aber et al., 1989; Stoddard, 1994; Aber et al., 1998), and has been variously defined as an ecosystem where the inorganic N input is in excess of total combined plant and microbial N demand. In this hypothetical model, the ecosystem is viewed as progressing through a series of stages of N status, from strong N limitation (stage 0) to increased N sufficiency (stage 1) to initial symptoms of N saturation such as elevated N leaching (stage 2) and ultimately to N saturation-induced ecosystem decline (stage 3) (Aber et al., 1998; Rose et al., 2015a). Parallel to the progression of this continual sequence is a shifting N allocation along the plant-litter-soil continuum: enhanced N deposition is taken up by N-limited plants, which enriches N content of plant tissues and litter, the litter N is transferred to soil organic matter, stimulating N mineralization and nitrification, and eventually results in elevated N loss from the ecosystem via NO_3^- leaching and denitrification (i.e., conversion of NO_3^- to N gases) (Lovett and Goodale, 2011).

While the nitrogen saturation hypothesis provides a conceptual reconciliation of the diverse ecosystem responses to elevated N deposition, not all experimental observations have supported this hypothesis. For example, in studies of temperate forests where N was experimentally amended to the forest floor, NO_3^- leaching and gaseous loss were often the first to respond to the treatment, rather than the last as suggested by the nitrogen saturation hypothesis (Aber et al., 2003). Moreover, in cross-site manipulation studies, the major sink for added N in forest ecosystems was

found in soil, rather than plant biomass (Pardo et al., 2006). This contrasts with the plant-litter-soil pathway and highlights the emerging paradigm that soil processes may largely regulate N availability to plants under different N-availability regimes (Schimel and Bennett, 2004), and thus control how deposition-induced N saturation is manifested in terrestrial ecosystems.

Based on these recent observations, Lovett and Goodale (2011) presented a new conceptual model of forest N saturation processes that focuses on the mass balance of N rather than the temporal dynamics of N saturation indicators. The mass balance is characterized by inputs of N from atmospheric deposition, internal sinks in the plants and soils, and outputs to leaching and gaseous loss (Lovett and Goodale, 2011). The key features of the conceptual model are that added N can flow simultaneously to all sinks and losses in the system, depending on the respective strength of the sinks and the factors that control them (Lovett and Goodale, 2011). The authors further distinguished "capacity N saturation" where the N sinks in the plants and soils are restricted by their N demand, from "kinetic N saturation" where the sinks are effective but lower than the N input rate (Lovett and Goodale, 2011). Therefore, N losses from the ecosystem can occur simultaneously with N retention when the rate of N addition exceeds the rate at which N can be incorporated into the plant and soil sinks (i.e., kinetic saturation), even if the capacity of those sinks is not saturated.

However, although this new conceptual model is broadly applicable to many terrestrial ecosystems receiving N deposition, it remains difficult to quantify the proposed N sinks and loss processes on the long timescales required to evaluate the status of ecosystem N saturation (Rose et al., 2015a). Previous studies have applied N and oxygen (O) isotopes of NO_3^- at natural abundances (notated as $\delta^{15}N$ and $\delta^{18}O$, respectively; $\delta=(((R_{sample}/R_{standard})-1)\times1000)$ and $R=^{15}N/^{14}N$ or $^{18}O/^{16}O$) to assess watershed-scale processing of atmospheric NO_3^- as an indicator of ecosystem

N saturation status (Rose et al., 2015b). Particularly, the $\delta^{18}O$ signatures of microbial (e.g., -10 to 15‰) and atmospheric (e.g., 45 to 100‰) NO_3^- are significantly different (Kendall et al., 2007), making $\delta^{18}O$ a valuable tool for distinguishing between atmospheric and microbial sources contributing to NO_3^- leaching. On the other hand, although significant overlap exists between the ranges of $\delta^{15}N$ values for microbial and atmospheric NO_3^- (Kendall et al., 2007), $\delta^{15}N$ has been used to elucidate the biological NO_3^- cycling in soils, given that the main biological processes (i.e., nitrification, denitrification, and microbial and plant uptake) have distinct isotope effects on $\delta^{15}N$ (Mariotti et al., 1981; Denk et al., 2017). While dual NO_3^- isotopes clearly represent a powerful and minimally invasive tool to infer patterns and controls on N dynamics at various spatiotemporal scales, two uncertainties remain with regard to the interpretation of natural abundance NO_3^- isotope measurements in the context of ecosystem N saturation. First, source apportionment using the dual NO_3^- isotopes is often compromised by uncertainties in relevant isotope effects and isotopic end-members. In previous studies, a wide range of $\delta^{18}O$ end-members of nitrification has been variously estimated using baseflow, soil water, or groundwater $\delta^{18}O$-NO_3^- values, or from an expected value based on assumed or measured $\delta^{18}O$ of soil H_2O and O_2 (Kendall et al., 2007; Rose et al., 2015b), making $\delta^{18}O$-based source apportionment more challenging. Moreover, recent work has revealed kinetic and equilibrium isotope effects associated with enzymatic incorporation of each of the three O atoms from H_2O and O_2 into the product NO_3^-, which have traditionally not been considered in defining the $\delta^{18}O$ of nitrified NO_3^- (Casciotti et al., 2010; Buchwald and Casciotti, 2010). Similarly, although both $\delta^{15}N$ and $\delta^{18}O$ of soil NO_3^- may reflect isotopic imprints of denitrification due to the large isotope effect for denitrification as compared to other NO_3^- consumptive pathways, the isotopic signal of denitrification is often noisy and can be obscured by co-occurring NO_3^- production in natural soil environment (Granger and Wankel, 2016). The

second uncertainty in applying the dual NO_3^- isotopes to examine ecosystem N dynamics concerns the scale-dependent nature of dual NO_3^- isotope measurements (Hall et al., 2016). While NO_3^- concentration and isotopes have been intensively measured in watershed outlets to quantify overall N saturation degree at the ecosystem scale, there is mounting evidence that stream export of unprocessed atmospheric NO_3^- is co-regulated by hydrological drivers such that increased contribution of atmospheric NO_3^- was found during high-flow events, complicating quantification of the strength of N sinks in the plant-soil system using dual NO_3^- isotopes (Rose et al., 2015b).

In this study, we conducted field measurements of soil NO_3^- concentration and dual isotopes to quantify soil N cycling rates at three study sites along an ecosystem N availability gradient. Different from most previous studies, soil NO_3^- leaching flux was quantified by combining soil lysimeter sampling with a soil water model to circumvent the potential complication from the hydrological factors. Moreover, the $\delta^{15}N$ and $\delta^{18}O$ end-members of soil nitrification quantified using the NO_3^- ^{17}O anomaly ($\Delta^{17}O$) during laboratory incubations (presented in Chapter 3) were used in a NO_3^- isotopic mass balance model to characterize the N saturation status at the three study sites and to provide insights into how dual NO_3^- isotopes might best be used to inform N cycling at the watershed scale.

5.2 MATERIALS AND METHODS

5.2.1 Study area and soil characteristics

Field measurements were conducted at three sites in and around Pittsburgh, Pennsylvania, USA: a poorly drained, grassy, upland meadow in a forest clearing (hereafter, meadow site), an urban

upland hardwood forest experiencing partial cutting (forest site), and a restored urban riparian floodplain with herbaceous vegetation (riparian site). Both forest and riparian sites are within the Nine Mile Run (NMR) watershed, Pittsburgh. The NMR basin drains a highly dissected portion of the unglaciated Appalachian Plateau Physiographic Province, with the underlying geology consisting of cyclic sequences of Pennsylvanian age limestone, siltstone, shale, and sandstone (Bain et al., 2014; Rossi et al., 2017). Vegetation at the upland forest site is characterized by red oak (*Quercus rubra*), Norway maple (*Acer platanoides*), and black cherry (*Prunus serotina*) (Pittsburgh Parks Conservancy). Soils at the forest site are Ultisols (Gilpin-Upshur complex), consisting of a topmost layer of moderately decomposed plant material (~1 cm) followed by channery silt loam and channery loam down to ~75 cm depth (Soil Survey Staff, Natural Resources Conservation Service, United States Department of Agriculture, 2017). The riparian site was located about 10 m from the streambank of the upper NMR channel and about 2.5 m above the channel bottom. The site was bracketed by an interstate (I-376) and several combined sewer overflows (CSO) and thus presumably received elevated N input from anthropogenic sources. The riparian area was subject to a stream restoration project in early 2000s, in which large amount of overbank sediments were removed to reconnect floodplain with the stream channel (Bain et al., 2014). Soils at the riparian site are Entisols with silt loams down to ~80 cm depth overlying stratified gravelly sand (Soil Survey Staff, Natural Resources Conservation Service, United States Department of Agriculture, 2017). The meadow site was located within the upland Laurel Hill region of southwestern Pennsylvania. Laurel Hill is an anticlinal mountain that is part of the Allegheny Mountain System within the larger Appalachian Plateau Province (Shappe et al., 1984). Geology underlying this area consists of Allegheny Group sandstones, shales, and coal (Shappe et al., 1984). Elevation of this site is about 600 m. While the Laurel Hill region lies within the mixed

mesophytic forest region of Pennsylvania, characterized by beech-maple and northern hardwood forest types (Pennsylvania Department of Conservation and Natural Resources), the sampling site was created from a forest clear cut and dominated by grassy vegetation. Soils at the meadow site are Ultisols (Hazleton-Clymer complex), consisting of silt clay loams, channery silt loams, and cobbly clay loams to a depth of ~160 cm (Soil Survey Staff, Natural Resources Conservation Service, United States Department of Agriculture, 2017).

Surface soils (0 - 7 cm) at each site were collected to characterize soil chemical and biological properties (see Table 3.1 of Chapter 3 for more details). In brief, soil pH ranged from 5.0 to 5.6 for the three sites. The forest soil was highly humified and had the highest total and organic C content and N content, followed by the riparian and meadow soils. C:N ratio was 14.7, 17.3, and 19.6 for the meadow, forest, and riparian soils, respectively. $\delta^{15}N$ of total N ranged from 2.2‰ to 3.9‰ for the three soils. Nitrification potential was significantly higher in the forest (21.5 μg $N \cdot g^{-1} \cdot d^{-1}$) and riparian (14.7 μg $N \cdot g^{-1} \cdot d^{-1}$) soils than in the meadow (2.6 μg $N \cdot g^{-1} \cdot d^{-1}$) soil. Denitrification potential was 3.6, 8.5, and 9.7 μg $N \cdot g^{-1} \cdot d^{-1}$ for the meadow, forest, and riparian soils, respectively.

5.2.2 Field experiment setup

At each site, a 5 by 5 m plot was set up for field measurements and sampling. Within each plot, three porous cup suction lysimeters (Soil Moisture Corp., USA) were installed (1 m apart) at 30 cm depth to sample soil water below the main rooting zone. Prior to installation, the suction cup lysimeters were soaked for 24 h in 1 N HCl and rinsed three times with deionized Milli-Q water to clean potential adsorption sites in the ceramic cups (Rossi et al., 2017). At the center of each plot, soil moisture measured as volumetric water content was monitored at depths of roughly 5,

15, and 25 cm (Onset S-SMC-M005 Soil Moisture Sensor), and soil temperature was measured at 5 cm depth (Onset S-TMB-M017 Temperature Sensor). Soil temperature and moisture measurements were taken once every 10 minutes throughout the study period. A fence post hosting three ion exchange resin columns was set up adjacent to each plot for measurement of atmospheric NO_3^- and ammonium (NH_4^+) deposition fluxes at monthly to bimonthly scale (operated by Rebecca Forgrave from the Elliott research group).

5.2.3 Sample collection and analysis

Nine surface soil samples were randomly collected within each plot monthly from September 2016 to August 2017 using a stainless-steel corer (5 cm inner diameter and 7 cm depth). Soil water was sampled on the same day by applying a vacuum of ~80 kPa relative to ambient pressure to the lysimeters. The soil samples were stored at 4 ℃ and immediately transported back to the laboratory where the nine soil samples were mixed to form three composite samples. The composite samples were then slightly air-dried and sieved through a 4 mm mesh for later analyses. The gravimetric soil water content was determined for each composite sample by drying a known weight of moist soil in an oven at 105 ℃ until a constant weight was obtained. The sieved soil samples were extracted with 2 M potassium chloride for determination of extractable NH_4^+. We followed Costa et al. (2011) to extract soil NO_3^- for chemical and isotopic analyses. In brief, 35 g (dry weight equivalent) of the sieved soil samples was combined with 70 mL deionized Milli-Q water and vortexed for 10 minutes at 3200 rpm. The slurry was then centrifuged for 10 minutes at 2000 rpm, and the resultant supernatant was filtered through a sterile 0.2 μm filter.

Nitrate and nitrite (NO_2^-) concentrations of the soil water samples and soil extracts were determined using a Dionex Ion Chromatograph ICS-2000 with a precision (1σ) of ±5.0 μg $N \cdot L^{-1}$

and ±2.5 μg $N \cdot L^{-1}$, respectively. Soil extractable NH_4^+ was determined on a fluorometer (Trilogy, Turner Designs, USA) using a modified fluorometric OPA method for soil KCl extracts (Kang et al., 2003; Taylor et al., 2007) with a precision of ±7.0 μg $N \cdot L^{-1}$. The $\delta^{15}N$ and $\delta^{18}O$ of NO_3^- in the soil water samples and soil extracts were measured using the denitrifier method (Sigman et al., 2001; Casciotti et al., 2002). In brief, denitrifying bacteria lacking the nitrous oxide (N_2O) reductase enzyme (*Pseudomonas aureofaciens*) are used to convert 10 to 20 nmol of NO_3^- into gaseous N_2O. Using He as a carrier gas, the N_2O is then purified in a series of chemical traps, cryofocused, and finally analyzed on a GV Instruments Isoprime continuous flow isotope ratio mass spectrometer at the *Regional Stable Isotope Laboratory for Earth and Environmental Science Research* at the University of Pittsburgh. International NO_3^- reference standards IAEA-N3, USGS34, and USGS35 were used to calibrate the $\delta^{15}N$ and $\delta^{18}O$ measurements. The long-term precision for the $\delta^{15}N$ and $\delta^{18}O$ analyses are ±0.3‰ and ±0.5‰, respectively.

5.2.4 Nitrate leaching flux

We used a simple soil water balance model developed by Oelmann et al. (2007) and Leimer et al. (2014) to estimate daily water leaching flux from 0-30 cm soil layer for each site. The model is based on the water balance equation:

$$P + UF = DF + ET_a - \Delta S \qquad \text{Equation (1)}$$

where P is precipitation (mm), UF is upward flux (mm), DF is downward flux (mm), ET_a is actual evapotranspiration (ET) (mm), and ΔS is the daily change in soil water storage calculated using depth-weighted volumetric soil water content measured at the three soil depths ($\Delta S = S_{t1} - S_{t2}$, where S_{t1} and S_{t2} denote two consecutive observations at midnight, $\Delta S<0$ denotes increase in soil water storage between t1 and t2). By definition, UF broadly represents a variety of eco-

hydrological processes (e.g., hydraulic lifting, capillary rise, and surface runoff) that contribute to increases in soil water storage other than precipitation. For the forest and riparian sites, daily precipitation data spanning the whole study period was obtained from a rain gauge located about 5 km from these two sites (Three Rivers Wet Weather Network). On-site precipitation at the meadow site was measured and reported by the National Atmospheric Deposition Program (site ID: NTN PA83). To derive soil water fluxes (i.e., *UF* and *DF*) using Equation (1), daily potential ET (PET) was estimated for the three sites using the FAO Penman-Monteith equation as following:

$$PET = \frac{0.408\Delta(R_n - G) + \gamma\frac{900}{T+273}u_2(e_s - e_a)}{\Delta + \gamma(1 + 0.34u_2)} \quad \text{Equation (2)}$$

where R_n is net radiation at soil surface ($MJ \cdot m^{-2} \cdot d^{-1}$), G is soil heat flux ($MJ \cdot m^{-2} \cdot d^{-1}$), T is mean air temperature (°C), u_2 is wind speed at 2 m height ($m \cdot s^{-1}$), e_s is saturation vapor pressure (kPa), e_a is actual vapor pressure (kPa), Δ is slope of saturation vapor pressure curve ($kPa \cdot °C^{-1}$), and γ is the psychrometric constant ($kPa \cdot °C^{-1}$). It is important to note that the calculated PET is representative to ET_a of a hypothetical well-watered grass that has a 0.12 m canopy height, a leaf area of 4.8, a bulk surface resistance of 70 $s \cdot m^{-1}$, and an albedo of 0.23 (Allen et al., 1994). Daily-aggregated T, u_2, e_s, and e_a values were obtained from meteorological stations of nearby airports for the three sites (Arnold Palmer Regional Airport for the meadow site and Allegheny County airport for the forest and riparian sites). Net radiation (R_n) measured on daily timescale was available for central Pennsylvania region through NOAA Global Monitoring Division (Station ID: PSU). According to Oelmann et al. (2007) and Leimer et al. (2014), daily *UF* and *DF* were estimated using a deterministic algorithm given in Equations (3) to (5):

$$\text{if } \Delta S + P < 0 \text{ then } ET_a = 0,\ DF = 0,\ UF = -(\Delta S + P) \quad \text{Equation (3)}$$

$$\text{if } \Delta S + P < 0 \text{ while } \Delta S + P \leq \text{PET then } ET_a = \Delta S + P,\ DF = 0,\ UF = 0 \quad \text{Equation (4)}$$

$$\text{if } \Delta S + P > \text{PET then } ET_a = \text{PET},\ DF = \Delta S + P - ET_a,\ UF = 0 \quad \text{Equation (5)}$$

To better match with changes in the soil water storage (i.e, ΔS), the precipitation data was adjusted to account for delayed water infiltration due to presence of a snow cover. Specifically, snowfall is assumed whenever precipitation occurs while air temperature <0 °C, contributing to a 1-dimensional snowpack on soil surface (Smith et al., 2011). The snowpack increases whenever more snowfall occurs; otherwise, there is no change in snowpack. The snowpack melts completely and thus releases water to underlying soil whenever the mean daily air temperature is above 0 °C (Zheng et al., 1993). We define the net daily water leaching flux to be the difference between *DF* and *UF*. Therefore, monthly NO_3^- leaching from 0 - 30 cm soil layer of each site was calculated by multiplication of monthly mean NO_3^- concentration in the lysimeter water samples and monthly sums of simulated water leaching flux. Annual NO_3^- leaching flux at each site was then estimated as the sum of the monthly estimates during the one-year study period.

5.2.5 Nitrate isotopic mass balance

Based on the measured soil NO_3^- pool and NO_3^- leaching flux, a NO_3^- isotopic mass balance model was used to provide insights into the rate of soil NO_3^- cycling and overall N saturation status on an annual basis for the three sites. The isotopic mass balance model conceptualizes the soil NO_3^- pool as an open, continuous flow-through system with competing plant-microbe-soil sinks (Houlton et al., 2006; Fang et al., 2015). On an annual basis, soil NO3- pool is assumed to be under steady state, that is, no net NO_3^- accumulation in the soil, so that mass and isotopes of input and output fluxes must be balanced (Fang et al., 2015) (Equations 6 to 8):

$$F_A + F_N = F_R + F_L \qquad \text{Equation (6)}$$

$$F_A \times \delta^{15}N_A + F_N \times \delta^{15}N_N = F_R \times (\delta^{15}N_S - {}^{15}\varepsilon_R) + F_L \times \delta^{15}N_L \qquad \text{Equation (7)}$$

$$F_A \times \delta^{18}O_A + F_N \times \delta^{18}O_N = F_R \times (\delta^{18}O_S - {}^{18}\varepsilon_R) + F_L \times \delta^{18}O_L \qquad \text{Equation (8)}$$

In Equations 6 to 8, subscripts A, N, R, and L denote atmospheric NO_3^- deposition, gross soil nitrification, gross NO_3^- retention, and soil NO_3^- leaching, respectively; F, $\delta^{15}N$, and $\delta^{18}O$ denote annual flux and N and O isotopic end-members of the respective processes; $\delta^{15}N_S$ and $\delta^{18}O_S$ are the measured annual mean values of surface soil $\delta^{15}N\text{-}NO_3^-$ and $\delta^{18}O\text{-}NO_3^-$, respectively. Importantly, F_R is equal to gross NO_3^- uptake by plant and soil microbes plus denitrification. We did not attempt to partition these two processes in the model due to the high uncertainties in the isotope effects associated with the respective pathways (Denk et al., 2017). Instead, overall N and O isotope effects ($^{15}\varepsilon_R$ and $^{18}\varepsilon_R$) were estimated for the gross NO_3^- retention, which reflect the relative importance of denitrification (Chapter 3). Moreover, given the findings from culture studies that both assimilatory and dissimilatory NO_3^- reduction impart coupled enrichment of $\delta^{15}N\text{-}NO_3^-$ and $\delta^{18}O\text{-}NO_3^-$ (Granger et al., 2008; Granger et al., 2010), it is further assumed that $^{15}\varepsilon_R = {}^{18}\varepsilon_R$. Therefore, F_N and F_R can be uniquely solved in tandem with $^{15}\varepsilon_R$ and $^{18}\varepsilon_R$ using the field-measured fluxes and isotopes of NO_3^- deposition and leaching (annual flux and isotopic compositions of NO_3^- deposition was provided by Rebecca Forgrave) and the laboratory-characterized $\delta^{15}N_N$ and $\delta^{18}O_N$ (Chapter 3) (Table 1). A sensitivity analysis was conducted by changing each of the model input parameters within a respective range constrained by annual mean ± 1 standard deviation (σ) to assess uncertainty in the model estimates.

Table 5.1 Annual mean value (±SD) of atmospheric NO_3^- deposition flux and isotopic end-members used in the NO_3^- isotopic mass balance calculation.

	NO_3^- deposition flux ($kg\ N \cdot ha^{-1} \cdot yr^{-1}$)	$\delta^{15}N_A$ (‰)	$\delta^{18}O_A$ (‰)	$\delta^{15}N_N$ (‰)	$\delta^{18}O_N$ (‰)
meadow site	2.9±1.7	0.0±2.0	56.1±12.7	-16.7±2.4	-4.4±2.1
forest site	2.9±1.3	0.7±2.9	55.9±10.2	2.3±2.1	-0.9±2.1
riparian site	8.0±4.0	-1.9±1.7	48.9±4.7	2.4±2.2	-1.2±2.2

5.2.6 Statistical analysis

Linear regressions and Pearson's correlation coefficient were used to detect relationships among independent variables. Due to unequal variance revealed by Levene's test (e.g., NO_3^- concentrations measured at the meadow site were significantly lower than those measured at the forest and riparian sites), a nonparametric Kruskal Wallis ANOVA test for pairwise comparison was used to determine significant differences among NO_3^- concentrations and isotopic compositions measured at the three sites. All statistical tests were performed using MATLAB (Mathworks, Natick, MA, USA).

5.3 RESULTS

5.3.1 Meteorological data and potential evapotranspiration

Annual precipitation was 1361 mm for the forest and riparian sites and 1429 mm for the meadow site for the study year. For all three sites, precipitation was relatively evenly distributed throughout the study year, with peak precipitation occurring in late spring through summer as thunderstorms (April to August) (Figure 5.1a). Precipitation was dominantly rain, with less than 10% of annual precipitation falling as snow at the three sites. Soil temperature at 5 cm depth closely tracked air temperature but never fell below 0 °C, indicating that soil was not frozen during winter (Figure 5.1b). Net radiation had clear seasonal variation, with higher net radiation during warmer months (Figures 5.1b and 5.1c). The modeled annual potential ET was 910 mm for the forest and riparian sites and 772 mm for the meadow site (Figure 5.1d). The ratio of potential ET to precipitation was

0.67 for the forest and riparian sites and 0.53 for the meadow site, indicating that ET was limited by energy at all three sites.

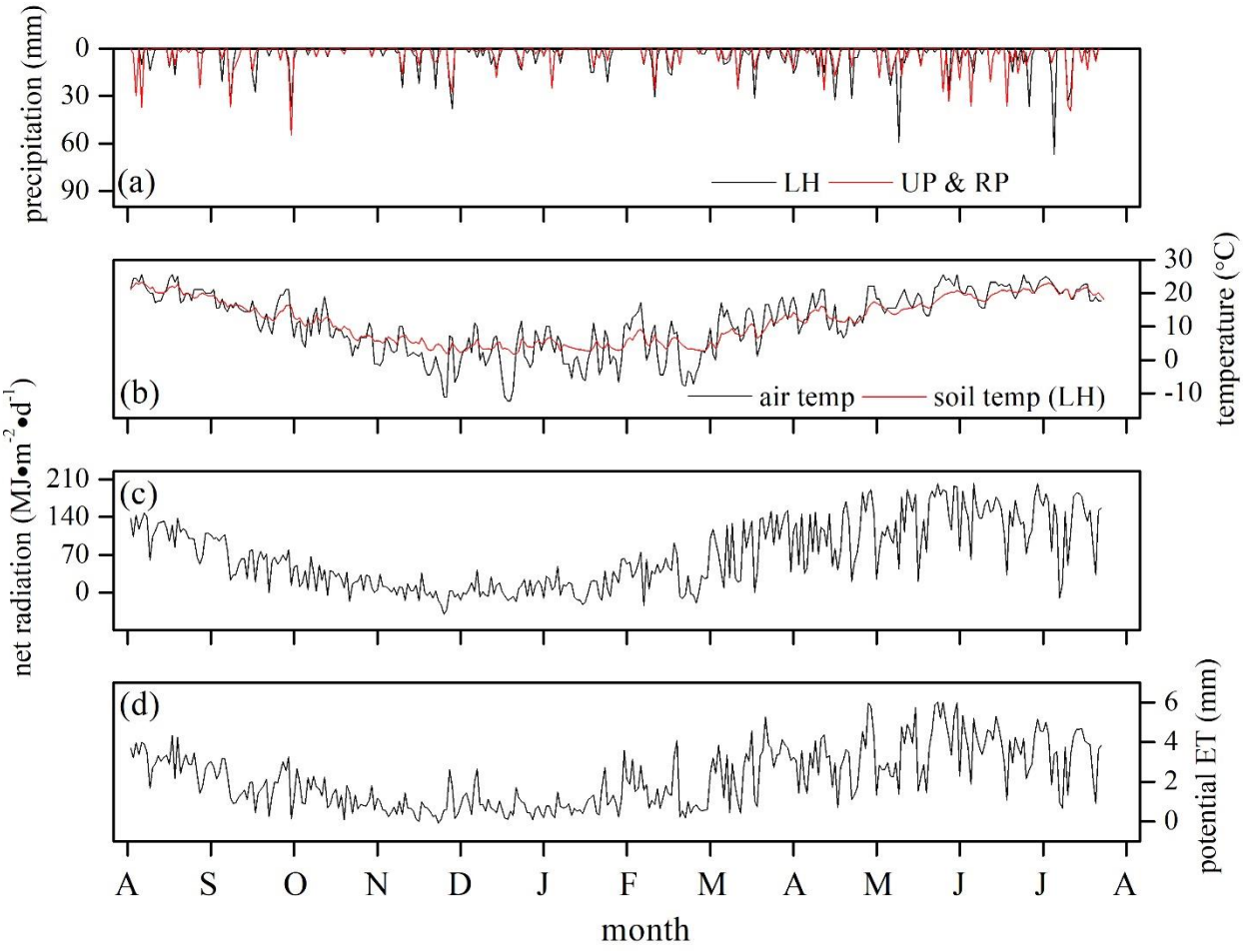

Figure 5.1 Temporal variations in precipitation (a), air and soil temperature (b), net radiation (c), and modeled potential evapotranspiration (d) during the study year. For graphical clarity, soil temperature and potential ET were only shown for the meadow site.

5.3.2 Soil water dynamics

Soil water content measured at the three depths varied between 0.1 $cm^3 \cdot cm^{-3}$ and 0.4 $cm^3 \cdot cm^{-3}$ for the forest site and between 0.2 $cm^3 \cdot cm^{-3}$ and 0.5 $cm^3 \cdot cm^{-3}$ for the meadow and riparian sites (Figure

5.2). For all three sites, soil water content measured at 5 cm depth exhibited more variability than that measured at deeper layers (Figure 5.2). Larger fluctuations in soil water content at all three depths occurred during warmer months, while short-term soil saturation, as indicated by broad plateaus in the time series of soil water content, was observed periodically at the meadow and riparian sites during wintertime likely due to winter precipitation and reduced ET (Figure 5.2). Water storage in the 0 - 30 cm soil horizon was highly responsive to precipitation at the three sites, as highlighted by the significant relationships between daily precipitation and the modeled daily change in soil water storage (Figure 5.3). The modeled upward flux was significantly lower than the downward water flux, accounting for 9%, 8%, and 5% of the downward flux on an annual basis for the meadow, forest, and riparian sites, respectively (Figure 5.4). Monthly net water leaching from the 0-30 cm soil layer exhibited large variability, ranging from 5.4 to 140.7 mm, 8.7 to 88.5 mm, and 9.1 to 91.5 mm for the meadow, forest, and riparian sites, respectively (Figure 5.5a). The inter-month variability could be largely explained by precipitation (Figure 5.5b). Annual net water leaching amounted to 722 mm, 594 mm, and 693 mm for the meadow, forest, and riparian sites, respectively.

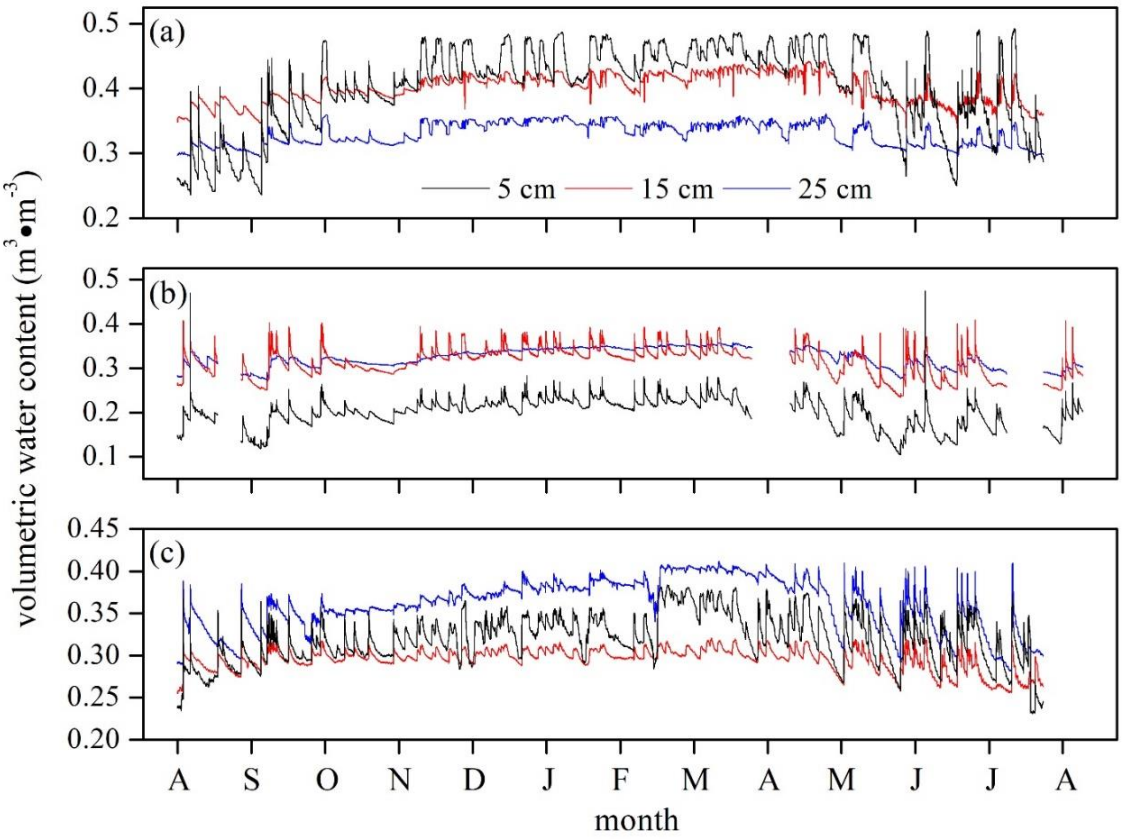

Figure 5.2 Temporal variation in soil water content for the meadow (a), forest (b), and riparian (c) sites. Depths of soil water content data is below ground surface. Data gap in soil water content for the forest site was due to equipment power outage.

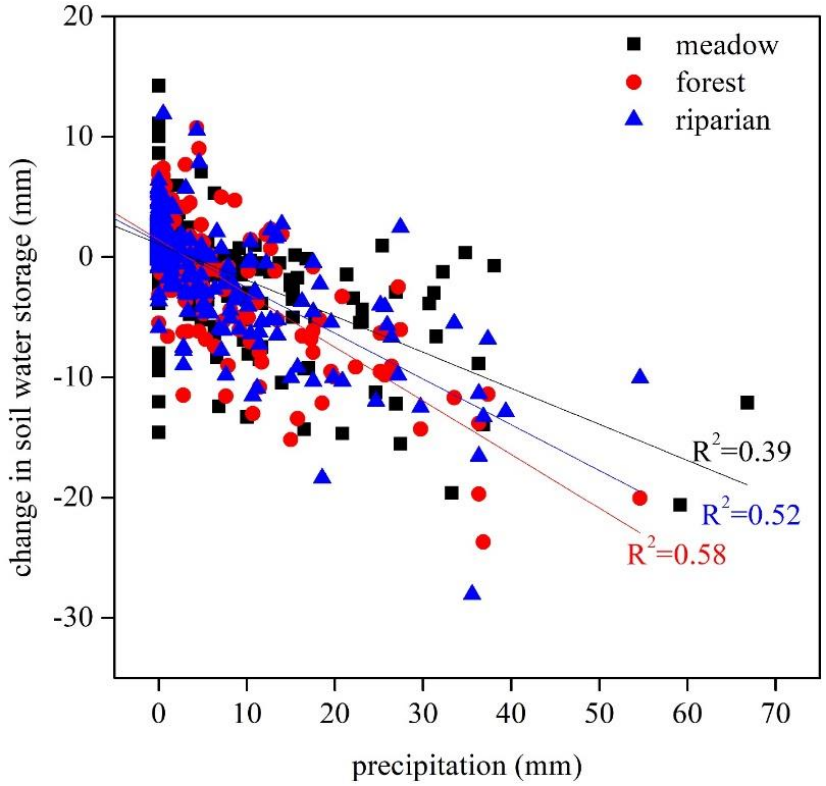

Figure 5.3 Relationship between daily precipitation and change in soil water storage in 0-30 cm soil horizon for the three sites. Negative values indicate increase in soil water storage.

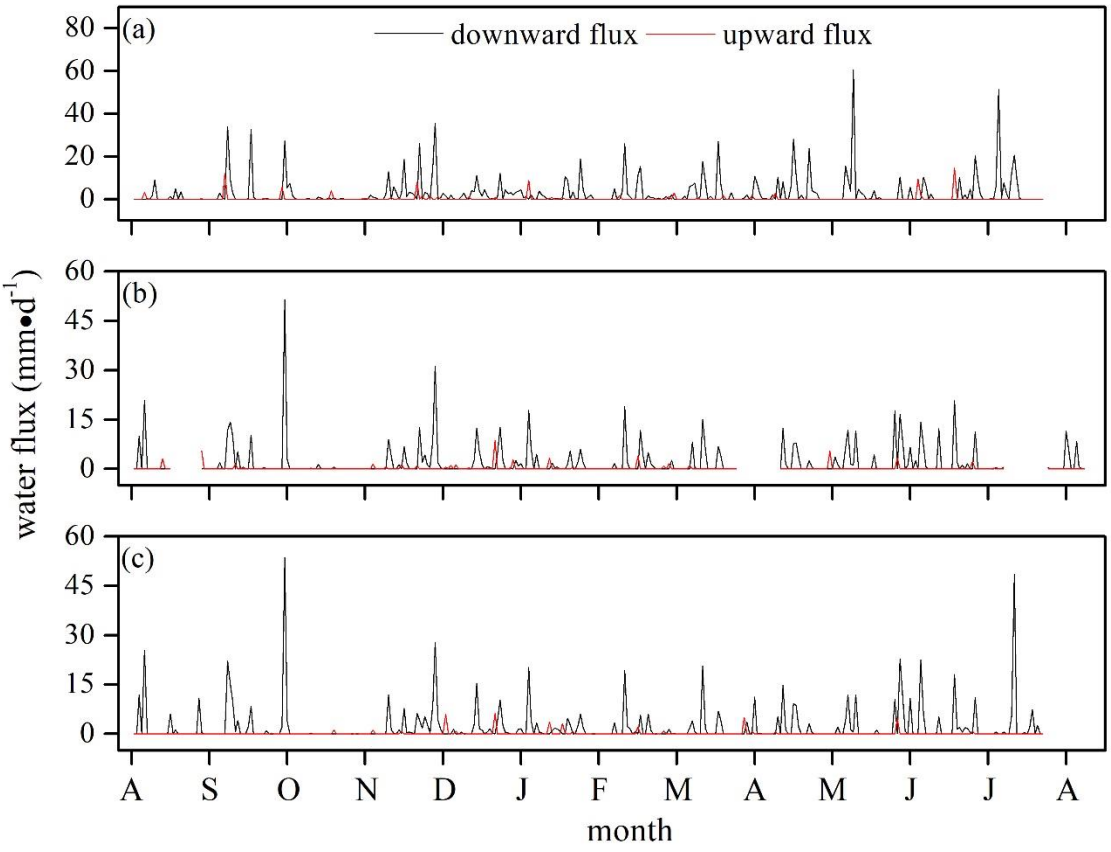

Figure 5.4 Temporal variation in the modeled upward flux and downward flux for the meadow (a), forest (b), and riparian (c) sites.

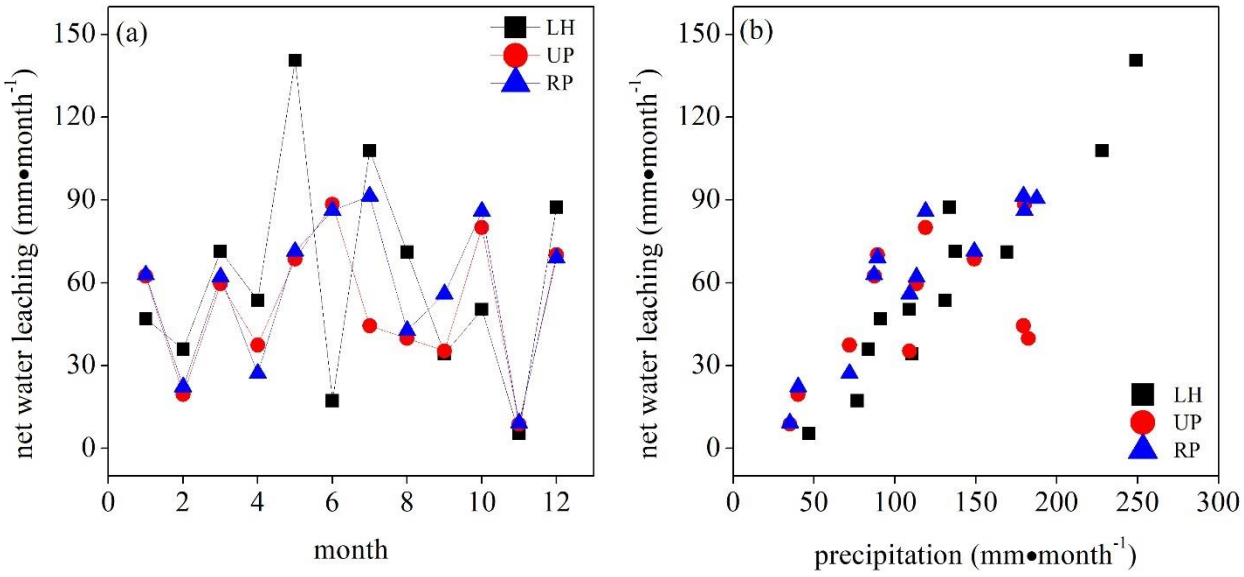

Figure 5.5 Monthly water leaching flux (a) and its relationship with monthly precipitation (b) for the three sites. Data gap in soil water content for the forest site was filled using linear extrapolation of water content data measured in the same month for calculation of the net monthly leaching flux.

5.3.3 Ammonium and nitrate concentrations and isotopes

On an annual basis, soil NH_4^+ concentrations were significantly higher in the meadow soil (16.1±3.7 μg $N \cdot g^{-1}$) than in the forest (2.2±0.7 μg $N \cdot g^{-1}$) and riparian (4.7±2.3 μg $N \cdot g^{-1}$) soils, while NO_3^- concentrations were significantly lower in the meadow soil (1.0±0.5 μg $N \cdot g^{-1}$) than in the other two soils (10.2±3.2 and 7.1±3.7 μg $N \cdot g^{-1}$, respectively) (Fig. 5.6a and 5.6b). Similar to surface soil NO_3^- concentrations, NO_3^- concentrations in lysimeter water were significantly lower at the meadow site (0.3±0.2 mg $N \cdot L^{-1}$) than at the forest (1.0±0.5 mg $N \cdot L^{-1}$) and riparian (2.9±1.9 mg $N \cdot L^{-1}$) sites. NO_3^- concentrations in surface soil and soil solution at 30 cm depth had larger temporal variations in the forest and riparian sites than in the meadow site (Figure 5.6b and 6.5c). In particular, high NO_3^- concentrations up to 7 mg $N \cdot L^{-1}$ were observed in soil solution at the riparian site. However, none of the measured concentrations exhibited clear seasonal patterns at either site when soil temperature was used as a proxy of seasonality.

$\delta^{15}N$ of NO_3^- in surface soils varied within a relatively narrow range from -0.3±3.3‰ to 2.3±3.0‰ for the three sites on an annual basis (Figure 5.6d), whereas $\delta^{15}N$ of NO_3^- in soil solution collected at 30 cm depth was significantly lower in the meadow soil (-2.6±1.9‰) than in the forest (3.4±1.9‰) and riparian (3.0±1.4‰) soils (Fig. 5.6f). Notably, significantly higher $\delta^{18}O$ values were recorded in surface soil at the meadow site (14.6±4.4‰) (Figure 5.5f), while no significant difference in $\delta^{18}O$ was detected in soil solution among the three sites (Figure 5.5g). Comparing the

measured $\delta^{15}N$ and $\delta^{18}O$ values to the isotopic end-members of nitrification and atmospheric deposition in dual isotope space, NO_3^- in surface soil and soil solution were closely associated with nitrification at the forest and riparian sites (Figure 5.7). Both $\delta^{15}N$ and $\delta^{18}O$ of NO_3^- in surface soil were elevated relative to the isotopic end-members of nitrification at the meadow site, so that the measured $\delta^{15}N$ and $\delta^{18}O$ values generally fell onto a 1:1 line intersecting the nitrification end-members in the dual isotope space (Figure 5.7a). Although the measured $\delta^{18}O$ of NO_3^- in soil solution was not very different from the $\delta^{18}O$ end-member of nitrification, $\delta^{15}N$ was significantly higher than the $\delta^{15}N$ end-member of nitrification at the meadow site (Figure 5.7b).

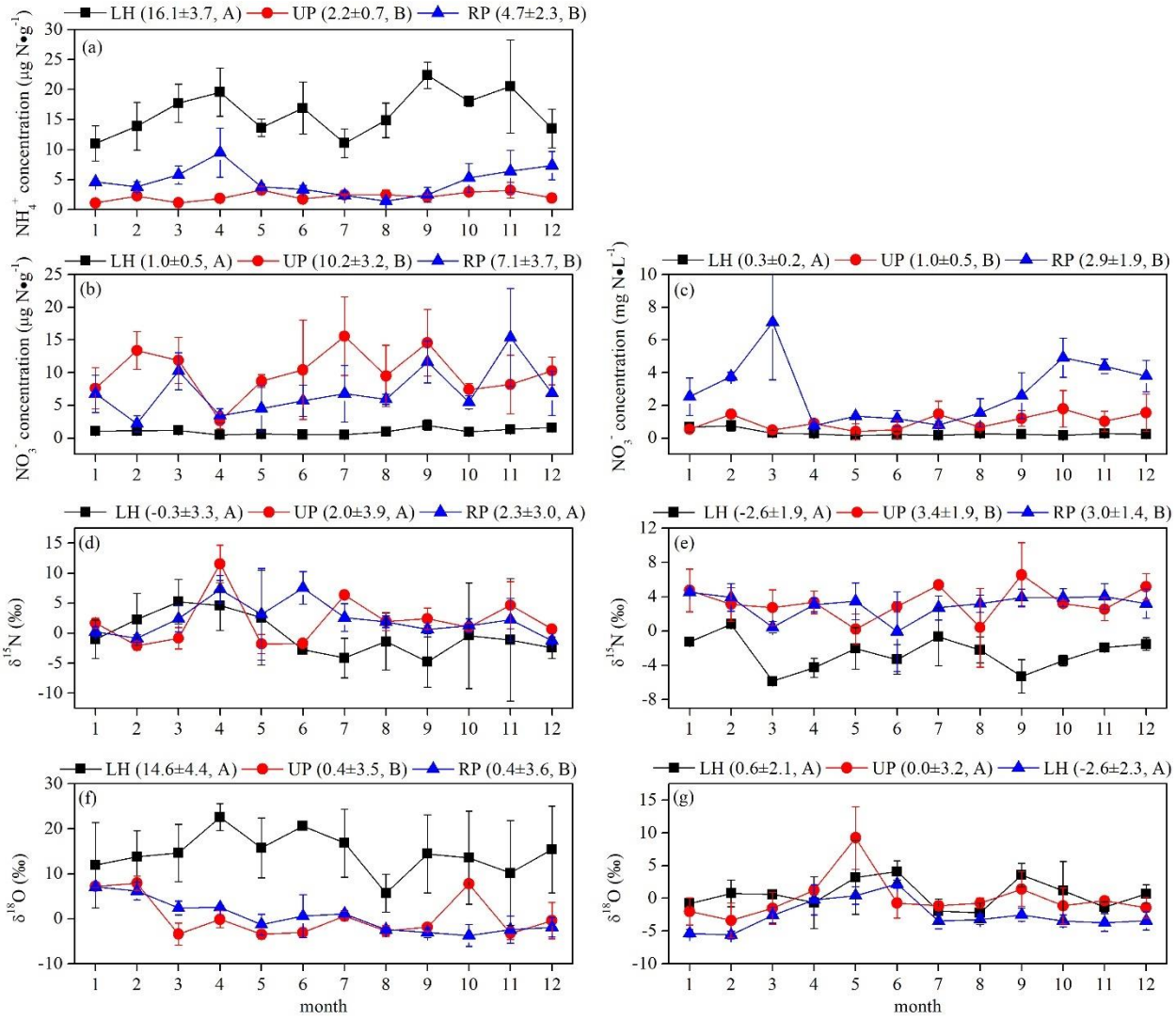

Figure 5.6 Ammonium and nitrate concentrations and nitrate isotopes of monthly collected surface soil and lysimeter samples from the three sites. Annual mean values for each site are shown above each panel. Statistically significant difference in mean values among the three sites is indicated by letters. "LH", "UP", and "RP" denote the meadow, forest, and riparian sites, respectively.

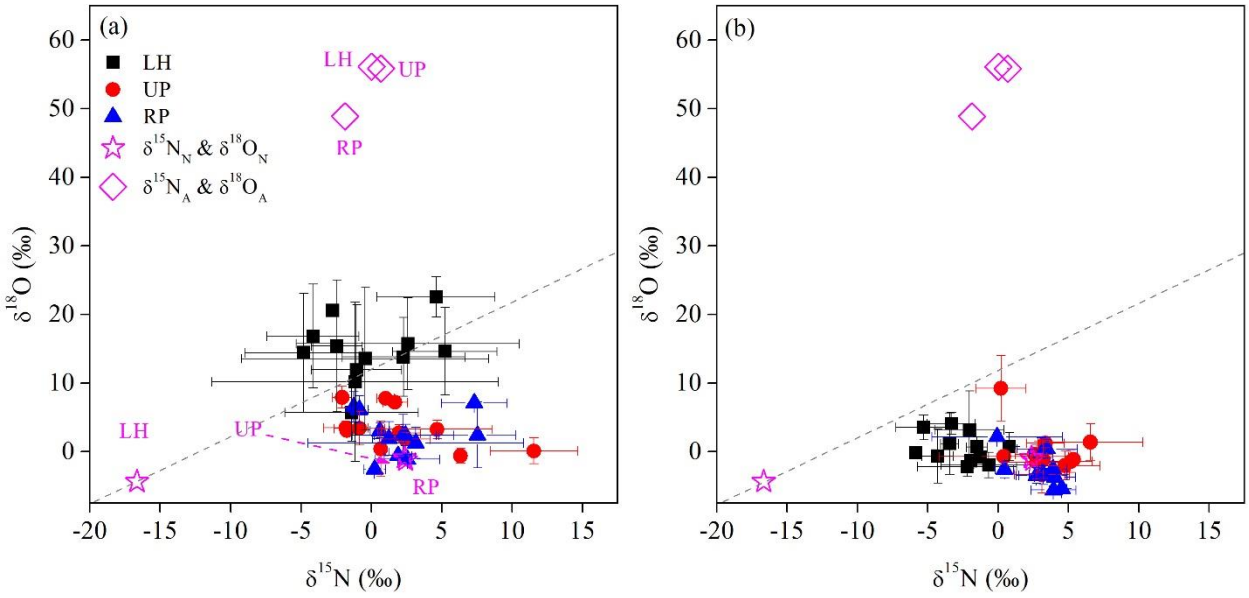

Figure 5.7 Dual isotope plot ($\delta^{15}N$ and $\delta^{18}O$) showing the measured $\delta^{15}N$ and $\delta^{18}O$ of NO_3^- in surface soil and soil solution at 30 cm depth and their relationships with the isotopic end-members of nitrification (star) and atmospheric deposition (diamond). The dashed line represents an illustrative trend of isotopic enrichment relative to the nitrification end-members of the meadow soil with a $\delta^{18}O$/ $\delta^{15}N$ slope of 1. "LH", "UP", and "RP" refer to the meadow, forest, and riparian sites, respectively.

5.3.4 Nitrate leaching flux

Monthly NO_3^- leaching deeper than 30 cm was co-regulated by NO_3^- concentrations in soil water leachate and the modeled water leaching flux, ranging from 0.003 to 0.04 g $N \cdot m^{-2} \cdot month^{-1}$, 0.01 to 0.14 g $N \cdot m^{-2} \cdot month^{-1}$, and 0.021 to 0.44 g $N \cdot m^{-2} \cdot month^{-1}$ for the meadow, forest, and riparian sites, respectively (Figure 5.8). Higher NO_3^- leaching flux was estimated in March and October at the riparian site as a result of high NO_3^- concentrations measured in these two months (Figure 5.7c). Annual NO_3^- leaching to >30 cm soil depth was highest in the riparian site (19.9±4.2 kg $N \cdot ha^{-1} \cdot yr^{-1}$) followed by the forest site (5.9±1.4 kg $N \cdot ha^{-1} \cdot yr^{-1}$) and the meadow site (2.2±0.3 kg $N \cdot ha^{-1} \cdot yr^{-1}$). The estimated annual NO_3^- leaching was similar to annual NO_3^- deposition flux at the meadow site but was significantly higher at the forest and riparian sites (Table 5.1).

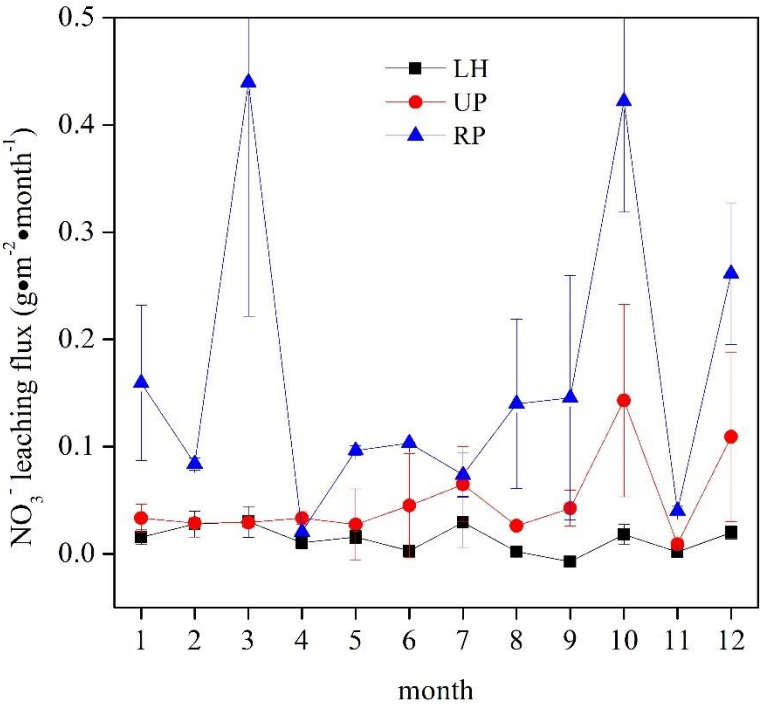

Figure 5.8 Estimated monthly NO_3^- leaching flux for the three study sites. "LH", "UP", and "RP" refer to the meadow, forest, and riparian sites, respectively.

5.3.5 Nitrate isotopic mass balance

Due to the high variability in the measured and modeled NO_3^- fluxes, annual mean $\delta^{15}N$ and $\delta^{18}O$ values, instead of flux-weighted mean values, of NO_3^- deposition and soil NO_3^- leaching were used in the NO_3^- isotopic mass balance calculation to prevent propagation of error resulting from the low sampling frequency (i.e., monthly). Based on the NO_3^- isotopic mass balance, gross nitrification and NO_3^- retention rates (57 to 270 kg $N \cdot ha^{-1} \cdot yr^{-1}$) were estimated to be one order of magnitude higher than NO_3^- leaching and deposition fluxes at all three sites (Figure 5.9). Gross nitrification and NO_3^- retention rates were highest at the riparian site followed by the forest site and the meadow site (Figure 5.9). The estimated nitrification and NO_3^- retention rates were only slightly sensitive to the flux and isotopic composition of soil NO_3^- leaching (<±25% variation), while moderate sensitivity of the rate estimates to NO_3^- deposition flux was detected (<±50% variation) (Figure 5.10). The estimated nitrification and NO_3^- retention rates were highly sensitive to the isotopic end-members of nitrification and the measured $\delta^{15}N$ and $\delta^{18}O$ of surface soil NO_3^-, with potential rate overestimation being up to 70% (Figure 5.10). Despite the potential for high uncertainty using this approach, the estimated gross nitrification and NO_3^- retention rates based on the NO_3^- isotopic mass balance calculation are well within the range derived from ^{15}N tracer studies in forest ecosystems worldwide (Table 5.2). $^{15}\varepsilon_R$ and $^{18}\varepsilon_R$ were estimated to be 16.1‰ for the meadow site, whereas $^{15}\varepsilon_R$ and $^{18}\varepsilon_R$ were not appreciably different from zero for the forest and riparian sites (Figure 5.9).

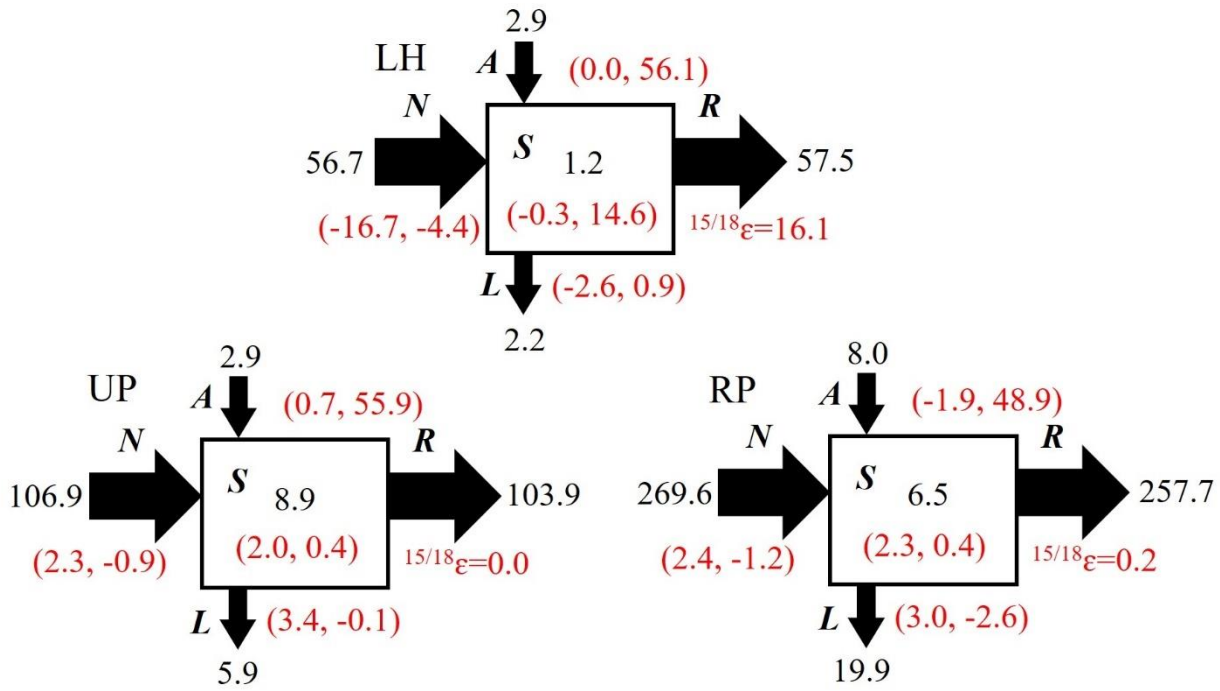

Figure 5.9 Nitrate isotopic mass balance for the three study sites. Letters "A", "L", "N", "R", and "S" denote atmospheric NO_3^- deposition, NO_3^- leaching, gross nitrification, gross NO_3^- retention, and soil NO_3^- pool, respectively. Numbers in black are measured or estimated annual flux in unit of kg N·ha^{-1}·yr^{-1} for the respective processes or soil NO_3^- pool. Isotopic compositions ($\delta^{15}N$ and $\delta^{18}O$) of NO_3^- are shown with red text in parenthesis for the respective processes or soil NO_3^- pool. $^{15}\varepsilon_R$ and $^{18}\varepsilon_R$ are also shown in red. "LH", "UP", and "RP" refer to the meadow, forest, and riparian sites, respectively.

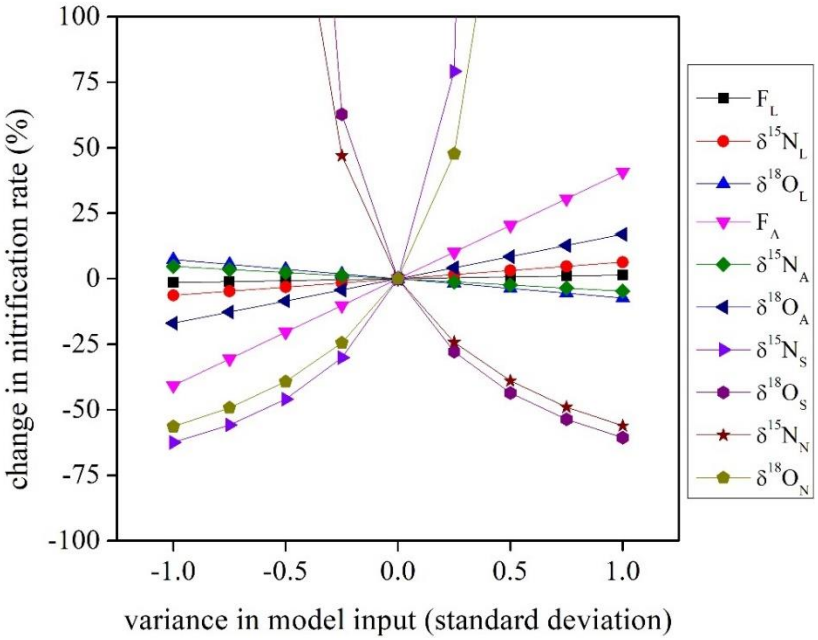

Figure 5.10 Variations in the estimated nitrification rate of the meadow site as a function of variations in model input parameters.

Table 5.2 Gross nitrification and nitrate retention rates in forest ecosystems.

Ecosystem	soil depth (cm)	Nitrification (kg N·ha^{-1}·yr^{-1})	Nitrate retention (kg N·ha^{-1}·yr^{-1})	Reference
annual grassland, California	9	266 - 1533	369 - 1599	Davidson et al. (1990)
conifer plantation and forest, California	7.5	73 - 398	113 - 891	Davidson et al. (1992)
coniferous forests geographically spanning New Mexico to Oregon	15	197 - 1409	493 - 1263	Stark and Hart (1997)
mixed hardwood and planatation pine forest, Massachusetts	15	450	456	Berntson and Aber (2000)
temeprate forest, Germany	7.5	212 - 756	310 - 555	Corre et al (2003)
temperate forests, Massachusetts	15	140 - 596		Venterea et al. (2004)
volcanic rainforest, Chile	10	186	337	Huygens et al. (2008)

tropical montane forest, Puerto Rico	10	195 - 642	193 - 582.2	Templer et al. (2008)
temperate deciduous and coniferous forests, Belgium	10	118 - 242		Staelens et al. (2012)
N-enriched meadow, forest, and riparian ecosystems	7	57 - 270	58 - 258	This study

5.4 DISCUSSION

5.4.1 Soil nitrate leaching flux

The estimated soil NO_3^- leaching fluxes for the three study sites are the product of the modeled water leaching fluxes and the NO_3^- concentrations measured in the lysimeter samples. Using the soil water balance model, annual water leaching fluxes were estimated to be 722 mm, 594 mm, and 693 mm for the meadow, forest, and riparian sites, respectively (Figure 5.4), accounting for 51%, 44%, and 52% of precipitation at the three sites. Together with the low ratios of potential ET to precipitation (i.e., 0.53 to 0.67), the estimated high water leaching fluxes indicate that all three study sites could be characterized by a water-excess and energy-limited hydrological regime with high water leaching potential. The high water availability was further supported by the lack of clear seasonality of the modeled water leaching fluxes (Figure 5.5a) and the positive correlation between precipitation and the modeled water leaching fluxes (Figure 5.3; Figure 5.5b), indicating that precipitation was the primary driver of water dynamics in surface soil at all three sites (Figure 5.3). Notably, the modeled water leaching flux was lower at the forest site than at the riparian site (Figure 5.4), despite the similar meteorological conditions for those two sites. The lower water leaching flux at the forest site might be due to higher bulk density (and thus higher compaction)

of surface soil as indicated by the significantly lower volumetric soil water content measured at 5 cm depth, limiting deep water drainage (Smith et al., 2011).

It is important to note that the estimated water leaching fluxes based on the soil water balance model may be subject to error propagated from uncertainty in estimating the potential ET. For example, a ±10% measurement error for net radiation was not uncommon in previous studies (Wilson et al., 2002). Additionally, while the simplified Penman-Monteith equation offers a convenient way to empirically estimate potential ET, there is evidence that ecosystems dominated by vegetation types other than grass may have potential ET significantly different from that of grass ecosystems in a humid environment (Sun et al., 2010). Therefore, the adopted hydrological modeling approach that sets an ET limit using potential ET estimated based on the FAO Penman Monteith equation may cause large estimation errors, especially for modeling ET for the forest and riparian sites. We recognize that the current study may include some of the above errors, as well as errors associated with using off-site meteorological data as model input. More research is needed to develop more specialized versions of FAO Penman-Monteith models to account for the ecosystem complexity in contrast to annual crops or grasslands.

Regardless of the potential uncertainty in the modeled water leaching fluxes, the estimated annual NO_3^- leaching fluxes for the three study sites are well within the range reported for urban grasslands and forests where climatic and hydrological conditions were similar to our study sites (e.g., 1.4 to 24 kg $N \cdot ha^{-1} \cdot yr^{-1}$, Baltimore long-term ecological study sites Groffman et al. (2009)). Annual NO_3^- leaching loss was more than twice as high in the forest (5.9 kg $N \cdot ha^{-1} \cdot yr^{-1}$) and riparian (19.9 kg $N \cdot ha^{-1} \cdot yr^{-1}$) sites as the meadow site (2.2 kg $N \cdot ha^{-1} \cdot yr^{-1}$). However, even at the meadow site, hydrological NO_3^- loss via soil leaching was comparable to atmospheric NO_3^- input (2.9 kg $N \cdot ha^{-1} \cdot yr^{-1}$; Table 5.1). The revealed high N leaching relative to atmospheric NO_3^-

deposition at all three study sites might be largely due to ecosystem disturbances, including grass mowing (meadow site), tree cutting (forest site), and soil re-establishment (riparian site). Furthermore, the extremely high NO_3^- leaching at the riparian site might be partially sourced from leaking sanitary or combined sewers or from CSOs during high flow events. The extensive NO_3^- leaching at the riparian site might be particularly vulnerable for stream export due to tight hydrological connection between the riparian area and the surface NMR system. However, based on weekly stream water sampling, Divers et al. (2013) estimated that the annual export of dissolved inorganic N via NMR was 3.4 to 5.6 kg $N \cdot ha^{-1} \cdot yr^{-1}$. The low NO_3^- export relative to the estimated riparian NO_3^- leaching suggests a high N retention capacity of NMR, consistent with previous N budget studies in urban ecosystems (Groffman et al., 2003; Wollheim et al., 2005; Kaushal et al., 2011). One potential cause of the high N retention is that NO_3^- concentrations might be significantly reduced by denitrification and/or immobilization during downward transport towards deep groundwater. However, it is also possible that the NO_3^- export might be underestimated by the low sampling frequency that is not able to account for NO_3^- export during flashy high flow events (Divers et al., 2013). Therefore, our results together with observations from other urban ecosystems (e.g., Groffman et al., 2009) suggest that surface soils of disturbed urban ecosystems can be a significant source of NO_3^- to the environment. While the role of deep water reservoirs in regulating hydrological NO_3^- export clearly merits further exploration, long-term, high frequency measurement of stream water NO_3^- export is needed in future studies to better constrain N retention and its underlying mechanisms in urban ecosystems.

5.4.2 Fast soil nitrate cycling as a signal of ecosystem capacity nitrogen saturation

In N saturation studies, measurements of dual NO_3^- isotopes at natural abundances have been most often used to indicate the degree of N saturation and ecosystem openness (Pardo et al., 2006). The tracing power of the dual NO_3^- isotopes stems from the observations that atmospheric processes generate NO_3^- that is far more enriched in $\delta^{18}O$ than is the NO_3^- produced by microbial nitrification, allowing partitioning of the relative contributions of these two NO_3^- sources in soils and streams (Kendall et al., 2007). In this study, the measured $\delta^{18}O$ of NO_3^- in surface soils and soil leaching water was significantly lower when compared with that of atmospheric NO_3^- from the same site (Figure 5.6 and Table 5.1), suggesting that atmospheric NO_3^- was rapidly recycled and diluted by nitrified NO_3^- in surface soil. This is consistent with most previous measurements of $\delta^{18}O$-NO_3^- in forested watersheds that conclude that nitrification was the primary source of stream NO_3^- under baseflow conditions, even in watersheds with moderately high NO_3^- deposition and export (Pardo et al., 2006; Sebestyen et al., 2008; Rose et al., 2015a and 2015b). Moreover, similar to previous stream $\delta^{18}O$-NO_3^- studies, a clear seasonal pattern of $\delta^{18}O$ of NO_3^- was lacking in surface soil and soil leaching water (Figure 5.6). Pardo et al. (2006) observed similar proportions of atmospheric NO_3^- in streams during both the winter and non-winter months in a mixed hardwood catchment in the northeastern United States and attributed this pattern to significant storage capacity in well-mixed subsurface reservoirs that dampened seasonal differences in stream water NO_3^- isotopic signatures and persistent microbial NO_3^- production and consumption in surface soil even during the winter months. Indeed, integrating the field observations with the laboratory-characterized isotopic endmembers of nitrification (Table 3.1; see Chapter 3 for more details), the NO_3^- isotopic mass balance revealed fast nitrification and NO_3^- retention rates for all three study sites on an

annual basis, which were one order of magnitude higher than the measured NO_3^- deposition and leaching fluxes (Figure 5.9).

The revealed fast internal cycling of NO_3^- in surface soils at the three sites highlights the intimate interactions between soil microbial N cycling and ecosystem N availability. As overall ecosystem N availability increases due to continuous N input, a larger and larger fraction of the soil microbial community may meet their N needs from local N sources and thus reduce their dependence on N from external sources (e.g. atmospheric NO_3^- deposition) (Schimel and Bennett, 2004). Therefore, the increased N availability may reduce the competition between plants and microbes for the excess N, promoting decomposition of organic matter (i.e., mineralization) in surface soils (Schimel and Bennett, 2004). As a result, NH_4^+ may increasingly dominate soil N pools as observed at the rural meadow site (Figure 5.6), and progressively more NO_3^- production may be favored in N-rich soil microsites (Davidson et al., 1992). As overall N availability further increases, plant and heterotroph competition for NH_4^+ becomes low enough to allow nitrifiers to flourish and the N economy of the system becomes progressively more NO_3^- dominated, as observed at the urban forest and riparian sites (Figure 5.6). Since NH_4^+ supply to nitrifiers is not limiting under high N availability, nitrifiers may likely live in close association with mineralizers so that NO_3^- becomes the dominant N form in soil, and more plants and soil microbes may shift to relying on NO_3^- for their N (Davidson et al., 1992; Stark and Hart, 1997; Schimel and Bennett, 2004).

Thus, assuming steady state of the soil NO_3^- pool, the results from the NO_3^- isotopic mass balance calculation indicate that all three study sites were likely undergoing capacity N saturation, because the total N sink in the soils was much larger than the N input rates via atmospheric deposition (Figure 5.9), making kinetic saturation unlikely. The total capacity for N accumulation

within soils and plants has been shown to be dependent on the effectiveness of C accumulation in ecosystems (Nadelhoffer et al., 1999; Janssens and Luyssaert, 2009). In particular, N can be retained in plants and soils through a C accumulation sink, in which N is accumulated with C in a constant C:N ratio, or a stoichiometric sink, in which N is accumulated without corresponding C accumulation by changing the C:N ratio of the organic matter (Lovett and Goodale, 2011). The C:N ratio of the organic soil horizon has been identified in other studies as a reasonable indicator of ecosystem N saturation and NO_3^- leaching (MacDonald et al., 2002). Based on monitoring data from 181 forests across Europe, MacDonald et al. (2002) suggested that forests with a C:N ratio of <25 are N-enriched and have a high risk of NO_3^- leaching due to increased gross nitrification rates. Therefore, the high soil C:N ratios (14.6 to 19.6; Table 3.1) of the three study sites support the idea that NO_3^- leaching equal to or higher than deposition NO_3^- input was due to restricted capacity of the plants and soils to assimilate added N.

Importantly, the conclusion that the three study sites were undergoing capacity N saturation is not contradictory to the estimated high gross NO_3^- cycling rates from the NO_3^- isotopic mass balance calculation because of the specific time frame associated with each ecosystem N sink (Lovett and Goodale, 2011). Specifically, incorporation of N into microbial biomass which then dies and is re-mineralized, may represent a sink or source of N on time scales of hours to months, but does not contribute to N sequestration over the annual time scales inherent to the NO_3^- isotopic mass balance. The fast NO_3^- cycling without net N accumulation in microbial biomass or soil organic matter over long term is also consistent with the prevalence of the nitrification signal of leached NO_3^- observed at all three sites (Figure 5.7) and the approximately zero or even negative difference between NO_3^- retention and production revealed by the NO_3^- isotopic mass balance calculation, characteristic of capacity saturation (Figure 5.9). Although C cycling rates were not

measured in this study, our results suggest that soil rather than tree biomass is the primary sink for atmospheric N inputs to the three study sites. This implies little accumulation of woody biomass with high C:N ratios and long turnover times and that elevated N deposition to urban ecosystems is not contributing to the northern latitude CO_2 sink as suggested by modeling scenarios which assume that tree biomass accumulates 80% of atmospheric N inputs (Nadelhoffer, et al., 1999; Templer et al., 2005).

However, while this study highlights the value of coupled NO_3^- flux measurements and simple mass balance calculations for constraining the fate of atmospherically deposited NO_3^- and the ecosystem N saturation status, these calculations must be interpreted cautiously because of their potential uncertainty (Figure 5.10). In particular, the estimated gross nitrification and NO_3^- retention rates were highly sensitive to variations in the dual NO_3^- isotopes measured in surface soil and the isotopic end-members of nitrification (Figure 5.10). Nevertheless, our conclusion about capacity saturation is not likely to be compromised by the potential uncertainties in the rate estimates, as the gross nitrification and N retention rates would still be much higher than the NO_3^- deposition fluxes if the low estimates (i.e., 70% lower than current) were used for comparison (Figures 5.9 and 5.10). It has long been recognized in ^{15}N tracer studies that measurement of long term N sink strength in soil is particularly challenging because soil pools of C and N are large and have high spatial variability, making a small difference resulting from N accumulation very difficult to detect by direct sampling (MacDonald et al., 2002). Based on our results, we suggest that direct measurements of NO_3^- isotopic composition for atmospheric deposition and soil leaching provide an integrative means by which the fate of atmospherically deposited NO_3^- can be assessed and thus should be applied in tandem with ^{15}N tracers in future studies to better understand ecosystem N saturation over large time scales.

5.4.3 Scale-dependent linkages between stable nitrate isotopes and ecosystem nitrate dynamics

Based on the NO_3^- isotopic mass balance, $^{15}\varepsilon_N$ and $^{18}\varepsilon_N$ were not appreciably different from zero at the forest and riparian sites, while large $^{15}\varepsilon_N$ and $^{18}\varepsilon_N$ (16.1‰) were estimated for the meadow site, indicating that denitrification was an important retention pathway in the meadow soil (Figure 5.9). Moreover, the measured $\delta^{15}N$ (-0.3±3.3‰) and $\delta^{18}O$ (14.6±4.4‰) of NO_3^- in surface soil at the meadow site were significantly higher than those of nitrification-produced NO_3^- quantified in the laboratory incubation using the meadow soil (-16.7‰ and -4.4‰; Chapter 3). Plotting $\delta^{18}O$ versus $\delta^{15}N$ of NO_3^- in surface soil indicates that denitrification fractionated $\delta^{18}O$ and $\delta^{15}N$ of NO_3^- in surface soil following a linear trajectory with a slope close to 1 (Figure 5.7a). This is consistent with the upper bound of slopes invoked as evidence for denitrification in previous field studies in terrestrial and groundwater (Groffman et al., 2006; Houlton et al. 2006; Hall et al., 2016), and similar to laboratory experiments with denitrifying bacteria (Granger et al., 2008). As revealed in the laboratory incubation experiments (Chapter 3), denitrification might be particularly favored in the meadow soil due to higher percentage of clay content (Table 3.1) and potential inhibition of NO_3^- assimilation induced by the high soil NH_4^+ availability (Figure 5.6a). In addition, the high soil water content observed at 5 cm depth at the meadow site (Figure 5.2a) suggests that the meadow soil might frequently experience water-logging conditions, especially during the winter months (Figure 5.2a), facilitating denitrification activity. Indeed, previous studies have similarly demonstrated greater denitrification potential in surface than subsurface soil horizons (Groffman et al. 2006), highlighting the importance of C and N availability as controls on denitrification in surface soils, as opposed to O_2 diffusion limitation in the subsurface (Hall et al., 2016).

Thus, the measured dual NO_3^- isotopes in surface soil at the meadow site provide direct evidence for persistent co-occurrence of nitrification and denitrification under field conditions. It has been shown in culture studies and soil incubation experiments that nitrification tends to decrease $\delta^{15}N$ of soil NO_3^- relative to NH_4^+ by 25 to 35‰ under optimum substrate conditions (Mariotti et al. 1981; Casciotti et al., 2003). Nitrification also imprints a characteristic $\delta^{18}O$ to NO_3^- that reflects kinetic and equilibrium isotope effects during incorporation of the three O atoms from soil H_2O and O_2 into nitrified NO_3^- (Casciotti et al., 2010; Buchwald and Casciotti, 2010). On the other hand, denitrification fractionates NO_3^- isotopes in a coupled manner, increasing of $\delta^{15}N$ and $\delta^{18}O$ of residual NO_3^- by 5 to 37‰ (Granger et al., 2008; Denk et al., 2017). Consequently, in cases where fractionation from nitrification and denitrification are both expressed at the microsite (i.e., μm) scale, it is possible that their effects could be mutually obscured over larger spatial scales (i.e., cm) characteristic of soil samples due to their opposite effects on $\delta^{15}N$ and $\delta^{18}O$ of NO_3^- (Hall et al., 2016). Without the independent constraints on the $\delta^{15}N$ and $\delta^{18}O$ of nitrification-produced NO_3^- revealed in the laboratory incubation experiments (Chapter 3), the co-occurring nitrification and denitrification would have been obscured and we would have had little isotopic evidence for source apportionment of surface soil NO_3^- between nitrification and atmospheric NO_3^- deposition.

Interestingly, in contrast to the $\delta^{15}N$ and $\delta^{18}O$ of NO_3^- in surface soil, $\delta^{15}N$ (-2.6±1.9‰) and $\delta^{18}O$ (0.6±2.1‰) values in soil leaching NO_3^- were significantly lower (Figure 5.6). A plausible explanation for this NO_3^- isotope disparity is that soil extractions sampled the anaerobic microsites inside the meadow soil where denitrification can occur, whereas water collected in lysimeters may largely reflect NO_3^- dissolved in relatively mobile water in the soil matrix that is largely contributed by nitrification in the aerobic soil macro-pores (Hall et al., 2016). From this perspective, soil leaching water is less efficient than soil extractions in recording NO_3^- isotope

effects from denitrification in redox-heterogeneous surface soils via dual NO_3^- isotopes. By extension, as stream discharge is mostly sustained by groundwater recharged by soil water in mobile phase (Smith et al., 2011), dual NO_3^- isotopes in stream water, which have often been measured to infer denitrification at the ecosystem scale, may not fully capture the denitrification hotspots in surface soil.

On the other hand, the differences in dual NO_3^- isotopes between surface soil and soil leaching water were absent at the two urban study sites (Figure 5.6). The prevalence of the nitrification signal in NO_3^- leached from surface soil highlights the dominant control of hydrological drivers on export of unprocessed atmospheric NO_3^- at the watershed scale. Specifically, if biological NO_3^- cycling in soil is more rapid than hydrological transport, as is typical in watersheds with greater soil water residence times, only minor contributions of unprocessed atmospheric NO_3^- to streams can result, whereas water and NO_3^- can be quickly routed to streams along preferential subsurface flowpaths and overland saturation flows during rain and snowmelt events (Durka et al., 1994; Sebestyen et al., 2008; Rose et al., 2015b). Thus, even in apparently N-limited forest ecosystems, loss of atmospheric NO_3^- via stream export may be inevitable (Lovett and Goodale, 2011). Furthermore, the hydrological regime of a specific watershed is collectively defined by landscape characteristics, including geology, pedology, and topography (Jencso et al., 2009; Hopkin et al., 2015), which is in turn profoundly altered by human activities in urban watersheds (Groffman et al., 2003). In a previous stream $\delta^{18}O\text{-}NO_3^-$ study in NMR, Divers et al. (2014) found that retention of atmospheric NO_3^- was nearly complete (>92%) during baseflow conditions but was significantly decreased during storm events such that ~34% of stream water NO_3^- load was sourced from atmospheric deposition. Our direct sampling of NO_3^- in leaching water from surface soils at the forest and riparian sites provides an independent line of

evidence that any atmospheric NO_3^- that passes through the surface soil horizon is likely recycled and its $\delta^{18}O$ value is reset. Therefore, the increased export of atmospheric NO_3^- can be attributed to impervious surfaces and storm sewer systems in this highly urbanized watershed that work together to direct dry and wet deposition to NMR during storm events (Divers et al., 2014).

In sum, our results highlight a scale-dependent linkage between dual NO_3^- isotopes and complex NO_3^- dynamics in natural and human-dominated ecosystems. Future studies should couple isotope measurements with hydrological models to better understand nitrification and denitrification at the watershed scale using dual NO_3^- isotopes.

5.5 CONCLUSION

Understanding the factors that most influence NO_3^- cycling in and transport through soils has important implications for the study and management of ecosystem N saturation. Based on dual NO_3^- isotope measurements in surface soil and soil leaching water at three sites differing in N availability, we show that:

(1) Hydrological NO_3^- loss from surface soil can exceed atmospheric NO_3^- input in disturbed ecosystems with high N inputs and thus can be a significant source of NO_3^- to the environment.

(2) $\delta^{18}O$ of NO_3^- in surface soils and soil leaching water were significantly lower than that of atmospheric NO_3^-, indicating that atmospheric NO_3^- was rapidly recycled and diluted by nitrification-produced NO_3^- in surface soil.

(3) Gross nitrification and NO_3^- retention rates were one order of magnitude higher than NO_3^- deposition and leaching fluxes, reflecting capacity N saturation in these N-enriched ecosystems.

The use of dual NO_3^- isotopes to probe ecosystem NO_3^- dynamics is scale-dependent and should be coupled with hydrological monitoring for unbiased inference of nitrification and denitrification at the watershed scale.

6.0 CONCLUSIONS

This dissertation has presented a comprehensive investigation of the dynamics of soil NO and its driving processes using multi-isotope analysis at both laboratory and field scales. The novel results of this work enhance our understanding of microbial pathways of soil NO production and the effects of soil N transformations on regulating ecosystem N saturation status.

Chapter 2 documented a new method that collects soil-emitted NO through NO conversion to NO_2 in excess O_3 and subsequent NO_2 collection in a 20% triethanolamine solution as nitrite and nitrate for $\delta^{15}N$ analysis using the denitrifier method. The precision and accuracy of the method were quantified through repeated collection of an analytical NO tank and inter-calibration with a modified EPA NO_x collection method. The results show that the efficiency of NO conversion to NO_2 and subsequent NO_2 collection in the TEA solution is >98% under a variety of controlled conditions. The method precision (1σ) and accuracy across the entire analytical procedure are ±1.1‰. The method was validated in a series of soil rewetting experiments at both laboratory and field scales. The results show that $\delta^{15}N$ of rewetting-triggered NO pulses was low, ranging from -59.8‰ to -23.4‰, and sensitive to the amended N substrates.

In Chapter 3, a $\Delta^{17}O$-based numerical tracing model was developed and used to simultaneously derive rates and isotope effects of gross nitrification and NO_3^- consumption using the triple NO_3^- isotopes ($\delta^{15}N$, $\delta^{18}O$, and $\Delta^{17}O$). Through laboratory soil incubations and field soil sampling after a snowmelt event, we show that the temporal dynamics of $\Delta^{17}O$-NO_3^- can provide quantitative gross rate estimates for soil nitrification and NO_3^- consumption. Coupling $\Delta^{17}O$-NO_3^- with the dual NO_3^- isotopes using the numerical model placed strong constraints on the $\delta^{15}N$ and $\delta^{18}O$ endmembers of nitrification-produced NO_3^- and revealed distinct N isotope effects for

nitrification and NO_3^- consumption among the incubated soils with contrasting soil microbial community structure. Non-zero $\Delta^{17}O\text{-}NO_3^-$ values, up to 4.7‰, were measured in a meadow soil following the snowmelt event. Integrating the field observations with the incubation results uncovered isotopic overprinting of nitrification on denitrification in the surface soil following the snowmelt, which has important implications for explaining the discrepancies between field- and culture-derived isotope systematics of denitrification. These results show that $\Delta^{17}O\text{-}NO_3^-$ is a conservative and powerful tracer of soil nitrification and NO_3^- consumption.

The research presented in Chapter 4 represents the first isotopic characterization of soil NO production in an agricultural soil. A series of controlled laboratory experiments were conducted where the soil was amended with a $\Delta^{17}O$-enriched NO_3^- fertilizer and incubated during aerobic and anaerobic conditions. Based on the soil $\Delta^{17}O\text{-}NO_3^-$ measurements, we demonstrate for the first time that enzymatic NO_2^- and NO_3^- interconversion can occur in soils under anaerobic conditions. Due to this reversibility and the expression of the equilibrium N isotope effect associated with the interconversion, NO produced from denitrification has low $\delta^{15}N$ values (-47.7±0.3‰ to -22.8±2.2‰), while the net isotope effect for NO production from NO_2^- was constrained to be 22.2±1.4‰. During aerobic conditions, nitrification and denitrification contributed 71% and 29% of net NO production. Therefore, denitrification is a significant, yet under characterized source of soil NO production even under conditions strongly favoring nitrification. A large net isotope effect of 69‰ was inferred for NO production from NH_4^+ oxidation, suggesting that NO produced from nitrification and denitrification are distinguishable using $\delta^{15}N$-NO measurements.

Chapter 5 examined ecosystem N saturation status of three anthropogenically impacted field sites differing in N availability using dual NO_3^- isotope measurements in monthly collected

surface soil and soil leaching water samples. The results show that hydrological NO_3^- loss from surface soil can exceed atmospheric NO_3^- input in disturbed ecosystems with high N inputs and that NO_3^- leaching from surface soils can be a significant source of NO_3^- to the environment. Moreover, $\delta^{18}O$ of NO_3^- in surface soils and soil leaching water were significantly lower than that of atmospheric NO_3^-, indicating that atmospheric NO_3^- was rapidly recycled and diluted by nitrification-produced NO_3^- in surface soil. Integrating the field observations with the incubation results in an isotopic mass balance model showed that gross nitrification and NO_3^- retention rates were one order of magnitude higher than NO_3^- deposition and leaching fluxes, reflecting capacity N saturation in these N-enriched ecosystems. Based on these results, we concluded that the use of dual NO_3^- isotopes to probe ecosystem NO_3^- dynamics is scale-dependent and should be coupled with hydrological monitoring for unbiased inference of nitrification and denitrification at the watershed scale.

The results of this work demonstrate the complex processes driving soil NO production and N transformations at both laboratory and field scales. We have shown that multi-isotope measurements ($\delta^{15}N$-NO, $\delta^{15}N$-NO_3^-, $\delta^{18}O$-NO_3^-, and $\Delta^{17}O$-NO_3^-) offer a new perspective on these processes and thus provide important implications for modeling soil NO emission and its underlying mechanisms. Future efforts should be dedicated to applying these techniques at field scales to better resolve complexity of soil N transformations and NO emissions.

APPENDIX A

A.1 COMPARIONS OF THE DFC-TEA METHOD WITH OTHER PUBLISHED METHODS FOR NO_X COLLECTING AND ISOTOPIC ANALYSIS

Table A.1 Comparisons of the DFC-TEA method with other published methods for NO_x collection and isotopic analysis.

Characteristics	modified EPA method	Fibiger method	Li and Wang method	DFC-TEA method
Collection setup	bulk air sample is sucked into pre-evacuated gas sampling bulb containing NO_2 trapping solution	sample flow is forced to pass through a NO_x-trapping bubbler	sample flow is forced to pass through a NO-NO_2 convertor and then a NO_2-trapping denuder	sample flow is forced to pass through a NO-NO_2 convertor and then a NO_2-trapping bubbler
NO-NO_2 conversion	NO is oxidized by ambient-level O_2 to NO_2	NO and NO_2 are directly collected and oxidized to NO_3^- in $KMnO_4$/NaOH solution	solid oxidizer consisting of granules impregnated with CrO_3/H_3PO_4	excess O_3
NO_2 collection	H_2SO_4/H_2O_2 solution		denuder coated with KOH/guaiacol solution	20% triethanolamine solution
NO_x recovery	>97.5%	100±5%	100% (inferred from breakthrough test)	98.5±3.5%
NO_x concentration tested	tens to hundreds of ppmv	22 – 1070 ppbv	5 ppmv	9 – 749 ppbv
Reagent N blank	not reported	~5 μM	not reported	~0.12 μM
Sample pre-treatment for isotopic analysis	sampling bulb needs to stand for at least 72 h for NO oxidation and NO_2 trapping; the absorbing solution is then collected and neutralized using 1 M $NaHCO_3$	$KMnO_4$ is removed through reduction with H_2O_2 to MnO_2 precipitate; the MnO_2 precipitate is removed from solution by centrifugation and decanting; after	denuder is eluted with methanol and water; the elute is first dried in a vacuum desiccator and then collected in tin boats.	solution is neutralized using 12 N HCl

Characteristics	modified EPA method	Fibiger method	Li and Wang method	DFC-TEA method
		decanting, the solution is neutralized using 12 N HCl.		
Isotopic analysis	denitrifier method (NO_3^- conversion to N_2O) coupled to IRMS	denitrifier method (NO_3^- conversion to N_2O) coupled to IRMS	online combustion (NO_2^- conversion to N_2) coupled to IRMS	denitrifier method (NO_3^-/NO_2^- conversion to N_2O) coupled to IRMS
Isotopic calibration	certified NO_3^- standards	certified NO_3^- standards	a standard reagent ($\delta^{15}N = 0.4‰$)	certified NO_3^- and NO_2^- ($\delta^{15}N = -79.6‰$) standards
Precision	better than ±0.5‰	±1.5‰	±0.3‰	±1.1‰
Inter-calibration	not conducted	not conducted	reference NO tank used for the method evaluation was directly measured by a GC-IRMS; agreed within 0.2‰	inter-calibrated with the modified EPA method; agreed within 0.3‰
Minimum NO_2^- /NO_3^-concentration required in collection media	not available	>2 µM (calculated through error propagation assuming a sample $\delta^{15}N$-NO_x not very different from blank $\delta^{15}N$-NO_3^-, e.g., $\delta^{15}N$-NO_x=0.5‰)[5]	not available	>3 µM (experimentally determined using a reference NO tank with low $\delta^{15}N$-NO, i.e., $\delta^{15}N$-NO= -71.4‰)
Temperature and relative humidity effects	not relevant	not relevant	not tested; NO conversion and collection are potentially severely interfered by variations in relative humidity of sample flow.	tested; no significant effect under tested laboratory and field conditions
Tested interference	ammonia	ammonia	not reported	ammonia, nitrous acid (indirectly)
Laboratory application	not applied	coupled to smog chambers for $\delta^{15}N$-NO_x measurements of diesel engine	coupled to a closed non-steady-state chamber for $\delta^{15}N$-NO measurements of fertilization-induced	coupled to a dynamic steady-state chamber system for $\delta^{15}N$-NO measurements

Characteristics	modified EPA method	Fibiger method	Li and Wang method	DFC-TEA method
		emissions and biomass burning	NO emission in agricultural soils	of rewetting-induced soil NO pulses
Field application	δ^{15}N-NO_x of vehicular tailpipe exhausts	coupled to a mobile platform for δ^{15}N-NO_x measurement of on-road vehicular exhaust plume	not applied	coupled to a dynamic steady-state chamber system for δ^{15}N-NO measurements of rewetting- and N fertilization-induced soil NO pulses

A.2 SUPPLEMENTARY DESCRIPTION OF THE DFC SYSTEM

A.2.1 Flux calculation

The DFC is a technique that has been developed to continuously measure soil-atmosphere fluxes of various compounds including NO (Yang and Meixner, 1997; Van Dijk et al., 2002). In contrast to closed static chambers, the DFC is designed to maintain a constant flow of outside air through the chamber containing soil samples or enclosing soil surface areas of interest. The gas flux at the soil-air boundary layer is then determined by the mass balance in the enclosed headspace as following (Pape et al., 2009),

$$V \times \frac{M_N}{V_m} \times \frac{d\mu_{\text{cham}}}{dt} = A \times F - Q \times (\mu_{\text{cham}} - \mu_{\text{in}}) \times \frac{M_N}{V_m} \qquad \text{Equation (A-1)}$$

where t denotes time; V is the chamber volume; Q is the flow rate of the chamber purging flow; A is the surface area enclosed by the chamber or the mass of incubated soil samples in the chamber; μ_{cham} and μ_{in} are the gas mixing ratios of the purging inflow and the outflowing chamber air,

respectively. M_N/V_m is the conversion factor (i.e., ppbv to ng·m^{-3}), where M_N is the gas molecular weight and V_m is the molar volume at measured temperature in the chamber headspace and assumed pressure of 1 atm. When the system operates under a steady state with zero air being the purging flow, $d\mu_{cham}/dt = 0$ in Equation (A-1), and the mass budget equation can be reduced and rearranged to (Pape et al., 2009):

$$F = \frac{Q}{A} \times \mu_{\text{cham}} \times \frac{M_N}{V_m} \qquad \text{Equation (A-2)}$$

Importantly, by using Equation (A-2) to measure soil NO flux, it assumes that (1) the chamber headspace is completely mixed, such that NO concentration (μ_{cham}) is uniform throughout the chamber headspace and (2) NO behaves conservatively, so that there are no reactions with other air constituents or with the chamber walls (Pape et al., 2009).

In the developed DFC system, zero air free of NO_x and O_3 is produced in the air purification unit (Figure 2.1 in Chapter 2) up to 20 slpm for purging the flux chamber. NO, NO_2, and ammonia (NH_3) concentrations in the chamber headspace are measured alternately by a chemiluminescent analyzer (Model 17i, Thermo Fisher Scientific) at 10 s intervals for flux calculations. The precision of NO, NO_2, and NH_3 measurements are ±0.4 ppbv, ±0.6 ppbv, and ±0.6 ppbv, respectively.

A.2.2 Fabrication and testing of the field chamber

A field soil flux chamber has been fabricated and tested for its suitability for NO flux and δ^{15}N-NO measurements, following considerations suggested by Pape et al. (2009) and Yu et al. (2014). The chamber consists of a cylindrical flow-through chamber (39 cm I.D. and 30 L inner volume) made of 5 mm thick transparent acrylic plastic (Figure A-1). The chamber interior surface was lined with 0.05 mm thick FEP film (DuPont, USA) to enhance chemical resistance to NO (Pape et

al., 2009). During field soil flux measurements, the chamber is fitted to the top of a stainless steel chamber base inserted 10 cm into soil (Figure A-1a). A rubber gasket and twelve wing nuts are used to obtain a gas-tight seal for the chamber closure. For testing the chamber in the laboratory, the chamber base was replaced by a stainless steel sheet (Figure A-1b). Soil temperature, air temperature and relative humidity of the chamber atmosphere are continuously monitored using two HOBO sensors installed through the chamber ceiling and sealed with plugs (Figure A-1).

Because soil gas effluxes are driven both by diffusion and mass flow, with diffusion being controlled by gas concentration gradient and mass flow by pressure gradient at soil surface (Davidson et al., 2002), accurate soil gas flux measurements using a DFC require careful system design to eliminate artifacts and biases in measured fluxes. As can be seen in Equation (A-2), when the soil gas flux (F) is positive (net emission to the atmosphere) and constant, the gas concentration in the chamber headspace (μ_{cham}) is inversely related to the purging flow rate (Q) under steady state. In this sense, a large purging flow rate that prevents prolonged accumulation of measured gas is desirable for maintaining an undisturbed gas concentration gradient at the soil-chamber air interface. On the other hand, however, if the purging flow rate is too large, the chamber headspace is artificially pressurized, resulting in higher-than-ambient chamber pressures and, consequently, suppressed mass flows from enclosed soils.

In our field DFC system, we used a purging flow rate between 5 slpm and 20 slpm, corresponding to a mean air residence time ($\tau_{cham}=V/Q$) ranging from 1.5 to 6.0 minutes under complete mixing conditions. This range of τ_{cham} falls within the middle range reported in the literature (see Table 4 in Pape et al. (2009) for a summary) and is considered a compromise between minimizing disturbance on pressure and concentration gradients. In addition, the outflow duct of the chamber (2 inch I.D.) is enlarged compared to the inflow duct (1 inch I.D.) to reduce

the purging-induced pressure buildup inside the chamber[10] and covered by a stainless steel wind shield to prevent episodic pressure change triggered by horizontal wind blowing (Figure A-1) (Xu et al., 2006). The pressure difference between the chamber headspace and the ambient atmosphere is then estimated to be at the lower range as reported in the literature, less than a few Pa, because, as stated above, the resistance at the chamber outlet is effectively minimized and the applied purging flow rate is common (see Table S1 in Yu et al. (2014) for a summary on the effects of chamber configuration on the pressure difference).

The chamber has been tested for the assumption of complete and conservative mixing inherent to flux calculation using Equation (A-2). The analytical solution of the differential Equation (A-1) is a first order exponential decay function depicting evolution of the gas concentration toward steady state,

$$\mu_{\mathrm{cham}}(t) = \mu_{\mathrm{in}} + F \times \frac{A \times V_m}{Q \times M_N}\left(1 - e^{-\frac{t}{\tau_{cham}}}\right) \qquad \text{Equation (A-3)}$$

Although a direct and accurate observation of this equilibration process for NO is hardly possible in our system due to the delay effects introduced by the limited response times of the chemiluminescent analyzer (>30 s), the temporal evolution of the equilibration was investigated using chamber relative humidity measurements that are recorded without any time delay. Five soil samples obtained from an urban forest, Pittsburgh, PA, (100 g dry soil per sample) wetted to 100% WFPS, were placed inside the chamber as the source of water vapor, and the chamber air temperature and relative humidity were recorded every 5 s before and after chamber closure (Figure A-1b).

Figure A-2a shows the temporal buildup of water vapor concentration in the chamber under continuous purging of ambient laboratory air at 5 slpm and 20 slpm. These rates correspond to a theoretical τ_{cham} of 6.0 min and 1.5 min, respectively, under the experimental condition. An

exponential fit to the measured water vapor concentration yielded a τ_{cham} of 6.1 min and 1.7 min, respectively. The small difference between the measured and theoretical τ_{cham} values may result from uncertainties in geometric calculation of the chamber volume (V). We therefore conclude that complete mixing conditions in the chamber headspace are closely approximated when a purging flow rate between 5 slpm and 20 slpm is used.

Furthermore, we tested NO transmission from the field DFC system, because biases may be generated in NO flux and δ^{15}N-NO measurements if there are significant NO losses on the chamber wall and/or losses via reactions with other air constituents. NO transmission from the field chamber was measured and calculated by purging the chamber with a flow of known NO concentration (μ_{in}) and subsequent measurement of NO concentration in the chamber headspace (μ_{cham}), according to Equation (A-4).

$$\text{NO transimission} = \left(\frac{\mu_{\text{cham}}}{\mu_{\text{in}}}\right) \times 100 \qquad \text{Equation (A-4)}$$

The results show that NO transmission is greater than 98.3±0.3% over the tested ranges of μ_{in} (0-100 ppbv) and chamber purging flow rate (5-20 slpm) (Figure A-2b), indicating that NO loss is insignificant in the chamber

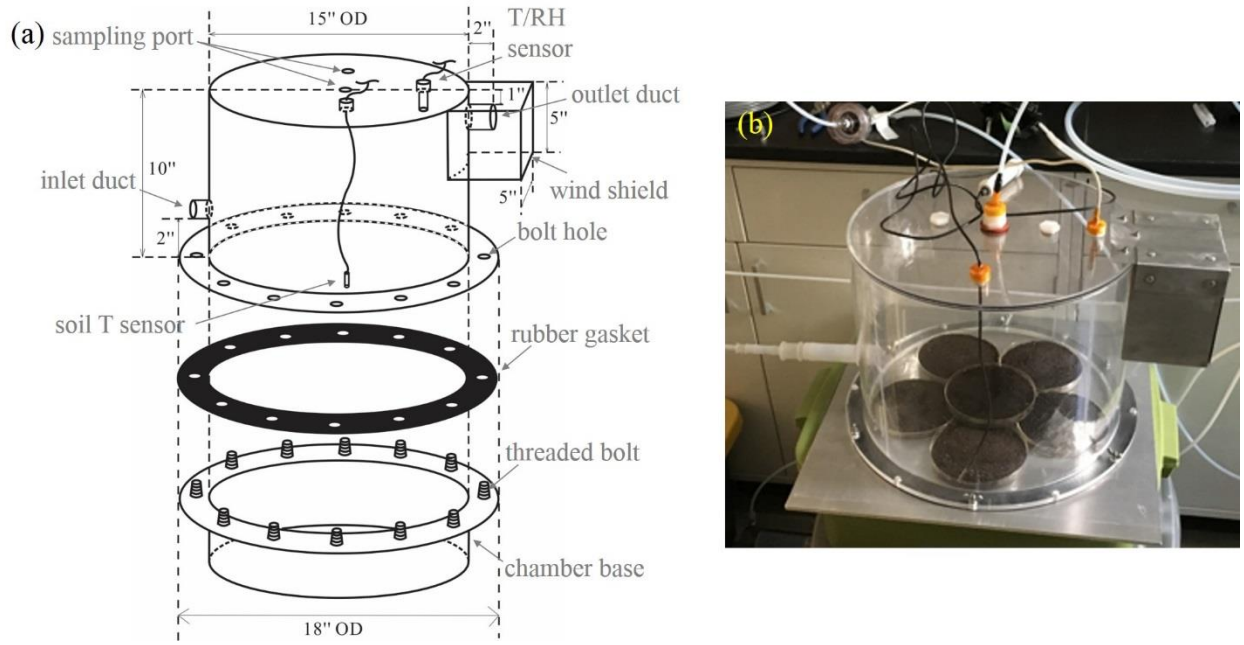

Figure A.1 Schematic (a) and picture (b) of the field chamber.

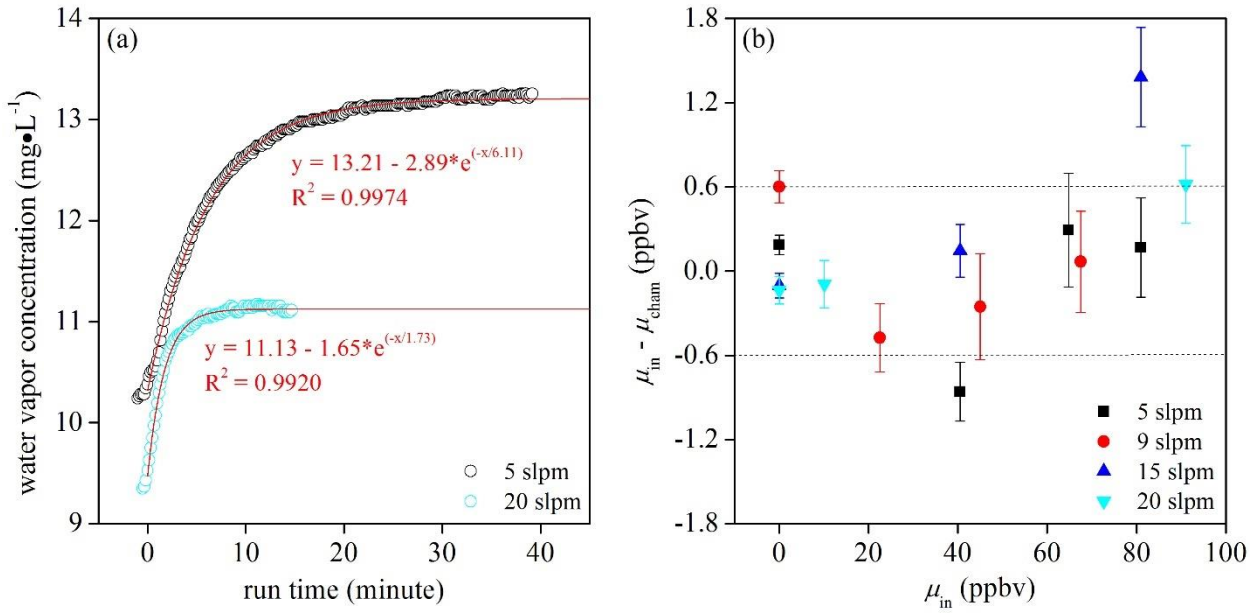

Figure A.2 (a) Temporal buildup of water vapor concentration under purging of two different flow rates after wetting of soil samples in the chamber; (b) difference between μ_{in} and μ_{cham} under different μ_{in} and purging flow rates. The dashed lines bracket the

uncertainty range of μ_{in} - μ_{cham} with an expected value of zero (±0.6 ppbv), propagated from the precision of NO concentration measurement (±0.4 ppbv).

A.2.3 DFC system specifications

A schematic of the developed DFC system is shown in Figure 1 of the main text. Opaque 0.25 inch O.D. PTFE tubing was used to connect the entire system. Specifications of each component of the DFC system are provided in Table A-2.

Table A.2 Specifications of the DFC system components.

ID	Component	Description
1	Diaphragm pump	
• Diaphragm pump for the Air purification unit		Catalog number GH-79200-00, Cole Parmer; free-air capacity = 21.2 $L \cdot min^{-1}$.
• Diaphragm pump for the chemiluminescent analyzer		Model N026.3, KNF Neuberger.
• Diaphragm pump for the NO collection train		Model N86 KTP, KNF Neuberger; all sample exposed parts are PTFE-coated; free-air capacity = 5.5 $L \cdot min^{-1}$.
2	Air purification columns	Three activated charcoal (catalog number NC9643579, Fisher Scientific) columns and three Purafil (catalog number NC0275433, Fisher Scientific) columns collected in series; absorbents were packed in in-line scrubber assemblies (catalog number NC0955678, Fisher Scientific); inner volume of each column = 0.5 L.
3	Drying columns	Two Dri-Rite and 5 Å molecular sieve columns connected in series (catalog number EW-01418-50, Cole Parmer); inner volume of each column = 0.5 L.
4	Humidifier	Milli-Q water in 1000 mL Pyrex gas washing bottle with plain tip stopper.
5	NO tank	50.4 ppmv NO in N_2, Matheson; purity >99.8%; analytical tolerance =±1.0%.
6	NO_2 tank	100.2 ppmv NO_2 in N_2, Matheson; analytical tolerance =±1.0%.
7	NH_3 tank	50.1 ppmv NH_3 in N_2, Matheson; analytical tolerance =±1.0%.
8	Mass flow controller	
• Mass flow controller for the NO tank		Model SmartTrak 50, Sierra Instruments; Flow range = 0 - 50 sccm N_2; accuracy = ±1.5% full scale.

ID	Component	Description
•	Mass flow controller for the NO_2 tank	Catalog number GH-32660-08, Cole Parmer; flow range = 0 -200 sccm N_2/Air; accuracy = ±1% full scale.
•	Mass flow controller for the NH_3 tank	Catalog number GH-32660-08, Cole Parmer; flow range = 0 -200 sccm N_2/Air; accuracy = ±1% full scale.
•	Mass flow controller for the zero air for the laboratory DFC system	Model SmartTrak 50, Sierra Instruments; Flow range = 0 - 10 slpm Air; accuracy = ±1.5% full scale.
•	Mass flow controller for the zero air for the field DFC system	Model SmartTrak 50, Sierra Instruments; Flow range = 0 - 50 slpm Air; accuracy = ±1.5% full scale.
•	Mass flow controller for the NO collection train	Model SmartTrak 50, Sierra Instruments; Flow range = 0 - 5 slpm Air; accuracy = ±1.5% full scale.
9	Flux chamber	1000 mL standard jar made of PFA (Part 100-1000-01, Savillex) fitted with a PFA transfer closure (Part 600-110-28, Savillex). See text S1.1 for the information about the field DFC chamber.
10	Temperature and relative humidity sensor	Model RHT50, Extech Instruments; non-sensing exterior parts of the sensor was wrapped by FEP tape (catalog number 7562A13, McMaster-Carr) to enhance chemical resistance to the measured gas species.
11	In-line PTFE particulate filter assembly	Zylon membrane disc filter (pore size 5 μm, diameter = 47 mm, Part number P4PH047, Pall Corporation) secured by an in-line filter holder (part number 1119, Pall Corporation).
12	HONO scrubber	250 mL fritted gas washing bottle (LG-3761-102, Wilmad-LabGlass) containing 50 mL of 1 mM phosphate buffer solution at pH 7.0 (Zhou et al., 1999).
13	Moisture exchanger	Model ME-110-48COMP-4, Perma Pure LLC. In cases where condensing condition is encountered in the chamber, the flow is reduced in water vapor concentration before entering the NO collection train by being equilibrated with ambient air.
14	Reaction tube	PTFE tubing (catalog number 5239K15, McMaster-Carr), length 240 cm, I.D. 9.5 mm, wrapped by aluminum foil to prevent light penetration.
15	Gas washing bottle containing TEA solution	500 mL fritted gas washing bottle (LG-3761-104, Wilmad-LabGlass) containing 70 mL of 20% (v/v) triethanolamine solution; the fritted stopper of the gas washing bottle was lengthened to be just above the bottom of the bottle, and this resulted in using 70 mL of the solution to just cover the frit.
16	ozone generator	Model 146i, Thermo Fisher Scientific.
17	NO-NO_x-NH_3 chemiluminescent analyzer	Model 17i, Thermo Fisher Scientific.

A.3 PROTOCOL OF NO_2^- AND NO_3^- MEASUREMENT USING THE MODIFIED SPONGY CADMIUM REDUCTION METHOD

Both NO_2^- and NO_3^- are produced from the reaction between NO_2 and TEA. To measure NO_2^- +NO_3^- concentration in the TEA collection samples, a few modifications were made to the spongy cadmium method (Jones, 1984). Because sample pH affects the NO_3^- reduction to NO_2^- and subsequent color development for the colorimetric NO_2^- determination (Jones, 1984), fresh and spent 20% TEA solutions were titrated with 12 N HCl and 85% H_3PO_4, respectively, to guide the pH adjustment (Figure A-3).

To measure NO_2^-+NO_3^- concentration of the TEA collection samples, 5 mL of each sample is pipetted into a 15 mL Falcon tube. 100 μL of 12 N HCl is added to each sample to neutralize the pH to ~8.2 (Figure A-3). 0.2 g wet spongy cadmium, generated from the single displacement reaction between zinc metal sticks and 20% (w/v) $CdSO_4$ solution, is then added to each sample to initiate the NO_3^- to NO_2^- reduction. The sample tubes are capped and secured in a rack on a mechanical shaker so that the tubes are horizontal for maximum mixing. The samples are shaken at 100 excursions·min^{-1} for 2 h. After the shaking, 4 mL of reduced sample is transferred into a new 15 mL Falcon tube. 160 μL of nitrite color reagent (0.05 g N-(1-naphthyl)-ethylenediamine dihydrochloride, 0.5 g Sulfanilamide, 5 mL of 85% H_3PO_4 in 45 mL of MilliQ water) and 480 μL of 85% H_3PO_4 are then added to each sample. The addition of 85% H_3PO_4 lowers the sample pH to ~3.0 and allows maximum color development. The sample tubes are immediately capped, flipped over three times, and allowed to sit for 10 min for color development. The sample absorbance at 540 nm is then measured within 10 min on a UV-visible spectrophotometer. NO_2^- concentration in the TEA collection samples is measured using the same protocol without the

cadmium reduction step. Long-term average of the absorbance value of a 10 μM NO_2^- in 20% TEA solution is about 0.3.

Control tests using 10 μM NO_2^- or NO_3^- in 20% TEA solution (n=4) indicate that 2 h shaking time gave complete NO_3^- reduction, but did not cause overreduction of NO_2^- originally present in the solution. Repeated measurements of a 10 μM NO_2^- or NO_3^- standard in 20% TEA (n=8) indicate that the precision (1 σ) of the method is ±0.09 μM and ±0.36 μM for NO_2^- and NO_3^-, respectively. Due to the multiple reduction and neutralization steps involved in the spongy cadmium reduction method, NO_2^- and NO_3^- standards were always prepared in 20% TEA solution for calibrating the TEA collection samples.

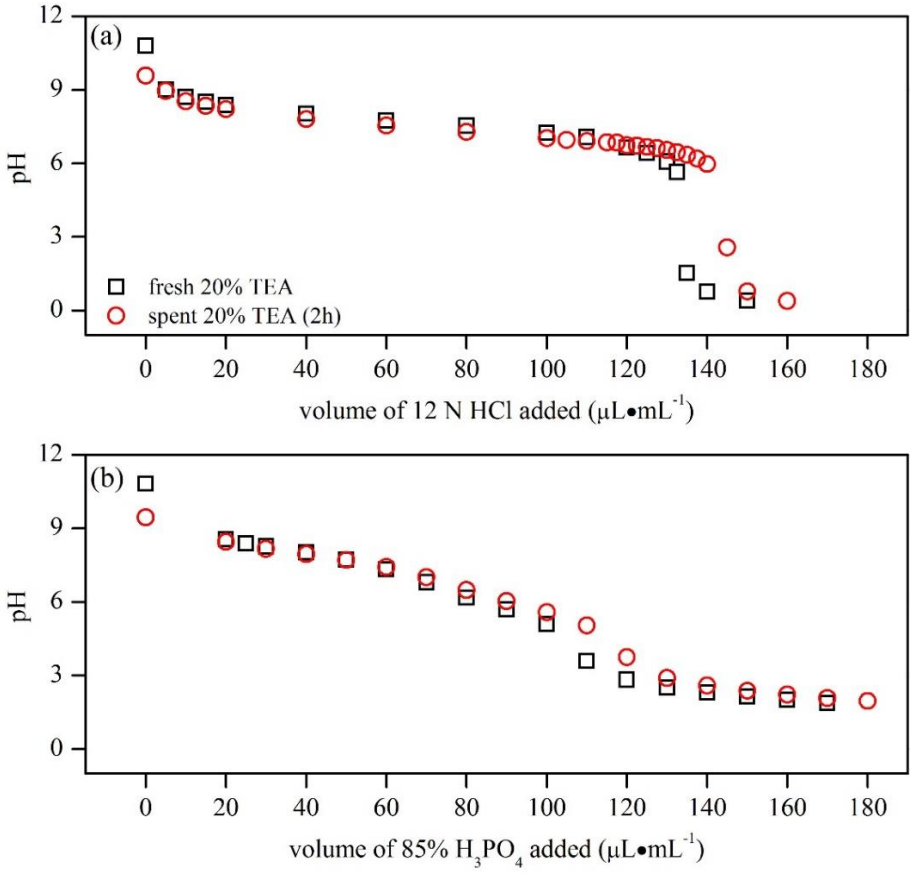

Figure A.3 Titration of fresh and spent 20% TEA solution with 12 N HCl (a) and 85% H_3PO_4 (b).

A.4 THE TOTAL N BLANK AND THE BLANK-MATCHING STRATEGY

We investigated the blank size associated with the 20% TEA solution through analysis of both deionized water and blank 20% TEA solution using the denitrified method. As shown in Figure A-4, injecting deionized water to the sample vials led to N_2O-N yield. This indicates a N blank inherent in the denitrifier medium (Sigman et al., 2001; Casciotti et al., 2002). Higher N_2O-N yield resulting from the injections of blank 20% TEA solution indicates the N blank specific to the 20% TEA solution. The N blank of the 20% TEA solution was calculated by subtracting the N blank originating from the denitrifier medium from the total N blank and was estimated to be 0.12±0.04 μM.

The total N blank associated with the $\delta^{15}N$ analysis of the TEA collection samples using the denitrifier method (i.e., TEA N blank + blank N associated with the denitrifier medium) was also assessed independently through quantifying shrinkage of the N isotope-ratio scale between USGS34 and RSIL20 measured in each run of the TEA collection samples (Coplen et al., 2004).

$$f_B = 1 - \frac{\left(\frac{1+\delta^{15}N_{RSIL20\_m}\times 1000}{1+\delta^{15}N_{USGS34\_m}\times 1000}\right)-1}{\left(\frac{1+\delta^{15}N_{RSIL20\_a}\times 1000}{1+\delta^{15}N_{USGS34\_a}\times 1000}\right)-1} \qquad \text{Equation (A-5)}$$

In Equation A-5, f_B is the fraction of N_2O-N derived from the total N blank; $\delta^{15}N_{RSIL20\text{-}a}$ and $\delta^{15}N_{USGS34\text{-}a}$ are the accepted $\delta^{15}N$ values of RSIL20 and USGS34 relative to N_2 in air, respectively; $\delta^{15}N_{RSIL20\text{-}m}$ and $\delta^{15}N_{USGS34\text{-}m}$ are the measured $\delta^{15}N$ values of RSIL20 and USGS34 relative to IAEA-N3, respectively. The molar amount of the total N blank, calculated as the difference between the total amount of measured N_2O-N in the sample vials and the amount of N_2O-N generated from the standards, was then determined using f_B and the known molar amount of the injected standards. The estimated f_B ranged between 0.04 and 0.18 and was significantly, positively

correlated with $\delta^{15}N_{RSIL20\text{-}m}$ and the sample volume (Figure 2.2a in Chapter 2). Fitting a linear equation to the molar amount of the total N blank and the sample volume indicates that the N blank likely consisted of a constant component of 0.46±0.12 nmol and a sample volume-dependent component of 0.23±0.06 nmol·mL^{-1}, consistent with the blank size estimated by injecting blank 20% TEA solution (Figure A-4).

The isotope effect of the total N blank is corrected during the $\delta^{15}N$ analysis using a blank-matching strategy (i.e., application of the identical treatment principal). As illustrated in Figure 2.2, the blank-matching strategy requires that isotope standards (i.e., IAEA-N3, USGS34, and RSIL20) are prepared in the same matrix (i.e., 20% TEA) as collection samples; then, concentrations of the standards and samples are adjusted via dilution by 20% TEA solution such that same injection volume (±5%) is used for all the standards and samples. Consequently, systematic error associated with the total N blank is implicitly and automatically corrected during the $\delta^{15}N$ analysis because the size and $\delta^{15}N$ value of the total N blank is matched between all the standards and samples in a given analytical run (Figure 2.2 in Chapter 2).

The percentage difference (P_{diff}) in the major N_2O (*m/z* 44) peak area between each collection sample (P_{sample}) and RSIL20 measured within the same batch (P_{RSIL}) is calculated to quantify how precisely the blank-matching strategy is implemented:

$$P_{diff} = \frac{P_{sample} - P_{RSIL}}{P_{RSIL}} \times 100\% \qquad \text{Equation (A-6)}$$

The calculated P_{diff} ranged from -9.8% to 15.9% for all the collection samples, averaging 1.1±5.1% (Figure A-5a). P_{diff} is not sensitive to the sample concentration (linear regression, P>0.05) (Figure A-5a), indicating that the sample concentrations were precisely measured and diluted for the $\delta^{15}N$ analysis. No discernible relationship emerged between P_{diff} and the measured $\delta^{15}N$ values (Figure A-5b).

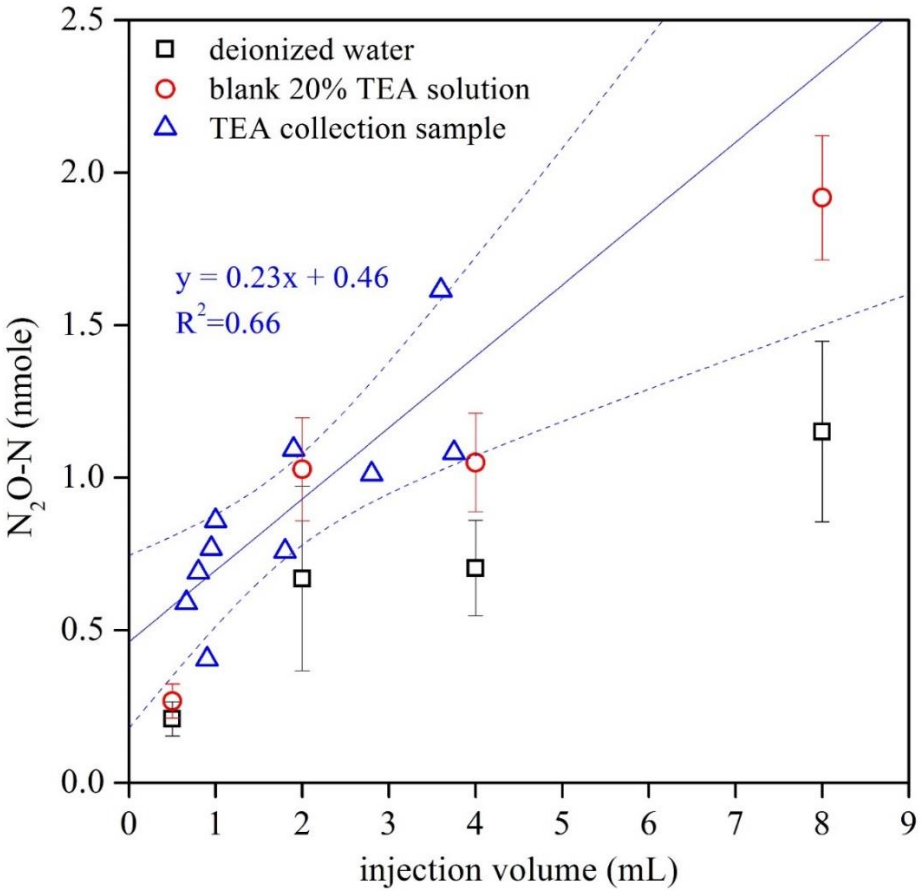

Figure A.4 The N_2O-N blank associated with the bacterial medium and the 20% TEA solution as a function of the injection volume. For the injections of deionized water and blank 20% TEA solution, the N_2O-N yield was calculated from the major ion peak area, calibrating with standard additions. The solid and dashed lines denote a linear regression line and the corresponding 95% confidence interval of the N_2O-N blank associated with the TEA collection samples.

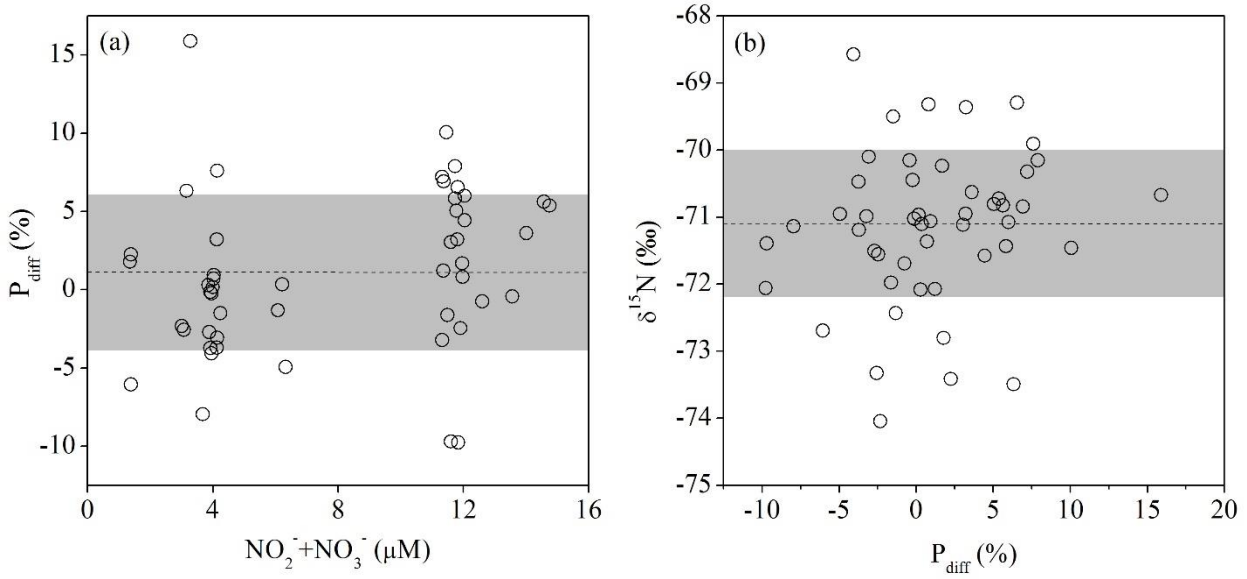

Figure A.5 The calculated P_{diff} of the NO tank collection samples as a function of sample $NO_2^-+NO_3^-$ concentration (a) and its effect on the measured $\delta^{15}N$ values (b). The dash line and the shaded area represent the mean ± (1 σ) of the y-variable.

A.5 EXTENDED MODELING OF THE NO CONVERSION IN EXCESS O_3

Reaction of NO with excess O_3 forms NO_2 (R1 in Table A-2). In a dark environment, the efficiency of NO to NO_2 conversion is limited by the formation of higher nitrogen oxide species, i.e. nitrate radical (NO_3) and dinitrogen pentoxide (N_2O_5), from further oxidation of NO_2 (R2-R5 in Table A-2). In order to model the NO conversion in the reaction tube, the reaction time is needed. Following Fuch et al. (2009) the reaction time of the reaction tube was experimentally determined by sampling zero air that contained a constant NO concentration (27 ppbv) using the NO collection train and varying the excess O_3 concentration (266-2890 ppbv). The ending point of the reaction tube was attached onto the sampling inlet of the chemiluminescent analyzer for NO concentration

determination. The NO concentration decay was then fitted to a single exponential function assuming pseudo first order loss of NO in excess O_3 (Equation A-7).

$$\frac{[NO]_t}{[NO]_0} = e^{(-[O_3]\times k\times t_R)} \qquad \text{Equation (A-7)}$$

In Equation A-7, $[NO]_t/[NO]_0$ is the ratio of the measured NO concentration exiting the reaction tube to the initial NO concentration; $[O_3]$ is the O_3 concentration; k is the rate constant of reaction R1; t_R is the reaction time. Due to the inner tubing of the chemiluminescent analyzer, the estimated reaction time represents the reaction tube plus the analyzer inner tubing. To correct this overestimate, the reaction time of the inner tubing was estimated by repeating the experiment with the mixing point of the sample and O_3 flow being directly attached to the analyzer inlet for NO concentration determination. The results show that the reaction time of the inner tubing of the chemiluminescent analyzer and the reaction tube plus the inner tubing were estimated to be 1.4 s and 6.4 s, respectively, with a reaction time of the reaction tube of 5 s at the measured flow temperature (22 °C) (Figure A-6).

Based on this reaction time and a O_3 concentration of 2911 ppbv, numerical model calculations including reactions R1-R6 in Table A-2 indicate that NO is quantitatively converted in the reaction tube and that the specific conversion of NO to NO_2 is between 98.7% and 99.0% over a wide range of NO concentrations (0-1000 ppbv) at 22 °C (Figure A-7a). Notably, the remainder of the converted NO exists primarily as N_2O_5, as the efficiency of NO conversion to NO_2+N_2O_5 is always >99% under the modeled conditions (Figure A-7b).

Deviations from the controlled laboratory condition could result in variations in the modeled NO conversion efficiency. Since the rate constants for reactions R1-R5 are strongly temperature-dependent, the NO conversion efficiency was further modeled over a temperature range of 0-40 °C with an assumed constant NO concentration of 100 ppbv. The result shows that

deviation from the optimal temperature range (~10-20 °C) can cause a <0.5% reduction in the modeled efficiency of NO to NO_2 conversion, while the efficiency of NO conversion to NO_2+N_2O_5 is still always >99% (Figure A-8). Emissions of biogenic volatile organic carbons (BVOC) from vegetated soil could potentially affect the NO conversion via reactions of BVOCs with NO_3 and O_3. The effect of BVOC emissions on the conversion efficiency was assessed by including the reactions of isoprene, a major BVOC in the atmosphere (Atkinson and Arey, 2003), with NO_3 and O_3 in the numerical model calculation (R7 and R8 in Table A-2). Interestingly, the efficiency of NO to NO_2 conversion increased by as much as 0.3% over 0 °C to 40 °C when isoprene is present at the same concentration as NO (i.e., 100 ppbv; Figure A-9), possibly due to NO_3 scavenging that suppresses accumulation of N_2O_5. Therefore, it is reasonable to assume that BVOC emissions do not affect the NO conversion significantly under the applied conditions. In sum, our extended modeling on the NO conversion in excess O_3 indicates that the conversion of NO to NO_2 is not likely to fall below 98% over a temperature range of 0-40°C in conjunction with high BVOC emissions.

Table A.3 Reactions involving in the NO conversion in excess O_3.

No.	Reaction	Rate constant (at 22 °C)	Reference
R1	$\mathbf{NO + O_3 \rightarrow NO_2 + O_2}$	1.86×10^{-14}	Atkinson et al., 2006
R2	$\mathbf{NO_2 + O_3 \rightarrow NO_3 + O_2}$	2.98×10^{-17}	Atkinson et al., 2006
R3	$\mathbf{NO + NO_3 \rightarrow 2NO_2}$	2.67×10^{-11}	Atkinson et al., 2006
R4	$\mathbf{NO_2 + NO_3 + M \rightarrow N_2O_5 + M}$	1.19×10^{-12}	Atkinson et al., 2006
R5	$\mathbf{N_2O_5 + M \rightarrow NO_2 + NO_3 + M}$	2.88×10^{-2}	Atkinson et al., 2006
R6	$\mathbf{NO_3 \rightarrow wall\ loss}$	2.00×10^{-1}	Dubé et al., 2006
R7	$\mathbf{NO_3 + CH_2 = C(CH_3)CH = CH_2 \rightarrow products}$	6.86×10^{-13}	Atkinson et al., 2006
R8	$\mathbf{O_3 + CH_2 = C(CH_3)CH = CH_2 \rightarrow products}$	1.19×10^{-17}	Atkinson et al., 2006

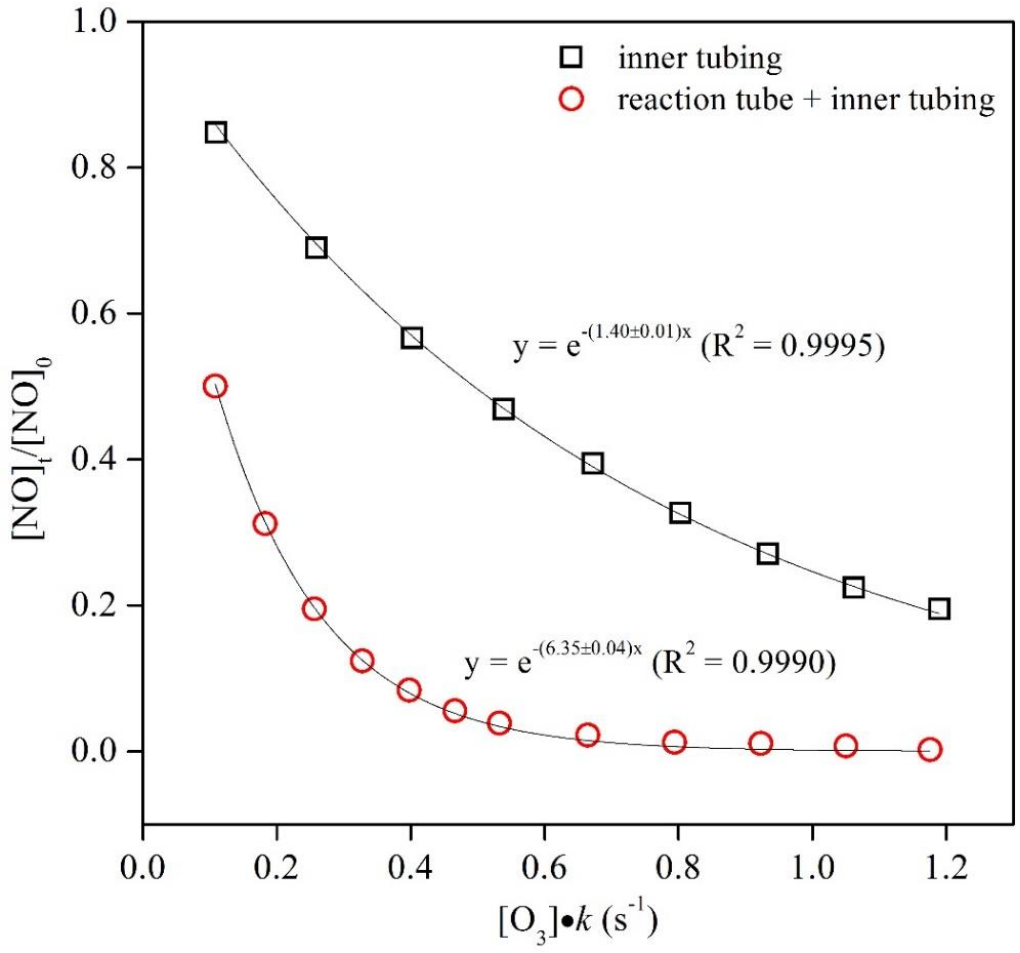

Figure A.6 Exponential fits for determining the reaction time (t_R) of the inner tubing of the chemiluminescent analyzer and the reaction tube plus the inner tubing using Equation (A-7).

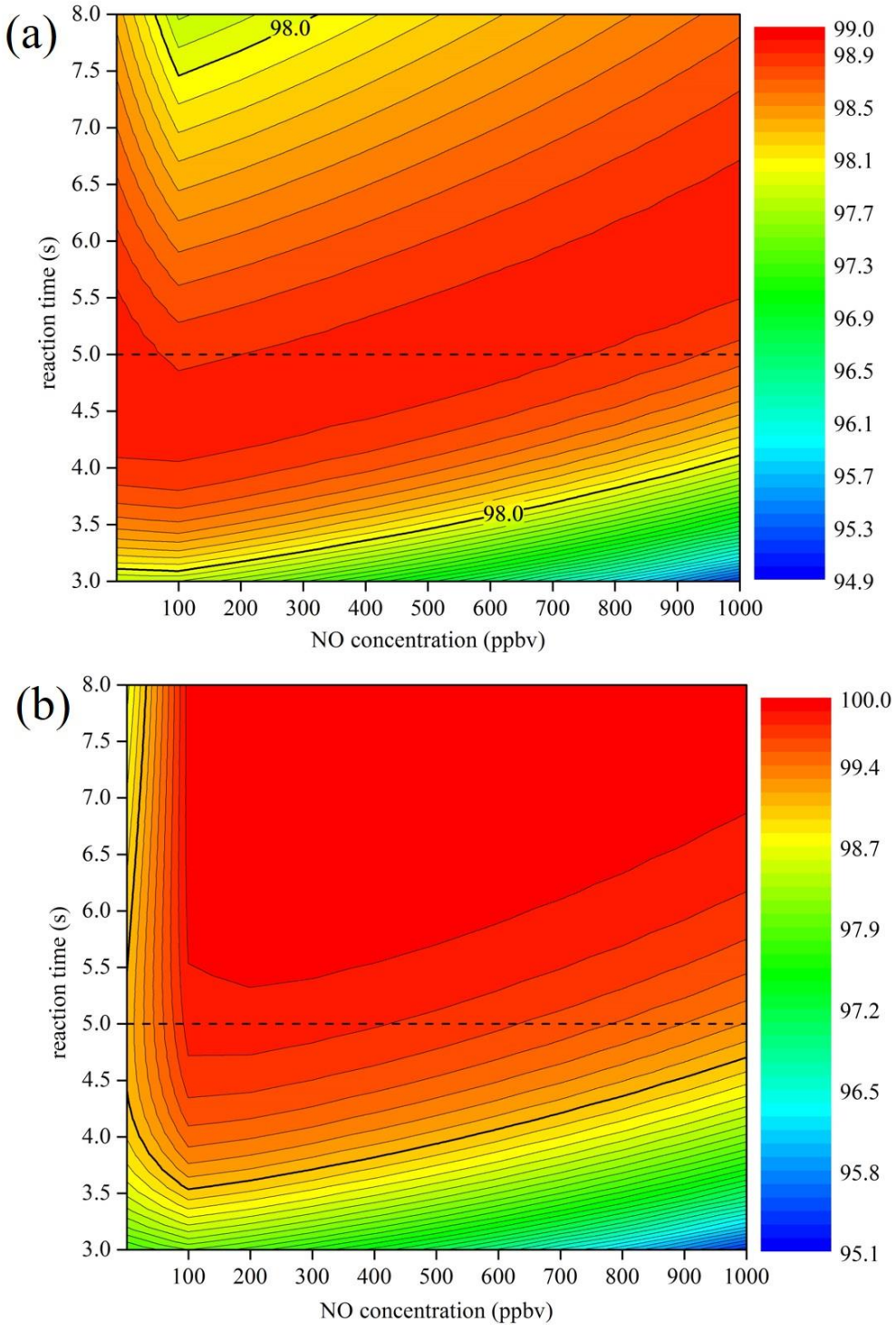

Figure A.7 Modeled efficiency of NO to NO_2 conversion (a) and NO to NO_2 + N_2O_5 conversion (b) as a function of NO concentration after the mixing of the sample and O_3 flows

and the reaction time at 22 °C. The dashed line denotes the estimated reaction time (5 s) of the reaction tube.

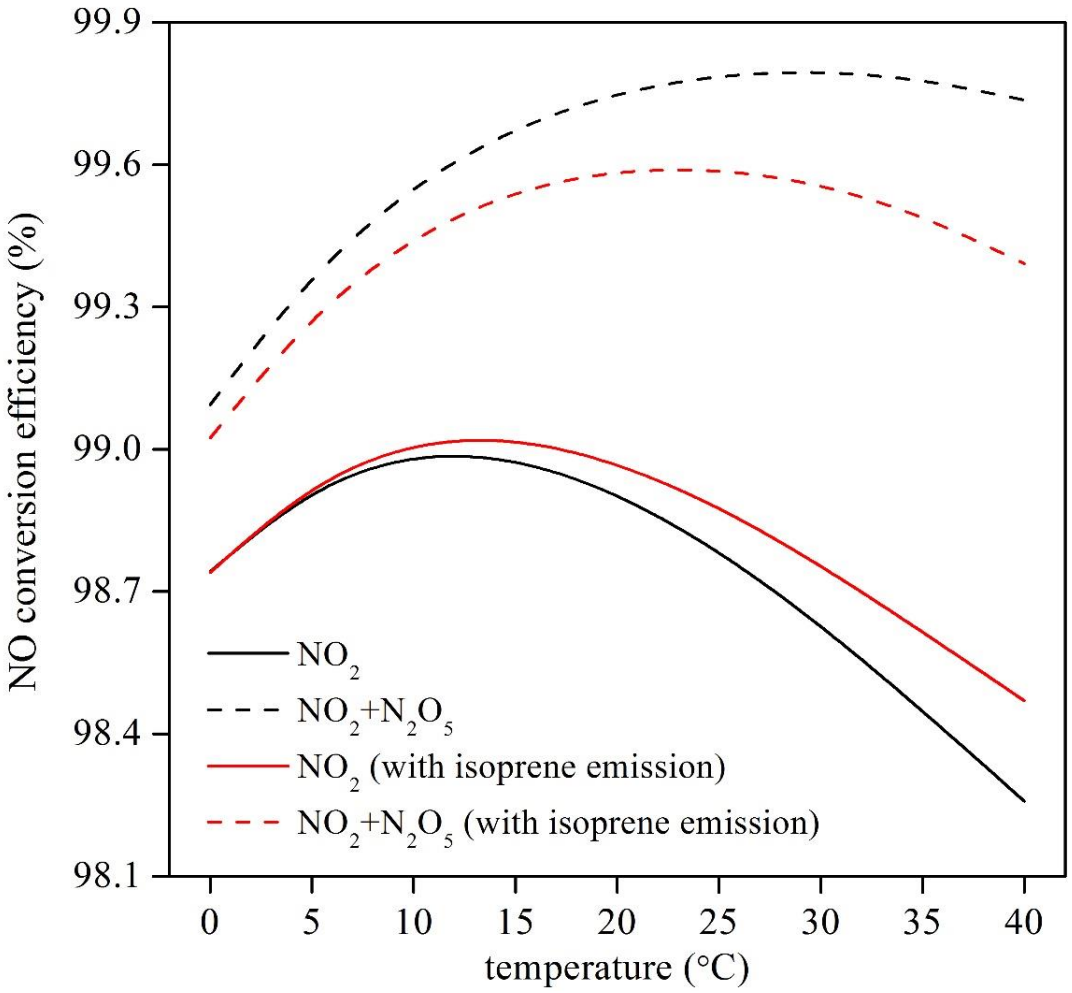

Figure A.8 Effects of temperature variation and soil isoprene emission on the modeled efficiencies of NO conversion to NO_2 and NO_2+N_2O_5. A reaction time of 5 s and NO and isoprene concentrations of 100 ppbv were used in the model calculations.

A.6 DETERMINATION OF THE THEORETICAL $\Delta^{17}O$ OF NO_2 PRODUCED FROM $NO+O_3$ REACTION

Positive $\Delta^{17}O$ values were observed in N_2O generated from the NO collection samples, indicating that NO_2^- and NO_3^- in the collection samples were impacted by mass-independent reactions through exchange with O_3 and that a correction of the isobaric interference on the *m/z* 45 is required. To further understand the transfer of the $\Delta^{17}O$ anomaly from O_3 during the NO conversion, we measured the $\Delta^{17}O$ of the terminal oxygen atoms of the O_3 produced from the O_3 generator on two different days by bubbling the mixed zero air and O_3 flow through a 15 µM NO_2^- solution in water for 2 h. The NO_2^- was quantitatively oxidized to NO_3^- after bubbling. The $\Delta^{17}O$ of the produced NO_3^- was measured to be 16.3±0.7‰ (n=5) and resulted in a $\Delta^{17}O$ of 48.8±2.2‰ for the terminal oxygen atoms of the produced O_3 ($\Delta^{17}O(O_3)_{trans}$). This is based on previous observations that show only the terminal atom from the O_3 molecule is abstracted in the aqueous phase NO_2^- oxidation (Michalski and Bhattacharya, 2009; Liu et al., 2001).

$$NO + O_3 \rightarrow NO_2 + O_2$$

Assuming that the $\Delta^{17}O$ anomaly is only located in the terminal atom and that the oxygen atom transfer in reaction S1 proceeds with a probability of 8% for the abstraction of the central oxygen atom of the O_3 by NO (Equation A-8) (Savarino et al., 2008), the $\Delta^{17}O$ of the transferred oxygen atom ($\Delta^{17}O(O_3)_{trans}$) is calculated to be 45.0±3.7‰, equivalent to a theoretical $\Delta^{17}O$ of 22.5±1.8‰ for the NO_2 produced from reaction S1 in Table A-3.

$$\Delta^{17}O(O_3)_{\text{trans}} = 1.18 \times \left(\frac{2}{3} \times \Delta^{17}O(O_3)_{\text{term}}\right) + 6.6 \qquad \text{Equation (A-8)}$$

A.7 SUPPLEMENTARY FIGURE SHOWING THE SETUP OF THE FIELD REWETTING EXPERIMENT

Figure A.9 Pictures showing (a) the University of Pittsburgh *Mobile Air Quality Laboratory*, (b) field DFC system, (c) tarp for drying urban fallow soil, and (d) field chamber.

A.8 SOIL NO_X EMISSIONS IN THE LABORATORY AND FIELD SOIL REWETTING EXPERIMENTS

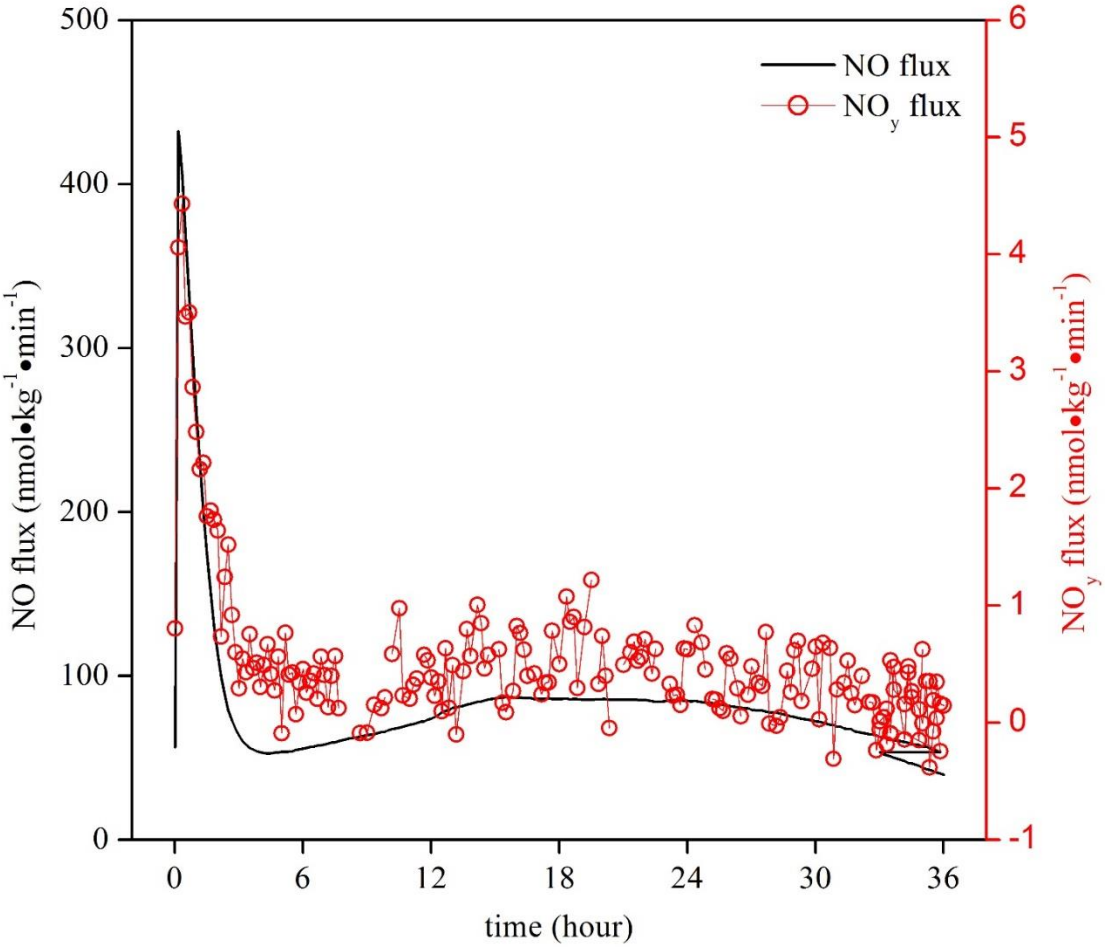

Figure A.10 Soil NO and NO_y emissions in the laboratory soil rewetting experiment. Emissions were calculated based on three replicate measurements. The average ratio of NO_y flux to NO flux was 0.59±0.44%.

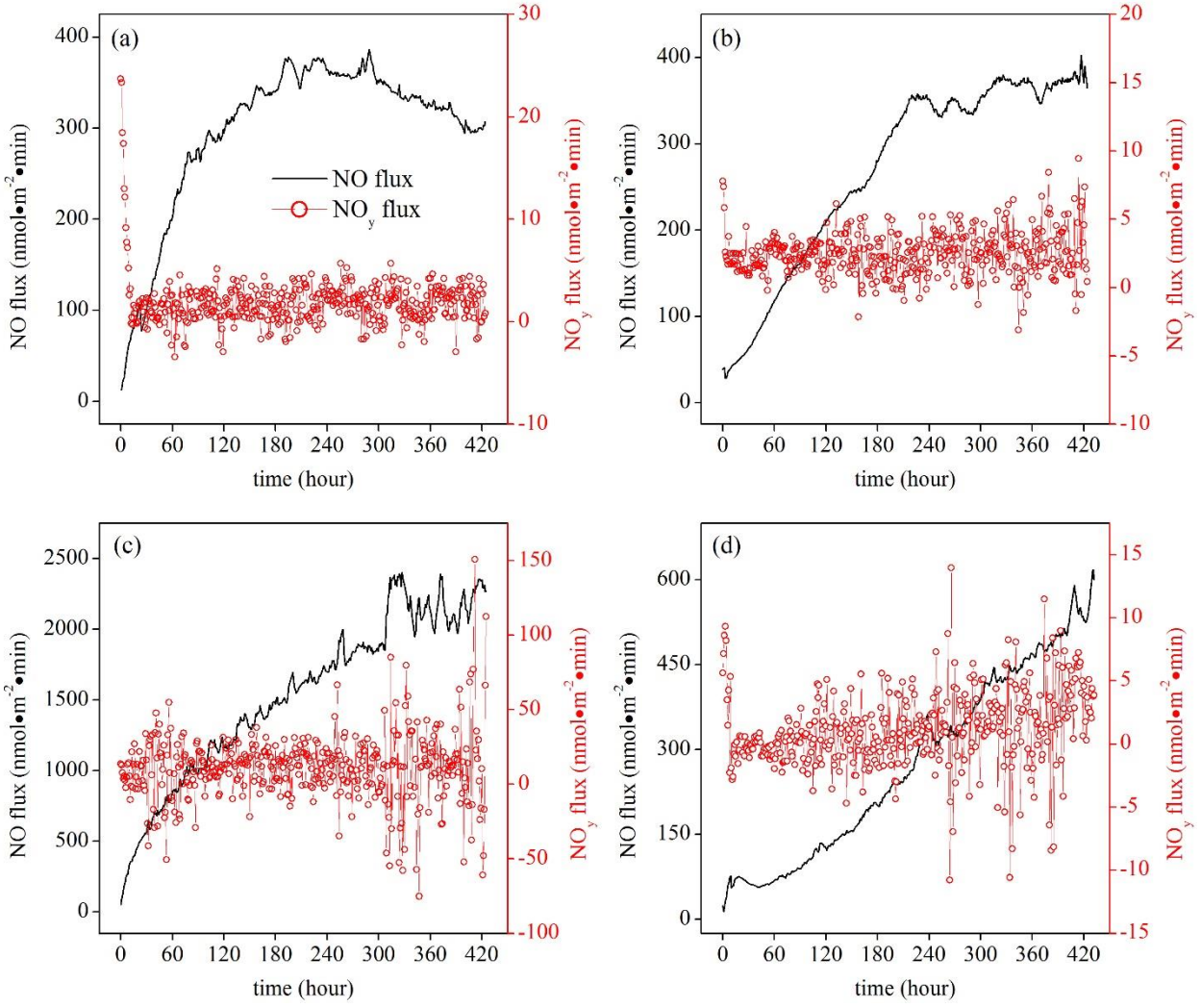

Figure A.11 Soil NO and NO_y emissions in the field soil rewetting experiment. The average ratios of NO_y flux to NO flux were 0.57±0.61% for the MilliQ water addition (a), 1.14±0.99% for the NO_3^- addition (b), 0.79±1.68% for the NO_2^- addition (c), and 0.23±1.20% for the NH_4^+ addition (d). The high NO_y fluxes in the first 10 min reflect the purging out of ambient NO_2 after the chamber closure and were not included in the ratio calculations.

A.9 COMPLETE DATASETS FOR COLLECTION OF NO AND NO_2 REFERENCE GAS TANKS AND PULSED NO EMISSIONS

Table A.4 Complete dataset: NO and NO_2 reference gas tanks.

Sample	Time (min)	T (°C)	RH (%)	NO_2^- +NO_3^- (μM)	Recovery (%)	NO_2^- percent (%)	P_{diff} (%)	$\delta^{15}N^a$ (‰)	$\Delta^{17}O$ (‰)
NO_2 collection – laboratory DFC system									
1002 ppbv NO_2	135	23.8	25.6	125.6	96.1	87.3	6.7	-39.9	
1002 ppbv NO_2	135	23.7	25.4	133.8	102.4	87.7	-3.7	-41.1	
1002 ppbv NO_2	135	23.6	25.2	134.8	103.1	87.1	7.3	-40.9	
1002 ppbv NO_2	135	23.7	25.0	136.1	104.0	87.6	3.1	-39.6	
Mean				132.5	101.4	87.4	3.3	-40.4	
Standard error (1 σ)				4.7	3.6	0.3	5.1	0.7	
NO collection – laboratory DFC system									
12 ppbv NO	120	22.8	43.3	1.4	94.7	96.1	2.2	-73.4 (-72.2)	
12 ppbv NO	120	23.0	45.7	1.4	95.2	98.6	1.8	-72.8 (-71.6)	
12 ppbv NO	120	23.2	44.8	1.4	95.1	96.1	-6.1	-72.7 (-71.4)	
34 ppbv NO	120	24.1	27.8	4.2	105.1	93.6	-1.5	-69.5 (-68.4)	
34 ppbv NO	120	24.8	27.1	4.0	98.1	94.3	-0.2	-70.4 (-69.3)	
34 ppbv NO	120	25.1	26.8	4.1	102.4	91.1	-3.1	-70.1 (-69.0)	
34 ppbv NO	120	25.2	26.5	3.9	97.4	93.4	-0.1	-71.0 (-69.9)	
101 ppbv NO	120	23.0	33.8	12.0	99.5	94.7	6.0	-71.1 (-70.0)	18.9
101 ppbv NO	120	23.0	34.1	12.0	99.1	94.0	0.8	-69.3 (-68.2)	19.1
101 ppbv NO	120	23.3	34.4	11.9	98.7	92.0	-2.5	-71.6 (-70.5)	18.3
101 ppbv NO	120	23.4	34.6	11.5	95.7	95.3	-1.6	-72.0 (-70.9)	19.0
749 ppbv NO	120	22.6	45.6	14.0	97.8	93.6	3.6	-70.6 (-69.5)	21.2
749 ppbv NO	120	22.7	48.1	14.8	103.0	92.0	5.4	-70.7 (-69.6)	20.5
749 ppbv NO	120	22.9	48.3	13.6	94.7	88.0	-0.4	-70.2 (-69.1)	19.9
749 ppbv NO	120	23.0	48.2	14.6	101.7	89.3	5.6	-70.8 (-69.7)	20.9
NO collection – laboratory DFC system – temperature effect									
34 ppbv NO	120	12.0	90.9	4.1	102.6	90.2	7.6	-69.9 (-68.8)	
34 ppbv NO	120	11.4	92.0	4.0	100.3	90.9	0.9	-71.1 (-69.9)	
34 ppbv NO	120	11.2	92.4	4.0	100.2	86.1	0.7	-71.4 (-70.3)	
34 ppbv NO	120	11.3	92.7	3.9	96.1	89.8	0.3	-72.1 (-71.0)	
101 ppbv NO	120	30.6	28.7	12.6	104.5	85.3	-0.8	-71.7 (-70.6)	19.3
101 ppbv NO	120	30.7	28.3	11.3	94.2	92.4	7.2	-70.3 (-69.2)	20.0

Sample	Time (min)	T (°C)	RH (%)	NO_2^- +NO_3^- (μM)	Recovery (%)	NO_2^- percent (%)	P_{diff} (%)	$\delta^{15}N^a$ (‰)	$\Delta^{17}O$ (‰)
101 ppbv NO	120	31.0	28.7	11.4	94.4	92.1	1.2	-72.1 (-70.9)	20.5
101 ppbv NO	120	31.0	29.4	11.8	98.1	88.2	6.5	-69.3 (-68.2)	20.2
NO collection – laboratory DFC system – interference									
34 ppbv NO + 500 ppbv NH_3	120	23.2	33.4	3.9	97.5	89.9	-3.7	-70.5 (-69.4)	
34 ppbv NO + 500 ppbv NH_3	120	23.0	33.0	4.0	98.4	88.3	-4.1	-68.6 (-67.5)	
34 ppbv NO + 500 ppbv NH_3	120	22.7	32.9	4.1	102.7	86.4	-3.7	-71.2 (-70.1)	
101 ppbv NO + 500 ppbv NH_3	120	23.2	47.4	11.3	94.1	96.8	-3.2	-71.0 (-69.9)	19.7
101 ppbv NO + 500 ppbv NH_3	120	23.1	46.7	11.8	98.1	89.8	3.2	-71.0 (-70.0)	18.0
101 ppbv NO + 500 ppbv NH_3	120	23.1	46.3	11.7	97.7	92.2	5.8	-71.4 (-70.3)	20.1
101 ppbv NO + 500 ppbv NH_3	120	23.0	45.7	12.0	100.3	87.1	4.4	-71.6 (-70.5)	20.0
101 ppbv NO + HONO scrubber	120	22.9	86.4	11.6	96.4	92.5	3.0	-71.1 (-70.0)	19.7
101 ppbv NO + HONO scrubber	120	22.1	90.0	11.5	95.6	89.0	10.1	-71.5 (-70.4)	19.8
101 ppbv NO + HONO scrubber	120	22.1	90.0	11.6	96.7	89.4	-9.7	-71.4 (-70.3)	20.0
101 ppbv NO + HONO scrubber	120	21.9	92.5	11.7	98.1	88.3	7.9	-70.2 (-69.1)	18.9
NO collection – field DFC system									
25 ppbv NO	120	21.7	39.2	3.3	108.3	94.3	15.9	-70.7 (-69.5)	
25 ppbv NO	120	21.4	40.7	3.2	104.9	98.8	6.3	-73.5 (-72.3)	
25 ppbv NO	120	21.3	41.3	3.0	100.1	91.5	-2.3	-74.0 (-72.9)	
25 ppbv NO	120	21.2	41.9	3.1	102.4	92.7	-2.6	-73.3 (-72.2)	
34 ppbv NO	120	22.5	48.5	3.7	91.3	99.7	-8.0	-71.1 (-70.0)	
34 ppbv NO	120	22.4	50.4	3.9	96.8	92.6	-2.7	-71.5 (-70.4)	
34 ppbv NO	120	21.5	51.0	4.1	102.7	88.1	3.2	-69.4 (-68.2)	
34 ppbv NO	120	21.3	51.8	4.0	99.6	90.8	0.2	-71.0 (-69.9)	
56 ppbv NO	120	21.7	43.9	6.1	95.1	95.4	-1.3	-72.4 (-71.4)	
56 ppbv NO	120	20.8	45.2	6.2	97.3	92.7	0.4	-71.1 (-70.1)	
56 ppbv NO	120	20.9	45.2	6.3	95.6	90.6	-4.9	-71.0 (-69.9)	
101 ppbv NO	120	22.2	35.3	11.4	93.9	90.9	6.9	-70.8 (-69.7)	19.8
101 ppbv NO	120	21.7	36.4	11.8	97.8	90.9	-9.8	-72.1 (-71.0)	
101 ppbv NO	120	21.5	37.1	12.0	98.9	87.5	1.7	-70.2 (-69.1)	19.6
101 ppbv NO	120	21.5	37.6	11.8	97.6	88.9	5.0	-70.8 (-69.8)	19.0
Mean					98.5	91.7	1.1	-71.1 (-70.0)	19.7
Standard error (1 σ)					3.5	3.4	5.1	1.1 (1.1)	0.8

a: Relative to N_2 in the air. $\delta^{15}N$ values before the isobaric correction are shown in the brackets.

Table A.5 Complete dataset: NO collection, laboratory soil rewetting experiment.

Sample	Time (min)	T (°C)	RH (%)	$NO_2^-+NO_3^-$ (μM)	Recovery [a] (%)	NO_2^- percent (%)	Dilution factor	P_{diff} (%)	$\delta^{15}N$ [b] (‰)	$\Delta^{17}O$ (‰)
Replicate 1										
1	30	23.6	62.7	9.2	105.1	95.4	1.7	3.3	-37.1 (-36.1)	19.4
2	30	23.3	60.6	7.6	100.9	95.6	1.4	-2.5	-38.8 (-37.7)	
3	30	23.1	60.0	5.6	110.0	89.6	1.0	1.1	-40.5 (-39.5)	
4	120	23.0	58.3	6.8	106.2	92.0	1.2	3.1	-49.3 (-48.3)	
5	120	23.0	56.7	5.5	104.4	89.2	1.0	-3.6	-52.9 (-51.9)	
6	120	22.6	45.6	7.4	93.3	97.6	1.3	6.0	-53.7 (-52.6)	
7	120	22.4	41.3	9.6	113.5	85.0	1.7	-0.4	-53.6 (-52.6)	18.8
Replicate 2										
1	30	24.4	61.1	9.3	102.6	96.4	1.7	5.4	-36.8 (-35.7)	18.8
2	30	23.3	62.4	9.0	106.2	94.5	1.6	4.7	-37.4 (-36.4)	17.7
3	30	23.0	62.6	6.4	109.4	88.9	1.2	4.6	-39.5 (-38.4)	
4	120	22.9	61.2	6.5	100.8	97.4	1.2	2.7	-47.8 (-46.7)	
5	120	22.9	46.7	8.5	96.5	95.4	1.5	1.7	-52.5 (-51.4)	
6	120	22.9	35.0	9.0	97.9	98.0	1.6	-2.1	-53.4 (-52.3)	19.4
7	120	23.0	28.4	5.5	93.5	88.6	1.0	4.0	-51.8 (-50.8)	
Replicate 3										
1	30	23.9	61.5	10.3	100.7	92.3	1.9	-5.5	-36.3 (-35.3)	18.4
2	30	23.2	60.4	8.7	97.7	93.2	1.6	4.0	-37.7 (-36.8)	
3	30	22.9	62.1	6.4	108.0	90.5	1.2	0.1	-39.6 (-38.6)	
4	120	22.8	59.1	6.2	98.4	93.5	1.1	9.9	-47.8 (-46.7)	
5	120	22.8	52.4	8.7	101.1	94.8	1.6		-50.6 (-49.5)	20.5
6			*not collected*							
7	120	22.7	38.7	6.1	97.6	91.6	1.1	-1.9	-52.8 (-51.8)	
Mean					102.2	92.9		1.8		19.0
Standard error (1 σ)					5.6	3.4		3.8		0.9

a: NO recovery was calculated by dividing the measured $NO_2^-+NO_3^-$ concentration by the theoretical concentration calculated using the collection time, sample flow rate (1.6 slpm), NO concentration measured in the chamber headspace, and the TEA solution volume. The TEA solution volume was corrected for evaporative loss by weighing the gas washing bottle containing the solution before and after each sample collection.

b: Relative to N_2 in the air. $\delta^{15}N$ values were corrected for the isobaric correction using the measured $\Delta^{17}O$ values. For those samples without sufficient mass for the $\Delta^{17}O$ measurement, an average $\Delta^{17}O$ value, 19.0‰, was used for the correction. $\delta^{15}N$ values before the isobaric correction are shown in the brackets.

Table A.6 Complete dataset: NO collection, field rewetting experiment.

Sample	Time (min)	T (°C)	RH (%)	NO_2^- +NO_3^- (μM)	Recovery[a] (%)	NO_2^- percent (%)	Dilution factor	P_{diff} (%)	$\delta^{15}N$[b] (‰)	$\Delta^{17}O$ (‰)
MilliQ addition										
1	120	22.1	71.3	15.9	105.7	86.3	2.8	8.8	-41.3 (-40.1)	20.7
2	120	28.2	70.1	23.1	101.5	91.3	1.3	5.8	-44.3 (-43.3)	18.7
3	120	27.8	72.6	22.5	96.4	90.0	1.3	6.8	-42.2 (-41.2)	18.8
NO_3^- addition										
1	120	26.1	70.4	10.8	112.6	88.8	1.9	8.3	-39.4 (-38.3)	19.7
2	120	28.4	68.8	21.1	104.6	93.4	1.2	9.0	-40.7 (-39.8)	18.0
3	120	28.3	70.7	23.6	102.1	91.7	1.3	6.6	-40.7 (-39.7)	18.7
NO_2^- addition										
1	45	20.6	74.8	7.0	96.4	95.6	1.2	3.7	-23.4 (-22.3)	
2	45	22.0	72.3	17.8	118.8	92.9	1.0	7.1	-25.6 (-26.6)	18.5
3	45	24.9	67.2	24.6	123.7	92.3	1.5	8.0	-28.2 (-27.2)	19.0
4	45	28.0	65.6	33.4	126.5	90.8	2.0	4.7	-30.9 (-30.0)	17.2
5	35	30.7	61.2	27.6	112.9	95.6	1.6	10.2	-32.3 (-31.4)	17.1
6	30	28.7	65.7	27.9	126.6	91.5	1.7	4.3	-34.4 (-33.4)	18.6
NH_4^+ addition										
1	120	20.7	67.0	5.7	96.4	88.2	1.0	7.2	-56.0 (-54.9)	
2	120	25.8	61.4	17.7	107.7	88.9	1.0	2.5	-59.8 (-58.7)	19.2
3	120	28.2	61.3	27.8	97.2	90.9	1.6	4.6	-57.6 (-56.6)	18.5
Mean					108.6	91.2		6.5		18.7
Standard error (1 σ)					11.0	2.6		2.2		0.9

a: NO recovery was calculated by dividing the measured NO_2^-+NO_3^- concentration by the theoretical concentration calculated using the collection time, sample flow rate (1.6 slpm), NO concentration measured in the chamber headspace, and the TEA solution volume. The TEA solution volume was corrected for evaporative loss by weighing the gas washing bottle containing the solution before and after each sample collection.

b: Relative to N_2 in the air. $\delta^{15}N$ values were corrected for the isobaric correction using the measured $\Delta^{17}O$ values. For those samples without sufficient mass for the $\Delta^{17}O$ measurement, an average $\Delta^{17}O$ value, 18.7‰, was used for the correction. $\delta^{15}N$ values before the isobaric correction are shown in the brackets.

APPENDIX B

B.1 DERIVATION OF THE $\Delta^{17}O$ DILUTION MODEL

To derive the isotopic dilution model with $\Delta^{17}O$-NO_3^- as the input, following assumptions are made: (1) soil NO_3^- pool is an open, completely mixed system, (2) $\Delta^{17}O$-NO_3^- is linear in terms of mixing, (3) both nitrification and NO_3^- consumption (including microbial NO_3^- assimilation and possibly denitrification) can be described by zero-order kinetics during each interval of measurements, (4) nitrification-produced NO_3^- has $\Delta^{17}O=0$, and (5) NO_3^- consumption does not in itself alter $\Delta^{17}O$-NO_3^-.

Consider a NO_3^- pool with an initial nonzero $\Delta^{17}O$ ($\Delta^{17}O_0$; ‰) in the soil. We define Q as the multiple of soil NO_3^- concentration ($[NO_3^-]$; $\mu g\ N \cdot g^{-1} soil_{dw}$) and $\Delta^{17}O$. At time t = 0, $Q_0 = [NO_3^-]_0 * \Delta^{17}O_0$. With the assumptions stated above we can write down expressions for the rate of change of Q:

$$\frac{dQ_t}{dt} = R_N * \Delta^{17}O_N - R_{NC} * \Delta^{17}O_t \qquad \text{Equation (B-1)}$$

Where R_N = rate of gross nitrification ($\mu g\ N \cdot g^{-1} \cdot d^{-1}$), R_{NC} = rate of gross NO_3^- consumption ($\mu g\ N \cdot g^{-1} \cdot d^{-1}$), $\Delta^{17}O_N = \Delta^{17}O$ of nitrified $NO_3^- = 0‰$. Substituting $\Delta^{17}O_t = Q_t/[NO_3^-]_t$ and $\Delta^{17}O_N = 0$, we rewrite Equation (A1) as:

$$\frac{dQ_t}{dt} + R_{NC} \cdot \frac{Q_t}{[NO_3^-]_t} = 0 \qquad \text{Equation (B-2)}$$

Define net nitrification rate $n = R_N - R_{NC} = ([NO_3^-]_t - [NO_3^-]_0)/t$. Now $[NO_3^-]_t = [NO_3^-]_0 + n*t$, giving:

$$\frac{dQ_t}{dt} + \frac{R_{NC}}{[NO_3^-]_0 + n*t} * Q_t = 0 \qquad \text{Equation (B-3)}$$

This first order linear differential equation in the form of dy/dx + f(x)y = 0 can be solved with the initial conditions to give:

$$\frac{[NO_3^-]_t}{[NO_3^-]_0} * \frac{\Delta^{17}O_t}{\Delta^{17}O_0} = \left(\frac{\Delta^{17}O_t}{\Delta^{17}O_0}\right)^{-\frac{R_{NC}}{n}} \quad \text{Equation (B-4)}$$

By substituting n with R_N and R_{NC}, natural log transformation, and rearrangement, Equation (A4) gives the $\Delta^{17}O$ dilution equations:

$$R_N = -\frac{[NO_3^-]_t - [NO_3^-]_0}{t} * \frac{\ln\left(\frac{\Delta^{17}O_t}{\Delta^{17}O_0}\right)}{\ln\left(\frac{[NO_3^-]_t}{[NO_3^-]_0}\right)} \quad \text{Equation (B-5)}$$

$$R_{NC} = -\frac{[NO_3^-]_t - [NO_3^-]_0}{t} * \left(1 + \frac{\ln\left(\frac{\Delta^{17}O_t}{\Delta^{17}O_0}\right)}{\ln\left(\frac{[NO_3^-]_t}{[NO_3^-]_0}\right)}\right) \quad \text{Equation (B-6)}$$

B.2 EQUATIONS USED IN THE $\Delta^{17}O$-BASED NUMERICAL MODEL

R_{NM} (μmol $N \cdot g^{-1} \cdot d^{-1}$) = rate of net mineralization

R_N (μmol $N \cdot g^{-1} \cdot d^{-1}$) = rate of gross nitrification

R_{NC} (μmol $N \cdot g^{-1} \cdot d^{-1}$) = rate of gross NO_3^- consumption

$\alpha = (\varepsilon/1000)+1$

$^{14}F = {}^{14}N/({}^{15}N+{}^{14}N)$

$^{15}F = {}^{15}N/({}^{15}N+{}^{14}N)$

$^{16}F = {}^{16}O/({}^{16}O+{}^{17}O+{}^{18}O)$

$^{17}F = {}^{17}O/({}^{16}O+{}^{17}O+{}^{18}O)$

$^{18}F = {}^{18}O/({}^{16}O+{}^{17}O+{}^{18}O)$

$$\frac{d[^{14}N]_{OrgN}}{dt} = -R_{NM} * {}^{14}F_{orgN}$$

$$\frac{d[^{15}N]_{OrgN}}{dt} = -R_{NM}/{}^{15}\alpha_{NM} * {}^{15}F_{orgN}$$

$$\frac{d[^{14}N]_{NH4}}{dt} = R_{NM} * {}^{14}F_{orgN} - R_N * {}^{14}F_{NH4}$$

$$\frac{d[^{15}N]_{NH4}}{dt} = R_{NM}/{}^{15}\alpha_{NM} * {}^{15}F_{orgN} - R_N/{}^{15}\alpha_N * {}^{15}F_{NH4}$$

$$\frac{d[^{14}N]_{NO3}}{dt} = R_N * {}^{14}F_{NH4} - R_{NC} * {}^{14}F_{NO3}$$

$$\frac{d[^{15}N]_{NO3}}{dt} = R_N/{}^{15}\alpha_N * {}^{15}F_{NH4} - R_{NC}/{}^{15}\alpha_{NC} * {}^{15}F_{NO3}$$

$$\frac{d[^{16}O]_{NO3}}{dt} = 2 * R_N * \left[\left(\frac{1}{2} * {}^{16}F_{O2} + \frac{1}{2} * {}^{16}F_{H2O}\right) * (1 - f_{eq}) + f_{eq} * {}^{16}F_{H2O}\right] + R_N * {}^{16}F_{H2O} - 3 * R_{NC} * {}^{16}F_{NO3}$$

$$\frac{d[^{17}O]_{NO3}}{dt} = 2 * R_N * \left[\left(\frac{1}{2} * {}^{17}F_{O2}/\left({}^{18}\alpha_{O2}\right)^{\beta} + \frac{1}{2} * {}^{17}F_{H2O}/\left({}^{18}\alpha_{H2O-1}\right)^{\beta}\right) * (1 - f_{eq}) + f_{eq} * {}^{17}F_{H2O}/\left({}^{18}\alpha_{eq}\right)^{\beta}\right]$$
$$+ R_N * {}^{17}F_{H2O}/\left({}^{18}\alpha_{H2O-2}\right)^{\beta} - 3 * R_{NC}/\left({}^{18}\alpha_{NC}\right)^{\beta} * {}^{17}F_{NO3}$$

$$\frac{d[^{18}O]_{NO3}}{dt} = 2 * R_N * \left[\left(\frac{1}{2} * {}^{18}F_{O2}/{}^{18}\alpha_{O2} + \frac{1}{2} * {}^{18}F_{H2O}/{}^{18}\alpha_{H2O-1}\right) * (1 - f_{eq}) + f_{eq} * {}^{18}F_{H2O}/{}^{18}\alpha_{eq}\right] + R_N$$
$$* {}^{18}F_{H2O}/{}^{18}\alpha_{H2O-2} - 3 * R_{NC}/{}^{18}\alpha_{NC} * {}^{18}F_{NO3}$$

B.3 SUPPLEMENTARY FIGURES AND TABLES ACCOMPANYING CHAPTER 3

Table B.1 Parameters used in the $\Delta^{17}O$-based numerical model.

Parameter	Description	Value (range tested)	Reference
β	Three-oxygen-isotope exponent	0.52 (0.51 to 0.53)	Miller, 2002; Young et al., 2002
$^{15}\varepsilon_{NM}$	N isotope effect for net mineralization	Model optimized	
$^{15}\varepsilon_{N}$	N isotope effect for NH_4^+ oxidation to NO_3^-	Model optimized	

$^{15}\varepsilon_{NC}$	N isotope effect for NO_3^- consumption	Model optimized	
$^{18}\varepsilon_{NC}$	O isotope effect for NO_3^- consumption	Coupled to $^{15}\varepsilon_{NC}$	
$^{18}\varepsilon_{O2}$	O isotope effect for O_2 incorporation by NH_4^+ oxidation	13.9‰ (8.9 to 13.9)*	Casciotti et al., 2010
$^{18}\varepsilon_{H2O-1}$	O isotope effect for H_2O incorporation by NH_4^+ oxidation	13.9‰ (8.9 to 13.9)*	Casciotti et al., 2010
$^{18}\varepsilon_{eq}$	Equilibrium isotope effect for NO_2^- /water O exchange	13.5‰	Buchwald and Casciotti, 2013
f_{eq}	Fractional O exchange between NO_2^- and water catalyzed by ammonia-oxidizer	0.2 (0 to 1)	Buchwald and Casciotti, 2010
$^{18}\varepsilon_{H2O-2}$	O isotope effect for H_2O incorporation by NO_2^- oxidation	15.5‰ (12.8 to 18.2)	Buchwald and Casciotti, 2010
$\delta^{18}O_{O2}$	Soil oxygen $\delta^{18}O$ value	23.5‰	Kroopnick and Craig, 1972
$\delta^{18}O_{H2O}$	Soil water $\delta^{18}O$ value	-10‰ (-10 to 0)†	

* The isotope effects for O atom incorporation from O_2 and H_2O during NH_4^+ oxidation to NO_2^- have only been determined as a "combined" isotope effect ranging between 17.9‰ and 37.6‰. A value of 27.8‰ was chosen and equally partitioned between the H_2O and O_2 pool (Granger and Wankel, 2016).

† Assumed to be the same as the $\delta^{18}O$ of the added deionized Milli-Q water.

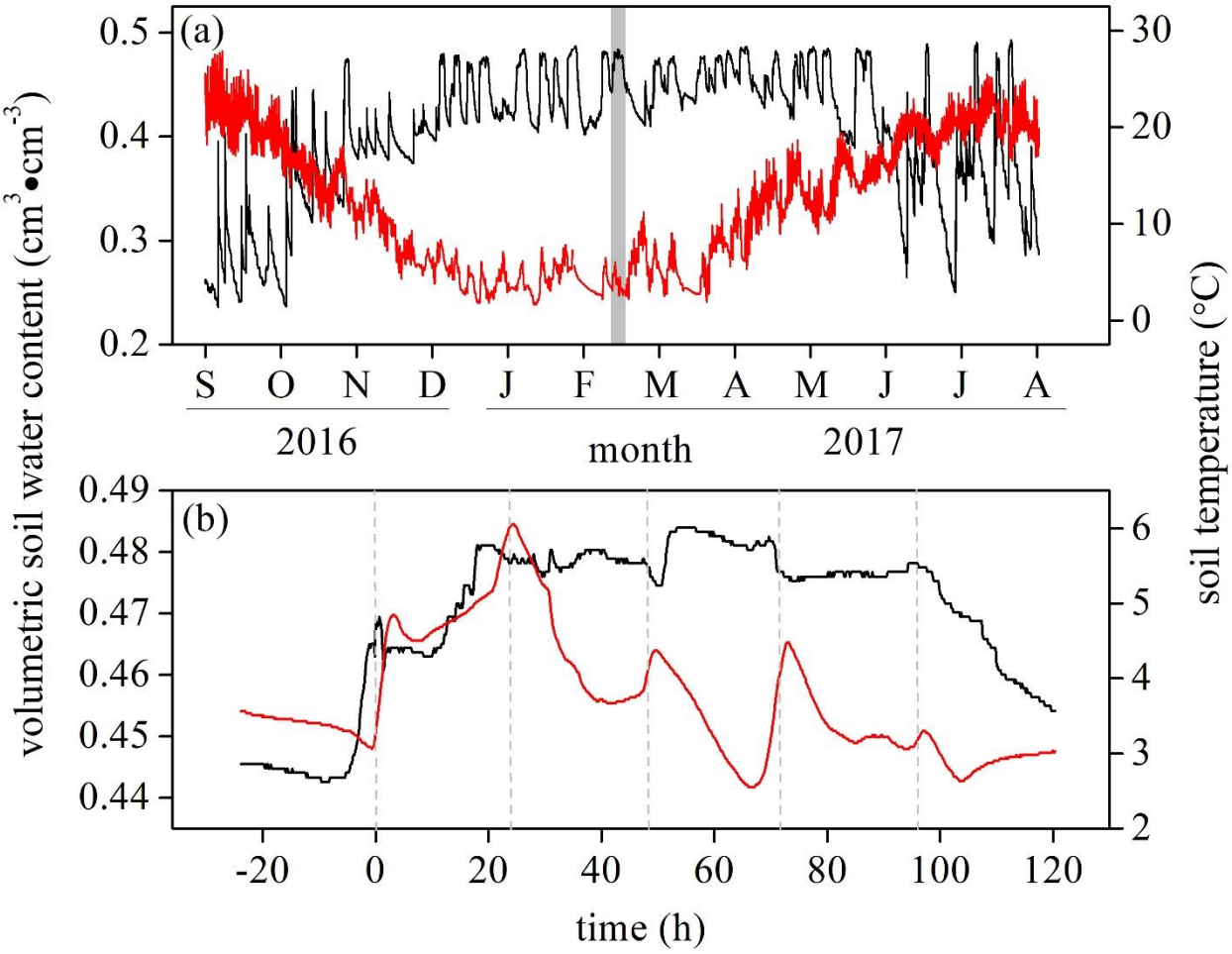

Figure B.1 Temporal variations in soil temperature (red line) and volumetric soil water content (black line) at 5 cm depth on an annual basis (a) and during the field sampling following the snowmelt (b) at the upland meadow site. The gray box in (a) denotes time period during which the field sampling was conducted. The vertical dashed lines in (b) denote times when the surface soils were collected following the snowmelt.

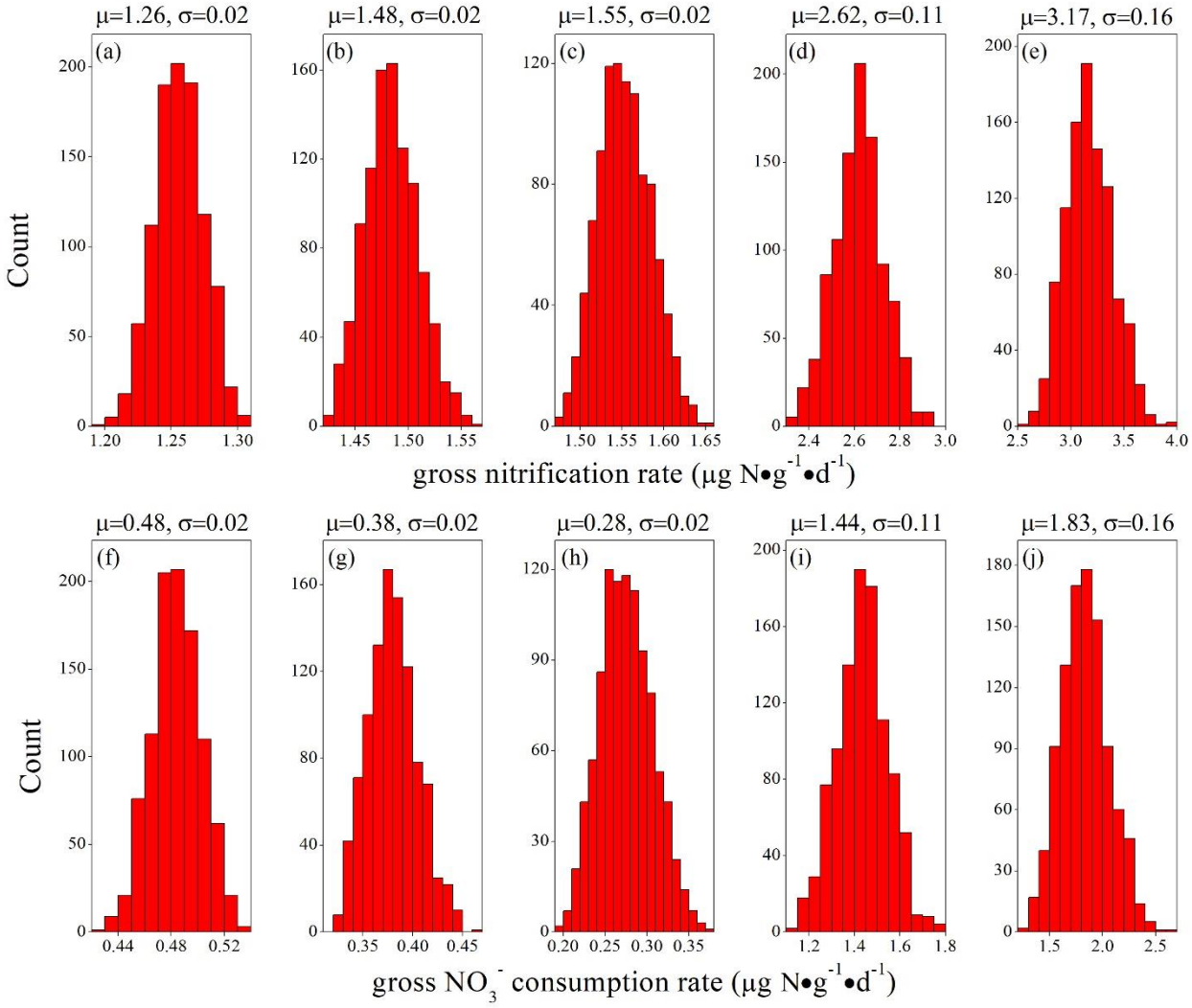

Figure B.2 Histograms of the modeled gross nitrification (a to e) and NO_3^- consumption (f to j) rates for the meadow soil, generated from 1000 times of Monte Carlo simulation that simultaneously varied β, O isotope effects of nitrification and NO_3^- consumption, $\delta^{18}O$ of the O sources, and degree of O exchange between NO_2^- and H_2O over the respective ranges given in Table B-1. Mean (μ) and standard deviation (σ) of the simulated results are shown above each panel.

APPENDIX C

Table C.1 Control tests on robustness of the soil incubation and extraction methods.

Anaerobic soil incubation[a]										
	NO_2^- ($\mu g\ N \cdot g^{-1}$)	SD	NO_3^- ($\mu g\ N \cdot g^{-1}$)	SD	$\delta^{15}N$ (‰)	SD	$\delta^{18}O$ (‰)	SD	$\Delta^{17}O$ (‰)	SD
Control	5.5	0.1	34.0	0.3	23.8	0.5	27.4	0.2	2.2	0.4
Spiked	8.5	0.2	49.2	0.5	16.9	0.3	35.9	0.3	7.4	0.4
Recovery (%)	101.2		101.0							
Back-calculated triple isotopes of the added Chilean NO_3^-					1.6		54.9		19.1	
	NO_2^- ($\mu g\ N \cdot g^{-1}$)		NO_3^- ($\mu g\ N \cdot g^{-1}$)		$\delta^{15}N$ (‰)		$\delta^{18}O$ (‰)		$\Delta^{17}O$ (‰)	
without C_2H_2	0.7	0.1	40.1	0.5	11.3	0.4	31.2	0.3	6.5	0.3
with C_2H_2	0.9	0.1	38.9	0.7	12.1	0.3	30.5	0.4	6.1	0.4
Aerobic soil incubation[b]										
	NO_2^- ($\mu g\ N \cdot g^{-1}$)		NO_3^- ($\mu g\ N \cdot g^{-1}$)		$\delta^{15}N$ (‰)		$\delta^{18}O$ (‰)		$\Delta^{17}O$ (‰)	
Control			44.4	0.5	-4.5	0.1	16.7	0.1	0.1	0.2
Spiked	5.1	0.0	61.7	0.1	-3.1	0.3	27.2	0.2	5.6	0.4
Recovery	101.3		105.4							
Back-calculated triple isotopes of the added Chilean NO_3^-					0.5		54.3		19.7	

a: 3.0 μg NO_2^--N·g^{-1} and 15.1 μg NO_3^--N·g^{-1} were amended using the Chilean nitrate fertilizer.

b: 5.0 μg NO_2^--N·g^{-1} and 16.4 μg NO_3^--N·g^{-1} were amended using the Chilean nitrate fertilizer.

Table C.2 Summary of NO collection samples rerun using *Pseudomonas chloroaphis* and the denitrifier method. All the samples were collected using the laboratory version of the DFC system.

Sample	Time (min)	T (°C)	RH (%)	NO_2^-+NO_3^- (μM)	Recovery (%)	NO_2^- percent (%)	$\delta^{15}N$ (‰)
34 ppbv NO (n=4)	120	24.8	27.1	4.1	100.7	93.1	-70.5±0.2
101 ppbv NO (n=4)	120	23.1	34.2	11.9	98.2	94.0	-70.1±1.0
101 ppbv NO + 500 ppbv NH_3 (n=4)	120	23.1	46.5	11.7	97.5	91.5	-70.8±0.4
101 ppbv NO + HONO (n=4)	120	22.3	89.7	11.6	96.7	89.8	-70.1±0.7
Mean					**98.3**	**92.1**	**-70.4**
Standard error (1 σ)					**1.7**	**1.8**	**0.6**

Table C.3 Data table: concentrations of NO_3^- and NO_2^- and net NO production rates during the anaerobic incubation.

Sampling time (h)	NO_3^- (μg N·g^{-1})	SD	NO_2^- (μg N·g^{-1})	SD	f_{NO} (μg N·g^{-1}·h^{-1})	SD
0.0	49.3	0.1	0.4	0.1	0.063	0.008
25.3	45.6	0.1	1.2	0.3	0.070	0.002
48.3	42.2	0.6	1.9	0.2	0.073	0.003
73.8	38.5	0.3	2.8	0.2	0.076	0.002
97.6	35.1	0.6	4.2	0.3	0.082	0.003
121.6	31.6	0.9	5.2	0.4	0.080	0.000
145.0	28.2	0.9	5.4	0.6	0.081	0.001
169.1	24.7	0.2	6.9	0.1	0.081	0.000

Table C.4 Data table: isotopic compositions of NO_3^-, NO_2^-, and NO during the anaerobic incubation.

Time (h)	δ^{15}N-NO_3^- (‰)	SD	δ^{18}O-NO_3^- (‰)	SD	Δ^{17}O-NO_3^- (‰)	SD	δ^{15}N-NO_2^- (‰)[a]	SD	δ^{15}N-NO (‰)	SD
0.0	4.7	0.3	33.4	0.2	10.0	0.2	NA	NA	-47.7	0.3
25.3	8.7	0.2	31.2	0.4	8.4	0.5	NA	NA	-43.5	0.7
48.3	12.8	0.2	29.9	0.9	6.0	0.3	NA	NA	-40.2	1.2
73.8	17.4	0.8	27.7	0.3	4.5	0.4	NA	NA	-37.1	0.9
97.6	22.6	0.6	26.3	0.3	2.9	0.2	NA	NA	-32.8	1.2
121.6	26.7	0.7	26.1	0.9	1.6	0.2	-6.9	3.7	-29.1	0.4
145.0	31.0	1.2	24.5	1.3	1.1	0.6	-6.0	2.5	-26.8	0.3
169.1	36.7	1.5	23.1	0.3	0.7	0.1	0.9	1.3	-22.8	2.2

a: NA: not measured due to low NO_2^- concentration.

Table C.5 Data table: concentrations of NO_3^- and NH_4^+ and net NO production rates during the aerobic incubation.

Sampling time (h)	NO_3^- (μg N·g^{-1})	SD	NO_2^- (μg N·g^{-1})	SD	f_{NO} (μg N·g^{-1}·h^{-1})	SD
Low δ^{15}N-NH_4^+						
0.0	87.2	3.3	46.8	0.6	NA	NA
26.2	73.0	1.5	55.8	1.1	0.0080	0.0001
50.5	63.7	1.2	65.5	0.1	0.0077	0.0002
76.8	54.2	1.6	76.2	0.4	0.0074	0.0001
Intermediate δ^{15}N-NH_4^+						
0.0	88.9	0.7	45.3	0.2	NA	NA
26.4	74.8	0.8	55.2	0.2	0.0082	0.0000
50.3	64.5	1.4	65.0	0.1	0.0079	0.0001
74.4	53.7	0.7	75.4	0.3	0.0071	0.0001
High δ^{15}N-NH_4^+						
0.0	86.5	1.0	45.7	0.1	NA	NA
26.3	74.1	0.9	54.9	0.5	0.0085	0.0001
50.3	64.4	0.2	65.1	0.7	0.0080	0.0001
74.4	54.7	1.0	75.0	0.4	0.0075	0.0001

a: NA: no measurement.

Table C.6 Data table: isotopic compositions of NO_3^-, NH_4^+, and NO during the aerobic incubation.

Time (h)	$\delta^{15}N\text{-}NH_4^+$ (‰)	SD	$\delta^{15}N\text{-}NO_3^-$ (‰)	SD	$\delta^{18}O\text{-}NO_3^-$ (‰)	SD	$\Delta^{17}O\text{-}NO_3^-$ (‰)	SD	$\delta^{15}N\text{-}NO$ (‰)[a]	SD
Low $\delta^{15}N\text{-}NH_4^+$										
0.0	-0.5	0.2	2.7	0.1	18.9	0.2	5.7	0.2	NA	NA
26.2	4.0	1.6	-3.1	0.4	15.0	0.4	4.8	0.4	-54.9	0.8
50.5	7.4	2.5	-6.3	0.0	11.4	0.0	3.9	0.0	-53.3	0.5
76.8	11.4	0.2	-8.3	0.0	9.1	0.5	3.3	0.5	NA	NA
Intermediate $\delta^{15}N\text{-}NH_4^+$										
0.0	22.6	2.2	2.8	0.3	19.2	0.2	5.8	0.2	NA	NA
26.4	24.1	1.0	1.3	0.1	14.5	0.2	4.7	0.2	-37.4	1.3
50.3	29.7	1.3	0.8	0.5	11.4	0.4	3.9	0.4	-33.5	0.2
74.4	31.2	2.1	1.6	0.6	9.5	0.4	3.5	0.4	NA	NA
High $\delta^{15}N\text{-}NH_4^+$										
0.0	43.3	2.1	2.8	0.3	18.9	0.1	5.8	0.1	NA	NA
26.3	50.8	2.3	5.2	0.8	14.6	0.1	4.6	0.1	-17.9	1.9
50.3	53.9	3.4	8.0	0.1	11.7	0.1	4.0	0.1	-16.8	0.3
74.4	56.4	3.4	10.6	0.3	9.6	0.2	3.3	0.2	NA	NA

a: NA-no measurement.

Table C.7 Data table: Net production and isotopic composition of abiotically produced NO in nitrite-amended sterile soil.

Time (h)	$f_{NO\text{-}abiotic}$ ($\mu g\ N \cdot g^{-1} \cdot h^{-1}$)	SD	$\delta^{15}N\text{-}NO$ (‰)[a]	SD
0.4	0.0825	0.0046	-17.8	0.4
20.9	0.0552	0.0031	NA	NA
48.7	0.0309	0.0029	NA	NA
74.6	0.0181	0.0015	NA	NA
91.6	0.0124	0.0012	NA	NA
120.9	0.0079	0.0009	NA	NA
145.1	0.0047	0.0005	NA	NA
170.1	0.0035	0.0003	NA	NA
189.4	0.0026	0.0002	NA	NA

a: NA-no measurement.

APPENDIX D

D.1 DATA TABLES ACCOMPANYING CHAPTER 5

Table D.1 Nitrate concentration and dual isotope data for the meadow site.*

month/year	Soil extract				Lysimeter sample			
	sample name	μg N·g^{-1}	$\delta^{15}N$	$\delta^{18}O$	sample name	μM	$\delta^{15}N$	$\delta^{18}O$
September/2016	092016-LH-SE-H-L	1.4	-3.7	17.3	092016-LH-LY-L	18.5	-5.0	11.3
September/2016	092016-LH-SE-H-L	2.8	-9.5	4.7	092016-LH-LY-M	21.4	-7.4	10.3
September/2016	092016-LH-SE-H-L	1.6	-1.3	21.3	092016-LH-LY-R	9.0	-3.5	19.1
October/2016	102016-LH-SE-H-L	0.9	4.6	18.9	102016-LH-LY-L	6.8	-3.9	5.7
October/2016	102016-LH-SE-H-L	1.1	-10.6	1.6	102016-LH-LY-L	17.9	-3.8	-3.2
October/2016	102016-LH-SE-H-L	0.9	4.6	20.2	102016-LH-LY-L	9.0	-2.7	1.0
November/2016	112016-LH-SE-H-L	2.9	0.2	20.3	112016-LH-LY-L	13.7	-2.3	-0.6
November/2016	112016-LH-SE-H-L	3.0	-11.9	-2.5	112016-LH-LY-L	24.3	-1.6	-1.2
November/2016	112016-LH-SE-H-L	1.1	8.3	12.8	112016-LH-LY-L	18.8	-2.0	-2.2
December/2016	122016-LH-SE-H-L	3.1	37.0	19.9	122016-LH-LY-L	11.2	1.9	2.3
December/2016	122016-LH-SE-H-L	2.8	-3.7	4.4	122016-LH-LY-L	17.4	2.0	0.2
December/2016	122016-LH-SE-H-L	1.9	-1.2	22.0	122016-LH-LY-L	21.3	0.7	-0.4
January/2017	012017-LH-SE-H-L	0.9	2.3	18.7	012017-LH-LY-L	45.7	1.6	-0.4
January/2017	012017-LH-SE-H-L	1.8	-4.1	1.1	012017-LH-LY-L	70.9	1.2	-1.1
January/2017	012017-LH-SE-H-L	0.5	-1.4	16.1	012017-LH-LY-L	27.8	1.1	-0.9
February/2017	022017-LH-SE-H-L	1.1	0.5	11.2	022017-LH-LY-L	45.1	-0.2	0.2
February/2017	022017-LH-SE-H-L	1.4	0.6	15.6	022017-LH-LY-L	34.1	1.5	1.4
February/2017	022017-LH-SE-H-L	0.7	5.4	13.4	022017-LH-LY-L	78.2	-2.3	1.1
March/2017	032017-LH-SE-H-L	0.6	3.5	22.3	032017-LH-LY-L	13.4	-5.6	5.6
March/2017	032017-LH-SE-H-L	1.2	7.5	7.8	032017-LH-LY-L	25.6	-7.3	3.2
March/2017	032017-LH-SE-H-L	1.4	3.2	11.3	032017-LH-LY-L	20.1	-2.1	4.5
April/2017	042017-LH-SE-H-L	0.4	11.4	25.4	042017-LH-LY-L	11.9	4.1	-0.5
April/2017	042017-LH-SE-H-L	0.6	12.3	19.5	042017-LH-LY-L	13.2	3.3	3.2
April/2017	042017-LH-SE-H-L	0.4	4.6	23.0	042017-LH-LY-L	29.7	5.5	-4.7
May/2017	052017-LH-SE-H-L	0.7	8.2	20.5	052017-LH-LY-L	15.5	3.0	0.6
May/2017	052017-LH-SE-H-L	0.7	-3.0	11.0	052017-LH-LY-L	8.5	11.3	9.7
May/2017	052017-LH-SE-H-L	ND	NA	NA	052017-LH-LY-L	8.3	1.1	-0.7
June/2017	062017-LH-SE-H-L	ND	NA	NA	062017-LH-LY-L	NW	NA	NA
June/2017	062017-LH-SE-H-L	ND	NA	NA	062017-LH-LY-L	24.1	4.6	-5.3
June/2017	062017-LH-SE-H-L	0.5	-2.8	20.6	062017-LH-LY-L	4.7	2.1	-3.0
July/2017	072017-LH-SE-H-L	0.4	-6.5	9.1	072017-LH-LY-L	5.0	-3.1	-0.6

July/2017	072017-LH-SE-H-L	ND	NA	NA	072017-LH-LY-L	17.7	1.7	-3.3
July/2017	072017-LH-SE-H-L	0.5	-1.8	17.2	072017-LH-LY-L	NW	NA	NA
August/2017	082017-LH-SE-H-L	0.7	3.2	9.4	082017-LH-LY-L	11.4	-11.9	-0.8
August/2017	082017-LH-SE-H-L	1.5	-6.3	1.2	082017-LH-LY-L	13.4	1.3	-2.1
August/2017	082017-LH-SE-H-L	0.7	-1.1	6.5	082017-LH-LY-L	29.8	4.0	-3.7

* "ND" denotes NO_3^- concentration was below detection limit; "NW" denotes no water in lysimeter at the time of sampling; "NA" indicates that isotope data is not available.

Table D.2 Nitrate concentration and dual isotope data for the forest site.*

month/year	Soil extract				Lysimeter sample			
	sample name	μg N·g^{-1}	$\delta^{15}N$	$\delta^{18}O$	sample name	μM	$\delta^{15}N$	$\delta^{18}O$
September/2016	092016-UP-SE-H-L	9.9	0.4	-2.5	092016-UP-LY-L	190.2	10.7	4.3
September/2016	092016-UP-SE-H-L	20.0	4.0	-2.3	092016-UP-LY-L	142.2	3.4	-0.9
September/2016	092016-UP-SE-H-L	13.8	2.8	-0.7	092016-UP-LY-L	169.6	5.6	0.8
October/2016	102016-UP-SE-H-L	6.7	0.4	-8.4	102016-UP-LY-L	103.6	3.1	-2.6
October/2016	102016-UP-SE-H-L	7.1	1.6	-7.1	102016-UP-LY-L	189.8	2.9	-2.9
October/2016	102016-UP-SE-H-L	8.4	1.0	-7.9	102016-UP-LY-L	29.6	3.6	2.1
November/2016	112016-UP-SE-H-L	19.3	3.1	-4.1	112016-UP-LY-L	105.0	2.2	-0.1
November/2016	112016-UP-SE-H-L	17.3	1.7	-4.0	112016-UP-LY-L	23.4	1.5	0.1
November/2016	112016-UP-SE-H-L	78.0	9.2	-1.7	112016-UP-LY-L	91.6	4.1	-1.1
December/2016	122016-UP-SE-H-L	11.4	16.7	4.3	122016-UP-LY-L	203.8	5.3	-1.2
December/2016	122016-UP-SE-H-L	7.8	0.6	-2.7	122016-UP-LY-L	57.5	6.6	0.1
December/2016	122016-UP-SE-H-L	11.6	0.8	-2.7	122016-UP-LY-L	72.4	3.6	-3.1
January/2017	012017-UP-SE-H-L	5.1	1.3	-7.6	012017-UP-LY-L	51.2	5.4	-2.0
January/2017	012017-UP-SE-H-L	6.5	1.1	-7.1	012017-UP-LY-L	22.1	6.8	0.0
January/2017	012017-UP-SE-H-L	11.2	2.7	-7.0	012017-UP-LY-L	41.5	2.0	-4.1
February/2017	022017-UP-SE-H-L	3.3	-1.7	-9.1	022017-UP-LY-L	29.0	5.3	-0.4
February/2017	022017-UP-SE-H-L	3.7	-2.9	-6.1	022017-UP-LY-L	12.3	2.4	-4.6
February/2017	022017-UP-SE-H-L	3.2	-1.7	-8.6	022017-UP-LY-L	32.1	1.6	-5.2
March/2017	032017-UP-SE-H-L	11.3	-1.9	-3.4	032017-UP-LY-L	14.2	2.8	-1.4
March/2017	032017-UP-SE-H-L	30.2	-1.3	-4.3	032017-UP-LY-L	11.3	1.3	-2.3
March/2017	032017-UP-SE-H-L	22.9	2.1	-1.3	032017-UP-LY-L	24.5	3.5	1.0
April/2017	042017-UP-SE-H-L	1.5	-14.8	-2.1	042017-UP-LY-L	77.4	4.5	1.5
April/2017	042017-UP-SE-H-L	2.6	-11.3	0.2	042017-UP-LY-L	80.3	3.5	0.4
April/2017	042017-UP-SE-H-L	4.0	-8.6	1.6	042017-UP-LY-L	45.6	2.8	1.2
May/2017	052017-UP-SE-H-L	4.3	-3.1	-4.6	052017-UP-LY-L	NW	NA	NA
May/2017	052017-UP-SE-H-L	5.8	-2.3	-3.3	052017-UP-LY-L	8.4	1.5	5.9
May/2017	052017-UP-SE-H-L	4.0	0.0	-2.5	052017-UP-LY-L	8.4	-1.1	12.6
June/2017	062017-UP-SE-H-L	19.1	-1.6	-2.5	062017-UP-LY-L	16.6	3.3	-0.9

June/2017	062017-UP-SE-H-L	7.0	-1.6	-2.9	062017-UP-LY-L	81.4	3.1	-2.9
June/2017	062017-UP-SE-H-L	5.2	-2.0	-3.8	062017-UP-LY-L	11.2	2.2	1.6
July/2017	072017-UP-SE-H-L	37.3	6.3	-0.5	072017-UP-LY-L	NW	NA	NA
July/2017	072017-UP-SE-H-L	15.2	6.8	1.6	072017-UP-LY-L	21.9	5.1	-0.6
July/2017	072017-UP-SE-H-L	6.2	6.0	0.7	072017-UP-LY-L	186.4	5.6	-1.6
August/2017	082017-UP-SE-H-L	8.8	2.9	-2.2	082017-UP-LY-L	12.5	-4.9	0.2
August/2017	082017-UP-SE-H-L	14.5	2.8	-1.9	082017-UP-LY-L	13.7	2.9	-1.2
August/2017	082017-UP-SE-H-L	5.2	0.2	-4.1	082017-UP-LY-L	24.6	3.2	-1.1

* "ND" denotes NO_3^- concentration was below detection limit; "NW" denotes no water in lysimeter at the time of sampling; "NA" indicates that isotope data is not available.

Table D.3 Nitrate concentration and dual isotope data for the riparian site.*

month/year	Soil extract				Lysimeter sample			
	sample name	μg N·g^{-1}	$\delta^{15}N$	$\delta^{18}O$	sample name	μM	$\delta^{15}N$	$\delta^{18}O$
September/2016	092016-RP-SE-H-L	8.1	0.2	-2.8	092016-RP-LY-L	1130.9	4.8	-1.4
September/2016	092016-RP-SE-H-L	14.4	0.2	-2.1	092016-RP-LY-L	570.9	2.8	-3.4
September/2016	092016-RP-SE-H-L	12.4	1.4	-4.2	092016-RP-LY-L	354.9	4.1	-2.8
October/2016	102016-RP-SE-H-L	6.2	2.6	-3.7	102016-RP-LY-L	443.3	4.5	-2.6
October/2016	102016-RP-SE-H-L	4.3	0.3	-7.9	102016-RP-LY-L	273.3	2.7	-4.3
October/2016	102016-RP-SE-H-L	5.9	0.9	-8.0	102016-RP-LY-L	335.9	4.4	-3.5
November/2016	112016-RP-SE-H-L	15.0	6.4	1.1	112016-RP-LY-L	324.6	4.2	-3.2
November/2016	112016-RP-SE-H-L	15.3	0.4	-4.0	112016-RP-LY-L	277.4	2.5	-5.2
November/2016	112016-RP-SE-H-L	36.8	0.0	-4.3	112016-RP-LY-L	337.7	5.4	-2.7
December/2016	122016-RP-SE-H-L	3.0	1.3	0.3	122016-RP-LY-L	266.5	4.2	-4.8
December/2016	122016-RP-SE-H-L	8.3	-1.1	-1.9	122016-RP-LY-L	203.8	1.2	-2.1
December/2016	122016-RP-SE-H-L	9.3	-1.4	-4.1	122016-RP-LY-L	340.5	4.2	-3.4
January/2017	012017-RP-SE-H-L	3.8	1.1	-6.9	012017-RP-LY-L	275.7	4.4	-4.7
January/2017	012017-RP-SE-H-L	7.0	-0.4	-7.0	012017-RP-LY-L	137.7	4.2	-5.9
January/2017	012017-RP-SE-H-L	9.5	0.1	-7.5	012017-RP-LY-L	129.7	4.9	-5.5
February/2017	022017-RP-SE-H-L	0.8	1.2	-8.4	022017-RP-LY-L	258.2	5.2	-4.9
February/2017	022017-RP-SE-H-L	3.3	-0.4	-4.5	022017-RP-LY-L	258.6	4.5	-6.0
February/2017	022017-RP-SE-H-L	2.5	-1.3	-5.6	022017-RP-LY-L	290.3	2.1	-5.9
March/2017	032017-RP-SE-H-L	12.4	2.6	2.4	032017-RP-LY-L	540.8	0.5	-4.3
March/2017	032017-RP-SE-H-L	5.6	1.3	1.4	032017-RP-LY-L	134.1	-0.1	-2.3
March/2017	032017-RP-SE-H-L	18.5	3.8	3.5	032017-RP-LY-L	723.1	0.9	-4.2
April/2017	042017-RP-SE-H-L	4.1	-9.8	2.4	042017-RP-LY-L	25.7	2.2	-1.6
April/2017	042017-RP-SE-H-L	2.1	-5.1	2.2	042017-RP-LY-L	23.5	3.2	-1.5
April/2017	042017-RP-SE-H-L	4.0	-7.0	3.0	042017-RP-LY-L	23.4	3.8	2.4
May/2017	052017-RP-SE-H-L	2.6	-2.5	-2.9	052017-RP-LY-L	21.3	5.6	-1.1
May/2017	052017-RP-SE-H-L	2.4	0.0	-2.3	052017-RP-LY-L	14.9	1.3	1.2

May/2017	052017-RP-SE-H-L	8.5	11.9	1.3	052017-RP-LY-L	12.9	3.5	1.2
June/2017	062017-RP-SE-H-L	7.4	-5.6	-1.9	062017-RP-LY-L	NW	NA	NA
June/2017	062017-RP-SE-H-L	3.0	-9.5	-2.5	062017-RP-LY-L	5.1	-3.4	1.8
June/2017	062017-RP-SE-H-L	6.8	0.4	6.1	062017-RP-LY-L	6.0	3.2	2.6
July/2017	072017-RP-SE-H-L	2.3	0.3	0.8	072017-RP-LY-L	12.2	2.3	-2.2
July/2017	072017-RP-SE-H-L	2.8	2.5	1.9	072017-RP-LY-L	26.6	1.6	-4.1
July/2017	072017-RP-SE-H-L	15.2	4.9	0.7	072017-RP-LY-L	43.8	4.3	-4.2
August/2017	082017-RP-SE-H-L	5.3	1.7	-2.1	082017-RP-LY-L	101.0	2.1	-3.3
August/2017	082017-RP-SE-H-L	5.8	1.0	-2.8	082017-RP-LY-L	176.8	4.0	-2.4
August/2017	082017-RP-SE-H-L	6.7	3.0	-2.5	082017-RP-LY-L	53.4	3.5	-4.0

* “ND” denotes NO_3^- concentration was below detection limit; “NW” denotes no water in lysimeter at the time of sampling; “NA” indicates that isotope data is not available.

BIBLIOGRAPHY

Aber, J., McDowell, W., Nadelhoffer, K., Magill, A., Berntson, G., Kamakea, M., McNulty, S., Currie, W., Rustad, L. and Fernandez, I., 1998. Nitrogen saturation in temperate forest ecosystems. *BioScience*, *48*(11), 921-934.

Aber, J.D., Goodale, C.L., Ollinger, S.V., Smith, M.L., Magill, A.H., Martin, M.E., Hallett, R.A. and Stoddard, J.L., 2003. Is nitrogen deposition altering the nitrogen status of northeastern forests?. *AIBS Bulletin*, *53*(4), 375-389.

Aber, J.D., Nadelhoffer, K.J., Steudler, P. and Melillo, J.M., 1989. Nitrogen saturation in northern forest ecosystems. *BioScience*, *39*(6), 378-286.

Adams, M.B., Kochenderfer, J.N. and Edwards, P.J., 2007. The Fernow watershed acidification study: ecosystem acidification, nitrogen saturation and base cation leaching. In *Acid Rain-Deposition to Recovery* (pp. 267-273). Springer, Dordrecht.

Akimoto, H., 2003. Global air quality and pollution. *Science*, *302*(5651), 1716-1719.

Allen, R.G., Smith, M., Perrier, A. and Pereira, L.S., 1994. An update for the definition of reference evapotranspiration. *ICID bulletin*, *43*(2), 1-34.

Altieri, K.E., Hastings, M.G., Peters, A.J., Oleynik, S., Sigman, D.M., 2014. Isotopic evidence for a marine ammonium source in rainwater at Bermuda. *Global Biogeochemistry Cycles*, *28*(10), 1066-1080.

Atkinson, R., Arey, J., 2003. Gas-phase tropospheric chemistry of biogenic volatile organic compounds: a review. *Atmospheric Environment*, *37*, 197-219.

Atkinson, R., Baulch, D. L., Cox, R. A., Crowley, J. N., Hampson, R. F., Hynes, R. G., Jenkin, M. E., Rossi, M. J., Troe, J., Subcommittee, I. U. P. A. C., 2006. Evaluated kinetic and photochemical data for atmospheric chemistry: Volume II–gas phase reactions of organic species. *Atmospheric Chemistry and Physics*, *6*(11), 3625-4055.

Babbin, A.R., Peters, B.D., Mordy, C.W., Widner, B., Casciotti, K.L. and Ward, B.B., 2017. Multiple metabolisms constrain the anaerobic nitrite budget in the Eastern Tropical South Pacific. *Global Biogeochemical Cycles*, *31*(2), 258-271.

Bain, D.J., Copeland, E.M., Divers, M.T., Hecht, M., Hopkins, K.G., Hynicka, J., Koryak, M., Kostalos, M., Brown, L., Elliott, E.M. and Fedor, J., 2014. Characterizing a major urban stream restoration project: Nine Mile Run (Pittsburgh, Pennsylvania, USA). *JAWRA Journal of the American Water Resources Association*, *50*(6), 1608-1621.

Bakken, L.R., Bergaust, L., Liu, B. and Frostegård, Å., 2012. Regulation of denitrification at the cellular level: a clue to the understanding of N2O emissions from soils. *Philosophical Transactions of the Royal Society B*, *367*(1593), 1226-1234.

Belser, L.W., Mays, E.L., 1980. Specific inhibition of nitrite oxidation by chlorate and its use in assessing nitrification in soils and sediments. *Applied and Environmental Microbiology*, 39(3), 505-510.

Berntson, G.M. and Aber, J.D., 2000. Fast nitrate immobilization in N saturated temperate forest soils. *Soil Biology and Biochemistry*, *32*(2), 151-156.

Bertram, T.H., Heckel, A., Richter, A., Burrows, J.P., Cohen, R.C., 2005. Satellite measurements of daily variations in soil NO_x emissions. *Geophysical Research Letter*, *32*(24), L24812.

Betlach, M.R. and Tiedje, J.M., 1981. Kinetic explanation for accumulation of nitrite, nitric oxide, and nitrous oxide during bacterial denitrification. *Applied and Environmental Microbiology*, *42*(6), 1074-1084.

Blackmer, A.M. and Bremner, J.M., 1977. Nitrogen isotope discrimination in denitrification of nitrate in soils. *Soil Biology and Biochemistry*, *9*(2), 73-77.

Bock, E., Wilderer, P.A. and Freitag, A., 1988. Growth of Nitrobacter in the absence of dissolved oxygen. *Water Research*, *22*(2), 245-250.

Booth, M.S., Stark, J.M., Rastetter, E., 2005. Controls on nitrogen cycling in terrestrial ecosystems: a synthetic analysis of literature data. *Ecological Monographs*, 75(2), 139-157.

Brunner, B., Contreras, S., Lehmann, M.F., Matantseva, O., Rollog, M., Kalvelage, T., Klockgether, G., Lavik, G., Jetten, M.S., Kartal, B. and Kuypers, M.M., 2013. Nitrogen isotope effects induced by anammox bacteria. *Proceedings of the National Academy of Sciences*, *110*(47), 18994-18999.

Bryan, B.A., Shearer, G., Skeeters, J.L. and Kohl, D.H., 1983. Variable expression of the nitrogen isotope effect associated with denitrification of nitrite. *Journal of Biological Chemistry*, *258*(14), 8613-8617.

Buchwald, C., Casciotti, K.L., 2010. Oxygen isotopic fractionation and exchange during bacterial nitrite oxidation. *Limnology and Oceanography*, 55(3), 1064-1074.

Buchwald, C., Grabb, K., Hansel, C.M. and Wankel, S.D., 2016. Constraining the role of iron in environmental nitrogen transformations: dual stable isotope systematics of abiotic NO 2− reduction by Fe (II) and its production of N 2 O. *Geochimica et Cosmochimica Acta*, *186*, 1-12.

Canfield, D.E., Glazer, A.N. and Falkowski, P.G., 2010. The evolution and future of Earth's nitrogen cycle. *Science*, *330*(6001), 192-196.

Cape, J. N., 2009. The use of passive diffusion tubes for measuring concentrations of nitrogen dioxide in air. *Critical Reviews in Analytical Chemistry*, 39(4), 289-310.

Casciotti, K.L., Böhlke, J.K., McIlvin, M.R., Mroczkowski, S.J., Hannon, J.E., 2007. Oxygen isotopes in nitrite: analysis, calibration, and equilibration. *Analytical Chemistry, 79*(6), 2427-2436.

Casciotti, K.L., 2009. Inverse kinetic isotope fractionation during bacterial nitrite oxidation. *Geochimica et Cosmochimica Acta, 73*(7), 2061-2076.

Casciotti, K.L., Buchwald, C., McIlvin, M., 2013. Implications of nitrate and nitrite isotopic measurements for the mechanisms of nitrogen cycling in the Peru oxygen deficient zone. *Deep Sea Research Part I: Oceanographic Research Papers*, 80, 78-93.

Casciotti, K.L., McIlvin, M., Buchwald, C., 2010. Oxygen isotopic exchange and fractionation during bacterial ammonia oxidation. *Limnology and Oceanography*, 55(2), 753-762.

Casciotti, K.L., Sigman, D.M., Hastings, M.G., Böhlke, J.K., Hilkert, A., 2002. Measurement of the oxygen isotopic composition of nitrate in seawater and freshwater using the denitrifier method. *Analytical Chemistry*, 74(19), 4905-4912.

Casciotti, K.L., Sigman, D.M., Ward, B.B., 2003. Linking diversity and stable isotope fractionation in ammonia-oxidizing bacteria. *Geomicrobiology Journal*, 20(4), 335-353.

Cawse, P.A. and Cornfield, A.H., 1971. Factors affecting the formation of nitrite in γ-irradiated soils and its relationship with denitrifying potential. *Soil Biology and Biochemistry, 3*(2), pp.111-120.

Cheng, Y., Wang, J., Wang, J., Chang, S.X., Wang, S., 2017. The quality and quantity of exogenous organic carbon input control microbial NO_3^- immobilization: A meta-analysis. *Soil Biology and Biochemistry*, 115, 357-363.

Chien, S.H., Shearer, G. and Kohl, D.H., 1977. The Nitrogen Isotope Effect Associated with Nitrate and Nitrite Loss from Waterlogged Soils 1. *Soil Science Society of America Journal, 41*(1), 63-69.

Coplen, T.B., Böhlke, J.K., Casciotti, K.L., 2004. Using dual-bacterial denitrification to improve $\delta^{15}N$ determinations of nitrates containing mass-independent ^{17}O. *Rapid Communication in Mass Spectrometry, 18*(3), 245-250.

Corre, M.D., Schnabel, R.R., Stout, W.L., 2002. Spatial and seasonal variation of gross nitrogen transformations and microbial biomass in a Northeastern US grassland. *Soil Biology and Biochemistry*, 34(4), 445-457.

Costa, A.W., Michalski, G., Schauer, A.J., Alexander, B., Steig, E.J., Shepson, P.B., 2011. Analysis of atmospheric inputs of nitrate to a temperate forest ecosystem from $\Delta^{17}O$ isotope ratio measurements. *Geophysical Research Letters*, 38(15).

Dahal, B., Hastings, M.G., 2016. Technical considerations for the use of passive samplers to quantify the isotopic composition of NO_x and NO_2 using the denitrifier method. *Atmospheric Environment*, *143*, 60-66.

Dähnke, K. and Thamdrup, B., 2016. Isotope fractionation and isotope decoupling during anammox and denitrification in marine sediments. *Limnology and Oceanography*, *61*(2), 610-624.

Dale, A.W., Sommer, S., Ryabenko, E., Noffke, A., Bohlen, L., Wallmann, K., Stolpovsky, K., Greinert, J. and Pfannkuche, O., 2014. Benthic nitrogen fluxes and fractionation of nitrate in the Mauritanian oxygen minimum zone (Eastern Tropical North Atlantic). *Geochimica et Cosmochimica Acta*, *134*, 234-256.

Davidson, E.A., 1992a. Sources of nitric oxide and nitrous oxide following wetting of dry soil. *Soil Science Society of America Journal*, *56*(1), 95-102.

Davidson, E. A., 1992b. Pulses of nitric oxide and nitrous oxide flux following wetting of dry soil: An assessment of probable sources and importance relative to annual fluxes. *Ecological Bulletins*, 149-155.

Davidson, E.A., Keller, M., Erickson, H.E., Verchot, L.V., Veldkamp, E., 2000a. Testing a conceptual model of soil emissions of nitrous and nitric Oxides. *Bioscience, 50*(8), 667-680.

Davidson, E.A., Savage, K.V.L.V., Verchot, L.V., Navarro, R., 2002. Minimizing artifacts and biases in chamber-based measurements of soil respiration. *Agricultural and Forest Meteorology*, *113*(1), 21-37.

Davidson, E.A., Verchot, L.V., 2000b. Testing the hole-in-the-pipe model of nitric and nitrous oxide emissions from soils using the TRAGNET database. *Global Biogeochemical Cycles*, *14*(4), 1035-1043.

Davidson, E.A., Hart, S.C. and Firestone, M.K., 1992. Internal cycling of nitrate in soils of a mature coniferous forest. *Ecology*, *73*(4), 1148-1156.

Davidson, E.A., Hart, S.C., Shanks, C.A., Firestone, M.K., 1991. Measuring gross nitrogen mineralization, and nitrification by ^{15}N isotopic pool dilution in intact soil cores. *European Journal of Soil Science*, 42(3), 335-349.

Davidson, E.A., Stark, J.M. and Firestone, M.K., 1990. Microbial production and consumption of nitrate in an annual grassland. *Ecology*, *71*(5), 1968-1975.

De Santis, F., Allegrini, I., Di Filippo, P., Pasella, D., 1996. Simultaneous determination of nitrogen dioxide and peroxyacetyl nitrate in ambient atmosphere by carbon-coated annular diffusion denuder. *Atmospheric Environment*, *30*(14), 2637-2645.

Decock, C., Six, J., 2013. An assessment of N-cycling and sources of N_2O during a simulated rain event using natural abundance ^{15}N. *Agriculture, Ecosystems & Environment*, 165, 141-150.

Denk, T.R., Mohn, J., Decock, C., Lewicka-Szczebak, D., Harris, E., Butterbach-Bahl, K., Kiese, R., Wolf, B., 2017. The nitrogen cycle: A review of isotope effects and isotope modeling approaches. *Soil Biology and Biochemistry*, 105, 121-137.

Denman KL, Brasseur G, Chidthaisong A. et al., 2007. Couplings between changes in the climate system and biogeochemistry. In: Climate Change 2007: The Physical Science Basis. Contribution of Working Group I to the Fourth Assessment Report of the Intergovernmental Panel on Climate Change (eds Solomon S, Qin D, Manning M, Chen Z, Marquis M, Averyt KB, Tignor M, Miller HL), pp. 499–587. Cambridge University Press, Cambridge, UK and NY, USA.

Divers, M.T., Elliott, E.M. and Bain, D.J., 2013. Constraining nitrogen inputs to urban streams from leaking sewers using inverse modeling: implications for dissolved inorganic nitrogen (DIN) retention in urban environments. *Environmental Science & Technology*, *47*(4), 1816-1823.

Divers, M.T., Elliott, E.M. and Bain, D.J., 2014. Quantification of nitrate sources to an urban stream using dual nitrate isotopes. *Environmental Science & Technology*, *48*(18), 10580-10587.

Dubé, W.P., Brown, S.S., Osthoff, H.D., Nunley, M.R., Ciciora, S.J., Paris, M.W., McLaughlin, R.J., Ravishankara, A.R., 2006. Aircraft instrument for simultaneous, in situ measurement of NO_3 and N_2O_5 via pulsed cavity ring-down spectroscopy. *Review of Scientific Instruments*, *77*(3), 034101.

Dunlea, E.J., Herndon, S.C., Nelson, D.D., Volkamer, R.M., San Martini, F., Sheehy, P.M., Zahniser, M.S., Shorter, J.H., Wormhoudt, J.C., Lamb, B.K., Allwine, E.J., 2007. Evaluation of nitrogen dioxide chemiluminescence monitors in a polluted urban environment. *Atmospheric Chemistry and Physics*, *7*(10), 2691-2704.

Durka, W., Schulze, E.D., Gebauer, G. and Voerkeliust, S., 1994. Effects of forest decline on uptake and leaching of deposited nitrate determined from ^{15}N and ^{18}O measurements. *Nature*, *372*(6508), 765.

Elliott, E.M., Kendall, C., Boyer, E.W., Burns, D.A., Lear, G.G., Golden, H.E., Harlin, K., Bytnerowicz, A., Butler, T.J., Glatz, R., 2009. Dual nitrate isotopes in dry deposition: Utility for partitioning NO_x source contributions to landscape nitrogen deposition. *Journal of Geophysical Research - Biogeoscience*, *114*(G4), G04020.

Elliott, E.M., Kendall, C., Wankel, S.D., Burns, D.A., Boyer, E.W., Harlin, K., Bain, D.J., Butler, T.J., 2007. Nitrogen isotopes as indicators of NO_x source contributions to atmospheric nitrate deposition across the midwestern and northeastern United States. *Environmental Science & Technology*, *41*(22), 7661-7667.

Fang, Y., Koba, K., Makabe, A., Takahashi, C., Zhu, W., Hayashi, T., Hokari, A.A., Urakawa, R., Bai, E., Houlton, B.Z., Xi, D., 2015. Microbial denitrification dominates nitrate losses from forest ecosystems. *Proceedings of the National Academy of Sciences*, 112(5), 1470-1474.

Fang, Y., Koba, K., Makabe, A., Zhu, F., Fan, S., Liu, X., Yoh, M., 2012. Low $\delta^{18}O$ values of nitrate produced from nitrification in temperate forest soils. *Environmental Science & Technology*, 46(16), 8723-8730.

Feig, G.T., Mamtimin, B. and Meixner, F.X., 2008. Soil biogenic emissions of nitric oxide from a semi-arid savanna in South Africa. *Biogeosciences*, *5*(6), pp.1723-1738.

Felix, D.J., Elliott, E.M., Gish, T.J., McConnell, L.L., Shaw, S.L., 2013. Characterizing the isotopic composition of atmospheric ammonia emission sources using passive samplers and a combined oxidation-bacterial denitrifier approach. *Rapid Communications in Mass Spectrometry*, 27(20), 2239-2246.

Felix, J. D., Elliott, E. M., 2013. The agricultural history of human-nitrogen interactions as recorded in ice core $\delta^{15}N\text{-}NO_3^-$. *Geophysical Research Letter*, *40*(8), 1642-1646.

Felix, J.D., Elliott, E.M., Shaw, S.L., 2012. Nitrogen isotopic composition of coal-fired power plant NO_x: influence of emission controls and implications for global emission inventories. *Environmental Science & Technology*, *46*(6), 3528-3535.

Fernandez, I.J., Adams, M.B., SanClements, M.D. and Norton, S.A., 2010. Comparing decadal responses of whole-watershed manipulations at the Bear Brook and Fernow experiments. *Environmental Monitoring and Assessment*, *171*(1-4), 149-161.

Ferretti, M., Marchetto, A., Arisci, S., Bussotti, F., Calderisi, M., Carnicelli, S., Cecchini, G., Fabbio, G., Bertini, G., Matteucci, G. and De Cinti, B., 2014. On the tracks of Nitrogen deposition effects on temperate forests at their southern European range–an observational study from Italy. *Global Change Biology*, *20*(11), 3423-3438.

Fibiger, D. L., Hastings, M.G., 2016. First measurements of the nitrogen isotopic composition of NO_x from biomass burning. *Environmental Science & Technology*, *50*(21), 11569-11574.

Fibiger, D.L., Hastings, M.G., Lew, A.F., Peltier, R.E., 2014. Collection of NO and NO_2 for isotopic analysis of NO_x emissions. *Analytical Chemistry*, *86*(24), 12115-12121.

Firestone, M.K., Davidson, E.A., 1989. Microbiological basis of NO and N_2O production and consumption in soil. In *Exchange of trace gases between terrestrial ecosystems and the atmosphere*; Andreae, M. O.; Schimel, D. S.; Robertson, G. P. Eds.; John Wiley & Sons Ltd: Berlin, pp 7-21.

Fleischer, K., Rebel, K.T., Van Der Molen, M.K., Erisman, J.W., Wassen, M.J., Van Loon, E.E., Montagnani, L., Gough, C.M., Herbst, M., Janssens, I.A. and Gianelle, D., 2013. The contribution of nitrogen deposition to the photosynthetic capacity of forests. *Global Biogeochemical Cycles*, *27*(1), 187-199.

Frame, C.H. and Casciotti, K.L., 2010. Biogeochemical controls and isotopic signatures of nitrous oxide production by a marine ammonia-oxidizing bacterium. *Biogeosciences*, *7*, 2695-2709.

Friedman, S.H., Massefski, W. and Hollocher, T.C., 1986. Catalysis of intermolecular oxygen atom transfer by nitrite dehydrogenase of *Nitrobacter agilis*. *Journal of Biological Chemistry*, *261*(23), 10538-10543.

Fry, B., 2006. *Stable isotope ecology* (Vol. 521). New York: Springer.

Fuchs, H., Dubé, W.P., Lerner, B.M., Wagner, N.L., Williams, E.J., Brown, S.S., 2009. A sensitive and versatile detector for atmospheric NO_2 and NO_x based on blue diode laser cavity ring-down spectroscopy. *Environmental Science & Technology*, *43*(20), 7831-7836.

Füssel, J., Lam, P., Lavik, G., Jensen, M.M., Holtappels, M., Günter, M. and Kuypers, M.M., 2012. Nitrite oxidation in the Namibian oxygen minimum zone. *The ISME Journal*, 6(6), 1200.

Galbally, I. E., Roy, C.R., 1978. Loss of fixed nitrogen from soils by nitric oxide exhalation. *Nature*, 275, 734-735.

Galloway, J.N., Townsend, A.R., Erisman, J.W., Bekunda, M., Cai, Z., Freney, J.R., Martinelli, L.A., Seitzinger, S.P., Sutton, M.A., 2008. Transformation of the nitrogen cycle: recent trends, questions, and potential solutions. *Science*, 320(5878), 889-892.

Gaye, B., Nagel, B., Dähnke, K., Rixen, T. and Emeis, K.C., 2013. Evidence of parallel denitrification and nitrite oxidation in the ODZ of the Arabian Sea from paired stable isotopes of nitrate and nitrite. *Global Biogeochemical Cycles*, *27*(4), 1059-1071.

Glasius, M., Carlsen, M.F., Hansen, T.S., Lohse, C., 1999. Measurements of nitrogen dioxide on Funen using diffusion tubes. *Atmospheric Environment*, *33*(8), 1177-1185.

Granger, J. and Sigman, D.M., 2009. Removal of nitrite with sulfamic acid for nitrate N and O isotope analysis with the denitrifier method. *Rapid Communication in Mass Spectrometry*, *23*, 3753-3762.

Granger, J., Sigman, D.M., Lehmann, M.F., Tortell, P.D., 2008. Nitrogen and oxygen isotope fractionation during dissimilatory nitrate reduction by denitrifying bacteria. *Limnology and Oceanography*, 53(6), 2533-2545.

Granger, J., Sigman, D.M., Rohde, M.M., Maldonado, M.T., Tortell, P.D., 2010. N and O isotope effects during nitrate assimilation by unicellular prokaryotic and eukaryotic plankton cultures. *Geochimica et Cosmochimica Acta*, 74(3), 1030-1040.

Granger, J., Wankel, S.D., 2016. Isotopic overprinting of nitrification on denitrification as a ubiquitous and unifying feature of environmental nitrogen cycling. *Proceedings of the National Academy of Sciences*, 113(42), E6391-E6400.

Groffman, P.M., Altabet, M.A., Böhlke, J.K., Butterbach-Bahl, K., David, M.B., Firestone, M.K., Giblin, A.E., Kana, T.M., Nielsen, L.P., Voytek, M.A., 2006. Methods for measuring denitrification: diverse approaches to a difficult problem. *Ecological Applications*, 16(6), 2091-2122.

Groffman, P.M., Bain, D.J., Band, L.E., Belt, K.T., Brush, G.S., Grove, J.M., Pouyat, R.V., Yesilonis, I.C. and Zipperer, W.C., 2003. Down by the riverside: urban riparian ecology. *Frontiers in Ecology and the Environment*, *1*(6), pp.315-321.

Groffman, P.M., Holland, E.A., Myrold, D.D., Robertson, G.P., Zou, X., 1999. Denitrification. In: Robertson, G.P., Bledsoe, C.S., Coleman, D.C., Sollins, P. (Eds.), Standard soil methods for long-term ecological research. Oxford University Press, New York, pp. 272–290.

Groffman, P.M., Williams, C.O., Pouyat, R.V., Band, L.E. and Yesilonis, I.D., 2009. Nitrate leaching and nitrous oxide flux in urban forests and grasslands. *Journal of Environmental Quality*, *38*(5), 1848-1860.

Groffmann, P.M., Zak, D.R., Christensen, S., Mosier, A., Tiedje, J.M., 1993. Early spring nitrogen dynamics in a temperate forest landscape. *Ecology*, 74(5), 1579-1585.

Hall, S.J., Matson, P.A., 1999. Nitrogen oxide emissions after nitrogen additions in tropical forests. *Nature*, *400*(6740), 152-155.

Hall, S.J., Weintraub, S.R., Bowling, D.R., 2016. Scale-dependent linkages between nitrate isotopes and denitrification in surface soils: implications for isotope measurements and models. *Oecologia*, 181(4), 1221-1231.

Hart, S.C., Stark, J.M., Davidson, E.A., Firestone, M.K., 1994. Nitrogen mineralization, immobilization, and nitrification. In: Weaver, R.M., Bottomley, S., Bezdicek, P., Smith, D., Tabatabai, S., Wollum, A. (Eds.), Methods of Soil Analysis. Part 2: Microbiological and Biochemical Properties. Soil Science Society of America, Inc., Madison, WI, pp. 985-1018.

Haslun, J.A., Ostrom, N.E., Hegg, E.L. and Ostrom, P.H., 2018. Estimation of isotope variation of N 2 O during denitrification by Pseudomonas aureofaciens and Pseudomonas chlororaphis: implications for N 2 O source apportionment. *Biogeosciences*, *15*(12), pp.3873-3882.

Hastings, M.G., Casciotti, K.L., Elliott, E.M., 2013. Stable isotopes as tracers of anthropogenic nitrogen sources, deposition, and impacts. *Elements*, *9*(5), 339-344.

Hastings, M.G., Jarvis, J.C., Steig, E.J., 2009. Anthropogenic impacts on nitrogen isotopes of ice-core nitrate. *Science*, *324*(5932), 1288-1288.

Heil, J., Liu, S., Vereecken, H. and Brüggemann, N., 2015. Abiotic nitrous oxide production from hydroxylamine in soils and their dependence on soil properties. *Soil Biology and Biochemistry*, *84*, 107-115.

Herrmann, A.M., Witter, E. and Kätterer, T., 2007. Use of acetylene as a nitrification inhibitor to reduce biases in gross N transformation rates in a soil showing rapid disappearance of added ammonium. *Soil Biology and Biochemistry*, *39*(9), 2390-2400.

Högberg, P., Fan, H., Quist, M., Binkley, D.A.N., Tamm, C.O., 2006. Tree growth and soil acidification in response to 30 years of experimental nitrogen loading on boreal forest. *Global Change Biology*, 12(3), 489-499.

Homyak, P.M., Blankinship, J.C., Marchus, K., Lucero, D.M., Sickman, J.O., Schimel, J.P., 2016. Aridity and plant uptake interact to make dryland soils hotspots for nitric oxide (NO) emissions. *Proceedings of the National Academy of Sciences*, *113*(19), E2608-E2616.

Homyak, P.M., Kamiyama, M., Sickman, J.O., Schimel, J.P., 2016. Acidity and organic matter promote abiotic nitric oxide production in drying soils. *Global Change Biology*, *23*(4), 1735-1747.

Homyak, P.M., Vasquez, K.T., Sickman, J.O., Parker, D.R. and Schimel, J.P., 2015. Improving nitrite analysis in soils: Drawbacks of the conventional 2 M KCl extraction. *Soil Science Society of America Journal*, *79*(4), 1237-1242.

Hooper, A.B. and Terry, K.R., 1979. Hydroxylamine oxidoreductase of Nitrosomonas: production of nitric oxide from hydroxylamine. *Biochimica et Biophysica Acta (BBA)-Enzymology*, *571*(1), 12-20.

Hopkins, K.G., Morse, N.B., Bain, D.J., Bettez, N.D., Grimm, N.B., Morse, J.L., Palta, M.M., Shuster, W.D., Bratt, A.R. and Suchy, A.K., 2015. Assessment of regional variation in streamflow responses to urbanization and the persistence of physiography. *Environmental Science & Technology*, 49(5), 2724-2732.

Houlton, B.Z., Sigman, D.M. and Hedin, L.O., 2006. Isotopic evidence for large gaseous nitrogen losses from tropical rainforests. *Proceedings of the National Academy of Sciences*, 103(23), 8745-8750.

Hudman, R.C., Jacob, D.J., Turquety, S., Leibensperger, E.M., Murray, L.T., Wu, S.; Gilliland, A.B., Avery, M., Bertram, T.H., Brune, W., Cohen, R.C., 2007. Surface and lightning sources of nitrogen oxides over the United States: Magnitudes, chemical evolution, and outflow. *Journal of Geophysical Research - Atmosphere*, *112*(D12).

Hudman, R.C., Moore, N.E., Mebust, A.K., Martin, R.V., Russell, A.R., Valin, L.C., Cohen, R.C., 2012. Steps towards a mechanistic model of global soil nitric oxide emissions: implementation and space based-constraints. *Atmospheric Chemistry and Physics*, *12*(16), 7779-7795.

Hudman, R.C., Russell, A.R., Valin, L.C., Cohen, R.C., 2010. Interannual variability in soil nitric oxide emissions over the United States as viewed from space. *Atmospheric Chemistry and Physics*, *10*(20), 9943-9952.

Hutchinson, G.L., Yang, W.X., Andre, C.E., 1998. Overcoming humidity dependence of the chromium trioxide converter used in luminol-based nitric oxide detection. *Atmospheric Environment*, 33(1), 141-145.

Huygens, D., Boeckx, P., Templer, P., Paulino, L., Van Cleemput, O., Oyarzún, C., Müller, C. and Godoy, R., 2008. Mechanisms for retention of bioavailable nitrogen in volcanic rainforest soils. *Nature Geoscience*, *1*(8), 543.

Inselsbacher, E., Wanek, W., Strauss, J., Zechmeister-Boltenstern, S., Müller, C., 2013. A novel ^{15}N tracer model reveals: plant nitrate uptake governs nitrogen transformation rates in agricultural soils. *Soil Biology and Biochemistry*, 57, 301-310.

IPCC *2013: the physical science basis*. Contribution of working group I to the fifth assessment report of the Intergovernmental Panel on Climate Change. **2013**.

Jacob, D.J., Heikes, E.G., Fan, S.M., Logan, J.A., Mauzerall, D.L., Bradshaw, J.D., Singh, H.B., Gregory, G.L., Talbot, R.W., Blake, D.R., Sachse, G.W., 1996. Origin of ozone and NO_x in the tropical troposphere: A photochemical analysis of aircraft observations over the South Atlantic basin. *Journal of Geophysical Research - Atmosphere*, *101*(D19), 24235-24250.

Jaeglé, L., Martin, R.V., Chance, K., Steinberger, L., Kurosu, T.P., Jacob, D.J., Modi, A.I., Yoboué, V., Sigha-Nkamdjou, L., Galy-Lacaux, C., 2004. Satellite mapping of rain-induced nitric oxide emissions from soils. *Journal of Geophysical Research - Atmosphere*, *109*(D21), D21310.

Jaeglé, L., Steinberger, L., Martin, R.V., Chance, K., 2005. Global partitioning of NO_x sources using satellite observations: Relative roles of fossil fuel combustion, biomass burning and soil emissions. *Faraday Discussion*, *130*, 407-423.

Jang, M., Czoschke, N.M., Lee, S., Kamens, R.M., 2002. Heterogeneous atmospheric aerosol production by acid-catalyzed particle-phase reactions. *Science*, *298*(5594), 814-817.

Janssens, I.A. and Luyssaert, S., 2009. Carbon cycle: nitrogen's carbon bonus. *Nature Geoscience*, *2*(5), 318.

Janssens, I.A., Dieleman, W., Luyssaert, S., Subke, J.A., Reichstein, M., Ceulemans, R., Ciais, P., Dolman, A.J., Grace, J., Matteucci, G. and Papale, D., 2010. Reduction of forest soil respiration in response to nitrogen deposition. *Nature Geoscience*, *3*(5), 315.

Jencso, K.G., McGlynn, B.L., Gooseff, M.N., Wondzell, S.M., Bencala, K.E. and Marshall, L.A., 2009. Hydrologic connectivity between landscapes and streams: Transferring reach-and plot-scale understanding to the catchment scale. *Water Resources Research*, *45*(4).

Jones, L.C., Peters, B., Lezama Pacheco, J.S., Casciotti, K.L. and Fendorf, S., 2015. Stable isotopes and iron oxide mineral products as markers of chemodenitrification. *Environmental Science & Technology*, *49*(6), 3444-3452.

Jones, M. N., 1984. Nitrate reduction by shaking with cadmium: alternative to cadmium columns. *Water Research*, *18*(5), 643-646.

Kaiser, J., Hastings, M.G., Houlton, B.Z., Röckmann, T., Sigman, D.M., 2007. Triple oxygen isotope analysis of nitrate using the denitrifier method and thermal decomposition of N_2O. *Analytical Chemistry*, 79(2), 599-607.

Kaiser, J., Röckmann, T., Brenninkmeijer, C.A., 2004. Contribution of mass-dependent fractionation to the oxygen isotope anomaly of atmospheric nitrous oxide. *Journal of Geophysical Research - Atmospheres*, 109(D3).

Kaneko, M. and Poulson, S.R., 2013. The rate of oxygen isotope exchange between nitrate and water. *Geochimica et Cosmochimica Acta*, *118*, 148-156.

Kang, H., Stanley, E.H., Park, S.S., 2003. A sensitive method for the measurement of ammonium in soil extract and water. *Communications in Soil Science and Plant Analysis*, 34(15-16), 2193-2201.

Kaushal, S.S., Groffman, P.M., Band, L.E., Elliott, E.M., Shields, C.A. and Kendall, C., 2011. Tracking nonpoint source nitrogen pollution in human-impacted watersheds. *Environmental Science & Technology*, 45(19), 8225-8232.

Keiluweit, M., Gee, K., Denney, A., Fendorf, S., 2018. Anoxic microsites in upland soils dominantly controlled by clay content. *Soil Biology and Biochemistry*, 118, 42-50.

Kemeny, P.C., Weigand, M.A., Zhang, R., Carter, B.R., Karsh, K.L., Fawcett, S.E. and Sigman, D.M., 2016. Enzyme-level interconversion of nitrate and nitrite in the fall mixed layer of the Antarctic Ocean. *Global Biogeochemical Cycles*, *30*(7), 1069-1085.

Kendall, C., Elliott, E.M. and Wankel, S.D., 2007. Tracing anthropogenic inputs of nitrogen to ecosystems. *Stable isotopes in ecology and environmental science*, pp.375-449.

Kester, R.A., De Boer, W., Laanbroek, H.J., 1997. Production of NO and N_2O by Pure Cultures of Nitrifying and Denitrifying Bacteria during Changes in Aeration. *Applied Environmental Microbiology*, *63*(10), 3872-3877.

Kirkham, D.O.N., Bartholomew, W.V., 1954. Equations for following nutrient transformations in soil, utilizing tracer data 1. *Soil Science Society of America Journal*, 18(1), 33-34.

Kremen, A., Bear, J., Shavit, U. and Shaviv, A., 2005. Model demonstrating the potential for coupled nitrification denitrification in soil aggregates. *Environmental Science & Technology*, *39*(11), 4180-4188.

Le Quéré, C., Andres, R.J., Boden, T., Conway, T., Houghton, R.A., House, J.I., Marland, G., Peters, G.P., Van der Werf, G., Ahlström, A. and Andrew, R.M., 2012. The global carbon budget 1959–2011. *Earth System Science Data Discussions*, *5*(2), 1107-1157.

LeBauer, D.S., Treseder, K.K., 2008. Nitrogen limitation of net primary productivity in terrestrial ecosystems is globally distributed. *Ecology*, 89(2), 371-379.

Leimer, S., Kreutziger, Y., Rosenkranz, S., Beßler, H., Engels, C., Hildebrandt, A., Oelmann, Y., Weisser, W.W., Wirth, C. and Wilcke, W., 2014. Plant diversity effects on the water balance of an experimental grassland. *Ecohydrology*, *7*(5), 1378-1391.

Lewicka-Szczebak, D., Well, R., Köster, J.R., Fuß, R., Senbayram, M., Dittert, K. and Flessa, H., 2014. Experimental determinations of isotopic fractionation factors associated with N_2O production and reduction during denitrification in soils. *Geochimica et Cosmochimica Acta*, *134*, 55-73.

Li, D., Wang, X., 2008. Nitrogen isotopic signature of soil-released nitric oxide (NO) after fertilizer application. *Atmospheric Environment*, *42*(19), 4747-4754.

Likens, G.E., Driscoll, C.T., Buso, D.C., 1996. Long-term effects of acid rain: response and recovery of a forest ecosystem. *Science*, *272*(5259), 244.

Lim, N.Y., Frostegård, Å. and Bakken, L.R., 2018. Nitrite kinetics during anoxia: The role of abiotic reactions versus microbial reduction. *Soil Biology and Biochemistry*, *119*, 203-209.

Liu, S., Lin, F., Wu, S., Ji, C., Sun, Y., Jin, Y., Li, S., Li, Z. and Zou, J., 2017. A meta-analysis of fertilizer-induced soil NO and combined NO+ N_2O emissions. *Global Change Biology*, *23*(6), 2520-2532.

Loick, N., Dixon, E.R., Abalos, D., Vallejo, A., Matthews, G.P., McGeough, K.L., Well, R., Watson, C.J., Laughlin, R.J. and Cardenas, L.M., 2016. Denitrification as a source of nitric oxide emissions from incubated soil cores from a UK grassland soil. *Soil Biology and Biochemistry*, *95*, 1-7.

Lovett, G.M. and Goodale, C.L., 2011. A new conceptual model of nitrogen saturation based on experimental nitrogen addition to an oak forest. *Ecosystems*, *14*(4), 615-631.

Ludwig, J., Meixner, F.X., Vogel, B. and Förstner, J., 2001. Soil-air exchange of nitric oxide: An overview of processes, environmental factors, and modeling studies. *Biogeochemistry*, *52*(3), 225-257.

Luz, B., Barkan, E., 2005. The isotopic ratios $^{17}O/^{16}O$ and $^{18}O/^{16}O$ in molecular oxygen and their significance in biogeochemistry. *Geochimica et Cosmochimica Acta*, 69(5), 1099-1110.

Macdonald, C.A., Anderson, I.C., Bardgett, R.D. and Singh, B.K., 2011. Role of nitrogen in carbon mitigation in forest ecosystems. *Current Opinion in Environmental Sustainability*, *3*(5), 303-310.

MacDonald, J.A., Dise, N.B., Matzner, E., Armbruster, M., Gundersen, P., Forsius, M., 2002. Nitrogen input together with ecosystem nitrogen enrichment predict nitrate leaching from European forests. *Global Change Biology*, 8(10), 1028-1033.

Maggi, F., Gu, C., Riley, W.J., Hornberger, G.M., Venterea, R.T., Xu, T., Spycher, N., Steefel, C., Miller, N.L., Oldenburg, C.M., 2008. A mechanistic treatment of the dominant soil

nitrogen cycling processes: Model development, testing, and application. Journal of Geophysical Research: *Biogeosciences*, 113(G2).

Magnani, F., Mencuccini, M., Borghetti, M., Berbigier, P., Berninger, F., Delzon, S., Grelle, A., Hari, P., Jarvis, P.G., Kolari, P. and Kowalski, A.S., 2007. The human footprint in the carbon cycle of temperate and boreal forests. *Nature*, *447*(7146), 849.

Mariotti, A., Germon, J.C., Hubert, P., Kaiser, P., Letolle, R., Tardieux, A., Tardieux, P., 1981. Experimental determination of nitrogen kinetic isotope fractionation: some principles; illustration for the denitrification and nitrification processes. *Plant and Soil*, 62(3), 413-430.

Mariotti, A., Landreau, A., Simon, B., 1988. ^{15}N isotope biogeochemistry and natural denitrification process in groundwater: application to the chalk aquifer of northern France. *Geochimica et Cosmochimica Acta*, 52(7), 1869-1878.

Mariotti, A., Leclerc, A. and Germon, J.C., 1982. Nitrogen isotope fractionation associated with the $NO_2^- \rightarrow N_2O$ step of denitrification in soils. *Canadian Journal of Soil Science*, *62*(2), pp.227-241.

Martin, T.S. and Casciotti, K.L., 2016. Nitrogen and oxygen isotopic fractionation during microbial nitrite reduction. *Limnology and Oceanography*, *61*(3), 1134-1143.

Mary, B., Recous, S., Robin, D., 1998. A model for calculating nitrogen fluxes in soil using ^{15}N tracing. *Soil Biology and Biochemistry*, 30(14), 1963-1979.

McCalley, C.K., Sparks, J. P., 2009. Abiotic gas formation drives nitrogen loss from a desert ecosystem. *Science*, *326*(5954), 837-840.

McIlvin, M.R., Casciotti, K.L., 2011. Technical updates to the bacterial method for nitrate isotopic analyses. *Analytical Chemistry*, *83*(5), 1850-1856.

McKenney, D.J., Johnson, G.P. and Findlay, W.I., 1984. Effect of temperature on consecutive denitrification reactions in Brookston clay and Fox sandy loam. *Applied and Environmental Microbiology*, *47*(5), 919-926.

McKenney, D.J., Lazar, C. and Findlay, W.J., 1990. Kinetics of the nitrite to nitric oxide reaction in peat. *Soil Science Society of America Journal*, *54*(1), 106-112.

McKenney, D.J., Shuttleworth, K.F., Vriesacker, J.R. and Findlay, W.I., 1982. Production and loss of nitric oxide from denitrification in anaerobic Brookston clay. *Applied and Environmental Microbiology*, *43*(3), 534-541.

Medinets, S., Skiba, U., Rennenberg, H. and Butterbach-Bahl, K., 2015. A review of soil NO transformation: Associated processes and possible physiological significance on organisms. *Soil Biology and Biochemistry*, *80*, 92-117.

Michalski, G., Meixner, T., Fenn, M., Hernandez, L., Sirulnik, A., Allen, E., Thiemens, M., 2004. Tracing atmospheric nitrate deposition in a complex semiarid ecosystem using $\Delta^{17}O$. *Environmental Science & Technology*, 38(7), 2175-2181.

Michalski, G., Savarino, J., Böhlke, J.K., Thiemens, M., 2002. Determination of the total oxygen isotopic composition of nitrate and the calibration of a $\Delta^{17}O$ nitrate reference material. *Analytical Chemistry*, 74(19), 4989-4993.

Michalski, G., Scott, Z., Kabiling, M., Thiemens, M.H., 2003. First measurements and modeling of $\Delta^{17}O$ in atmospheric nitrate. *Geophysical Research Letters*, 30(16).

Michalski, G., Kolanowski, M., Riha, K.M., 2015. Oxygen and nitrogen isotopic composition of nitrate in commercial fertilizers, nitric acid, and reagent salts. *Isotopes in Environmental and Health Study, 51*(3), 382-391.

Miller, M.F., 2002. Isotopic fractionation and the quantification of ^{17}O anomalies in the oxygen three-isotope system: an appraisal and geochemical significance. *Geochimica et Cosmochimica Acta*, 66(11), 1881-1889.

Miyazaki, K., Matsumoto, J., Kato, S., Kajii, Y., 2008. Development of atmospheric NO analyzer by using a laser-induced fluorescence NO_2 detector. *Atmospheric Environment, 42*(33), 7812-7820.

Morin, S., Savarino, J., Frey, M.M., Yan, N., Bekki, S., Bottenheim, J.W. and Martins, J.M., 2008. Tracing the origin and fate of NOx in the Arctic atmosphere using stable isotopes in nitrate. *Science*, *322*(5902), 730-732.

Morse, J.L., Durán, J., Groffman, P.M., 2015. Soil denitrification fluxes in a northern hardwood forest: the importance of snowmelt and implications for ecosystem N budgets. *Ecosystems*, 18(3), 520-532.

Müller, C., Stevens, R.J., Laughlin, R.J., 2004. A ^{15}N tracing model to analyse N transformations in old grassland soil. *Soil Biology and Biochemistry*, 36(4), 619-632.

Myrold, D.D., Tiedje, J.M., 1986. Simultaneous estimation of several nitrogen cycle rates using ^{15}N: theory and application. *Soil Biology and Biochemistry*, 18(6), 559-568.

Nadelhoffer, K.J., Emmett, B.A., Gundersen, P., Kjønaas, O.J., Koopmans, C.J., Schleppi, P., Tietema, A. and Wright, R.F., 1999. Nitrogen deposition makes a minor contribution to carbon sequestration in temperate forests. *Nature*, *398*(6723), 145.

Oelmann, Y., Kreutziger, Y., Bol, R. and Wilcke, W., 2007. Nitrate leaching in soil: Tracing the NO3− sources with the help of stable N and O isotopes. *Soil Biology and Biochemistry*, *39*(12), 3024-3033.

Oikawa, P.Y., Ge, C., Wang, J., Eberwein, J.R., Liang, L.L., Allsman, L.A., Grantz, D.A., Jenerette, G.D., 2015. Unusually high soil nitrogen oxide emissions influence air quality in a high-temperature agricultural region. *Nature Communication*, *6*, 8753.

Osaka, K.I., Ohte, N., Koba, K., Yoshimizu, C., Katsuyama, M., Tani, M., Tayasu, I., Nagata, T., 2010. Hydrological influences on spatiotemporal variations of $\delta^{15}N$ and $\delta^{18}O$ of nitrate in a forested headwater catchment in central Japan: Denitrification plays a critical role in groundwater. *Journal of Geophysical Research - Biogeosciences*, 115(G2).

Oswald, R., Behrendt, T., Ermel, M., Wu, D., Su, H., Cheng, Y., Breuninger, C., Moravek, A., Mougin, E., Delon, C., Loubet, B., 2013. HONO emissions from soil bacteria as a major source of atmospheric reactive nitrogen. *Science*, *341*(6151), 1233-1235.

Pape, L., Ammann, C., Nyfeler-Brunner, A., Spirig, C., Hens, K., Meixner, F.X., 2009. An automated dynamic chamber system for surface exchange measurement of non-reactive and reactive trace gases of grassland ecosystems. *Biogeosciences*, *6*(3), 405-429.

Pardo, L.H., Templer, P.H., Goodale, C.L., Duke, S., Groffman, P.M., Adams, M.B., Boeckx, P., Boggs, J., Campbell, J., Colman, B. and Compton, J., 2006. Regional Assessment of N Saturation using Foliar and Root $\delta^{15}N$. *Biogeochemistry*, *80*(2), 143-171.

Park, S., Pérez, T., Boering, K.A., Trumbore, S.E., Gil, J., Marquina, S., Tyler, S.C., 2011. Can N_2O stable isotopes and isotopomers be useful tools to characterize sources and microbial pathways of N_2O production and consumption in tropical soils?. *Global Biogeochemical Cycles*, *25*(1), GB1001.

Pérez, T., Garcia-Montiel, D., Trumbore, S., Tyler, S., Camargo, P.D., Moreira, M., Piccolo, M. and Cerri, C., 2006. Nitrous oxide nitrification and denitrification ^{15}N enrichment factors from Amazon forest soils. *Ecological Applications*, *16*(6), 2153-2167.

Peters, B.D., Babbin, A.R., Lettmann, K.A., Mordy, C.W., Ulloa, O., Ward, B.B. and Casciotti, K.L., 2016. Vertical modeling of the nitrogen cycle in the eastern tropical South Pacific oxygen deficient zone using high-resolution concentration and isotope measurements. *Global Biogeochemical Cycles*, *30*(11), 1661-1681.

Placella, S.A., Brodie, E.L., Firestone, M.K., 2012. Rainfall-induced carbon dioxide pulses result from sequential resuscitation of phylogenetically clustered microbial groups. *Proceedings of the National Academy of Sciences*, 109(27), 10931-10936.

Redling, K., Elliott, E., Bain, D., Sherwell, J., 2013. Highway contributions to reactive nitrogen deposition: tracing the fate of vehicular NO_x using stable isotopes and plant biomonitors. *Biogeochemistry*, *116*(1-3), 261-274.

Remde, A. and Conrad, R., 1991. Metabolism of nitric oxide in soil and denitrifying bacteria. *FEMS Microbiology Letters*, *85*(1), 81-94.

Rice, C.W., Tiedje, J.M., 1989. Regulation of nitrate assimilation by ammonium in soils and in isolated soil microorganisms. *Soil Biology and Biochemistry*, 21(4), 597-602.

Richter, A., Burrows, J.P., Nüß, H., Granier, C., Niemeier, U., 2007. Increase in tropospheric nitrogen dioxide over China observed from space. *Nature*, *437*(7055), 129-132.

Riemer, N., Vogel, H., Vogel, B., Anttila, T., Kiendler-Scharr, A., Mentel, T.F., 2009. Relative importance of organic coatings for the heterogeneous hydrolysis of N_2O_5 during summer in Europe. *Journal of Geophysical Research - Atmosphere*, *114*(D17), D17307.

Riha, K.M., Michalski, G., Gallo, E.L., Lohse, K.A., Brooks, P.D., Meixner, T., 2014. High atmospheric nitrate inputs and nitrogen turnover in semi-arid urban catchments. *Ecosystems*, 17(8), 1309-1325.

Robertson, G.P. and Vitousek, P.M., 2009. Nitrogen in agriculture: balancing the cost of an essential resource. *Annual Review of Environment and Resources*, *34*, 97-125.

Robinson, J.K., Bollinger, M.J., Birks, J.W., 1999. Luminol/H_2O_2 chemiluminescence detector for the analysis of nitric oxide in exhaled breath. *Analytical Chemistry*, 71(22), 5131-5136.

Rose, L.A., Elliott, E.M. and Adams, M.B., 2015a. Triple nitrate isotopes indicate differing nitrate source contributions to streams across a nitrogen saturation gradient. *Ecosystems*, *18*(7), 1209-1223.

Rose, L.A., Sebestyen, S.D., Elliott, E.M. and Koba, K., 2015b. Drivers of atmospheric nitrate processing and export in forested catchments. *Water Resources Research*, *51*(2), 1333-1352.

Rossi, R.J., Bain, D.J., Elliott, E.M., Divers, M. and O'neill, B., 2017. Hillslope soil water flowpaths and the dynamics of roadside soil cation pools influenced by road deicers. *Hydrological Processes*, *31*(1), 177-190.

Russow, R., Stange, C.F. and Neue, H.U., 2009. Role of nitrite and nitric oxide in the processes of nitrification and denitrification in soil: Results from ^{15}N tracer experiments. *Soil Biology and Biochemistry*, *41*(4), 785-795.

Rütting, T. and Müller, C., 2007. ^{15}N tracing models with a Monte Carlo optimization procedure provide new insights on gross N transformations in soils. *Soil Biology and Biochemistry*, *39*(9), 2351-2361.

Santoro, A.E. and Casciotti, K.L., 2011. Enrichment and characterization of ammonia-oxidizing archaea from the open ocean: phylogeny, physiology and stable isotope fractionation. *The ISME Journal*, *5*(11), 1796.

Scharko, N.K., Schütte, U.M., Berke, A.E., Banina, L., Peel, H.R., Donaldson, M.A., Hemmerich, C., White, J.R. and Raff, J.D., 2015. Combined flux chamber and genomics approach links nitrous acid emissions to ammonia oxidizing bacteria and archaea in urban and agricultural soil. *Environmental Science & Technology*, *49*(23), 13825-13834.

Schimel, J.P., Bennett, J., 2004. Nitrogen mineralization: challenges of a changing paradigm. *Ecology*, 85(3), 591-602.

Schimel, J.P., Jackson, L.E., Firestone, M.K., 1989. Spatial and temporal effects on plant-microbial competition for inorganic nitrogen in a California annual grassland. *Soil Biology and Biochemistry*, 21(8), 1059-1066.

Schleper, C. and Nicol, G.W., 2010. Ammonia-oxidising archaea–physiology, ecology and evolution. In *Advances in Microbial Physiology* (Vol. 57, pp. 1-41). Academic Press.

Schreiber, F., Wunderlin, P., Udert, K.M. and Wells, G.F., 2012. Nitric oxide and nitrous oxide turnover in natural and engineered microbial communities: biological pathways, chemical reactions, and novel technologies. *Frontiers in Microbiology*, *3*, 372.

Sebestyen, S.D., Boyer, E.W., Shanley, J.B., Kendall, C., Doctor, D.H., Aiken, G.R. and Ohte, N., 2008. Sources, transformations, and hydrological processes that control stream nitrate and dissolved organic matter concentrations during snowmelt in an upland forest. *Water Resources Research*, *44*(12).

Sebilo, M., Mayer, B., Nicolardot, B., Pinay, G. and Mariotti, A., 2013. Long-term fate of nitrate fertilizer in agricultural soils. *Proceedings of the National Academy of Sciences*, *110*(45), 18185-18189.

Sharpe, W.E., De Walle, D.R., Leibfried, R.T., Dinicola, R.S., Kimmel, W.G. and Sherwin, L.S., 1984. Causes of Acidification of Four Streams on Laurel Hill in Southwestern Pennsylvania 1. *Journal of Environmental Quality*, *13*(4), 619-631.

Shaw, L.J., Nicol, G.W., Smith, Z., Fear, J., Prosser, J.I. and Baggs, E.M., 2006. Nitrosospira spp. can produce nitrous oxide via a nitrifier denitrification pathway. *Environmental Microbiology*, *8*(2), 214-222.

Shi, W., Norton, J.M., 2000. Microbial control of nitrate concentrations in an agricultural soil treated with dairy waste compost or ammonium fertilizer. *Soil Biology and Biochemistry*, 32(10), 1453-1457.

Sigman, D.M., Casciotti, K.L., Andreani, M., Barford, C., Galanter, M.B.J.K., Böhlke, J.K., 2001. A bacterial method for the nitrogen isotopic analysis of nitrate in seawater and freshwater. *Analytical Chemistry*, 73(17), 4145-4153.

Singh, B.K., Bardgett, R.D., Smith, P., Reay, D.S., 2010. Microorganisms and climate change: terrestrial feedbacks and mitigation options. *Nature Reviews Microbiology*, 8(11), 779-790.

Skiba, U., Fowler, D. and Smith, K.A., 1997. Nitric oxide emissions from agricultural soils in temperate and tropical climates: sources, controls and mitigation options. *Nutrient Cycling in Agroecosystems*, *48*(1-2), 139-153.

Skiba, U., Smith, K.A., 1993. Nitrification and denitrification as sources of nitric oxide and nitrous oxide in a sandy loam soil. *Soil Biology and Biochemistry*, *25*(11), 1527-1536.

Smith, C.J., Chalk, P.M., Crawford, D.M., Wood, J.T., 1994. Estimating gross nitrogen mineralization and immobilization rates in anaerobic and aerobic soil suspensions. *Soil Science Society of America Journal*, 58(6), 1652-1660.

Smith, T.J., McNamara, J.P., Flores, A.N., Gribb, M.M., Aishlin, P.S. and Benner, S.G., 2011. Small soil storage capacity limits benefit of winter snowpack to upland vegetation. *Hydrological Processes*, *25*(25), 3858-3865.

Snider, D., Thompson, K., Wagner-Riddle, C., Spoelstra, J., Dunfield, K., 2015. Molecular techniques and stable isotope ratios at natural abundance give complementary inferences about N_2O production pathways in an agricultural soil following a rainfall event. *Soil Biology and Biochemistry*, 88, 197-213.

Soper, F.M., Boutton, T.W., Groffman, P.M., Sparks, J.P., 2016. Nitrogen trace gas fluxes from a semiarid subtropical savanna under woody legume encroachment. *Global Biogeochemical Cycles*, *30*(5), 614-628.

Staelens, J., Rütting, T., Huygens, D., De Schrijver, A., Müller, C., Verheyen, K. and Boeckx, P., 2012. In situ gross nitrogen transformations differ between temperate deciduous and coniferous forest soils. *Biogeochemistry*, *108*(1-3), 259-277.

Stange, C.F., Spott, O., Arriaga, H., Menéndez, S., Estavillo, J.M. and Merino, P., 2013. Use of the inverse abundance approach to identify the sources of NO and N_2O release from Spanish forest soils under oxic and hypoxic conditions. *Soil Biology and Biochemistry*, *57*, 451-458.

Stark, J.M., Hart, S.C., 1997. High rates of nitrification and nitrate turnover in undisturbed coniferous forests. *Nature*, 385(6611), 61-64.

Steinkamp, J., Ganzeveld, L.N., Wilcke, W., Lawrence, M.G., 2009. Influence of modelled soil biogenic NO emissions on related trace gases and the atmospheric oxidizing efficiency. *Atmospheric Chemistry and Physics*, *9*(8), 2663-2677.

Steinkamp, J., Lawrence, M.G., 2011. Improvement and evaluation of simulated global biogenic soil NO emissions in an AC-GCM. *Atmospheric Chemistry and Physics*, *11*(12), 6063-6082.

Stoddard J. L., 1994. Long-term changes in watershed retention of nitrogen. Its causes and aquatic consequences. In: Baker L. Ed. Environmental Chemistry of Lakes and Reservoirs. Washington, DC: American Chemistry Society. 223-84.

Su, H., Cheng, Y., Oswald, R., Behrendt, T., Trebs, I., Meixner, F.X., Andreae, M.O., Cheng, P., Zhang, Y., Pöschl, U., 2011. Soil nitrite as a source of atmospheric HONO and OH radicals. *Science*, *333*(6049), 1616-1618.

Sun, X., Ji, Q., Jayakumar, A. and Ward, B.B., 2017. Dependence of nitrite oxidation on nitrite and oxygen in low-oxygen seawater. *Geophysical Research Letters*, *44*(15), 7883-7891.

Sutka, R.L., Ostrom, N.E., Ostrom, P.H., Breznak, J.A., Gandhi, H., Pitt, A.J. and Li, F., 2006. Distinguishing nitrous oxide production from nitrification and denitrification on the basis of isotopomer abundances. *Applied and Environmental Microbiology*, *72*(1), 638-644.

Taylor, B.W., Keep, C.F., Hall Jr, R.O., Koch, B.J., Tronstad, L.M., Flecker, A.S., Ulseth, A.J., 2007. Improving the fluorometric ammonium method: matrix effects, background fluorescence, and standard additions. *Journal of the North American Benthological Society*, 26(2), 167-177.

Templer, P.H., Lovett, G.M., Weathers, K.C., Findlay, S.E. and Dawson, T.E., 2005. Influence of tree species on forest nitrogen retention in the Catskill Mountains, New York, USA. *Ecosystems*, *8*(1), 1-16.

Templer, P.H., Silver, W.L., Pett-Ridge, J., M. DeAngelis, K. and Firestone, M.K., 2008. Plant and microbial controls on nitrogen retention and loss in a humid tropical forest. *Ecology*, *89*(11), 3030-3040.

Thiemens, M.H., 2006. History and applications of mass-independent isotope effects. *Annual Review of Earth and Planetary Sciences*, 34, 217-262.

Tilman, D., Wedin, D., Knops, J., 1996. Productivity and sustainability influenced by biodiversity in grassland ecosystems. *Nature*, 379(6567), 718-720.

Tilsner, J., Wrage, N., Lauf, J. and Gebauer, G., 2003. Emission of gaseous nitrogen oxides from an extensively managed grassland in NE Bavaria, Germany. *Biogeochemistry*, *63*(3), 249-267.

Trevors, J.T., 1996. Sterilization and inhibition of microbial activity in soil. *Journal of Microbiological Methods*, *26*(1-2), 53-59.

Van Cleemput, O. and Baert, L., 1984. Nitrite: a key compound in N loss processes under acid conditions?. *Plant and Soil*, *76*(1-3), 233-241.

Van Dijk, S.M., Gut, A., Kirkman, G.A., Gomes, B.M., Meixner, F.X. and Andreae, M.O., 2002. Biogenic NO emissions from forest and pasture soils: Relating laboratory studies to field measurements. *Journal of Geophysical Research - Atmospheres*, *107*(D20).

Venterea, R.T. and Rolston, D.E., 2000. Nitric and nitrous oxide emissions following fertilizer application to agricultural soil: Biotic and abiotic mechanisms and kinetics. *Journal of Geophysical Research - Atmospheres*, *105*(D12), 15117-15129.

Venterea, R.T., Rolston, D.E.E. and Cardon, Z.G., 2005. Effects of soil moisture, physical, and chemical characteristics on abiotic nitric oxide production. *Nutrient Cycling in Agroecosystems*, *72*(1), 27-40.

Vinken, G.C.M., Boersma, K.F., Maasakkers, J.D., Adon, M., Martin, R.V., 2014. Worldwide biogenic soil NO_x emissions inferred from OMI NO_2 observations. *Atmospheric Chemistry and Physics*, *14*(18), 10363-10381.

Walker, C.B., De La Torre, J.R., Klotz, M.G., Urakawa, H., Pinel, N., Arp, D.J., Brochier-Armanet, C., Chain, P.S.G., Chan, P.P., Gollabgir, A. and Hemp, J., 2010. Nitrosopumilus maritimus genome reveals unique mechanisms for nitrification and autotrophy in globally distributed marine crenarchaea. *Proceedings of the National Academy of Sciences*, *107*(19), 8818-8823.

Walters, W.W., Goodwin, S. R., Michalski, G., 2015a. Nitrogen stable isotope composition ($\delta^{15}N$) of vehicle-emitted NO_x. *Environmental Science & Technology*, *49*(4), 2278-2285.

Walters, W.W., Tharp, B.D., Fang, H., Kozak, B.J., Michalski, G., 2015b. Nitrogen isotope composition of thermally produced NO_x from various fossil-fuel combustion sources. *Environmental Science & Technology*, *49*(19), 11363-11371.

Wang, Y., McElroy, M.B., Martin, R.V., Streets, D.G., Zhang, Q., Fu, T.M., 2007. Seasonal variability of NO_x emissions over east China constrained by satellite observations: Implications for combustion and microbial sources. *Journal of Geophysical Research - Atmospheres*, *112*(D6).

Ward, B.B., 2011. Nitrification: an introduction and overview of the state of the field. In *Nitrification* (pp. 3-8). American Society of Microbiology.

Wild, R.J., Edwards, P.M., Dubé, W.P., Baumann, K., Edgerton, E.S., Quinn, P.K., Roberts, J.M., Rollins, A.W., Veres, P.R., Warneke, C., Williams, E.J.A, 2014. Measurement of Total Reactive Nitrogen, NO_y, together with NO_2, NO, and O_3 via Cavity Ring-down Spectroscopy. *Environmental Science & Technology*, *48*(16), 9609-9615.

Wilson, K., Goldstein, A., Falge, E., Aubinet, M., Baldocchi, D., Berbigier, P., Bernhofer, C., Ceulemans, R., Dolman, H., Field, C. and Grelle, A., 2002. Energy balance closure at FLUXNET sites. *Agricultural and Forest Meteorology*, *113*(1), 223-243.

Wollheim, W.M., Pellerin, B.A., Vörösmarty, C.J. and Hopkinson, C.S., 2005. N retention in urbanizing headwater catchments. *Ecosystems*, 8(8), 871-884.

Wrage, N., Groenigen, J.V., Oenema, O. and Baggs, E.M., 2005. A novel dual-isotope labelling method for distinguishing between soil sources of N_2O. *Rapid Communications in Mass Spectrometry*, *19*(22), 3298-3306.

Wrage, N., Velthof, G.L., Van Beusichem, M.L. and Oenema, O., 2001. Role of nitrifier denitrification in the production of nitrous oxide. *Soil Biology and Biochemistry*, *33*(12-13), 1723-1732.

Xu, L., Furtaw, M.D., Madsen, R.A., Garcia, R.L., Anderson, D.J., McDermitt, D.K., 2006. On maintaining pressure equilibrium between a soil CO2 flux chamber and the ambient air. *Journal of Geophysical Research - Atmospheres*, *111*(D8).

Yang, W. X.; Meixner, F. X. Laboratory studies on the release of nitric oxide from sub-tropical grassland soils: The effect of soil temperature and moisture. In *Gaseous Nitrogen*

emissions from grasslands; Jarvis, S. C.; Pain, B. F. Eds.; Cab International: 1997; pp 67-71.

Yienger, J.J., Levy, H., 1995. Empirical model of global soil-biogenic NO_x emissions. *Journal of Geophysical Research - Atmospheres*, *100*(D6), 11447-11464.

Yoshida, N., Hattori, A., Saino, T., Matsuo, S. and Wada, E., 1984. $^{15}N/^{14}N$ ratio of dissolved N2O in the eastern tropical Pacific Ocean. *Nature*, *307*(5950), 442.

Young, E.D., Galy, A., Nagahara, H., 2002. Kinetic and equilibrium mass-dependent isotope fractionation laws in nature and their geochemical and cosmochemical significance. *Geochimica et Cosmochimica Acta*, 66(6), 1095-1104.

Yu, L., Zhu, J., Mulder, J., Dörsch, P., 2016. Multiyear dual nitrate isotope signatures suggest that N-saturated subtropical forested catchments can act as robust N sinks. *Global Change Biology*, 22(11), 3662-3674.

Yu, Z. and Elliott, E.M., 2017. Novel method for nitrogen isotopic analysis of soil-emitted nitric oxide. *Environmental Science & Technology*, *51*(11), pp.6268-6278.

Yu, Z.; Slater, L.D., Schäfer, K.V., Reeve, A.S., Varner, R.K., 2014. Dynamics of methane ebullition from a peat monolith revealed from a dynamic flux chamber system. *Journal of Geophysical Research - Biogeoscience*, *119*(9), 1789-1806.

Zhang, L., Altabet, M.A., Wu, T., Hadas, O., 2007. Sensitive measurement of NH_4^+ $^{15}N/^{14}N$ ($\delta^{15}NH_4^+$) at natural abundance levels in fresh and saltwaters. *Analytical Chemistry*, 79(14), 5297-5303.

Zhang, R., Tie, X., Bond, D.W., 2003. Impacts of anthropogenic and natural NO_x sources over the US on tropospheric chemistry. *Proceedings of the National Academy of Sciences*, *100*(4), 1505-1509.

Zhang, S., Fang, Y., Xi, D., 2015. Adaptation of micro-diffusion method for the analysis of ^{15}N natural abundance of ammonium in samples with small volume. *Rapid Communications in Mass Spectrometry*, 29(14), 1297-1306.

Zheng, D., Hunt Jr, E.R. and Running, S.W., 1993. A daily soil temperature model based on air temperature and precipitation for continental applications. *Climate Research*, *2*(3), 183-191.

Zhou, X., Qiao, H., Deng, G., Civerolo, K., 1999. A method for the measurement of atmospheric HONO based on DNPH derivatization and HPLC analysis. *Environmental Science & Technology*, *33*(20), 3672-3679.

Zhu-Barker, X., Cavazos, A.R., Ostrom, N.E., Horwath, W.R. and Glass, J.B., 2015. The importance of abiotic reactions for nitrous oxide production. *Biogeochemistry*, *126*(3), 251-267.

Zumft, W.G., 1997. Cell biology and molecular basis of denitrification. *Microbiology and Molecular Biology Reviews*, 61(4), 533-616.